Ge-on-Si LASER for Silicon Photonics

by
Rodolfo E. Camacho-Aguilera

B.S./ M.S. Materials Science & Engineering
Georgia Institute of Technology, 2008

Submitted to the Department of Materials Science and Engineering in Partial
Fulfillment of the Requirements for the Degree of
Doctor of Philosophy in Materials Science and Engineering
at the
Massachusetts Institute of Technology

June 2013

©2013 Massachusetts Institute of Technology. All rights reserved.

Signature of Author: ______________________________
Department of Materials Science and Engineering
April 23rd, 2013

Certified by: ______________________________
Lionel C. Kimerling
Thomas Lord Professor of Materials Science and Engineering
Thesis Supervisor

Accepted by: ______________________________
Gerbrand Ceder
Professor of Materials Science and Engineering
Chair, Departmental Committee on Graduate Students

"Do you want to get lucky or do you want to understand it?"

-Lionel C. Kimerling

"Germanium paved the way to Silicon microelectronics...now Silicon is paving the way to Germanium optoelectronics"

Ge-on-Si LASER for Silicon Photonics

By
Rodolfo E. Camacho-Aguilera

Abstract

Ge-on-Si devices are explored for photonic integration. Importance of Ge in photonics has grown and through techniques developed in our group we demonstrated low density of dislocations ($<1x10^{9}cm^{-2}$) and point defects Ge growth for photonic devices. The focus of this document will be exclusively on Ge light emitters.

Ge is an indirect band gap material that has shown the ability to act like a pseudo direct band gap material. Through the use of tensile strain and heavy doping, Ge exhibits properties thought exclusive of direct band gap materials. Dependence on temperature suggests strong interaction between indirect bands, Δ and L, and the direct band gap at Γ. The behavior is justified through increase in photoluminescence on Ge. The range of efficient emission is to 120℃ with the first band interaction, and above 400℃ on the second band interaction.

Low defect concentration in Ge is achieved through chemical vapor deposition at high vacuum ($\sim 1x10^{-8}$ mbar) in a two-step process. The high temperature growth and low concentration of particles permits epitaxial growth with low defect concentration. Chemical selectivity forbids Ge growth on oxide. Oxide trenches permit the growth on Si for a variety of shapes, without detrimentally affecting the strain of the Ge devices.

Dopant concentration above intrinsic growth concentration, $\sim 1x10^{19}cm^{-3}$ phosphorus, have been achieved through a series of methods non-CMOS, spin-on dopant; and CMOS, implantation and delta doping. All the techniques explored use enhanced dopant diffusion

observed in Ge under heavy n-type doping. A dopant source, or well, is used to distribute the dopants in the Ge without increasing the defect concentration.

The approach lead to the development of electrically injected devices, LEDs and LDs. Ge pnn double heterostructure diodes were made under low, ~$1x10^{18}cm^{-3}$, and heavy n-type doping, >$1x10^{19}cm^{-3}$. Both devices showed improved performance compared to pin Ge LED. Furthermore, heavy doped Ge diodes exhibit evidence of bleaching or transparency.

The techniques described permitted the development of Ge-on-Si laser with a concentration ~$1\text{-}2x10^{19}cm^{-3}$. It is the first demonstration of a Ge laser optically pumped working under the direct band gap assumption like other semiconductors. It represents the evidence of carrier inversion on an indirect band gap semiconductor. With $50cm^{-1}$ gain, the material shows Fabry-Perot cavity behavior.

Finally, we demonstrated a fully functioning laser diode monolithically integrated on Si. Ge pnn lasers were made exhibiting a gain >$1000cm^{-1}$ and exhibiting a spectrum range of over 200nm, making Ge the ideal candidate for Si photonics.

Acknowledgements

This work was supported by the Fully Laser Integrated Photonics (FLIP) program under APIC Corporation, and sponsored by the Naval Air Warfare Center - Aircraft Division (NAWC-AD) under OTA N00421-03-9-002. And the MURI Project for monolithically integrated laser devices supervised by Dr. Gernoke.

I was supported by a NSF Graduate Research Fellowship award number 1122374, and the NDSEG fellowship. Both gave me the freedom to choose the research that I found most interesting.

Travelling nurtures the mind but the people that are around us nurture our soul. I have been lucky to be in a position where I have been blessed with both sides. I moved from Mexico City to Atlanta, Georgia to study my undergrad career, and 9 years later I am concluding a path in the Massachusetts Institute of Technology. I would like to tell my old self that everything would be fine, and the hard work and any other difficulty is just a door blocking the next big steps, the next big trips, the next big discoveries. More importantly, I would like to tell myself that there are always people that make all the experiences easier and more valuable.

I cannot hold in simple words the gratitude I have for all the people that have been on my life that lead me to this point, all these people that made my life more colorful and full of stories. My parents, who have been an inspiration, have supported me through all the difficult point of my academic career and advised me on life. My brothers have also let me know what the meaning is of showing by example, and letting me know that there is always more things to do, and other ways of seeing the same problems.

My first advisor, Jud Ready, in Georgia Tech, deserves to be mentioned. He was the first person in academic to believe in me, and who made me an addict to research and discovery. I thank you for all the amazing experiences you let me search, and the doors that working with you has opened.

My advisor, Lionel Kimerling, taught me how to rationalize all the problems, to break them down, and to never, NEVER, give up. He is somebody I aspire to be. His ideas aggregated over years of experience permit to have an intuition that allowed my work to happen. I will never

forget the first interview,: "I have three projects, but one of them is extremely difficult and small chance of success". Thank you for letting me take that small chance.

Dr. Jurgen Michel helped with direction of the project and advise in what direction to take in the project, as understanding the behaviors observe in Ge devices electrically and optically.

Prof. Jifeng Liu and Dr. Xioachen Sun deserve special thanks, since they developed most of the initial theory on Ge, without you this work would not be possible. Your ingenuity and creativity gave me the foundation and tools to develop this work.

Dr. Jonathan Bessette gave me all the knowledge require for characterizing electrically my devices, understand optical behavior, and gave me his friendship to support all the rest.

Dr. Marco Romagnoli for his advice to characterize the devices under heavy current, and to successfully achieved a Ge laser.

Yan Cai deserves her own special place of honor. She developed hand by hand most of the device characterization, theoretical work and device fabrication for this work. She is a great researcher, a magnificent engineer and good friend.

My labmates, who made every day interesting, supported through the characterization and fabrication of the devices. Zhaohong Han helped through the understanding of the Ge bands effects, and even though the time has been short, the conversations progressed to several ideas that will resonate in this work. Neil Patel and Corentin Monmeyran helped to keep my sanity and through interesting conversations to explored new realms of Ge devices. Tim Milakovich helped on the TEM characterization of devices and conversations for the future work on Ge emitters.

All the technicians in MTL MIT gave me the foundations to develop my devices, and to keep digging for new techniques and new ideas in old tools. You showed me what is being a thinkerer.

Finally I want to thank my friends how are like my family; and Monika Avello. You have made this trip I called grad-school livable and enjoyable. You have been my support and my teachers. Every time I fall, I know I can count on them. I wish only I have been able to offer you as much help as you have offer me over the years.

Table of Contents

Chapter 1. Introduction 12

1.1 Ge light emitters 15

1.2 Thesis goal and outline 17

Chapter 2. Background and Theory 19

2.1 Ge Band Structure 20

2.1.1 Ge Band Engineering 21

2.1.2 Ge n-type dopants 24

2.1.3 Ge heavy doping 25

2.2 Gain and Light emission on Ge 28

2.2.1 Radiative Transitions 30

2.2.2 Non-radiative Transitions 32

2.2.3 Gain in Ge 44

2.3 Resonant Cavities 47

2.3.1. Fabry-Perot cavities 49

2.3.2. Microdisks 52

Chapter 3. Ge growth 56

3.1. Growth of n+ Ge films 56

3.1.1 Tensile strain and dislocations 66

3.1.2 Facet formation 76

3.1.3 Pressure dependence on Ge waveguides growth 81

3.2 Ge Nonbuffer growth 84

3.2.1 Materials preparation 86

3.2.2 Bufferless P-doped Ge 87

3.2.3 Bufferless B doped Ge 95

Chapter 4. n-type Doping 100

4.1 Doping Germanium 101

4.2 Dopant Solid Sources 108

4.2.1 Spin-on-Dopant 109

4.2.2 Implantation 116
4.3 Delta Doping [141] 127
Chapter 5. Bandgap Modifiers 141
5.1 Band Gap Narrowing [156] 142
5.1.2 Conclusions 151
5.2 Temperature effect 152
5.2.1 Band gap Shift 153
5.2.2 Conduction Bands contribution 158
5.2.3 Experimental Results 161
5.2.4 Conclusions 167
Chapter 6. pnn Ge LED 169
6.1 Introduction 169
6.2 Low doped Ge-LED <1x10^{19}cm^{-3} 172
6.2.1 Materials Preparation 173
6.2.2. Post-growth temperatures effect 176
6.2.3 I-V Diode Characteristic of Low doped-Ge 177
6.2.4 Photoluminescence and Electroluminescence of low doped-Ge 180
6.3 Highly doped Ge-LED >1x10^{19}cm^{-3} 184
6.3.1 Materials Preparation 184
6.3.2 IV Diode characteristic and Electroluminescence 188
6.3.3 Comparison of heavy and low doping 195
6.4 Conclusions 198
Chapter 7. Ge-on-Si Laser 200
7.1 Optical pump Lasers 200
7.1.1 Materials Setup 200
7.1.2 Optical Photoluminescence 204
7.1.3 Other resonators 206
7.1.4 Conclusions 208
7.2 Double Heterostructure Ge Laser Diode [22] 209
7.2.1 Materials Preparation 209
7.2.2 Simulation 213

7.2.3 Electrical Luminescence 219
7.2.4 Conclusion 229
Chapter 8. Summary and future work 230
8.1 Applications 231
8.2 Future Work 232
Appendix 236
Appendix. I RCA cleaning 236
Appendix II. Standard Ge growth 238
Appendix III. Highly doped Ge through Spin on Dopant 241
Appendix IV. n-Ge diodes 242
Appendix V. Ge Selective grown PNN device 244
Appendix VI. Contact resistant experiment 248
Appendix VII. a-Si Long annealing for H outdiffusion 250
Appendix VIII. Threshold energy for CCCH indirect Auger 251
References 253

Table of Figures

Figure 1.- Total energy breakdown simulation comparing 64 cores ATAC with different conditions and 11nm electrical mesh counterparts. The energy output is normalized to ATAC ideal which represents the best conditions for an all optical integrated system [7]. 13
Figure 2.- Schematic of an all Integrated Electronic-Photonic Circuit. The model can be expanded to as many cores (circuit control) as desired. 14
Figure 3.- Ge band structure. [28] 20
Figure 4.- Comparison of the band structure of unstrained, tensile strained, doped tensile strained Ge. 21
Figure 5.- Biaxial tensile strain calculation for Ge showing changes of bandgap in Γ (direct), L and Δ (indirect) valleys. At 1.8% strain, Ge becomes a direct band gap material, and at 2.7% it becomes indirect again. Desired strain resides between 0.2-0.3% with Γ valley emission at 1550nm wavelength. 24
Figure 6.- Shrinkage (**Δ**) of the Energy gaps of the L band (111) and the **Γ** band (000) with respect to the Fermi Level (**ξ**) at 4K as a function of doping [44] 26
Figure 7.- 0.25% strain n-type Ge simulation showing dependence with doping on Fermi Level and band gap energies. Band edge intersection appears at lower dopant concentrations after considering BGN effects. 28
Figure 8.- Comparison of PL with emission wavelength of different doped Ge samples. PL intensity increases linearly with dopant concentration. 29
Figure 9.- Typical non-radiative recombination mechanisms 33
Figure 10.- Threading dislocation density simulation showing dependence of doping to minority carrier lifetime in Ge. Calculation based on theoretical work 35
Figure 11.- Variation of carrier recombination lifetime as a function of dopant concentration in Ge .τA-Ge is the calculated Auger recombination using C=10^{-31}cm^6/s. The excitation level is defined as L=n_{ex}/n_{dop}. [52] 37
Figure 12.- Schematic of CCCH direct and indirect Auger recombination 38
Figure 13.- Temperature dependence of minority carriers lifetime in Ge. [51] 40
Figure 14.-Radiative lifetime of n-type (P) and p-type (B) dopants in Ge [51] 41
Figure 15.- Infrared absorption spectrum of Ge thin film with n= 1×10^{19} cm^{-3} derived from transmittance data. Regimes I-IV are respectively dominated by intra-L-valley FCA, L $\rightarrow$ Γ intervalley scattering absorption, indirect gap+intervalley scattering absorption, and direct gap absorption.[57] 43
Figure 16.- Absorption spectra of a n + Ge mesa sample under 0 and 100 mW optical pumping. Negative absorption coefficients corresponding to optical gain are observed in the wavelength range [58]. 45
Figure 17.- Doping and carrier injection dependence to intrinsic material gain (colorbar) in Ge emitting at 1550nm wavelength. 46
Figure 18.- Gain comparison simulation on tensile strained-Ge n-type doped ~4.2x10^{19}cm^{-3} at different injection levels and wavelength emissions. Expected bandwidth of >400nm. 47
Figure 19.- Fabry-Perot Laser basic design. Active layer is Ge in all our designs. 50
Figure 20.- Typical shape of FP laser diode and semiconductor optical amplifier device cavities. [64] 51
Figure 21.- Schematic comparing FP with WGM and the difference in between reflections. 52

Figure 22.- Ge disk simulation showing that coupling of the internal mode is lossy and extremely low, despite different designs. (a) and (b) show a completely enclosed Ge microdisk, while (c) shows a microdisk with a waveguide for coupling. They show that microdisks coupling is smaller than 0.01% making them unsuitable for lasers. 53
Figure 23.- Bulk Ge absorption along different wavelengths energies. 54
Figure 24.- Schematics depicting mechanisms during a CVD process and an schematic of the growth model limited by either mass transport (J_{gs}) or surface kinetics (J_s) [70] 58
Figure 25.-Schematic diagram showing the effect of kinetics, temperature and pressure on growth rate. 59
Figure 26.- Schematic and plot of two-step Ge epitaxial growth strain with growth temperature 62
Figure 27.- Schematic showing that under growth Ge film are relaxed. Due to differences in linear coefficient of thermal expansion between Si and Ge, Ge films are tensile strained. 63
Figure 28.- Blanket epitaxial Ge film, grown on Si with 20nm Ge buffer. Buffer thickness <20nm causes pinholes formation in blanket films, attributed to threading dislocations. 64
Figure 29.- SIMS analysis of Ge implanted samples and *in situ* doped Ge growth. *In situ* growth shows uniform doping with no addition of defects. Full activation of carriers is achieved. 66
Figure 30.- Effect of n- and p-type doping on 60° dislocation velocity in germanium at T = 500°C. A neutral impurity such as Sn has no effect on dislocation velocity at a concentration of $2x10^{19}cm^{-3}$. Correlation between temperature and speed increase on intrinsic Ge is shown.[92] 68
Figure 31.- Average etch pit density of intrinsic Germanium grown on squares surfaces of diverse widths after cycle annealing. 71
Figure 32.- Plane view TEM sample of waveguide growth Ge at doping conc. ~$1x10^{19}cm^{-3}$. The dislocation density is ~10^9cm^{-2} around the interface which represents the Ge buffer. n+Ge shows <10^8cm^{-2} dislocation density. 73
Figure 33.-Schematic showing that reducing the fact angle is equivalent to moving atoms to the interface 74
Figure 34.- XRD from Ge waveguides and thin films doped to $1x10^{19}cm^{-3}$. FHWM does not provide information due to the heavy amount of oxide in the Ge waveguides. There should be a blue shift in emission with these conditions, but due to the heavy doping, it is compensated. 75
Figure 35.- Profilometry of different undoped Ge mesas growth at 9.8mtorr at 720°C for 2hrs. Widths varying from 100µm to 5µm demonstrate growth limits due to window size. 77
Figure 36.- Height change from different Ge waveguides doped to $1x10^{19}cm^{-3}$. Growth conditions at 9.8mtorr with 350nm of oxide window. Ge waveguides width changes from 3µm to 1µm with steps of 0.1µm. Maximum height observed is ~650nm and minimum of ~450nm. Growth is terminated due to the (111) facets. 78
Figure 37.- Schematic showing Borgrstrom construction with a convex surface $0° < \theta < 180°$. In convex structures h_1 is slower than h_2. 78
Figure 38.- Wulff construction for cross-sectional morphology of Ge selectively grown in trenches with (a) a sidewall angle (ϕ) close to 45°, and (b) a sidewall angles (ϕ) close to 90°. The dotted lines demonstrate the Wulff construction of (111), (311) and (100) facets. The area enclosed by the dotted lines and the SiO_2 side wall determines the shape of the GeSi crystal (thick black lines). The profiles shown here correspond to the moment when the trench is just filled up. This model is compared to cross-

sectional SEM pictures of Ge grown in trenches with ~ 45° sidewall in (c) and ~ 90° sidewall in (d). The Wulff construction model is in good agreement with growth morphology shown in the SEM pictures.[100] 80
Figure 39.- Ge waveguide SEM growth under 9mtorr for 90min. 81
Figure 40.- Growth rates at different pressures under same time and conditions. Dashed line shows predicted growth rates, and dotted line the most possible case where the growth differences are noise on the measurement. 82
Figure 41.- Final thickness of growths at different pressures, and same temperature and time. Linear dependence to rate of deposition is obtained due to similar growth conditions in time and flow. 83
Figure 42.- (a) SIMS results showing P concentration in Ge-on-Si. Notice that the buffer acts as a dopant sink with concentrations above $1x10^{20}cm^{-3}$. (b) schematic shows typical Ge trench growth and where the dopant sink appears, which is in the Ge buffer. 85
Figure 43.- Bufferless Ge growth upper view SEM in constrained oxide window. A lateral constraint of <$2\mu m$ results in single crystalline epi-Ge growth. 87
Figure 44 . TEM image of the Si-Ge interface after bufferless growth in a constraint area. The[001] plane matches the lattice in both materials. 88
Figure 45.- Ge heavily doped to $1x10^{19}cm^{-3}$ grown without buffer. The dislocation density is ~$6x10^{8}cm^{-2}$. 89
Figure 46. XRD peaks of Germanium (004). Symmetrical measurement shows compressive strain in the z direction, translating into a ~0.25%tensile stress. Distribution of strain is observed through comparison of FHWM. 90
Figure 47. SEM image for Si/Ge interface with dimension constrained bufferless growth. [001] plane matches the lattice in both materials. Cross-section(a) and upperview (b) show faceting and continuity of the Ge channels. 91
Figure 48. SEMs show top-view of the Ge channel growth and their change in roughness as their width change. Observe that at thicknesses above 1um the faceting is no longer discernible. 91
Figure 49.- Normalized to peak intensity PL comparing buffer and bufferless Ge growths, showing the potential of higher doping shown through the red-shift to 1640nm= ~$3x10^{19}cm^{-3}$ n-type active dopant. Both films showed same tensile strain ~0.25% 92
Figure 50.- Ge growth with rate of 12:1 P:Ge flow for 5min and intrinsic growth for 90min. Heavy twinning is observed, prevented the continuity but keeping single crystalline body. 93
Figure 51.- Ge growth with rate of 12:1 P:Ge flow for 5min and intrinsic growth for 90min. Continuity is observed throughout the surface of the Ge waveguide. 94
Figure 52.- Plane-view TEM aligned to (220) plane to quantify the threading dislocations. It shows a variation from >$10^{9}cm^{-2}$ to ~$10^{8}cm^{-2}$ in the upper surfaces. 95
Figure 53.- Ge growth with rate of 12:1 B:Ge flow for 5min and intrinsic Ge growth after that. Ge waveguides show heavy twinning and the possibility of columnar bamboo growth. 96
Figure 54.- 2:1 B:Ge growth at 9.8mTorr. Multiple grains are formed showing evidence of bamboo formation. 97
Figure 55.- 4:1 B:Ge SEM cross-section and plane-view. Continuity and slight twinning is observed. Faceting indicates single crystal. 98

Figure 56.- Comparison of total active concentration of growth at different temperatures. Limits to the maximum active concentration are set at $1x10^{19}cm^{-3}$. [88] 100
Figure 57.- Solid Solubility of P, As and Sb in Ge[110, 111]. These lines represent single measurements taken. Solid solubility might differ from author to author.[112] 102
Figure 58.- Doubly charged diffusivities from extrapolated diffusivities [115, 123-125] for temperatures ranging between 600 to 750 °C. The diffusivity for heavy doped materials is up to two orders of magnitude higher than undoped and implanted samples. [125] 107
Figure 59.- Depiction of the strategy for doping Ge through dopant sources. 109
Figure 60.- Microscopy of SOD sample after annealing and removal of diffusion barrier. (A-C) represent different points where PL was performed. (C) shows the highest PL photoluminescence. SOD is not uniform as observed. 110
Figure 61.- Hall effect active dopant concentration measurements from SOD Ge samples under different annealing temperature (Celsius). Random active doping of SOD matrix is observed. 111
Figure 62.-PL of different annealing times and temperatures for same SOD. PL intensity has been normalized to max emission. Under similar conditions emission peak slightly shifts to 1600nm, caused only by dopant. 112
Figure 63.- Ge/Si interdiffusion on the substrate after 800˚C 20min . The substrate/Ge contact shows a heavy increase in Ge concentration that extends 200nm into the substrate. 113
Figure 64.- SIMS of interface accumulation of P dopants in the interfaces. Not uniform doping throughout the Ge body is caused by the slower diffusion due to the dopant concentration. Accumulation of the dopants in the substrate represents a secondary source of dopant loss. 114
Figure 65.- Comparison of room temperature PL spectra of n+Ge doped with $1x10^{19}cm^{-3}$ P, fabricated by in-situ doping, diffusion doping from spin-on dopants, and ion implantation. (Courtesy from J.Liu) 115
Figure 66.- Concept to prevent damaged germanium in the final structure 119
Figure 67.- Si implanted wafers. RTA for 3 min and slow annealing for 2 hrs are shown. Theoretical simulation matches the diffusion profiles. 119
Figure 68.- 750°C 30sec anneal without CMP. Band gap shift in implanted samples is larger than *in situ* material. The active dopant concentrations reach <$5.5x10^{19}cm^{-3}$. BGN relation is shown as the parameter to relate active doping to peak shift. 121
Figure 69.-Ge implantated P PL after different annealing temperatures (℃). Max peak shift observed at 1660nm~$2.7x10^{19}cm^{-3}$ active doping under 60 sec anneal. 122
Figure 70.- P and As PL after different annealing temperatures and times. Peak at 1685 nm ~ $3.75X10^{19}cm^{-3}$ active doping under 60 sec anneal. 123
Figure 71.-P and Sb coimplantation PL after different annealing temperatures and times. Peak at 1714nm ~$5.4x10^{19}cm^{-3}$ under 60 sec anneal 124
Figure 72.- P implantation sample pre- and post- CMP. Small transition is observed 125
Figure 73.- P and Sb coimplantation sample pre- and post- CMP. Difference in emission is due to slow diffusion of the dopants, causing nonuniform redistribution. Similar is observed in P and As coimplantation. 126
Figure 74.- SIMS analysis of P and As sample (a) before annealing, (b) after annealing at 700 C for 3min. 127

Figure 75.- Schematic of grown layers. The dopant reservoir are alternating layers of Ge and P. Dopant concentration in Ge increases dramatically in the dopant reservoir without being linear due to slow diffusion into the intrinsic undoped Ge used in the layers. 130
Figure 76.- SEM images of (a) in-situ doped Ge and (b) delta doped Ge grown with source grown at 400C. Notice difference in surface roughness which indicates the arrest of epitaxial growth. 131
Figure 77.- AFM measurements showing the progression in roughness with different annealing temperatures. (a) waveguide anneal at 600°C for 2min RMS of 38nm, (b) film anneal at 600°C for 30sec RMS of 42nm, (c) film anneal at 600°C for 60sec RMS of 37nm, and (d) film anneal at 700°C for 30 sec RMS of 35nm. 132
Figure 78.- XRD of Ge doped samples. All samples indicate an average 0.2-0.3% strain. The difference in shapes strives from the upper layer of defective Ge; broadening the X-ray emission. 133
Figure 79.- TEM measurements of different sections of a delta sample after annealed at 700°C for 30sec. (a) shows the buffer with a dislocation density >10^9cm^{-2}, (b) shows the delta layer with dislocation density around 2x10^9cm^{-2}. 134
Figure 80.- SIMS profiles of as-grown P delta doped Ge, with P deltas grown at (a) 400°C , (b) 450°C and (c) 360°C. Dopant diffusion from delta source increases the concentration of P in the underlying high temperature Ge region. 135
Figure 81.- SIMS profiles of dopant redistribution from delta doped Ge grown at 400°C. The diffusion of the dopant is time and temperature dependent, becoming more uniform at higher temperatures but limited by outdiffusion at longer times. 136
Figure 82.- Comparison of P solid solubility[110] in Ge and observed maximum active carrier concentration of delta doping at different temperatures. 139
Figure 83.- Schematic representing doped strained Ge band structure under (a) no effects, (b) temperature increase, and (c) renormalization (BGR) and bandgap narrowing (BGN) 141
Figure 84.- Schematic showing the differences between Ge doped under (a) no effect, (b) Burstein-Moss shift, and (c) BGN shift. 143
Figure 85.- PL intensity for heavily n-type doped Ge. BGN shift in emission compares to doping concentration of samples analyzed. Arrows show peak shift from the different doping concentrations, red shifting with increasing active dopant. 146
Figure 86.- Experimental observations of BGN as a function of n-type doping concentrations at 300K. A linear relationship is observed. The data falls between Jain's theory (L band) and equation 4 of this work for the minimum change (**Γ** band).Table shows parameters used for equation 3 and 4. 147
Figure 87.- FWHM comparison with Peak energy . The linear fitting just shows that there's an increase in FHWM with shift in BGN. 148
Figure 88.- FHWM comparison to doping concentration. 149
Figure 89.- Schematic of temperature effects shown as (a) lattice expansion described by Varshni, equation, and (b) multi-body interactions resulting on intravalley and intervalley carrier interactions. 153
Figure 90.- Ge waveguide PL showing the shape of Ge emission at 300K. 155
Figure 91.-Simulation of biaxial Strain change with substrate temperature and photon wavelength energy. As temperature increases, the bandgap increases, producing an effective blue shift in theory. 157

Figure 92.- Theoretical calculation comparing free electron density to temperature on the different conduction bands. As the temperature increases, the redistribution of electrons increases on the different conduction bands, achieving degeneracy on the Δ band. 160
Figure 93.- Comparison of integral PL intensity respect to temperature on n+Ge tensile strained at ~$1x10^{19}cm^{-3}$. An activation energy of ~0.102eV corresponds to Arrhenius calculations. [27] 161
Figure 94.- PL at high temperatures of Ge n+type (a) ~$3.5x10^{19}cm^{-3}$ and (b) ~$1x10^{19}cm^{-3}$. 162
Figure 95.-Peak energy representing of $Eg\Gamma$ versus temperature of observed PL. There are three regimes observed corresponding to the different points of L and Δ interactions. 163
Figure 96.- Integral PL and Peak energy plots against 1/kT of undoped strained Ge. Increase in PL and edge emission show both **Γ** BGN and L –valley contribution on **Γ.** 164
Figure 97.- Integral PL and Peak energy plots against 1/kT of degenerate doped strained Ge. Increase in PL and edge emission show both Γ BGN and L –valley contribution on Γ. Degenerate doping shows a larger BGN in the peak emission and faster drop in emission with increase in temperature. 165
Figure 98.- Peak energy of n+Ge ~$1x10^{19}cm^{-3}$ at high temperatures different regimes exist at high temperatures. 167
Figure 99.- Si/Ge/Si pnn heterojunction LED migrograph cross section showing all the elements of the device. 172
Figure 100.- Monte Carlo Simulation of implanted poly-Si with P at 50keV, dose of $1x10^{16}$ and 7 degrees angle. 174
Figure 101.-Device setup for characterizing through fiber coupling. 175
Figure 102.- Experimental setup diagram to determine the emission characteristics and behavior of the devices. (Courtesy from J. Bessette) 176
Figure 103.-Ge pnn-low doped SIMS analysis. Processing post-growth temperatures increase affects the overall device quality due to dopant loss. Both buffer and upper layer lose dopant. The buffer acts like a sink, as mentioned. The upper layer deposition temperature (<580 ℃) is high enough to lose the dopant concentration. 177
Figure 104.- I-V characteristics of low doped diode ~$7x10^{18}cm^{-3}$ 178
Figure 105.- Ge pnn Metal pads damage. It is theorized due to electromigration. (Courtesy from J. Bessette) 179
Figure 106.- Fiber coupling through different waveguides. (Courtesy of J.Bessette) 181
Figure 107.-Electroluminescence spectra of edge emission from cleaved pnn diode cross-section. Peak shift is attributed to high voltage. (Courtesy of J.Bessette) 182
Figure 108.-Comparison of EL emission from top and edge emission from same device. (Courtesy of J.Bessette) 183
Figure 109.- Doping implantation on poly-Si for B at 23keV 7° degrees tilt. Notice the Gaussian formed to permit proper doping throughout the contact. 186
Figure 110.- Kelvin Bridge resistor schematic. 187
Figure 111.-pnn Ge heterostructure LED design for higher dopant above >$1x10^{19}cm^{-3}$. 188
Figure 112.- I-V comparison of two different dopant concentration LEDs. Highly doped LED shows typical degenerate system under inversion. 189
Figure 113.- pnn Ge diode PL and EL at 130mA continuous current normalized spectra with temperature control to 300K. (Courtesy of J.Bessette) 190

Figure 114.- pnn Ge diode emission difference on peak emission (λp) with injected current. The maximum peak shift is equivalent to a temperature increase up to ~500˚C 191
Figure 115.- Low injection and high injection of highly doped Ge pnn LEDs. Emission and peak emission match with calculations. 192
Figure 116.- Ge LEDs power emission to injected current, comparing FHWM to current. Bleaching onset is observed at 350mA corresponding to a current density ~35kA/cm^2. 193
Figure 117.- Internal quantum efficiency of pnn Ge LED compared at different current. 194
Figure 118.- Simulation of pnn Ge diode efficiency at different lengths comparing how the absorption changes the efficiency of the device. 195
Figure 119.- Comparing low and high dopant concentration devices due to their power according to different biases. (Courtesy of J. Bessette) 196
Figure 120.- Comparing low and high dopant concentration devices due to their power output according to different currents, use to determine responsivity. 197
Figure 121.- Measured responsivity (R) of pnn Ge LED under heavy doping ~3.5x10^{19}cm^{-3}. 198
Figure 122.- n+Ge waveguides SEM micropraphs showing facet and structure, acting as a FP resonator. 201
Figure 123.- Ge waveguide 2-D simulation showing modal loss and number modes different thickness. 203
Figure 124.- Schematic of the setup used for testing and probing n+Ge waveguides. Q-switched laser with pulse duration of 1.5 ns and a repetition rate of 1 kHz was used with a photomultiplier/photodetector. 204
Figure 125.- PL emission progression of n+Ge waveguides under different probing conditions from Q-switch laser, and L-I curve showing the threshold of lasing. [177]. 205
Figure 126.- PL emission from n+Ge microdisk. The value extends to the high 1650nm with a resonance distance of 300nm. The peaks are seen as an artifact between the separation of microdisk and the optical fiber. 207
Figure 127.- Micrograph of Ge toroids 208
Figure 128.- Ge device CMP after Piranha clean 210
Figure 129.- pnn Ge LD device cross-section of the final device. 211
Figure 130.- Schematic of the measurement set-up 212
Figure 131- Simulation of Ge modal gain on 300nm thick Ge, permitting only 3 modes. Only TE modes have low enough losses for light emission. 213
Figure 132.-Simulation of total modal losses in Ge waveguides according from thickness of Ge. (Courtesy of Y.Cai) 214
Figure 133.-pnn Ge diode index of refraction change under 1.2V 215
Figure 134.- Carrier density simulation in pnn Ge diode, showing that the maximum current is concentrated on the interface. 216
Figure 135.- Heat Generation and Joule heat is concentrated in Ge body. 217
Figure 136.- Simulation of band gap behavior under 1.2V on pnn Ge diode. 217
Figure 137.-pnn Ge band bending change from type II to pseudo I under heavy bias. 218
Figure 138.- pnn Ge diode simulation of current input at different voltages. Two different behaviors are consistent with band bending in Ge device 219

Figure 139.- pnn Ge diode IV characteristics. The ideality factor used is 2, and leakage current is 95% applied bias. Resistance is <1Ω reaching limits of the characterization tool. Shoulder at 5mA is expected from laser behavior. 220
Figure 140.- Ge laser emission spectrum before (a) and after (b) threshold. The cavity length of the waveguide is 333µm and the waveguide height about 100nm. Current injection employed pulse widths of 50µs at 800Hz and 15°C. The detector spectral resolution was 1.2nm 221
Figure 141.- Cross-section FIB of Ge pnn diode after failure mode occurs. Notice that Ge and Si present no extra defects. 222
Figure 142.- L-I curve for a 270µm long waveguide device. 40µs electrical pulses were used at 1000Hz. Measurement temperature was 25°C. 223
Figure 143.- Spectra of Ge lasers with different Ge waveguide heights. The measured laser line wavelengths are (a)1576nm, (b)1622nm, and (c) 1656nm. 225
Figure 144.- Calculated net gain in 4.5x10^{19}cm^{-3} n-type strained Ge. Bandwidth of emission is >300nm. 226
Figure 145.- Simulation of gain clamping condition for two different Ge waveguide thicknesses (100nm: solid line; 300nm: dashed line). The axes plot the corresponding modal loss and gain spectrum for the two different injection levels that are needed to overcome the respective modal losses and to achieve lasing. 227
Figure 146.- Absorption of p+Ge/n+Ge/n+Si diode under different thicknesses of n+Ge 233
Figure 147.- Band alignment of Ge/Ge/Si diode under heavy bias. 234
Figure 148.- Schematic describing process for increasing dopant concentration through Spin on dopant. 241

Chapter 1. Introduction

In past decades, there has been a boom in information technology, allowed mainly by the shrinking size of transistors. This trend is forecasted by Moore's Law, which states that the number of transistors in an integrated circuit (IC) doubles nearly every 18 months [1]. As this trend continues, the other components of the devices also keep shrinking such as electrical connections. Such a trend leads to adjacent problems as parasitic capacitances, resistive losses, heat buildup, and so on. These are large technological barriers causing the semiconductor industry to become increasingly concerned about the viability of Moore's law [2]. Theoretical and experimental work has shown the plausibility of performance increase; however, as nanotechnology provides increased circuit densities, the RC delay increases leading to increase power density of Si devices. A device dimension under 130nm will be dominated by the passive power density[3]. Furthermore, current multicore architectures will not allow performance to scale with Moore's Law. This is specially seen in parallel applications where the ability to communicate within a single chip of multiple components decreases as the density of components increases. As the technology to make smaller and faster transistors improves, communication between different parts of chips or multiple chips will be constrained. Continued scalability depends on Si-CMOS technology maintaining the power density while boosting performance. Si photonics are an extremely promising solution to the problem [4] of communication between cores. Si photonics has been studied for integration of microelectronics and optical devices [5-7]. Application of photonics research is evident in the telecommunication fiber optics industry, where light is transported over the entire world carrying information of all sorts. On-chip Si photonics research has set the limitations for integration [8], those being CMOS compatibility and availability for photonic devices

fabrication. Of the active devices, light sources, lasers or LEDS, have not fulfilled the requirements.

The integration of microelectronics and photonics was further studied with All-to-All Computing (ATAC) architecture [6]. It consists of an architecture using on-chip optical communications instead of electronic paths for multicore communication, bypassing the energy and bandwidth limitations electrical pathways have. As seen in Figure 1, ATAC architecture decreases the energy requirements when compared to state of the art 11nm all electrical connection network architecture (EMesh). ATAC main limitation to outperform its electrical counterparts is the requirement of a gated light emitter such as an integrated on-chip laser.

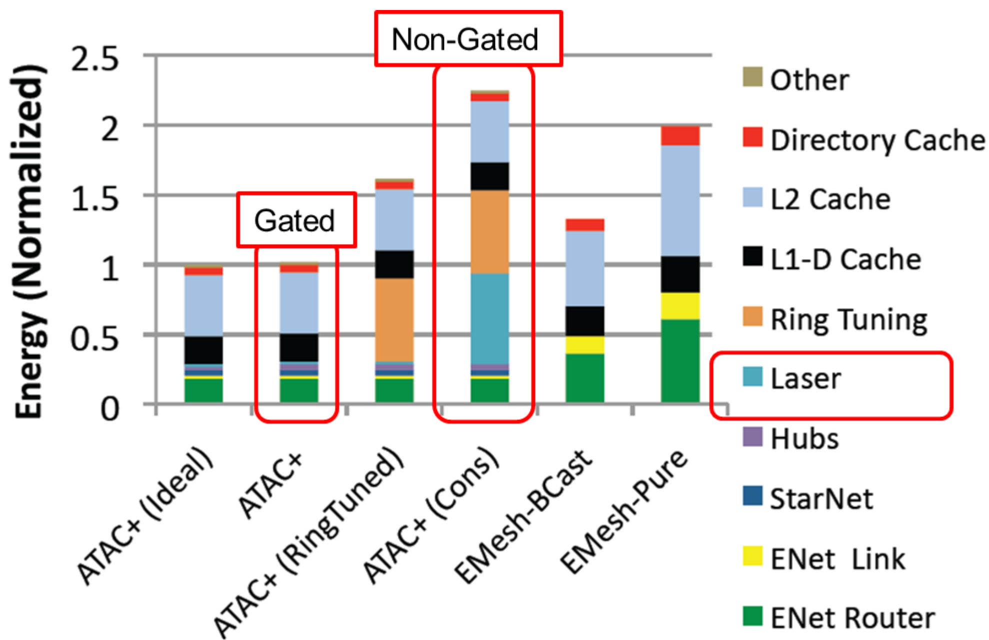

Figure 1.- Total energy breakdown simulation comparing 64 cores ATAC with different conditions and 11nm electrical mesh counterparts. The energy output is normalized to ATAC ideal which represents the best conditions for an all optical integrated system [7].

To achieve a gated light source on-chip laser, the device material has to be compatible with an integrated fabricated chip and operate without a modulator to reduce energy cost. The

first issue is dependent on the CMOS technology conditions and what is required to be CMOS compatible. With CMOS-compatibility, knowledge and expertise developed through the semiconductor industry for Si is retained. Furthermore, CMOS has the ability to scale. The second condition, modulation, is bounded to material selection properties.

Modulated Si on-chip III-V lasers have been demonstrated through evanescently coupling an active AlGaInAs multi quantum well through a Si waveguide [9]. Furthermore, the approach has been extended to a fully integrated laser on chip with modulators and photodetectors integrated as demonstrated by scientists at INTEL creating a Si photonics link [10]. Their design shows clear limitations such as hybrid laser bonding of III-V on Si and separation between the detection and light emission. Furthermore, the addition of non-temperature stable devices, such as III-V lasers [11, 12], and non-CMOS process, as bonding, endangers the integrity and operability of the microelectronic chip. CMOS Integration is needed for an entire chip being capable of generating and detecting the light without endangering the electrical chip. Furthermore, hybrid systems show serious limitations in yield, cost and integration. A vision of CMOS on-chip integration is depicted on Figure 2.

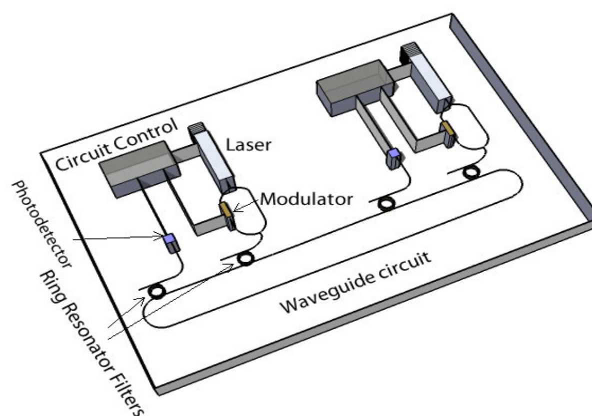

Figure 2.- Schematic of an all Integrated Electronic-Photonic Circuit. The model can be expanded to as many cores (circuit control) as desired.

Si-based photonic components are fully CMOS compatible. On material compatibility, Germanium (Ge) covers all CMOS prerequisites. Ge has been a widely investigated material since it was used for the first transistor [13, 14]. It was the semiconductor material of choice in the late 40's since it was grown with the best crystalline quality at that time [15]. It literally paved the road for Si-electronics. Ge was heavily researched and a vast amount of theories and experiments were built, which are still of prime importance today in more than just the microelectronics industry.

Ge, as well, has been demonstrated to work as the active material in modulators and photodetectors [16-19]. Of the ATAC network only a CMOS light source is missing. Ge is suggested as the only material capable of conforming to the CMOS standards and be a light emitter for photonic integration.

In this thesis work, it will be demonstrated that Ge can emit light as an LED[20] and as a laser [21, 22] in the near-infrared regime (NIR). These discoveries open the doors for full opto-electronic integration.

1.1 Ge light emitters

Recent work has established the potential of n-type Ge as a light emitting material for integrated Si photonic networks [16-19, 21]. The introduction of tensile strain and n-type dopants increase the radiative efficiency of the direct bandgap transition enabling room temperature operation of Ge LEDs[20, 21, 23]. The realization of an optically or electrically pumped Ge laser on Si has been hindered by loss mechanisms associated with injection, including scattering and absorption from cladding structures surrounding the active Ge region. These additional losses require the development of more concentrated doping profiles since the optical gain of Ge is strongly dependent on the presence of activated dopants and defects in the

Ge crystal matrix [24]. Minimizing loss through waveguide and laser cavity design is also crucial to achieving a functioning electrically pumped laser.

Ge has shown bleaching under heavy doping ~$1x10^{19}cm^{-3}$ and 0.25% tensile strain [25]. The measured Ge gain is ~$50cm^{-1}$. New evidence has shown that Ge gain values are higher than $2000cm^{-1}$ through ultra-fast pumping, and suggesting new paths of carriers recombination [26]. The gain can be utilized for formation of optical pump devices, as will be shown, but for electrical devices higher gain is required to overcome additional sources of loss. It will be shown that doping is directly correlated to the gain in Ge.

Moreover, Ge light emitters show a series of desirable properties:

- monolithic integration since it can be grown straight on Si
- multi-λ emission, providing access to wavelength division multiplexing
- ease of electrical injection with CMOS metals
- thermally stable up to 120 ℃
- process integrated with basic CMOS foundries
- high volume production, reducing the cost through scaling

Adding to these properties, simulations have shown that Ge can perform under similar conditions to typical III-V lasers, as seen in Table 1. Most importantly is that under new findings Ge keeps performing better than expected.

Table 1.- Ge and InGaAsP simulation comparison from known variables.

	Ge	InGaAsP
FCA (cm^{-1})	**45-340**	**~10**
J_{th} (kA/cm^2)	**5.8-16**	**1.15**
η_d	**0.15**	**0.23**
P_o (I=50mA) mW	**5.5 -18**	**9**

Ge has the possibility to revolutionize the technology of the world as we know it and pave the road for the future of microphotonics as it did in the past for microelectronics.

1.2 Thesis goal and outline

The goal of this thesis work is to investigate the properties of Ge under heavy doping, high carrier injection and high temperatures. As will be seen, knowledge of the material has been scattered since the beginning of the semiconductor race. Ge as a light emitter has small maturity and its properties have not been fully understood. Furthermore, the final goal is to demonstrate the procedure and results of a CMOS compatible laser through optical and electrical injection.

In **Chapter 2**, theoretical and experimental work on tensile strained Ge is shown. In order to understand interactions between conduction bands, different levels of strain and doping concentration, a theoretical framework is presented. A summary of carrier recombination and what it represents for Ge light emission is portrayed. A result of total gain in the material will be described. Laser cavity design is covered through description of the resonators made for this work, Fabry-Perot cavities and microdisks.

In **Chapter 3**, an explanation of the processing of Ge is described. Dependence on temperature, doping and pressure are explained, as well as abnormalities found in our system. A description for growth according to the dimensions desired is explained. Furthermore, a description of the correlation of doping with single crystallinity is shown with non-buffer growth, adding possible for new routes for Ge growth.

In **Chapter 4**, dopant descriptions and difficulties in contributing to the net carriers in the Ge band structure are illustrated. Different approaches used to overcome boundaries such as

the kinetics of growth are demonstrated. Processes developed through this work, such as spin-on-dopant, implantation diffusion and delta-doping, are described in detail.

In **Chapter 5**, band gap changes with increased doping and temperature are covered. The effects are divided between band-gap narrowing for dopants and electron-phonon interactions for thermal excitations. The importance between overlap of density of states between different bands and excess free carrier density is also described. Ge operation under high temperatures is compared to other semiconductors.

In **Chapter 6**, Ge pnn LEDs are shown at different doping concentrations. Electrical and optical characteristics are shown. Performance at higher temperatures and evidence of unexpected effects are described. Evidence of gain is shown under high injections.

In **Chapter 7**, Ge-on-Si LASER is described. Comparison between optically pumped and electrically pumped devices is shown. Simulations are shown that Ge can perform effectively as a laser under certain conditions. Description of loss mechanisms and optimization of the structure are discussed.

Finally, a summary with the findings for Ge light emitters will be shown. Simulations of possible new directions in the laser design and the study of the Ge band are portrayed.

Appendixes contain steps and conditions for fabrication of Ge devices.

Chapter 2. Background and Theory

The Ge theoretical background is reviewed to understand how Ge as an indirect bandgap semiconductor can become a laser. In order to use Ge as a lasing material, the material properties of interest are Ge band structure and engineering of it; Ge gain and optical properties; and the laser cavity design.

The properties of Ge band structure and the need for heavy n+doping and strain are presented. Band gap engineering is presented as a solution for achieving pseudo-direct band gap properties in Ge. Heavy doping further modifies the band structure by a phenomena call band-gap-narrowing (BGN).

The rates of Ge carrier recombination, Ge radiative and nonradiative rates, and possible losses are discussed. Absence of defects provides the best conditions for radiative recombination and can be attained through high temperature growths. The relevance of Ge material quality to device optical gain and its implications to achieve lasing are explained.

Laser cavity design is explored with Ge-on-Si cladded with SiO_2. Multiple types of cavities were analyzed; however, a simple design was pursued. Fabry-Perot cavities are described as the simplest design and most effective way for demonstration of the Ge laser.

For this work, it is demonstrated that for Ge lasing a dopant concentration of $>10^{19}cm^{-3}$, carrier injection densities of $>10^{19}cm^{-3}$, and Fabry-Perot cavities are the simplest and most effective design for this demonstration. Through the reading of this work it will be evident that these steps are necessary to understand and further treat the problem of Ge on Si laser devices.

2.1 Ge Band Structure

Ge is normally recognized as a poor light emitting material due to its indirect band structure, as depicted in Figure 3. Germanium indirect band gap emission is a multiparticle process requiring electrons, holes and multiple phonons. The indirect transition tends to be slow due to the multibody interactions. However, the direct band-to-band optical transition in Ge is a very fast process with a radiative recombination rates ~4-5 orders of magnitude higher than that of the indirect transition. The direct transition involves only two-carrier interactions, instead of three-carriers as in indirect transition, making its likelihood more probable. Thus, the direct gap emission of Ge is, in principle, as efficient as that of direct gap III-V materials [20, 25, 27]. Moreover, Ge direct band transition occurs at 0.8ev ~ 1550nm which is an important wavelength for telecommunications. It is identified that the conduction band (CB) minimas of interest for recombination are Γ (direct), L and Δ(indirect), as seen in Figure 3.

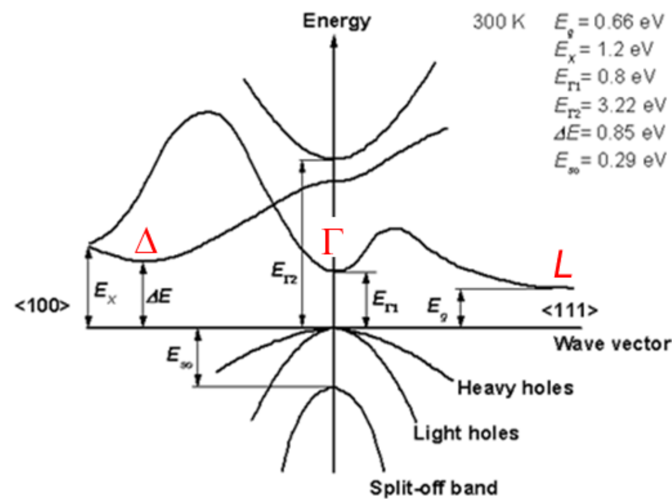

Figure 3.- Ge band structure. [28]

In order for Ge to work as a light emitter, a series of challenges, related to its band structure, have to be explored. First, the number of the electrons for the direct optical transition is deficient due to an indirect band structure. The Ge indirect bandgap is calculated to be $E_{gL}{}^{\mathrm{Ge}}$

= 0.66eV, and the direct bandgap is $E_{g\Gamma}^{Ge}$ =0.80eV. Fortunately, Ge can be made into a pseudo-direct band gap material through introduction of tensile strain, as can be seen in Figure 4. The band energy difference is minimal and easily band engineered through strain. Second, under strain, heavy n-type doping equalizes the chemical potential between the electrons in different bands. Finally, effects to each band due to the heavy doping introduce faster recombination paths, preferentially to the direct band gap.

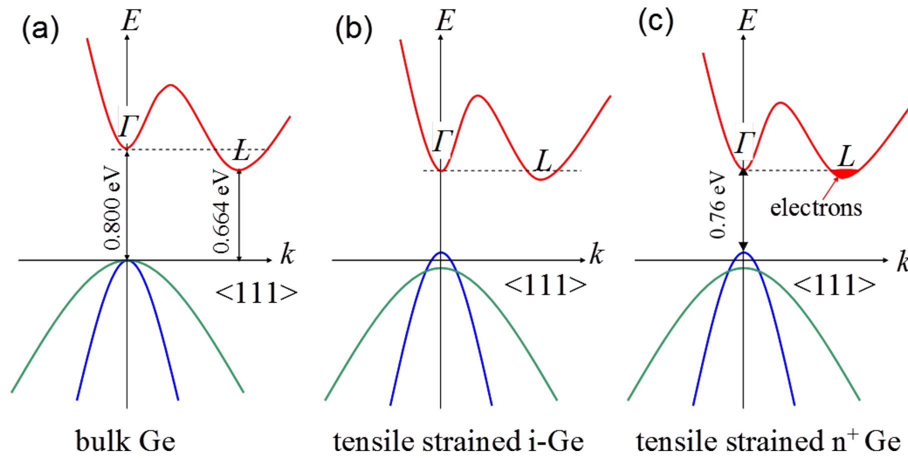

Figure 4.- Comparison of the band structure of unstrained, tensile strained, doped tensile strained Ge.

This section will be focused on the band-engineering of Ge to allow it to behave as a pseudo-direct gap material. The reasoning for n-type dopants and the effects that heavy doping has on the band structure is discussed.

2.1.1 Ge Band Engineering

Band engineering can be performed through the addition of defects, impurities or strain in the system. Ge has six equivalent valleys, each with its own direction. When applying an inhomogeneous stress, as the projection of the stress onto k-direction changes, the magnitude of the perturbation of energy varies. The difference in perturbation affects each band differently.

The bandgap energy shift due to strain can be calculated using the Pikus-Bir Hamiltonian, as already presented in other works [29-32]. The calculations involve the use of elastic potentials, deformation potentials and fundamental constants [33]. The strain state on (001)-oriented Silicon substrates is biaxial tension for Ge, as will be explained in further sections. The tensile strain can be defined as,

$$\varepsilon_{xx} = \varepsilon_{yy} = \frac{a_0 - a}{a} \quad ; \quad \varepsilon_{zz} = -2C_{12}/C_{11},$$

where C_{11} and C_{12} are the elastic stiffness constants, and a and a_0 are the lattice constants. There is no stress in the z direction, therefore the stress tensor obtained is,

$$\tau_{zz} = C_{12}\left(\varepsilon_{xx} + \varepsilon_{yy}\right) + C_{11}\varepsilon_{zz} = 0.$$

The Hamiltonian of each CB minima is,

$$E_C(\mathrm{CB}) = E_g + P + \frac{\hbar^2 k^2}{2m_{eff}}$$

in which k corresponds to the momentum vector on each CB minima. The valence band (VB) Hamiltonians are,

$$E_{HH}(\mathrm{CB}) = -P - Q$$

for the heavy holes and,

$$E_{LH}(CB) = -P + \frac{Q}{2} - \frac{E_{so}}{2}({E_{so}}^2 + 2E_{so}Q + 9Q^2)^{1/2}$$

for the light holes, which are k independent; where $P = a_h\left(\varepsilon_{xx} + \varepsilon_{yy} + \varepsilon_{zz}\right)$, $Q = \frac{b}{2}(\varepsilon_{xx} + \varepsilon_{yy} - 2\varepsilon_{zz})$ and E_{so} is the energy difference between valence bands and split-off bands calculated as 0.296 eV for Ge. a_h is the hydrostatic deformation potential; and b is a common deformation potential taken as ~-1.88. Deformation potential a_h is different for each band due to the asymmetry of the stress and orientation of the conduction band valleys. Table 2shows the values used in our calculations of the biaxial strain in Ge in different bands.

Table 2.- Values used for Pikur-Bir Band gap Hamiltonian for biaxial strain[32-37]

	Γ	L	Δ	HH	LH
a_h	-8.97	-2.78	-10.4	1.24	1.24
E_g	0.8	0.66	0.85	-	-
m_{eff}	0.038	0.22	0.321	0.284	0.043

The Hamiltonian is solved for k=<111> CB L valley and k~<100> CB Δ valley. Figure 5 shows the results biaxial strain under all bands. The results present a transition where direct band gap (Γ) transitions will be more favorable due to its lower energy gap. The transition occurs due difference in the deformation potential, where $|a_\Gamma|<|a_L|$. Figure 5 also shows that for Δ valley the shift occurs due to the symmetry plane on (100) where it is located. The decrease of energy of both indirect valleys permits faster thermalization, and scattering of phonons and carriers to the direct band Γ. When $E_{g\Gamma} < E_{gL}$, the E_g is ~0.5eV with 1.8 % tensile strain, meaning the Γ valley becomes the favorable valley for recombination. The small E_g is undesirable, and the large strain is difficult to achieve. The bandgap corresponds to a 2480nm photon transition which is a large red shift from the ideal 1550nm transition from unstrained-Ge. The 1.8% strain necessary for this shift is large enough to create non-uniformities and defects in Ge. Pseudo-direct band gap behavior with high radiative recombination at the Γ valley at ~1550nm is achieved through other means.

The solution consists of inducing smaller levels of strain, 0.2-0.3%, and heavily doping to overcome the difference between indirect and direct band gap as will be explained[25, 27, 38, 39]. The change to smaller strain alleviates fabrication restraints and avoids shifting the direct band emission to longer wavelengths.

The energy decrease on indirect valleys has further implications treated in later chapters.

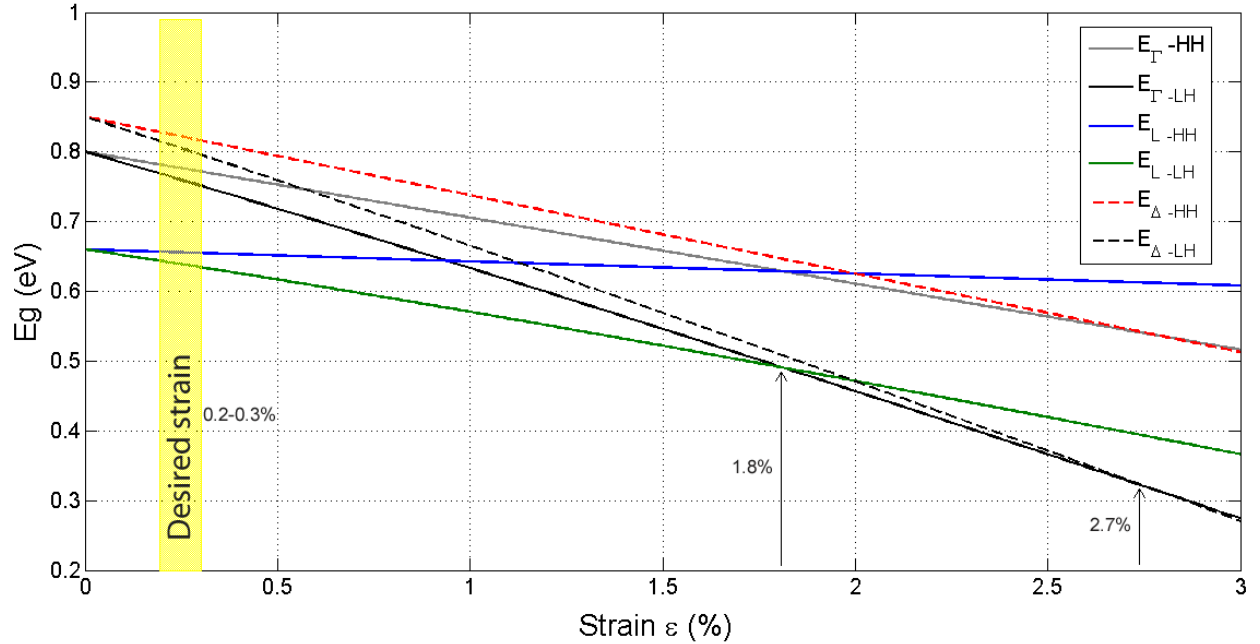

Figure 5.- Biaxial tensile strain calculation for Ge showing changes of bandgap in Γ (direct), L and Δ (indirect) valleys. At 1.8% strain, Ge becomes a direct band gap material, and at 2.7% it becomes indirect again. Desired strain resides between 0.2-0.3% with Γ valley emission at 1550nm wavelength.

2.1.2 Ge n-type dopants

The n-type dopants donate carriers to the CB, raising Fermi energy, E_f, above the Γ valley minima. Furthermore, as the dopant quantity increases the formation of an impurity band follows which is independent of k-space. According to the nature and quantity of the dopants, equilibrium of point defects exists in the forbidden band of a semiconductor. This happens due to a finite overlap of the electron wave functions between neighboring impurity centers. The individual electron levels broaden to form a real impurity band. The level broadens symmetrically shrinking the energy gap, which is called band gap narrowing (BGN). Such a reduction in the energy gaps are seen in Ge experimentally [40-43].

The Si Bohr radius is approximately one-third of the Ge radius. This makes Si impurity states more highly localized. As the ionization energies of the dopants increases, it is less likely an impurity band can be formed. In the L-valley of Ge, n-type shallow donor dopants have similar ionization energies, as seen in Table 3. The impurity band effect could be observed in any of these dopants, increasing the probability of impurity band formation using dopants with higher solubility, such as Phosphorus (P).

Table 3 .- Ionization energies of group V impurities in L-valley Ge (meV) [40]

As	**P**	**Sb**	**Bi**	**Li**
14	13	9.6	13	9.3

The Bohr model for hydrogen can be used to estimate the energy required for ionizations of shallow donors in the L-valley for Ge. The energy for hydrogen is modified by taken into account the dielectric constant of the Ge. The model is

$$E_{ionization} = \frac{m_e q^4}{8\epsilon^2 \epsilon_0^2 h^2} \sim E_H \frac{m_e}{m_0 \epsilon^2}$$

where E_H is 13.6eV, m_0 is the free electron mass, q is the elementary charge, ϵ_0 is the dielectric constant, and h is the Planck constant. At room temperature, ~300K, the dopants are all ionized contributing to the carrier concentration. Under heavy doping, impurity band behavior can change the carriers interaction among the bands.

2.1.3 Ge heavy doping

Properties of Ge under n-type heavy doping has been treated previously by Pankove et al. [44] and Haas[45]. They report a dependence of E_g on *n*, carrier concentration, when bands are under degeneracy. Degeneracy is defined as when *n* exceeds CB edge density of states. Under those conditions, band gap narrowing (BGN), or shrinkage, is observed by carriers filling up

the near-bandgap states. This is a many body effect involving phonon-electron interactions and the presence of impurity bands. As seen in Figure 6, the BGN effect shrinks the bands, lowering the doping requirement for direct gap behavior as the dopant concentration increases. The Fermi Energy level can be calculated from the equation,

$$\xi = E_i + kTln\frac{n}{n_i}$$

where ξ is the Fermi energy, and n can be calculated as the integral of the total electron density $\varrho(E)$ and Fermi-Dirac probability function f(E). $n = \int_{-\infty}^{\infty} \varrho(E)f(E)dE$, which is equal to the number of dopants N_D under a degenerate state, as was described in n-type Ge [46]. As E_F changes with heavy doping, the energy required to have the dopants excited into the different bands change.

A detailed study of BGN in Ge under 300K conditions is treated in chapter 5.

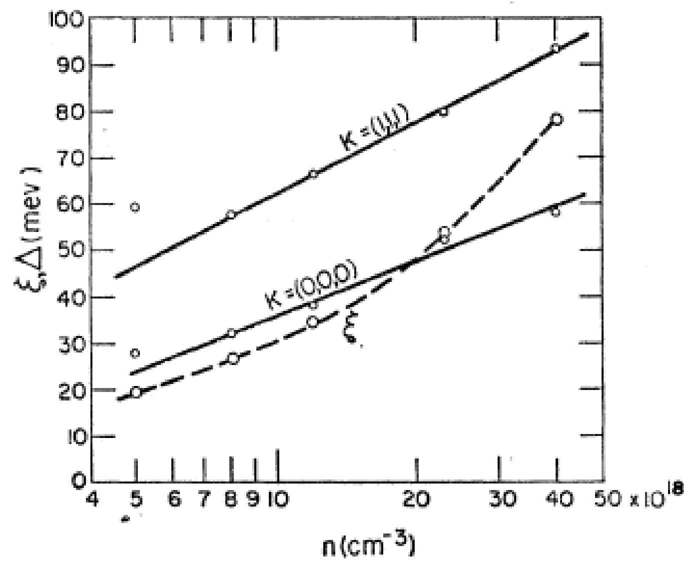

Figure 6.- Shrinkage (**Δ**) of the Energy gaps of the L band (111) and the **Γ** band (000) with respect to the Fermi Level (***ξ***) at 4K as a function of doping [44]

The onset of degeneracy with n-type dopants is when ξ matches CB minima. At that point any further dopants added to the matrix are fully ionized and contribute to the occupancy of electrons in the band. It is known that Ge degeneracy occurs with low 10^{18}cm^{-3} doping concentrations for the L valley [44]. For the Γ valley, degeneracy would occur at ~7x10^{19}cm^{-3} doping concentrations, the point when ξ equals the energy of E_g at 300K, though this degeneracy points ignore BGN effect on band shrinkage.

As have been seen, BGN affects the band structure, decreasing the energy of Γ valley bandgap. BGN, therefore, changes the doping level required for degeneracy. The degeneracy calculated with BGN is at ~3.5x10^{19}cm^{-3}, as seen in Figure 7. This value is consistent with experimental observations of this thesis. The lower point of degeneracy represents a point where the material can act as a pseudo-direct band gap material due to the availability of carriers at the Γ-valley.

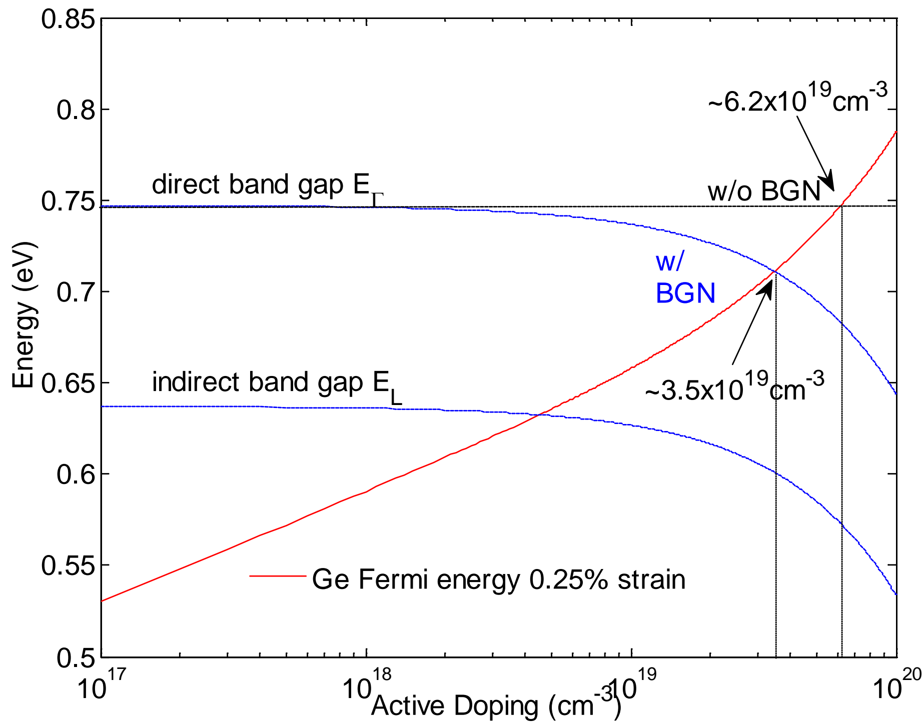

Figure 7.- 0.25% strain n-type Ge simulation showing dependence with doping on Fermi Level and band gap energies. Band edge intersection appears at lower dopant concentrations after considering BGN effects.

Pseudo-direct bandgap behavior permits Ge to act as a direct band gap semiconductor and have the possibility of gain and lasing with emission at ~1550nm wavelength.

2.2 Gain and Light emission on Ge

Ge is as an indirect band gap material known to have poor optical emission efficiency. Through research developed by previous members of our group[16, 19, 47], it was discovered that Ge bandgap can be tuned for enhanced photodetection and modulation. The results demonstrated the possibility of a pseudo-direct band gap as explained before.

Carrier lifetime and recombination determines the nature of emission in any semiconductor. Lifetimes can be differentiated between radiative and non-radiative. Radiative lifetime $\tau_{radiative}$ dominates on light emitting devices, such as lasers or LEDs. Non-radiative lifetime will depend on defects, carrier concentration, temperature, etc decreasing light emission from devices. Lifetime of the carriers (electrons) will depend heavily on the excess minority carrier density (holes). The recombination lifetime is defined as n/τ, where n is the carrier density and τ is the effective lifetime of the minority carriers accounting for both radiative and nonradiative lifetime. This simple expression is expanded to,

$$\tau = (\tau_{SRH}^{-} + \tau_{Surface}^{-} + Bn + Cn^{2})^{-}$$

where B stands for the radiative coefficient and C is the Auger recombination coefficient. Bn stands for $\tau_{radiative}^{-}$ and Cn^2 for τ_{Auger}^{-}. It follows that the radiative lifetime term should dominate so that the effective lifetime is generates light emission. It will be shown in the

following sections that as long as the material is defect-low, then heavy doping will lead to having B>>C and radiative recombination will dominating the expression.

Proof of pseudo-direct behavior can be extracted from photoluminescence (PL) measurements, in which an external light source at the absorption wavelength excites spontaneous emission. Ge PL results have been shown by other groups achieving PL[48] and EL[23, 41]. Kasper shows clear emission from MBE Ge samples. Due to the nature of MBE deposition, high crystal quality at high doping levels was produced. Kasper's group confirmed Sb concentration at $10^{20}cm^{-3}$ in Ge. Through comparison with intrinsic EL and doped PL measurements they observed BGN [49]. The results showed agreement with theory and led to the hypothesis of achievable carrier inversion in Ge, in other words, lasing. The increase in spontaneous emission follows with an increase in dopant concentration as was demonstrated by Sun, et al[30], as seen in Figure 8.

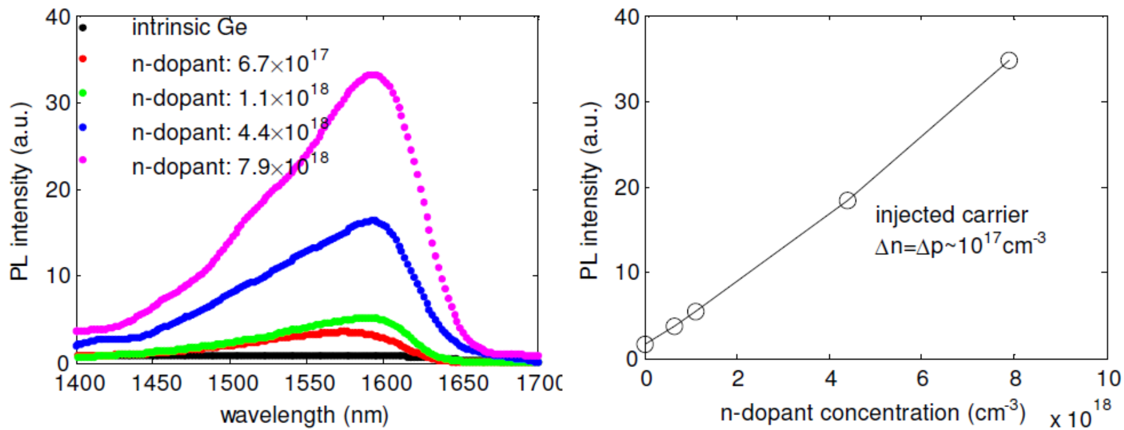

Figure 8.- Comparison of PL with emission wavelength of different doped Ge samples. PL intensity increases linearly with dopant concentration.

The increase in PL with dopant concentration shows that radiative lifetimes dominate under high doping, and the possibility of lasing. We will focus in how to obtain such lasing and the different loss mechanisms that can prevent it from occurring. First, the radiative transitions

in Ge, the meaning of gain and its implications for Ge will be discussed. Further, the non-radiative transitions, their function as loss, and the values observed in previous works will be discussed. Finally, theoretical work shows that Ge can be an effective gain material with gain bandwidths as large as >400nm determined by the injection of carriers.

2.2.1 Radiative Transitions

The study of the radiative transitions in semiconductors requires understanding band-to-band effects and mechanisms affecting their absorption of photons. Semiconductors mechanisms of importance for optical emitters are localized in band-to-band transitions. These band transitions refer to transitions from the conduction band, either direct or indirect, to the valence band. The three main mechanisms in band-to-band transitions in semiconductors are stimulated absorption, stimulated emission and spontaneous emission. Each of these properties and their importance for the understanding of gain in Ge will be reviewed.

Stimulated absorption produces new carriers by transforming the energy received from a photon into an electron-hole pair separated by the band gap. Stimulated emission is the main component for laser inversion. It provides a recombination path for carriers and more importantly is the source of new photons. Spontaneous emission is the dominant recombination path for carriers in LEDs. The emission characteristics depend in the material component and the injection level. The material component can be derived from the density of states. The injection will determine the fraction of carriers available for transition. Before discussing the radiative rate R, we will show the emission dependence on absorption coefficient.

The absorption coefficient α is the fraction of photons absorbed per unit distance and depends on the material properties along the light spectrum. The absorption is written as r

(photons per unit volume) divided by P, the optical intensity per unit area also known as the Poynting flux. The elements of r/P/hv become,

$$\alpha(\hbar\omega) = C_0 \frac{2}{V} \sum_{kb} \sum_{ka} |\hat{e} \cdot p_{ba}|^2 \delta(E_c - E_v - hv)(f_v - f_c),$$

where $C_0 = \frac{\pi e^2}{n_r c \varepsilon_0 m_0^2 \omega}$, p is the momentum variable corresponding to the reduced density of states, f_v-f_c is the Fermi factor dependent upon injection, c is the speed of light, n_r the effective index of refraction. The use of the momentum variable comes from Fermi's Golden rule, which describes the interaction between photons and electrons in semiconductors. When α ~ 0, we defined it as onset of transparency, or gain threshold g_{th}. As α is reaches equilibrium and ~0, it is referred to as bleaching.

Absorption is equal to all other mechanisms under equilibrium. The rate of absorption is described in terms of the spontaneous and stimulated emission as $r^{abs}=r^{stim}+r^{spon}$, and we know that they are described as

$$r^{spon}(hv) = (\frac{n_r^2 \omega^2}{\pi^2 \hbar c^2})\alpha(hv) \text{ and } r^{stim}(hv) = (1 - e^{[\hbar\omega - (F_2 - F_1)]/kT}) r^{spon}(hv) ,$$

where F_2 and F_1 are the quasi-Fermi levels under injection. Under equilibrium at the onset of transparency, the rates translate into,

$$\Gamma g = \alpha_i + \alpha_m + \alpha_s$$

where α_i are the intrinsic losses in the material; α_m are the mirror losses from the cavity; α_s are other losses usually attributed to non-radiative recombination; Γ is the material photon confinement; and g is optical gain. Under heavy injection, r^{stim}>>r^{spon} since $\alpha < 0$ as the injection increases; translating to larger g.

Non-radiative recombinations persist in any band-to-band transition. In order to understand the losses occurring due to defects, we need to determine the radiative rate R due to

spontaneous emission and non-radiative recombination processes. R can be expanded in terms of the total amount of dopant in the system as follows,

$$R(n) = An + Bn^2 + Cn^3 = \frac{n}{\tau},$$

where τ is the lifetime of the carriers, A is due to non-radiative recombination, B is due to spontaneous radiative recombination, and C accounts for non-radiative Auger recombination. In lasers and LEDs, R takes an important role in the total carrier concentration in the active region. This rate of carriers can be described as,

$$\frac{dn(t)}{dt} = \eta_i \frac{J(t)}{qd} - R(n) - v_g g(n) S(t),$$

where J is the carrier density, d is the thickness of the active gain material, q is the unit charge, η_i is the collection efficiency, g is the gain and S is the laser cavity photon density. It should be clear that under the case of LEDs, g is negative since inversion of carriers has not been achieved. This formulation is quite useful to describe electrical and optical properties of light emitters. It should be noted that a large R increases the J under equilibrium, which is not desired for efficient light emitters. Since non-radiative recombinations can be detrimental for emission and gain, they will be treated in depth.

2.2.2 Non-radiative Transitions

Non-radiative recombination mechanisms, or transitions, can be classified as either extrinsic or intrinsic. Extrinsic recombination is a stepwise decay through an intermediate energy level within the bandgap. These recombinations are usually due to surface recombination and defect recombination, or Schokley-Read-Hall recombination (SRH). Intrinsic recombination

mechanisms are always present, even in an ideal undisturbed crystal without impurities or defects.

These mechanisms are important for both intravalley and intervalley scattering mechanisms. Intervalley scattering are interactions between different bands while intravalley scattering are multi-body effects inside the same band. They describe carriers –electrons, holes, photons and phonons- absorbed and re-emitted in other unoccupied states. They can be classified as phonon-electron, thermalization; electron-electron, Auger recombination; and electron-photon, free carrier absorption. The latter two will be treated with further detail. Depicted in Figure 9, the main mechanisms are shown.

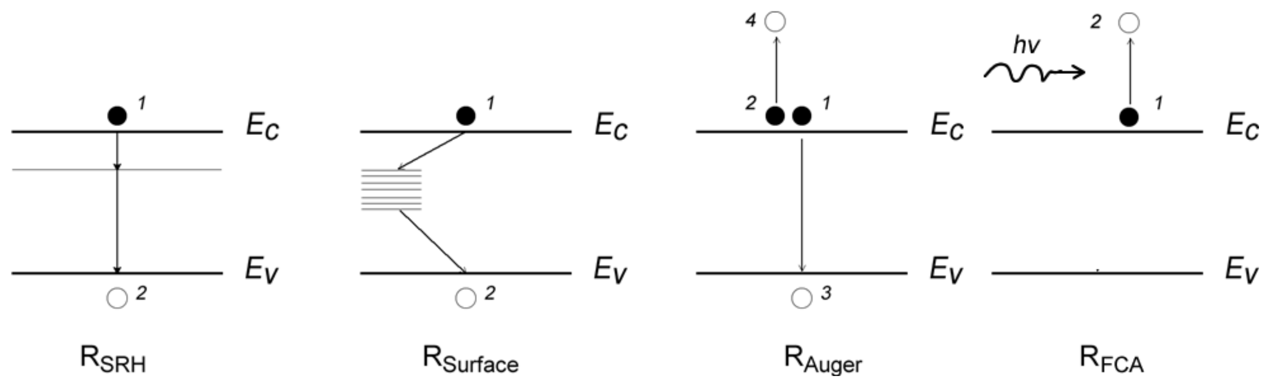

Figure 9.- Typical non-radiative recombination mechanisms

All these mechanisms can heavily influence the performance of the injection and carrier recombination, and inversion for lasers.

2.2.2.1.SRH

The defect or impurity recombination rate, also known as SRH, deals with all four possible transition rates into and out of traps. Traps are classified as: electron emission, electron capture, hole capture, and hole emission. It should be obvious that the theory has a nontrivial dependence on both electron and hole densities. Unfortunately, SRH is described through Boltzmann statistics, hence it is only valid under non-degenerate carrier densities. Ideally SRH

recombination could be avoided by producing a perfect crystal. In practice, this is not the case. Imperfections in the crystal lattice and the unavoidable introduction of impurities during crystal growth and wafer processing lead to the presence of defect levels that drive SRH recombination. The recombination can occur either in the bulk of the crystal through lattice defects and impurities or through surface recombination caused by dangling bonds at the wafer surface and material interfaces. Under heavy doping, shallow traps will not contribute to SRH recombination. Trap levels close to either band edge will be reduced as the doping concentration increases, therefore deep level traps are the only ones which affect recombination.

For lasers, the high injection regime is of primary interest and the rate simplifies to

$$R_{SRH} = \frac{N}{\tau_h + \tau_e},$$

where N is the injection level ($N >> n_i$), and $\tau_{e,h}$ are the minority lifetimes which are inversely proportional to the trap density. In the high-level case, the SRH lifetime is dependent only on the capture time constants and is therefore exclusively set by the trap density and capture cross-sections; it is independent of the trap energy level.

In bulk materials, the minority carrier lifetime dependence on threading dislocation density is summed up as,

$$\frac{1}{\tau_p} = \frac{1}{\tau_{p0}} + \pi^3 \rho_T D_p / 4,$$

where τ_{p0} is the bulk lifetime in the absence of dislocation effects, ρ_T is the threading dislocation density, and the D_p is the minority-carrier diffusion coefficient. Figure 10 shows the dependence that dislocation density to minority lifetime in n+Ge. Under heavy doping, the material quality is governed by a limit contained in the bulk radiative lifetime. The trend was reported for III-V materials[50] and matches closely to theory. However, experimental work

under heavy doping shows minority carrier lifetime as high as 10^{-7}s. This discrepancy would suggest a larger bulk lifetime and lower hole mobility. Furthermore, the difference between experimental values and theory suggest that theoretical values have to be reexamined for Ge.

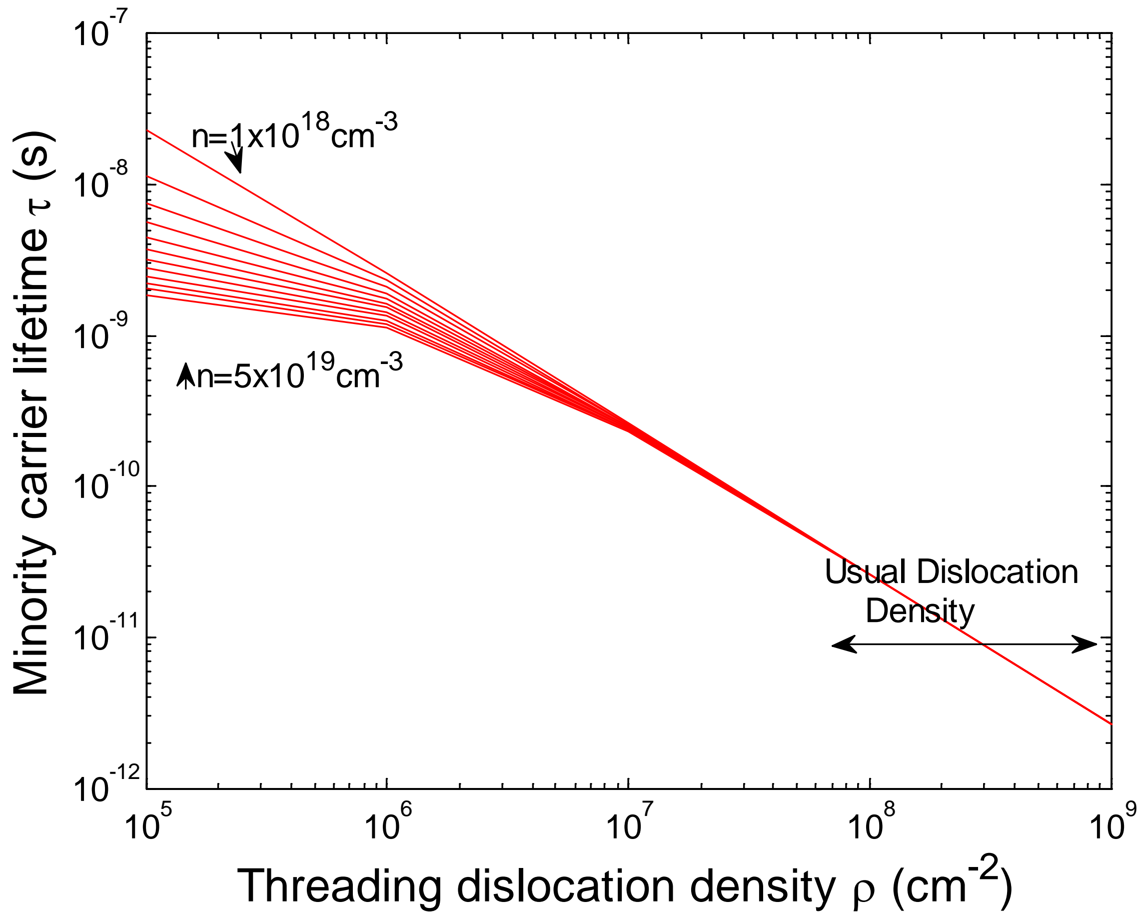

Figure 10.- Threading dislocation density simulation showing dependence of doping to minority carrier lifetime in Ge. Calculation based on theoretical work.

Hole mobility is bounded by the heavy doping and will affect the lifetime of the carrier. Below 10^{8}cm^{-2} threading dislocation densities, lifetimes are of the order of Auger recombination. At higher dislocation densities the effect strengthens SRH effects and significantly augments absorption loss of Ge.

The temperature effect on the minority carrier lifetimes needs also consideration. Under n+type semiconductors, the lifetime expression is reduced to,

$$\tau_{SRH} = \tau_{n0}(T)[1 + k\frac{N_t(T)}{n_0}],$$

where N_t is the point defect concentration, and τ_{n0} reflects the temperature dependences to the capture cross section and the thermal velocity. N_t increases exponentially with temperature due to increased solubility and its readily understood as a deep level trap. However, under heavy doping other nonlinear effects appear that overwhelm the SRH lifetime [51].

The equation that shows the correlation of doping with SRH is,

$$\tau_{SRH\ total} = \tau_{SRH}\left(1 + \frac{n_{dop}}{n_{thr}}\right) \sim \tau_{SRH} n_{dop}$$

where n_{thr} is the threshold doping calculated from generation traps and is ~4×10^{16}cm^{-3}[52]. However, as seen in Figure 11, under heavy doping Auger recombination will dominate. Large point defect densities affect minority carrier lifetimes with an inversely proportional relationship, but under heavy doping, Auger recombination is faster and decreases the effect of SRH recombination. The doping concentration of interest for Ge gain and lasing is above >1×10^{19}cm^{-3}, making Auger recombination the main loss mechanism.

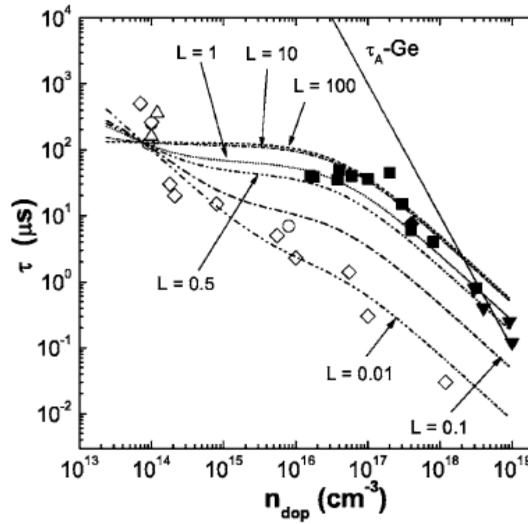

Figure 11.- Variation of carrier recombination lifetime as a function of dopant concentration in Ge .τ_A-Ge is the calculated Auger recombination using C=10^{-31}cm^6/s. The excitation level is defined as L=n_{ex}/n_{dop}. [52]

Moreover, under n-type degenerate doping, Ge shows nonlinear Auger recombination and the impact of the Auger process in the heavily doped material is not as strong as in Si or other semiconductors. An explanation of such effect is treated onward.

2.2.2.2. Auger Recombination

Auger recombination is the main source of non radiative transitions in semiconductors due to the cubic nature of the recombination, Cn^3, discussed previously. Auger recombination is an interaction of two excited carriers which energies interact to excite one to a higher energy level.

Auger processes can be divided in three main processes: direct band Auger, phonon assisted Auger, and impurity assisted Auger. The latter two can contribute at low temperatures and are insignificant as temperature increases since it involves a three-particle process, e-e-phonon.

The direct band Auger processes are classified into CCCH, CCHS and CHHS, where C stands for CB, H for the valence band (VB) and S for the Split-off band. They represent carrier interaction locations, those being CC, CH and HH, and where they will terminate, being CH and CS. The CCCH Auger recombination schematic is seen in Figure 12.

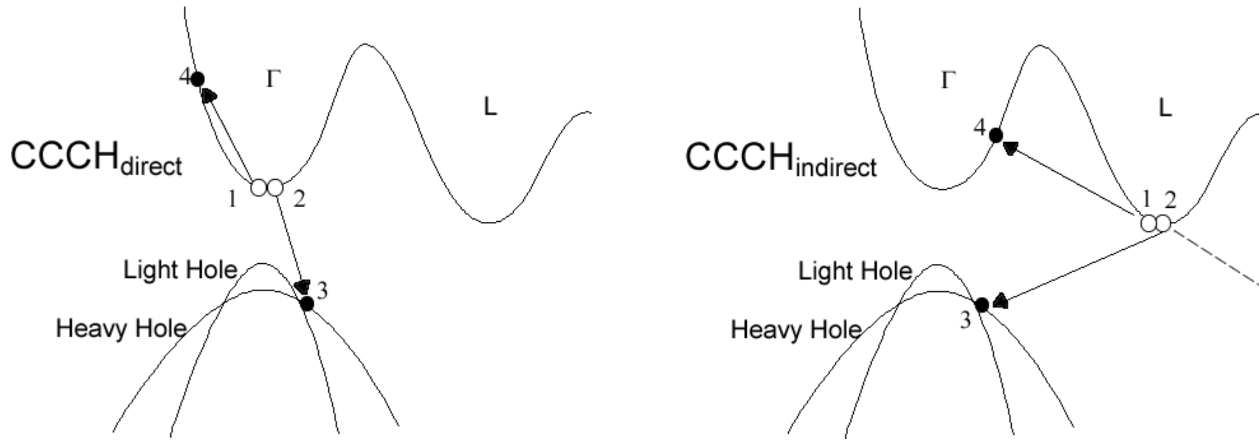

Figure 12.- Schematic of CCCH direct and indirect Auger recombination

Ge direct band Auger recombination has been usually overlooked due to the low level of carriers in the Γ valley. As injection can be as high as $1x10^{20}cm^{-3}$ carriers in lasers, the Auger direction recombination is low due to high threshold energy and low carrier density in Γ. The minimum energy, or threshold energy, for Auger recombination is calculated from energy and momentum conservation of CCCH heavy holes at Γ-valley,

$$E_T = \frac{2m_\Gamma + m_H}{m_\Gamma + m_H} E_{g\Gamma} = 0.8720eV\ (CCCH)$$

where m_i corresponds to the effective mass of H, heavy holes, and Γ, electrons in Γ $valley$; and in similar manner, the different interactions are calculated, as shown in Table 4. All the direct gap Auger recombinations require higher energy than the CCCH indirect gap transition.

Indirect band gap phonon-assisted Auger recombination studied for p-type Ge obtained that for 300K the Auger coefficient is $2.22x10^{-31}cm^6s^{-1}$ [53], which results in $\tau{\sim}10^{-10}$s. This value is mostly independent of temperature agreeing with experimental results, though it was

proven only for p-type materials. We predict that the result can be generalized for n-type Ge. CCCH indirect can be solved under the same conditions as direct to obtain,

$$E_T = m_H \frac{(2m_C + m_H)}{(2m_C + m_H - m_\Gamma)} E_{gL} = 0.0299\ (CCCH_{indirect})$$

where, m_C stands for the effective mass of L valley. The smaller energy required also translates into an increase probability of Auger transition that increases $\propto N^2$. This differs from established theory which states that increased Auger recombination will decrease the radiative emission instead of contributing to higher concentration of carriers in Γ. Details of the Auger threshold energy calculation can be found in the Appendix.

Table 4.-Threshold energy for different Auger recombination mechanisms

	Heavy Hole interaction (eV)	Light Hole interaction (eV)
CCCH direct	0.87	1.12
CCCH L indirect	0.20	0.030
CCCH Δ indirect	0.24	0.036
CHHS	0.56	1.44
CHHL	0.84	0.82

In most cases, n-type Ge minority lifetime is constant, as seen in Figure 13. It suggests that under heavy doping and low defect concentration, temperature will not decrease the performance of Ge, as observed from PL analysis[30]. Increase in minority carrier lifetime suggests that radiative lifetime is dominating, which can be caused by the indirect CCCH Auger recombination. As doping increases and temperature, probability of other Auger recombinations will increase. Considering that surface is correctly passivated, surface recombination can be ignored. The almost constant Auger recombination reduces the importance of Auger interactions at room temperature or above in Ge. In comparison, for III-V

materials, in which both temperature and carriers increase non-radiative recombination, the radiative recombination decreases with increasing temperature [54].

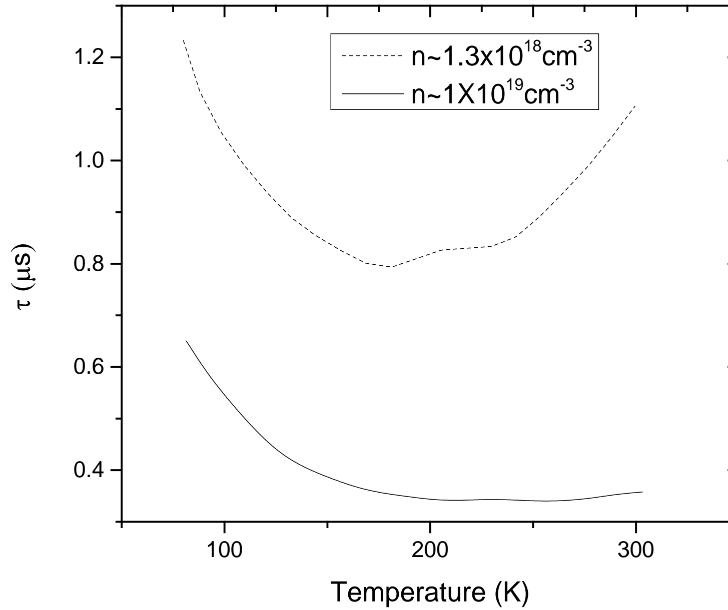

Figure 13.- Temperature dependence of minority carriers lifetime in Ge. [51]

In unstrained Ge, the decrease in minority lifetime is reduced under heavy doping, as seen in Figure 14. This refutes the Auger recombination theory in which nonradiative recombination increases linearly for both n-type and p-type dopants. The predicted Auger coefficient for heavy doping is $10^{-32}cm^6s^{-1}$, which increases the possibility of radiative recombination, and being one order of magnitude smaller than previously thought. The experimental result matches expected valued for n-type Ge under degenerate doping.

We mathematically demonstrated an Auger mechanism that increases carrier concentration on direct band transition, increasing radiative recombination –instead of decreasing it as with other semiconductors. We have shown that previously known Auger coefficients overestimate non-radiative coefficients. Furthermore, we have shown that under

high temperatures, Auger recombination can be considered constant or decrease. Chapter 5 covers the treatment of radiative recombination under diverse temperatures and doping, proving that non-radiative recombinations should not decrease light emission in Ge.

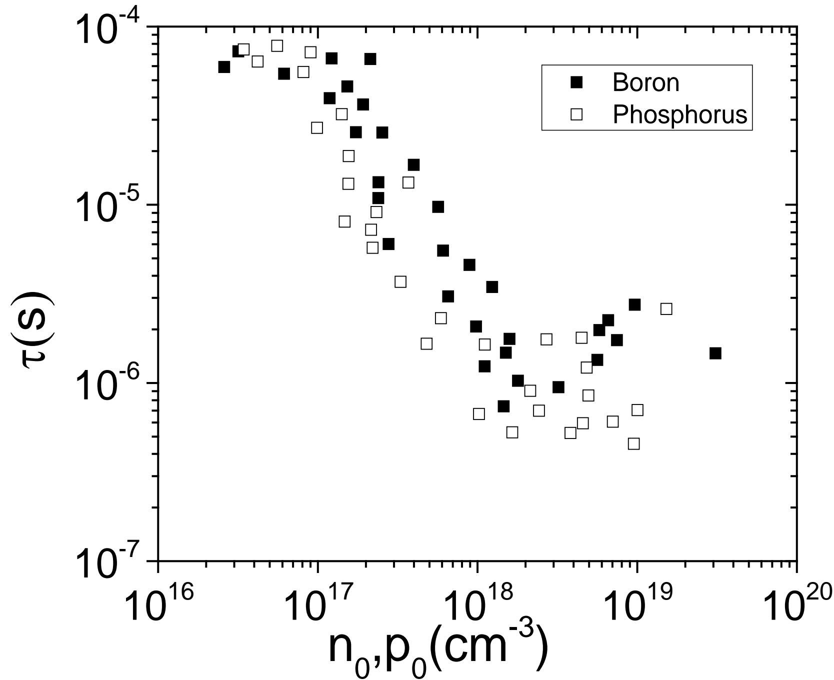

Figure 14.-Radiative lifetime of n-type (P) and p-type (B) dopants in Ge [51]

2.2.2.3. Free Carrier Absorption

Free carrier absorption is the action when the semiconductor, Ge, absorbs a photon and excites an electron into an unfilled state. As it is noticed, free carrier absorption is similar to Auger recombination, in the sense that there is an excited electron in the conduction band, instead of band-to-band absorption, and that it requires a photon. FCA, more than any other loss, affects the performance during lasing since it represents electron-photon interactions. The emission and absorption of photons reduce the efficient inversion and gain in the material. FCA usually

follows Drude's model of electrical conduction because the carriers excited into higher unbound states are considered free. It shows to follow Drude's model under low doping,

$$\alpha_{fca} = \frac{q^2\lambda^2 n_c}{4\pi^2 c^3 \varepsilon_0 n_r m_c \tau_c}$$

where q is the electron charge, λ is the photon waveguide, n_c is doping concentration, ε_0 is the permittivity of free space, n_r the refractive index of the material, m_c is the effective mass of carriers, and τ_c is the effective scattering time. The scattering time is usually estimated to carrier mobility, as $\tau = m\mu/c$. FCA depends greatly on the doping concentration. It has been shown that under low doping Ge FCA follows Drude's model [27], which has a quadratic relation with doping.

The free carriers scatter throughout the lattice, therefore, the interactions with phonons and impurities, apart from photons, have to be considered. It has been shown [26, 55, 56], that under heavy doping, FCA stops following Drude's model. It is important to notice that in cases of heavy injection, the model does not hold since the e-e and h-h interactions become stronger than the carrier-phonon, carrier-impurities, and carrier-photon interactions, attaining temperatures higher than the lattice.

The assumptions for free carriers, and single interactions between phonon and impurities, are appropriate only under low doping concentrations. As the dopant concentration increases, and degeneracy is reached, the interactions between phonons and electrons become stronger. It was shown under different semiconductors that Drude's model fails to explain these interactions on degenerate semiconductors [55]. The failure of Drude's theory on heavily doped Ge was proven by Wang, et al.[57], as seen in Figure 15. It showed that intervalley scattering absorption reduces the effects of free-carrier absorption. Furthermore, it shows that under the range of Ge light emission, intervalley scattering from L $\rightarrow\Gamma$ dominates. Calculating the free

carrier absorption from basic principles it is seen that it reduces an order of magnitude to values ~30-50cm^{-1}. The basic principles assume interaction of impurities, optical and acoustical phonons in 8 different interactions and one intervalley interaction [55]. The intervalley interaction is a mechanism providing carriers in Γ valley, which recombine readily, effectively reducing α_{FCA}.

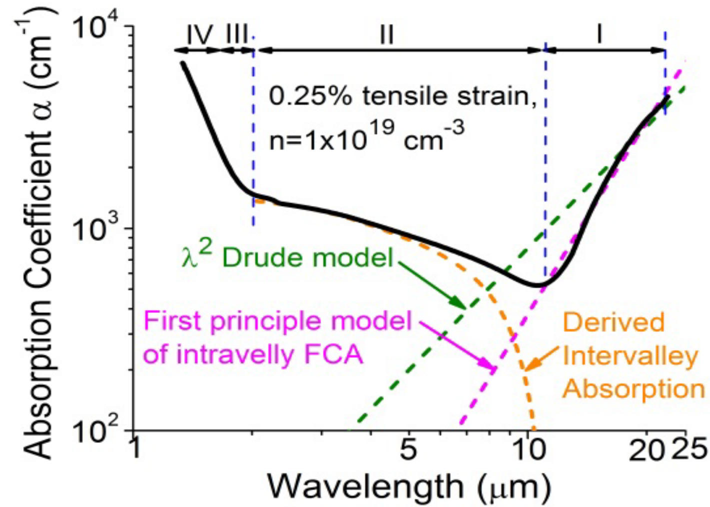

Figure 15.- Infrared absorption spectrum of Ge thin film with n= 1×10^{19} cm^{-3} derived from transmittance data. Regimes I-IV are respectively dominated by intra-L-valley FCA, L → Γ intervalley scattering absorption, indirect gap+intervalley scattering absorption, and direct gap absorption.[57]

As seen, Germanium is a complex system with many possible paths of recombination. This analysis showed that all major sources of losses will not be detrimental to Ge under doping n>1x10^{19}cm^{-3} and a temperature range of 300-400K, regimes explored for operation of Ge lasers.

2.2.3 Gain in Ge

Gain in semiconductors is described by the total losses in a system. The rate of absorption along with other loss mechanisms such as FCA, internal losses, and propagation losses describes gain. It will be discussed how these losses are used to calculate gain in doped and -strained Ge.

The case where loss mechanisms are reduced is called bleaching, since α is reducing to 0. As bleaching increases, the material eventually overcomes the losses, obtaining net positive gain. There is gain in the material when $g \geq 0$, hence the material gain larger than all the losses.

In Ge, it has been shown that the increase of dopants and tensile strain provides a situation for the material to act as a pseudo-direct band gap material. Ge bleaching and net gain have been experimentally measured by Sun, et al [25, 58], as seen in Figure 16. The gain measured was 50cm^{-1} for 1x10^{19}cm^{-3} doped-strained Ge. A model of the behavior under injections above 1x10^{19}cm^{-3} carriers, and wavelength emission ~1350-1800nm was constructed at doping concentrations above 1x10^{19}cm^{-3}[56].

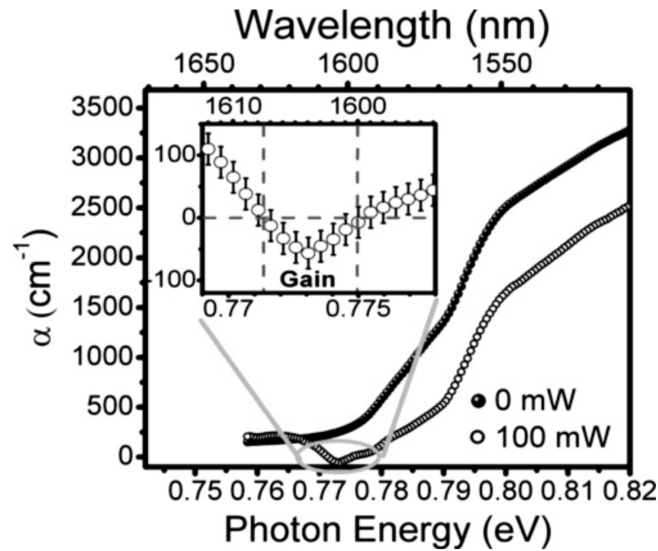

Figure 16.- Absorption spectra of a n + Ge mesa sample under 0 and 100 mW optical pumping. Negative absorption coefficients corresponding to optical gain are observed in the wavelength range [58].

The net gain of Ge can be calculated from the rate of stimulated emission minus all the losses at heavy doping. Figure 17 shows the results of our calculations for different carrier injections and doping concentrations. For positive gain, injections of the order of ~$5x10^{19}cm^{-3}$ are necessary. This observation matches the experimental work, as will be seen in Chapter 7. The model assumes BGN, impurity band and phonon-electron interactions, all of which aid the transitions under heavy injection levels. It is shown that gain in Ge is stronger than previously thought. Moreover, the dependence of doping on gain becomes evident. Higher gain can be achieved at the same injection level as long as the dopant concentration increases.

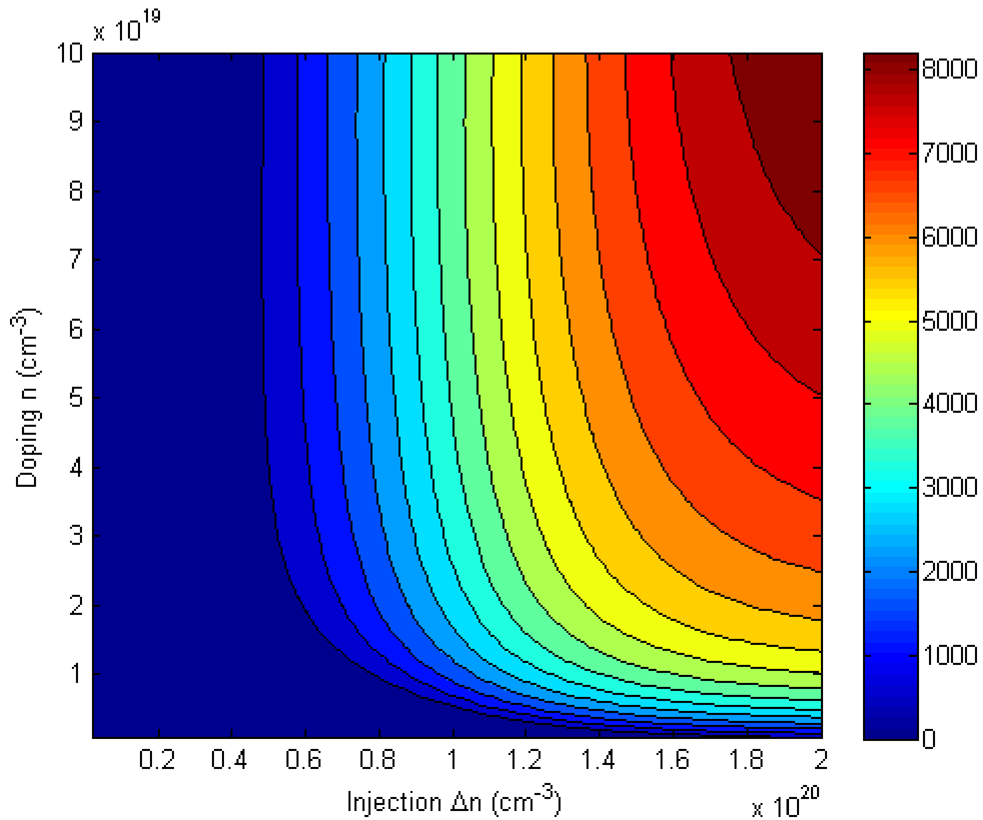

Figure 17.- Doping and carrier injection dependence to intrinsic material gain (colorbar) in Ge emitting at 1550nm wavelength.

At mid-10^{19}cm^{-3} doping concentration, Ge shows relatively low injection requirements, as shown in Figure 18. The increase in dopant concentration decreases the injection requirement, as stated before, and increases the bandwidth of emission. We showed that the bandwidth of emission can be as wide as 400nm at injection levels of 2×10^{20}cm^{-3}. Large carrier injection levels, such as this, cause aberrations and non-uniformities, including secondary perturbations that will not be treated in this thesis.

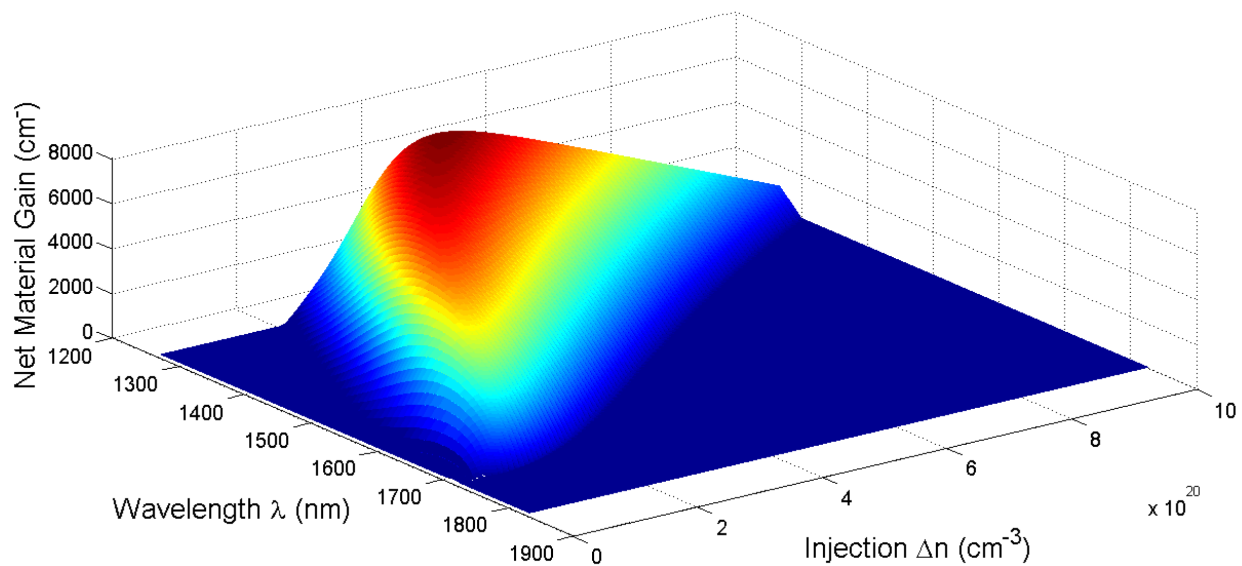

Figure 18.- Gain comparison simulation on tensile strained-Ge n-type doped ~4.2x10^{19}cm^{-3} at different injection levels and wavelength emissions. Expected bandwidth of >400nm.

A loss that is not considered in this model is the mirror loss from the cavity. Developing a laser from the gain medium requires some sort of optical feedback. Feedback with the gain material permits the amplification of the light. The optical feedback is provided by a reflective cavity. Section 2.3 will show how the appropriate design of such cavities permits lower loss lasers.

2.3 Resonant Cavities

A diode semiconductor laser is formed of an active material, which in our case will consist of an n+Ge cavity, and an optical resonator, or cavity. The active layer will generate the spontaneous emission and amplify a fraction of the spontaneous emission by stimulated emission[59, 60]. Optical Resonators or resonant cavities are structures designed to confine the light, through resonance frequencies determined by their configuration. Mode diode lasers use a

variety of cavity structures. The simplest of all is 1-D cavity known as Fabry-Perot (FP) etalon. More complex resonators use 2-D dimensions such as microdisks and microtoroids. In these cases the light circulates by reflecting at near-grazing incidence in a mechanism known as whispering gallery modes, WGM. FP and microdisks were the choice for our experiments, and they will be discussed carefully later on this section. A standard characterization of all cavities needs to be formulated based on their efficiency as cavities and containing the optical modes. There are also two main structures for guiding of light in the active layer, gain- and index-guiding structures[61]. Due to high level of refraction index in Ge compared to other semiconductors, Ge lasers would be an index guided structure. From the possible combinations, the simplest would be the index-guided Fabry-Perot cavity, making it an ideal structure for a first demonstration of a Ge laser.

The two key parameters characterizing optical resonators are modal volume, and quality factor, Q. The modal volume is the volume occupied by the confined optical mode. To define it, the resonating modes will be described as standing waves that can only occur satisfying Helmholtz equation with describes the allowed resonating modes under boundary conditions. It has the form of

$$\nabla^2 U(r) + k^2 U(r) = 0,$$

where $k = \frac{2\pi\lambda}{n}$ is the wavenumber, U(r) is the monochromatic wave function, and n is the index of refraction of the medium. In a lossless resonator, at the boundaries U=0. Such that the solution to Helmholtz equation needs to satisfy,

$$kd = q\pi,$$

where d is the distance between boundaries, and q is an interger. The solution simplifies to

$$\lambda q = 2nd,$$

which describes the round-trip distance between resonances [62]. This condition is used in all resonators, regardless of geometry. The other factor of description is the losses. This can be described by the finesse of the resonator (F). It appears since during travels in a resonator, waves experience phasor losses in the boundaries and throughout the medium. It is usually described as by spectral width δv of the resonances,

$$\delta v = v_F/\mathcal{F}.\ \text{Or}\ \mathcal{F} = \frac{n\lambda}{c\Delta\lambda}$$

The quality factor, Q, on the other hand, is directly proportional to finesse. Where

$$Q = \frac{2\pi v_0}{c\alpha_r}$$

The spectral width δv is equivalent to the full width half-maximum (FHWM), as seen above, it correlates directly with the losses in the mirror of the cavities, in the form

$$\Delta\lambda = \frac{n\lambda^2\alpha_r}{2\pi},$$

where α_r are the mirror losses. Such topic will be discussed in later chapters while analyzing the laser cavities. It can be observed that quality of a cavity will be directly proportional of the finesse in a system, as intuitively thought.

With the basic understanding of cavities formulated, a brief description on the design and simulation of the cavities is given as follows.

2.3.1. Fabry-Perot cavities

The Fabry-Perot cavity consists of an active material of a specific length 'l', and reflectivities of the front and back facets. The propagation is described by the gain 'g' and the total loss due to absorption and scattering in the medium 'α'. The amplitude condition for laser oscillation at

the threshold gain is given by $g_{th} = a + \frac{1}{l}\ln(\frac{1}{r_1 r_2})$. Since there is spontaneous emission of light within the active region in the laser, the actual gain is slightly less than g_{th}.

This planar microcavity has a limited length, and hence, a finite quantity of modes propagating. The modes, nevertheless, will be equally spaced in frequency, apart from shifts caused by the variation with wavelength in the phase change on reflection on each of the mirrors [63].

Under operations close to laser threshold, the gain g is linearized to the carrier density as, $g = g_{th} + \frac{\delta g}{\delta n}(n - n_{th})$. Once the gain balances with the loss, the material goes into transparency[61]. For laser oscillations, the gain must exceed the value of transparency, however due to scattering in the facets, the gain value has to be larger. Figure 19 shows the basic design of the Fabry-Perot laser. Notice that the system is simply cleaved, easing the testing of the device.

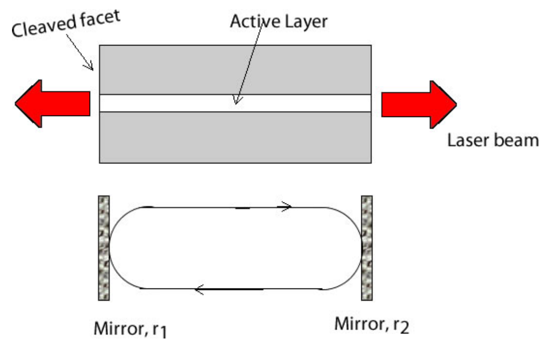

Figure 19.- Fabry-Perot Laser basic design. Active layer is Ge in all our designs.

Fabry-Perot cavities are the simplest cavities used in the design of lasers. FP cavities are a 1-D cavity with two mirrors, providing a round-trip path for the photons generated in the active material. Due to their simplicity they have been studied extensively and are a standard in industry[64]. The reason to use them in our investigation is due to the simplicity in their

production since they require a straight medium, which can be provided by a waveguide, ergo, the Ge waveguide.

Their characterization is simple as well, as depicted in Figure 20. Semiconductor optical amplifier and LEDs have a different shape for LI curves and luminescence. This easy and fast distinction makes them a perfect candidate for the Ge laser. However, since they depend heavily on the quality of the mirrors, Q-factor of these devices tends to be low, and production of single mode cavities is troublesome. Due to such impediments, other cavities where explored, such as microdisks.

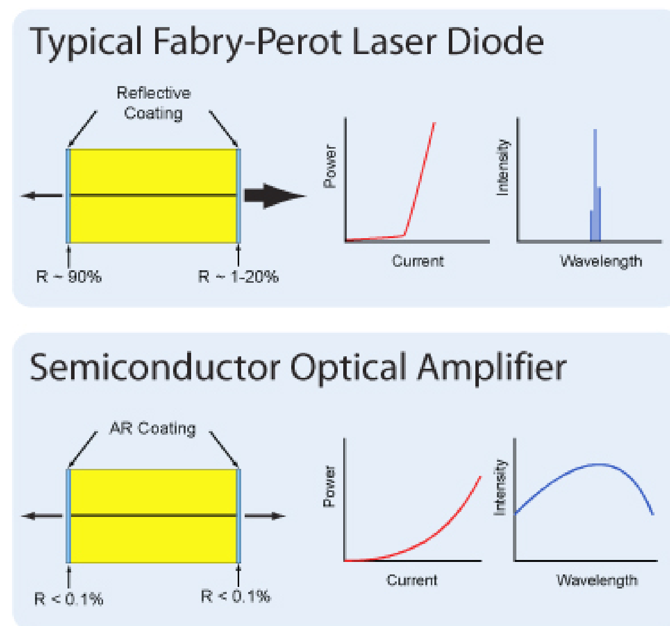

Figure 20.- Typical shape of FP laser diode and semiconductor optical amplifier device cavities. [64]

Higher efficiencies and single mode lasers can be achieved through DFB or DBR cavities. These designs involve diffraction gratings, feeding back the light by spatially modulating the complex refractive indexes of the optical waveguides. Even though their design will provide higher efficiencies, for a first demonstration it would involve too many unknown variables in terms of the fabrication quality.

2.3.2. Microdisks

Whispering gallery modes (WGM) consist of 2-D microresonators with circular shapes. The most usual shapes are microdisks, micropillars and toroids, all of which have been considered for semiconductor lasers [65-68]. All of these shapes can perform as efficient WGM resonators. The difference between FP and WGM are the number of reflections. In FP resonators with have two mirrors, sending the light back and forth in resonance. In WGM resonators, the light is reflected through to total internal reflection, as can be seen in Figure 21. The light will be confined in the active material, in this case the resonator, as long as the light is incident on the surface larger than the total internal reflection angle. Once the reflection overlaps into the starting wave, the material is said to be on resonance, acting as a WGM. The condition for resonance is similar to FP, in which the light has to travel the entire path, and reach resonance. In the case of circular resonators, hence, the wavelength has to travel a length πd, where d is the diameter of the resonator. This simplifies the resonance into,

$$\pi d = m\lambda$$

Where m is the number of modes, and λ is wavelength of interest. The calculation will depend as well on the materials index of refraction.

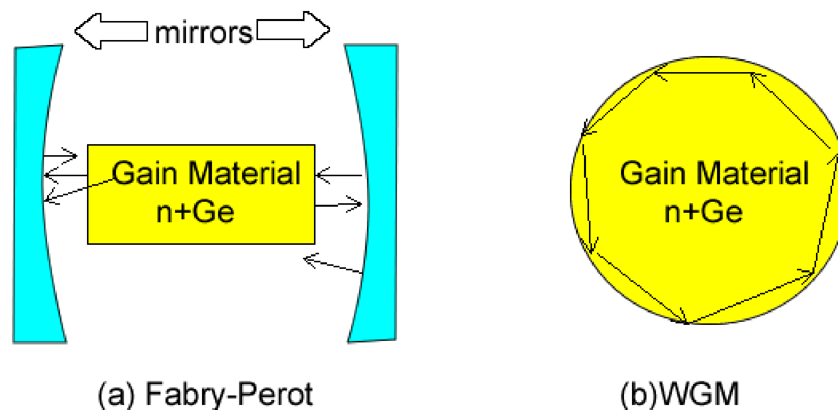

Figure 21.- Schematic comparing FP with WGM and the difference in between reflections.

WGM are typically used for lasers due a large Q. Our analysis showed that the resonances would been stronger than in FP, and selecting single modes through spaced waveguides would be simpler, as seen in Figure 22. However, the extraction efficiencies are low, despite changes on the design. Low extraction efficiencies make the characterization difficult and prevent to establish the source of lossy mechanisms. Furthermore, simulations show that the extraction efficiency is less than 0.01%, and with facets reduces to 0.003%. WGM have been successfully used in quantum well III-V lasers [65-68], and in other similar structures. Their use suggests the possibility to use them for Ge WGM lasers.

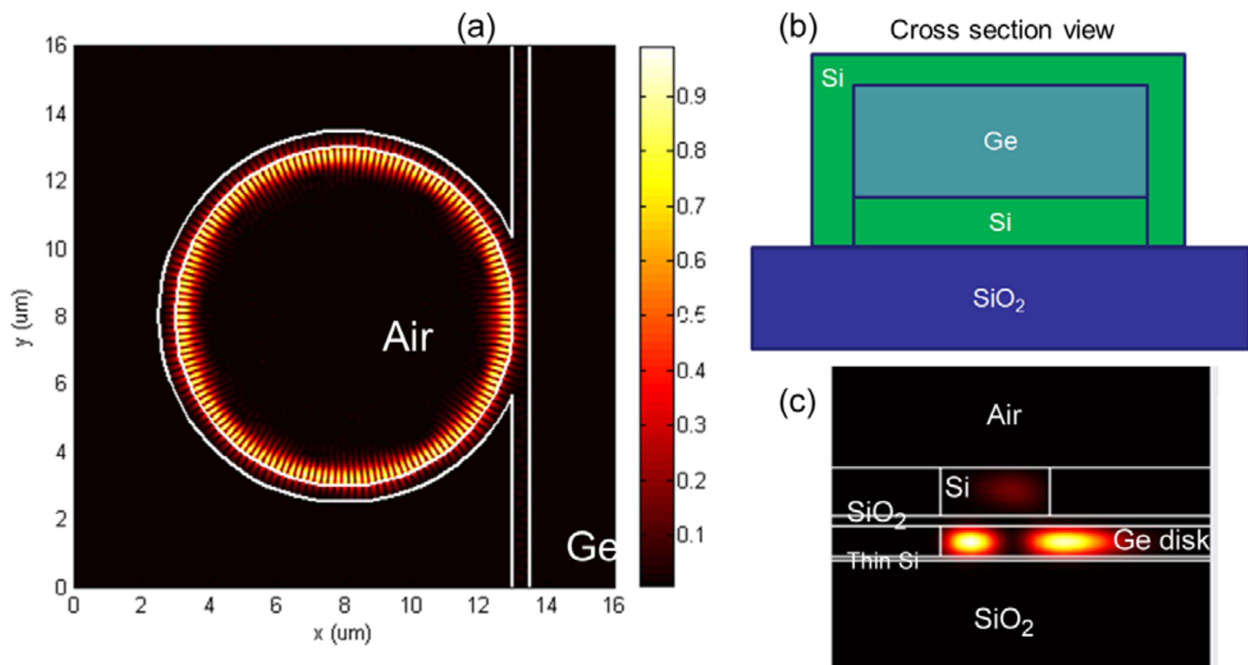

Figure 22.- Ge disk simulation showing that coupling of the internal mode is lossy and extremely low, despite different designs. (a) and (b) show a completely enclosed Ge microdisk, while (c) shows a microdisk with a waveguide for coupling. They show that microdisks coupling is smaller than 0.01% making them unsuitable for lasers.

Usual quality for WGM is Q~10^4, being 3 orders of magnitude larger than FP cavities. Their performance is limited by the surface quality of the material. Ge disks have an atomically smooth surface making them great candidates for WGM.

The structure of WGM resonators complicates injection of carriers. As was observed, Q and resonances are strong; however, they reside on the sides of the material. The injection occurs in the sides or center. With Ge, if the material is not under full inversion – all the active region is excited – then absorption will occur from unexcited regions. The absorption in bulk Ge in the wavelength of emission 1550nm is ~2500cm^{-1}[69], as seen in .Ge higher absorption makes WGM a less attractive material than FP in which carriers can easily be injected uniformly.

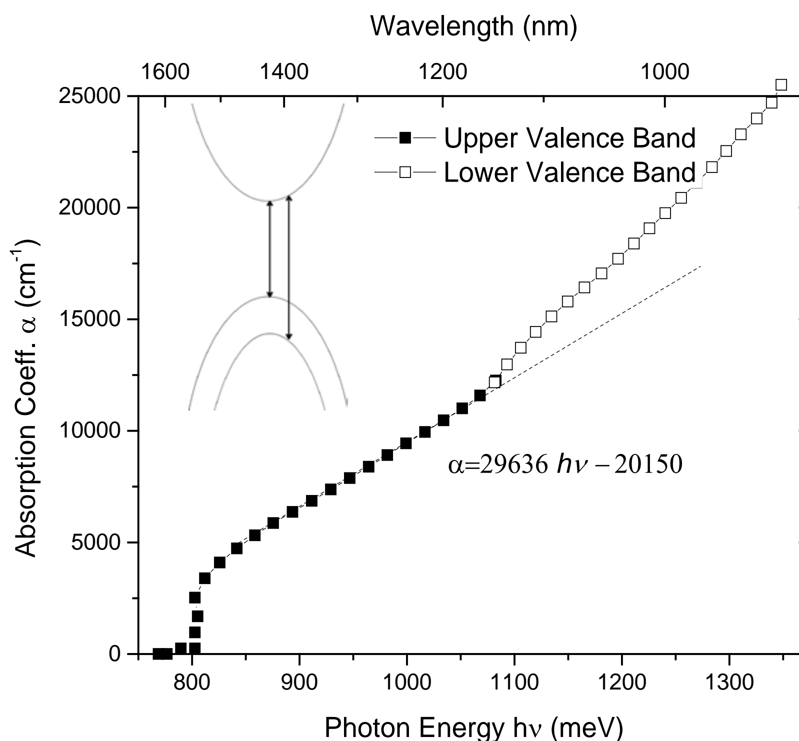

Figure 23.- Bulk Ge absorption along different wavelengths energies.

In the following chapters, the focus will be on FP resonators.

FP cavities will be understood as waveguides from this point on, due to the fabrication process. The following chapter will cover the fabrication, as in detail the growth techniques explored in CVD Ge.

Through this chapter we covered all the theory developed through our investigations, and used for analysis of the final devices. It is evident that the tensile strained Ge under degenerate doping requires further study under high injection and high temperatures where the regime has not been fully understood. A brief description of the dopant effect on the band is shown. The way defects affect heavily doped Ge and its performance require further analysis since free carrier absorption can be changed drastically with increasing loss mechanisms. The appropriate laser design will improve the efficiencies of future laser designs. The following chapters will cover the results from growth, doping, aberrations due to the high doping, and the diodes behavior. It will be demonstrated a functional laser Ge diode.

Chapter 3. Ge growth

In this chapter, we present the general fabrication of strained Germanium films. Ge growth on Si by chemical vapor deposition (CVD) is shown. The use of CVD provides the ability to generate the lowest defect concentration material with the highest dopant concentration achieved to date. We demonstrate the standard process used for the growth of all pnn diode devices and optically injected emitters. Then, we show that change in dimensions for Ge waveguides does not affect the tensile stress significantly. Additions to these processes to increase the dopant concentration will be treated in a later chapter. Finally, we present an alternative growth process for bufferless single crystal Ge as an alternative to the known method.

3.1. Growth of n+ Ge films

Germanium is a difficult material to grow on top of Si. In order to achieve the level of strain and dopant discussed, many approaches were considered [17, 32]. Of these many approaches CVD was considered to be the best to provide *in situ* doping and direct grown over Si. Since the critical thickness of Ge is far greater than the needed for the devices, at the high temperatures above 600°C, Ge films are completely relaxed. The strain is generated from the thermal expansion difference between Ge and Si. Once the system is cooled down to room temperature, it induces a ~0.2-0.3 % tensile strain. Through the appropriate control of gases the dopant concentration was also controlled. To understand this process, CVD processes are analyzed.

CVD processes possess a high level of complexity. They have different temperatures, concentration gradients, geometric effects and gas flow patterns in the reaction zone. Due to these many differences, it is difficult to translate the results of one chamber to a different one.

Through kinetic analysis, the react limiting factor can be determined. The two main factors controlling the rate are mass transport and surface kinetics. Mass transport control is the dominant factor if the transport of the reactants or reaction products across a boundary, δ, determines the deposition rate. If the mass transport is large across the boundary, then the system is controlled by surface kinetics.

Figure 24 shows a schematic of the different mechanisms considered to determine the limiting reaction limit.

1. Transport of the reactant gases into the reaction chamber. In our case, GeH_4 and PH_3.
2. Intermediate reactants from reactant gases. GeH, PH_2, PH and P_2.
3. Diffusion of reactant gases through the gaseous boundary layer to the substrate
4. Absorption of gases onto the substrate surface. GeH and PH.
5. Single or multiple-step reactions at the substrate surface.
6. Desorption of product gases from the substrate surface.
7. Forced exit of product gases from the system.

Analysis of these reactions have been kinetics that have been studied by Sun [27] and they were established to be surface reaction limited. For growth of crystalline Ge in CMOS chambers, laminar flow has to be avoided. Laminar flow prevents uniform growth through large badges of wafers, making an inappropriate technique for industry and, hence, our experimental studies.

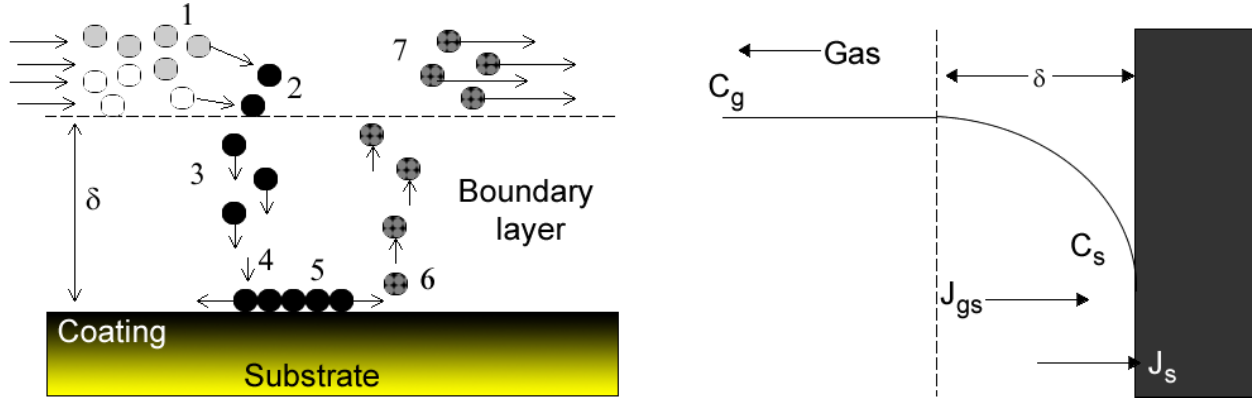

Figure 24.- Schematics depicting mechanisms during a CVD process and an schematic of the growth model limited by either mass transport (J_{gs}) or surface kinetics (J_s) [70] .

Molecular flow determines the pressure limit in the chamber. It can be described as,

$$C = \frac{8}{3\sqrt{\pi}}\left(\frac{2kT}{m}\right)^{\frac{1}{2}}(A^2/BL\,)$$

where L is the length of the tube, B, M molecular weight, T temperature, m is the mass of molecule, $A = \pi R^2$ is the area of the tube and $B = 2\pi R$ is the perimeter of the tube. Usual molecular flow us under 1mtorr. Since we are growing in this regime, viscous flow might occur. But the kinetics of thin films are fundamentally limited by temperature, as can be seen in diffusion equations. Since the boundary layer is $\delta \sim \infty$ in molecular flow, that the reactant diffusion through the boundary layer is larger than the surface kinetics. The expression for such diffusion is simplified into,

$$J_A = -\frac{D_{AB}}{RT}\left(\frac{C_{A_b}-C_s}{\delta}\right) >> J_s = k_s C_s$$

where J_A is the diffusion flux of specie A, D_{AB} is the diffusivity of reactants, C_{Ab} is the bulk stream concentration, C_s is the surface concentration of species, and k_s is the rate constant for the slowest surface reaction.

The reaction under steady state conditions should be equal to the corresponding mass flux making $J_s=J_{gs}$, where J_{gs} is the mass flux simplified from Fick's law to $h_g(C_g-C_s)$. On one hand, h_g, the gas mass transfer coefficient, is insensitive to temperature but sensitive to pressure, increasing with increasing pressure. On the other hand, k_s follows the Arrehnius equation, as was the case for phosphorus doping on Ge. Due to the high partial pressures, at equivalent temperatures the surface kinetics will control, as can be seen in Figure 25. This is not the case with our system growth where the growth rate is controlled completely by mass transport, as was described by previous works [27, 47], and the partial pressure is kept constant.

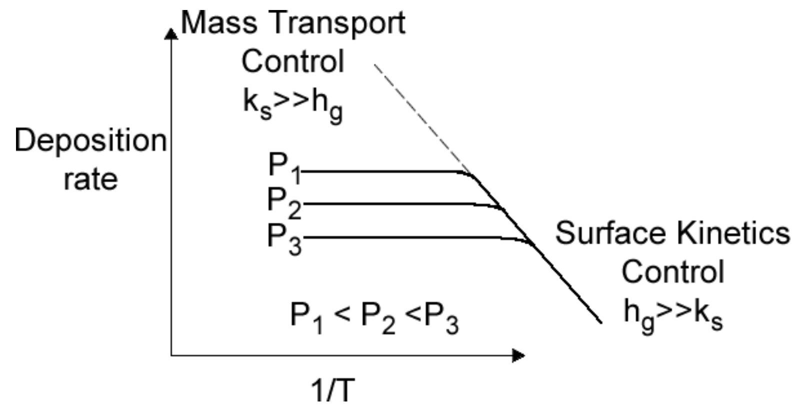

Figure 25.-Schematic diagram showing the effect of kinetics, temperature and pressure on growth rate.

Under these steady state conditions the growth rate of the films can be defined as $V=J/N_{Ge}$ [71], where N_{Ge} is the number of Ge atoms incorporated into a unit volume for the film. Under these conditions, the mass-transport controlled flow is,

$$V = \frac{C_G}{N_{Ge}} h_G$$

The C_G is directly proportional to the total pressure in the system from ideal Gas law. This condition will be shown again in further sections.

The surface reaction limitation on Ge permits the material to go under batch process which is on line with industry production. Furthermore, the growth process permits full control of Ge atoms and P atoms deposition, controlling the doping; and growth on Si, permitting tensile straining the material.

High quality epitaxial Ge, and a small density of dislocations is desired; however, the primary difficulty in Ge-on-Si epitaxy is 4% lattice mismatch between Si and Ge. This lattice mismatch must be accommodated either through strain or dislocations. The critical thickness for relaxation through introduction of dislocations depends on the lattice mismatch of the alloy but is only a few atomic layers for pure Ge-on-Si[72].

Kasper, et al. [73] used CVD to achieve the first successful growth of a SiGe heterostructure on Si in 1975. Masini, et al. have reviewed the development of this field [74]. The developments of ultra-high vacuum chemical vapor deposition (UHCVD) and molecular beam epitaxy (MBE) achieved low defect density Ge growth [75-77]. The first pseudomorphic growth of SiGe on Si by MBE was achieved by Bean et al. in 1984[78]. In 1986 Meyerson achieved the first low temperature UHCVD heteroepitaxy of SiGe on Si [79]. Both of discoveries were the beginning of the technology we use today. In one attempt, pure Ge epilayers were obtained by deposition of amorphous Ge on Si, followed by annealing for crystallization [80]. Heteroepitaxy of pure Ge on Si by CVD was finally achieved by Keuch, et al [81], however, the dislocation density was still too high to make the material usable for optical devices. The lattice mismatch of Ge with Si or SiGe interfaces generates a fairly high dislocation density, ~ $10^{11} – 10^{12} cm^2$[82].

One successful approach for reducing the dislocation density is through the use of buffer layers, as seen in the schematic in Figure 26. It consists of the growth of a dislocated

and highly defective film with a similar lattice constant to high quality material grown on top. Poor quality Ge is grown at low temperatures to act as the buffer. Since Ge is grown on top of Ge buffer, lattice mismatch is not an issue; additionally, the defects are buried in the buffer. This approach is treated carefully in Sun's thesis[27]. Calculations predict a reduction of the threading dislocation density with increasing buffer layer thickness [83-85], making it suitable for optical devices. Moreover, local epitaxy through selective growth yields theoretically lower threading defect density because of the possibility of elastic relaxation and defect necking.

Ge is grown directly on Si substrates by UHCVD. This work builds on the work by Luan [47, 77, 86] who used a two-step UHCVD growth process with post-growth cyclic annealing to produce high quality Ge epitaxial films with ~10^8 cm^{-2} dislocation densities. All Ge buffers in our research were grown at 360°Cwith thicknesses ranging from 15-100nm, followed by a 650°C 2hr Ge growth, yielding ~500nm epitaxial film. This process allows a tensile stress of~0.26%, as seen in Figure 26.

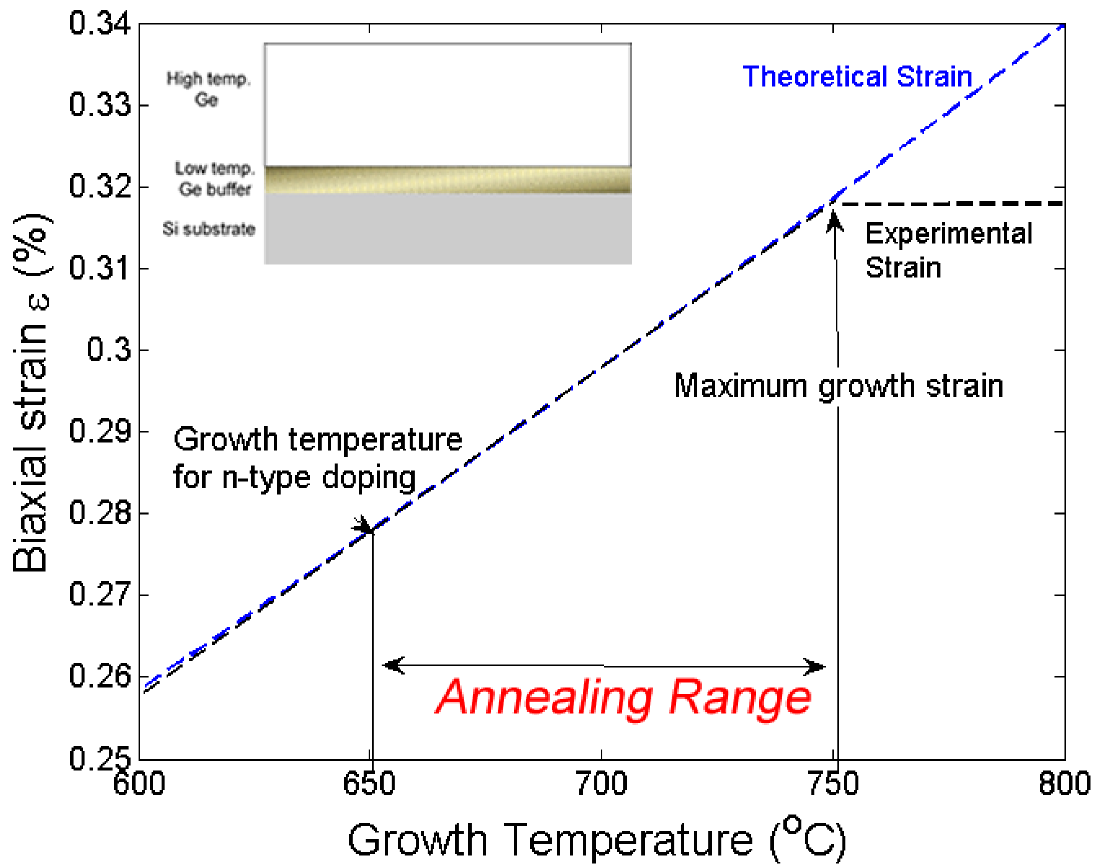

Figure 26.- Schematic and plot of two-step Ge epitaxial growth strain with growth temperature

As the Ge is deposited on Si under temperatures >650°C, the films are grown fully relaxed. The full relaxation was demonstrated by Jifeng Liu [16]. Once relaxation occurs, new dislocations are introduced in the interface. These dislocations extend to the edges and surface of the material. This gives them the possibility to propagate and generate threading dislocations, which are a major device performance barrier. Carrier lifetimes are reduced severely by an increase in threading dislocations. Through thermal cycling at 800-850°C the dislocation density can be reduced to ~10^6-10^7 cm^{-2}, as has been demonstrated [16].

As the Ge films are cooled down, the differences in linear expansion coefficient between Si and Ge leads to an effective tensile strain in Ge, as shown in Figure 27. The tensile

strain obtained is ~0.26% theoretically, and 0.25% experimentally making the Ge films a viable solution for Ge light emitting devices. With higher annealing temperatures the material will increase the tensile stress up-to 0.31% max.

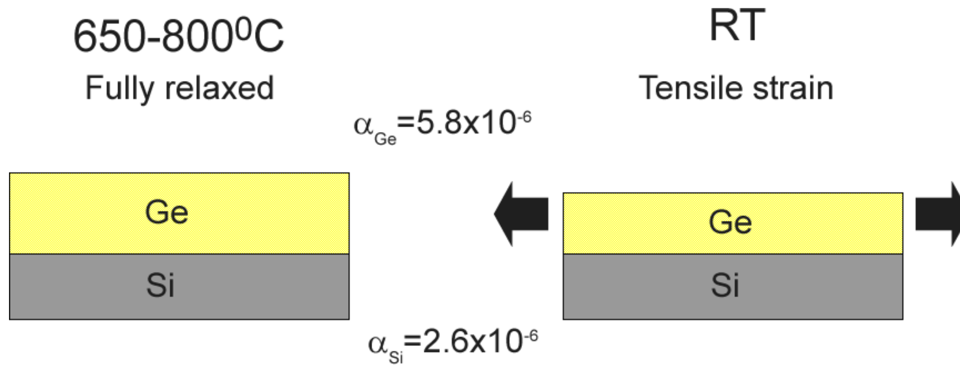

Figure 27.- Schematic showing that under growth Ge film are relaxed. Due to differences in linear coefficient of thermal expansion between Si and Ge, Ge films are tensile strained.

The total strain in the material is dependent on the temperature difference, accounting for a drop of 0.04% for every 100°C difference. The strain calculation is

$$\varepsilon = \int (\alpha_{Ge} - \alpha_{Si}) dT$$

where α_i is the linear expansion coefficient for Si and Ge, and ε is the total biaxial strain generated. This calculation applies in Si/Ge interfaces as long as the height of the material is larger than 300nm, from calculations of energy for plastic deformation[16]. The buffer acts as well as a center for plastic deformation release through misfit dislocations.

Figure 28 shows an SEM image of an epitaxial Ge layer grown on Si with a 20nm thick buffer layer. While this epitaxial film shows the onset of pit formation, buffers thicker than 20nm resulted in specular Ge surfaces without visible defects. The average distance in between pits, attributed to threading dislocations, is around 1μm resulting in a pit density of ~10^8cm^{-2}. The threading dislocation is typical for Ge thickness of 500nm [87]. The thin buffer cannot

accommodate for the lattice mismatch completely and due to the remaining mismatch pit formation occurs. We found that for buffers with a minimum thickness of 25nm, corresponding to ~100 Ge monolayers, high quality Ge film with specular surfaces can be grown.

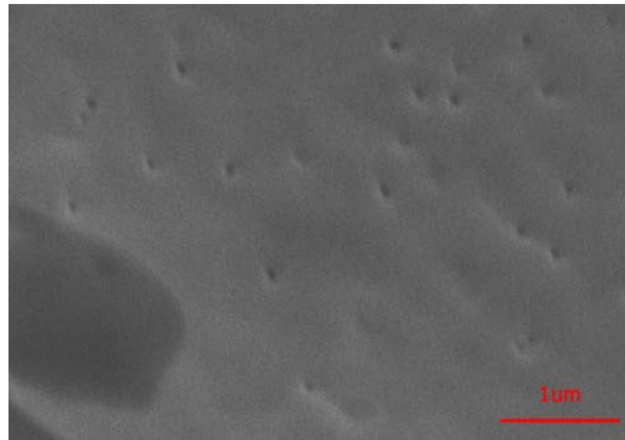

Figure 28.- Blanket epitaxial Ge film, grown on Si with 20nm Ge buffer. Buffer thickness <20nm causes pinholes formation in blanket films, attributed to threading dislocations.

With blanket Ge-on-Si growth being feasible, selective epitaxial growth was explored. This process provided a path to eliminate dislocations through annihilation at the interfaces. Luan showed that cyclic annealing is more effective in reducing dislocation density as mesa size shrinks, with the dislocation density dropping very rapidly for mesas smaller than 50 µm in diameter[47]. The samples remain stressed with ~0.2-0.3% tensile strain. Liu[16] showed that the tensile stress does not alter after annealing above 700°C.

The growth sequence provides chemically selective growth on Si and permits the use of SiO_2 as a window for Ge to grow within. The sidewalls of the oxide determine the dimensions of the Ge facet grown [88] . The facets dimensions were understood to be independent of temperature and pressure. Reactive ion etching (RIE) was the main mechanism affecting the

oxide well configuration. Different sets of RIE recipes were examined, which can be seen in the Appendix. Since RIE can depend heavily on the tool used, no generalizations were made.

The process growth yielded mesas in pattern oxide windows on the wafer, which served to outline the edges of the Ge mesas. The first layer is a SiO_2 thermally grown, which is *a posteriori* patterned into the shape of the device wanted. RIE etching and a slight BOE wet etching follow to open the structure to the Si substrate. The number of masks levels required prior to Ge deposition is only one[19]. Ge epitaxial growth proceeds as described by Luan and Cannon [47, 72]. This oxide barrier provides a high quality passivation surface, which proves useful during device design. This process is used for p-i-n and p-n-n [20] diode fabrication in previous work and the Ge-on-Si laser fabrication [21].

In situ doping of the material is demonstrated to be the most suitable way of increasing the uniformity of the dopant concentration. As seen in figure Figure 29, when comparing implanted samples with *in situ* doped samples, the latter showed more uniformity and a greater number of active dopants. The *in situ* process allows P doping side by side with Ge growth. The process allows the creation of n+Ge which is P doped Ge at $10^{19}cm^{-3}$.

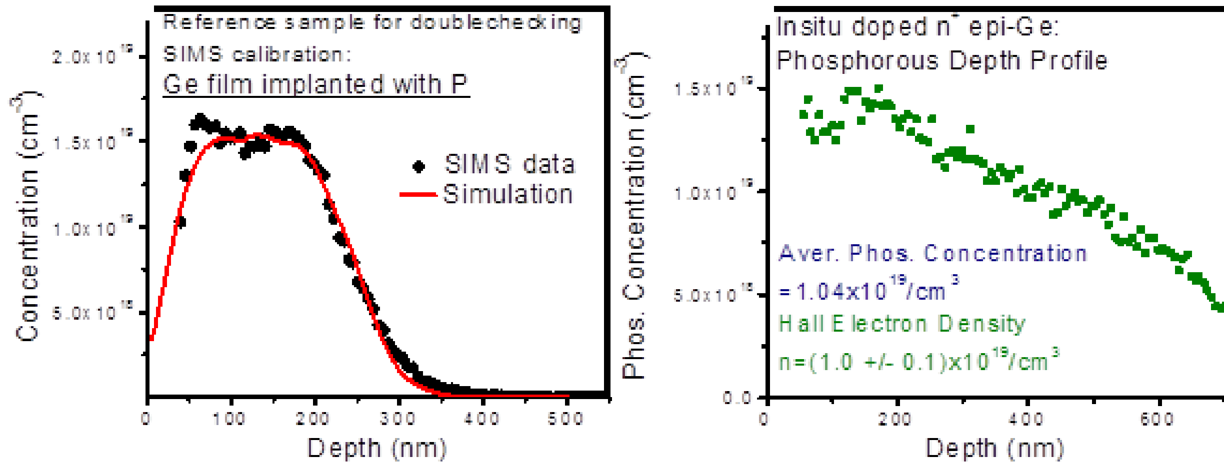

Figure 29.- SIMS analysis of Ge implanted samples and *in situ* doped Ge growth. *In situ* growth shows uniform doping with no addition of defects. Full activation of carriers is achieved.

Defect concentration is known to decrease under annealing. As will be seen, annealing decreases the total amount of dopant concentration due to diffusion of dopants. N-type dopants, as will be discussed, diffused faster in Ge than in Si. The enhanced diffusion in Ge prevents reaching concentrations above $2x10^{19}cm^{-3}$ while still keeping a low point defect concentration. Anneals can reduce the threading dislocations ($\sim10^{8}cm^{-2}$), but due to enhanced diffusion dopants will be out diffuse through anneals capable of removing the dislocations. Other methods have been explored to reduce the defect concentration, or even Ge buffer size, by constraining growth in one dimension. More of these approaches will be shown in the following sections.

3.1.1 Tensile strain and dislocations

Ge-on-Si heteroepitaxy has provided the tool for band gap engineering Ge, and provided new functionalities. Because of the difference in lattice parameters, a mismatch strain builds up in the growth layer with increasing thickness. Through the growth process described in the

previous chapter, we grew a Ge film with ~0.25-0.3% tensile strain. Growth in different geometries is considered in this thesis, especially Ge waveguides, for the formation of Fabry-Perot devices. In this section we will review the nature of dislocation in Ge under 1-D growth constraints and the effects of such growths on the overall tensile strain.

In Ge grown on Si (100) substrates, a layer of misfit dislocations forms at the interface. The misfit dislocations usually terminate in closed loops ending at precipitates, point defects, internal interface or by forming two threading dislocation arms directed toward the surface. We will explore the last two possibilities. As strain relaxation occurs, the misfit dislocation expands by lateral glide in <110> orthogonal directions.

Threading dislocations terminate most likely on the surface or at the oxide interfaces, as was proven by Chen[27]. The quantity of misfit dislocations, N_{TD}, and hence threading dislocations, correlates to plastic relaxation, δ , [87] by,

$$\delta = N_{TD} b l_{av}/4$$

where b is the burger vector, and l_{av} is the average misfit dislocation length projected into the (100) plane, measured to be $8\mu m$. With short threading dislocations of average length shorter than stated, present theory would not account for the strain generated. In the case of waveguides, in which the width is ~1 μm, the dislocation velocity, v_d, determines such plastic relaxation kinetics. Furthermore, the strain is reduced.

The dislocation velocity is dependent on stress, time-temperature and dopant type and concentration. In our growth the temperature range of interest is 650-750°C with a n-type dopant concentration ranging from 1-5x10^{19}cm^{-3}. At temperatures above ~500°C the dislocation velocities are nearly equal under any stress [89], providing an appropriate frame for analysis.

Increasing the dopant concentration of n-type dopants shows an increase in the dislocation velocity, as seen in Figure 30. Dislocation velocity can be described by $v_D = v\theta$, where v is the dislocation velocity for intrinsic materials, and θ is the dopants concentration[90]. Since the strain relaxation rates vary linearly with dislocation velocity, enhanced dopant concentration can lead to elastic relaxation at the surface and decrease strain. The speed of heavily doped Ge n-type 1×10^{19}cm^{-3} is ~0.06-0.1cm/s under the temperature range for Ge growth[91], being 400-650 ℃.

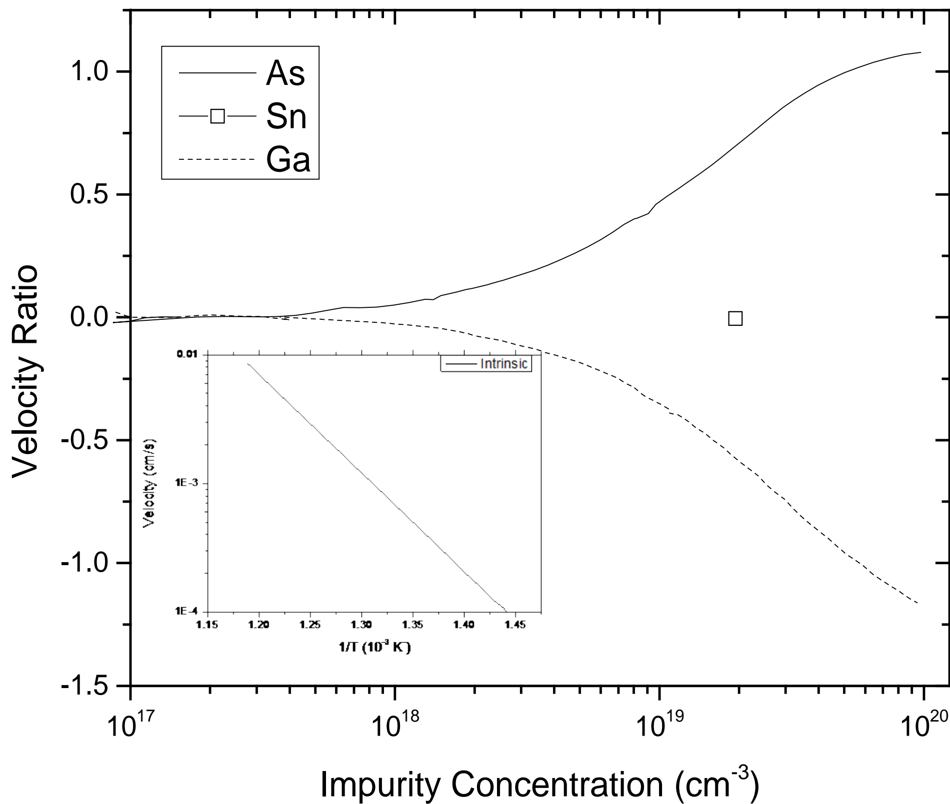

Figure 30.- Effect of n- and p-type doping on 60° dislocation velocity in germanium at T = 500°C. A neutral impurity such as Sn has no effect on dislocation velocity at a concentration of 2×10^{19}cm^{-3}. Correlation between temperature and speed increase on intrinsic Ge is shown.[92]

The high dislocation speeds facilitate glidding and termination of dislocations on the sidewalls on oxide walls widths under ~0.01cm, during the cooling process from Ge growth from 650℃ to 25℃. Dislocations terminations are statically limited. In order to correctly estimate the necessary area - oxide walls widths- the termination process has to be analyzed from the types of threading dislocation present.

The type of threading dislocation present in epitaxial growth can be divided as sessile and glissile dislocations. The former are pure edge dislocations on Ge which move on the $[1\bar{1}0]$ and $[1\bar{1}0]$ directions, avoiding interaction in (001) plane. These dislocations have no shear stress under biaxial stress[93] and will not glide under thermal stress. The glissile dislocations are mixed 60˚ dislocations with Burgers vector in $[101]$, $[10\bar{1}]$, $[01\bar{1}]$ and [011]; they are invisible to the $(1\bar{1}1)$ and $(\bar{1}11)$. They are the only dislocations that will glide under thermal stress. There are some mechanisms by which a sessile dislocation can become two glissile dislocations, however, the energy of transformation is of the order of 10eV/nm and too high to overcome even at the melting temperatures for Ge. Interactions between sessile and glissile dislocations form new glissile dislocation. The energy of formation of this dislocation is smaller and more probable in Ge samples. Note that most of the dislocations observed in Ge are of glissile type and prompt to terminate during annealing, decreasing the density of dislocations.

Furthermore, gliding reaction time of different dislocations slows down the process of termination, causing anneals to lose effect. Further analysis indicated that every dislocation reaction cause reduction in the dislocation density, which can be set as

$$\frac{d\rho}{dm} = -k\rho^2$$

where ρ is the dislocation density, m is the number of anneals cycles, and k is the reaction rate constant[47], however, this model is incomplete for multiple anneals. For a single anneal, the model accurately predicts the reduction of dislocations on intrinsic Ge to threading dislocations ~10^8cm^{-2}. This model shows that the increase in anneal cycles permits the reduction of dislocations but it lacks to consider clusters of dopants preventing their termination. Clusters of dislocations will no react and pile-up, increasing the average threading dislocation count to ~10^8cm^{-2} after 10 anneal cycles.

With no anneal cycle, as the case in our growth, permits the dislocation concentration to start at ~10^9cm^{-2} in intrinsic Ge. The second anneal reduces the threading dislocation density below 10^8cm^{-2}. Starting threading dislocation in heavily doped n-type Ge 1x10^{19}cm^{-3} is registered at ~10^8cm^{-2}, and expected to decrease in subsequent anneals.

Moreover, on smaller grown area dimensions, the dislocations travel shorter distances and can be annihilated at the oxide walls. Analysis had been done showing dramatic reduction on dislocation density with reduced areas deposited, as seen in Figure 31. An analysis performed with doped-Ge is missing. Extrapolating these findings, it is expected to reduce dislocation density equivalently by the reducing 1-D of the oxide walls, forming waveguides.

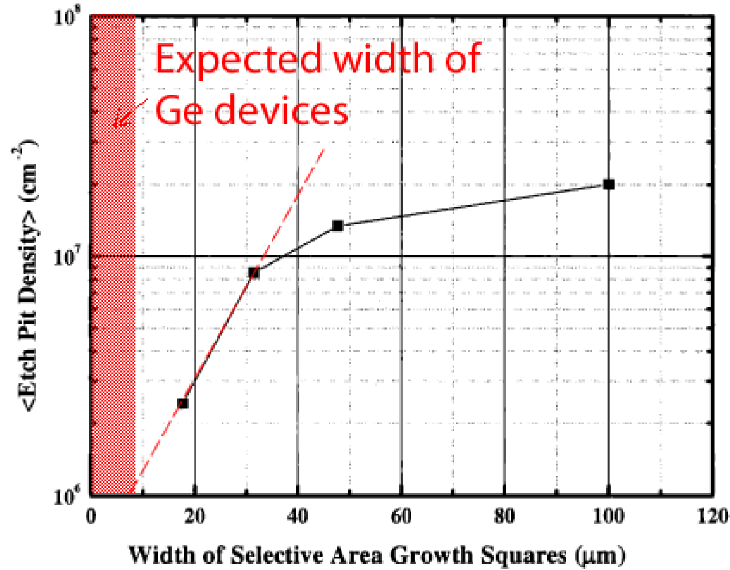

Figure 31.- Average etch pit density of intrinsic Germanium grown on squares surfaces of diverse widths after cycle annealing.

Ge device geometry selected is confined to rectangular prisms, for example, 1-D oxide confined waveguides. The width of these waveguides are <3μm, being less than ℓ_{av}. At these small dimensions, the dislocation mobility is high enough to permit relaxation of the Ge film and decrease threading dislocations density during growth. With an average threading dislocation density of ~10^{9}cm^{-2}, and considering random termination on the Ge-Si interface or oxide walls, the dislocations would travel an average of distance in the <110> direction of $w/\sqrt{2}$, *w* being the width of the waveguide or thickness of the waveguide, ~0.5-1μm.

Two main variables are changed: ℓ_{av} of dislocations, depending on width and thickness of the growth; and terminated dislocations, due to enhanced speed. This is confirmed through TEM micrographs, as seen in Figure 32, where dislocation density is below 10^{8}cm^{-2}. Plane-view TEM shows a transition from heavily dislocated, on the Ge buffer, to defect free in the thick n+Ge. The low level of defects is explained through the reduced distance the dislocations have

to travel before terminating in the interface. The dislocation density reduction is not total, as suggested from the gliding speeds. The terminal dislocation density indicates anchoring of the dislocations through screws and jig dislocations, and the existence of sessile dislocations. Nevertheless, the change in dimensions reduces the dislocation density below Ge films, confirming that the etch pit density reduces by size of growth due to defect necking mechanism[94, 95].

The epitaxial necking explanation of defect trapping is based on the assumption that, in the ⟨110⟩ {111} slip system, threading dislocations (associated with the stress-relieving misfit segments at the epitaxial interface) lie in the {111} planes in the ⟨110⟩ directions. The "trapping" of these threading segments line directions would project into the oxide sidewalls should the dimensions allow.

In our work we observe that cooling of the Ge growth and dimensions limit the total number of dislocations terminated. During Ge growth the film is fully relaxed – avoiding any external stress – preventing movement of the dislocations, therefore, reducing the total number of dislocations terminated. Dislocation density reduction still occurs during cooling but the decrease in dislocation portrays an issue in total strain retained. Since both dopants and area growth available present a decrease of dislocations, it is not clearly identified which of these two effects dominates in our growth.

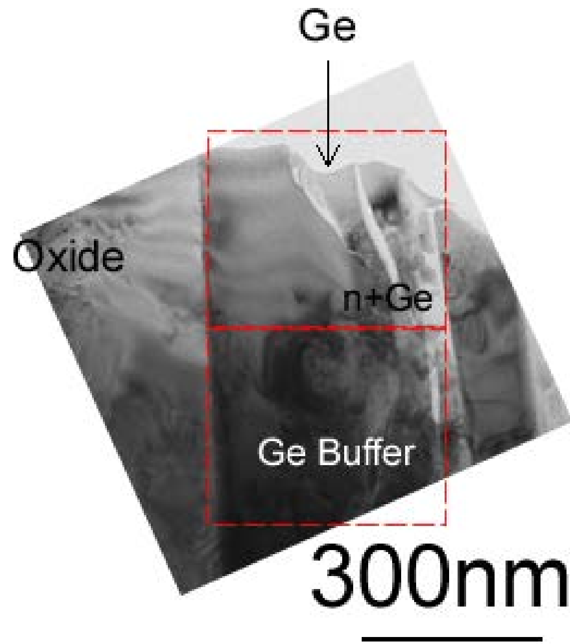

Figure 32.- Plane view TEM sample of waveguide growth Ge at doping conc. ~$1x10^{19}cm^{-3}$. The dislocation density is ~$10^{9}cm^{-2}$ around the interface which represents the Ge buffer. n+Ge shows <$10^{8}cm^{-2}$ dislocation density.

Different Ge waveguide structures possess different strain in their systems. It was previously demonstrated[76] a process to induce strain in Ge through its buffer according to the growth temperature and relaxation of the lattice. We only focused into 650°C due to optimal growth condition for doping concentration. At this temperature, Ge films grow with a tensile strain of ~0.2-0.3% tensile strain. It has been shown that this condition is not kept in mesas [96], and similar effect is expected on waveguides.

Faceting at reduced areas can induce to elastic relaxation of the strain as shown in the schematic in Figure 33. Stress in a thin film is due to lattice or thermal mismatch between the film and the substrate. In the case of Ge-on-Si, this mismatch is achieved during growth where Ge is relaxed and stressed while cooling. The stress is maximized in the interface, and translates to the rest of the body.

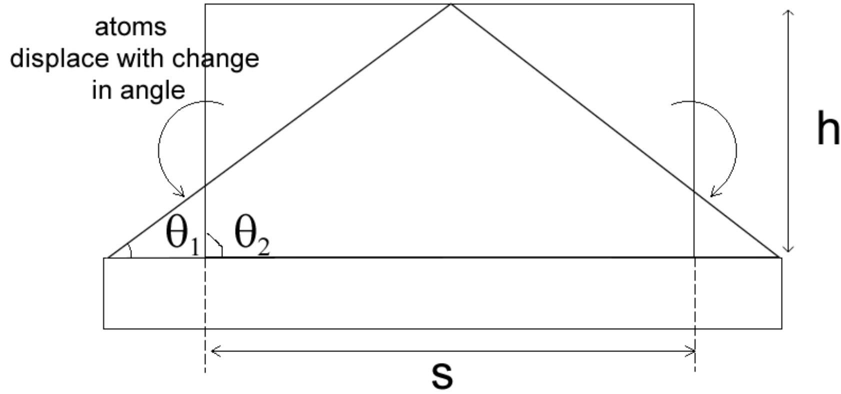

Figure 33.-Schematic showing that reducing the fact angle is equivalent to moving atoms to the interface

The strain energy decreases due to elastic relaxation by faceting. The loss in strain is not as significant as with mesas since waveguides are limited in 1-D. For a piece of rectangular mesa with average width s, thickness h, and a facet that makes an angle of θ with the surface, the amount of decrease in strain energy per unit volume, is given as

$$E = 2c\left[\left(\frac{h}{s}\right)\ln\left(\frac{s}{h}e^{\frac{3}{2}}tan\theta\right)\right]$$

where $c = {\sigma_b}^2(1 - v_{Si})/2\pi G_{Si}$. Here σ_b is the biaxial stess of the uniform blanket Ge film (around 0.2-0.3% with our growth parameters), and $v_{Si} = 0.278$ and $G_{Si} = 51GPa$, which are the Poisson ratio and the shear modulus of Si (100) substrate, following Liu's approach[16, 97]. The average loss for a 0.25% strain sample would translate into ~0.03% loss in strain, which matches with our observations. The value is calculated from $E = Y_{100}(\varepsilon_0^2 - \varepsilon_f^2)$, where Y_{100} =102.66, is the Young modulus of germanium.

The reduction in dislocation quantity translates into loss in strain since the dislocations accommodate the stress and strain in the system. Misfit dislocations form to reduce the strain energy, hence, as the dislocations reduce the strain energy increases. The calculated strain change from ~10^9cm^{-2} to ~10^8cm^{-2} dislocation density is ~0.01%. The approximation can be

derived from Cantu's[98] and the fact that we have 4 families of preferred dislocations [011] acting perpendicular to (100) plane. As seen in Figure 34, the release on tensile strain surmounts to a change on strain of ~0.03±0.02%. With a release on strain the peak emissions on PL would blue shift due to the increase in energy in the Γ valley. This is not observed, as demonstrated in further chapters. Since PL shift is not significant, and the error in measurement can lead to a 0.02% error, we observed that the strain is changed by 10% compared to films.

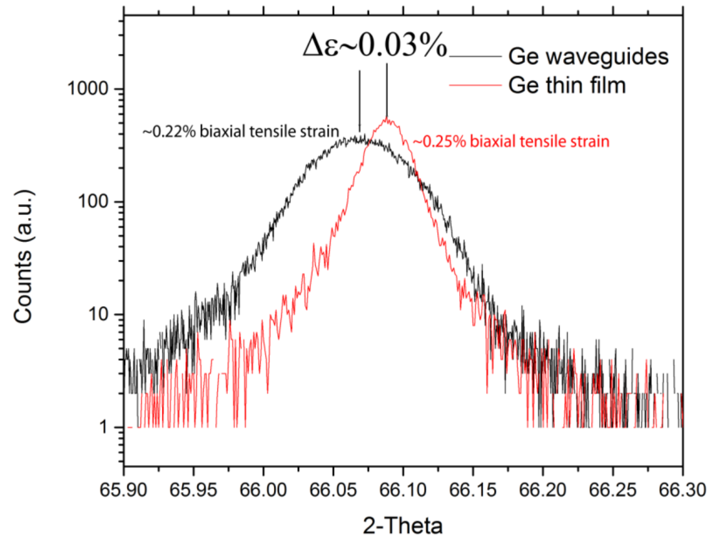

Figure 34.- XRD from Ge waveguides and thin films doped to $1x10^{19}cm^{-3}$. FHWM does not provide information due to the heavy amount of oxide in the Ge waveguides. There should be a blue shift in emission with these conditions, but due to the heavy doping, it is compensated.

It was demonstrated that Ge doping and dimensions constrains permit a lower level of threading dislocations than Ge film growth or nondoped intrinsic material. The reduction on threading dislocations reduces the stress on the film, hence, the strain on the Ge devices. Fortunately, reduction on stress is less than 0.03% making the shift insignificant for the energy transitions on the different bands.

3.1.2 Facet formation

Germanium growth occurs with facet formation. Such facets, acting upon each other, limit the total thickness of the Ge devices. In this section, we show the dependence on size and pressure on the growth of Germanium waveguides. Reduction of defects under certain conditions is discussed.

Germanium was originally produced in the form of films, for the use of photodetectors, modulators or LEDs. These films would be etched, refill with oxide or other materials. The approach led to inefficient devices due to inclusion of defects during etching. The approach explored previously by our group showed to be the best alternative. Using oxide windows, exposing bare crystal Si for Ge growth showed to passivate the walls and increase performance of modulators and photodetectors. In this work we followed the same approach.

Starting with bare-Si prime wafers, we growth a thermal oxide, ranging from 200-800nm. Photolithography was used to make a mask for RIE etching. During the etching, a slight amount of oxide should be left to avoid the resist interact with the Si surface. BOE etching is performed to remove the last 10-50nm of oxide, exposing the Si surface. The dimensions of the Si channel are limited to the photolithography, being 700nm the limit. More details to this approach can be found in the Appendix.

During growth it was believed that growth would be uniform in height through the wafer. It was seen in Liu, et al[88] that Ge tend to form facets. The facets are angle dependent[16] with the oxide walls and are predominantly (100), (311) and (111). More importantly, the growth is under constrain dimensions. As the facets growth at different speeds, once a facet is terminated, it shuns the growth of the others. As seen in Figure 35**,** undoped Ge

grown at 720℃ showed a clear decrease in dimensions on the same sample as the dimensions of the oxide window were decreased.

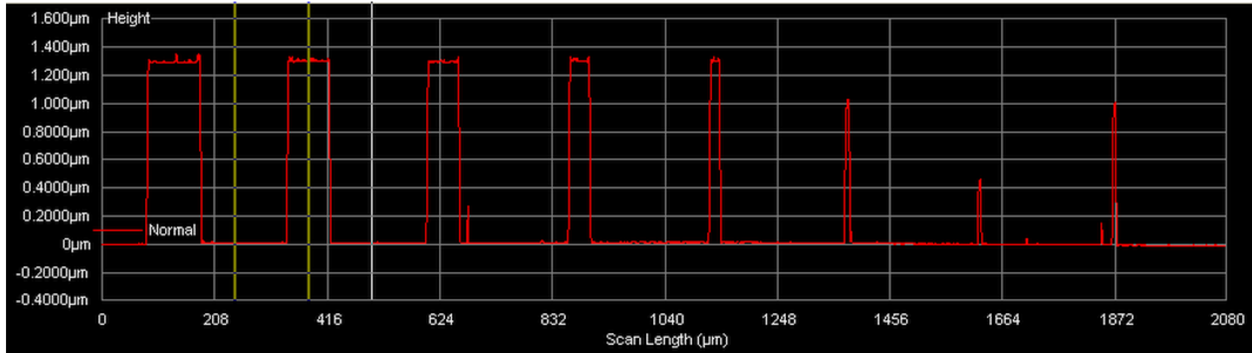

Figure 35.- Profilometry of different undoped Ge mesas growth at 9.8mtorr at 720°C for 2hrs. Widths varying from 100µm to 5µm demonstrate growth limits due to window size.

The effect is not exclusive of undoped Ge. As seen in Figure 36, the decrease occurs more abruptly the smaller the sample dimensions due to terminated facets. To explain the fill and height differences, the problem has to be addressed from facet orientation formation and growth speed.

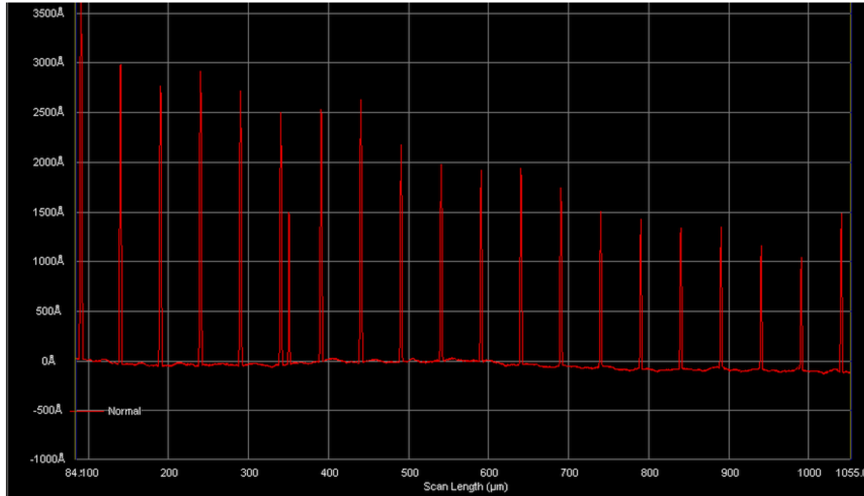

Figure 36.- Height change from different Ge waveguides doped to $1x10^{19}cm^{-3}$. Growth conditions at 9.8mtorr with 350nm of oxide window. Ge waveguides width changes from 3µm to 1µm with steps of 0.1µm. Maximum height observed is ~650nm and minimum of ~450nm. Growth is terminated due to the (111) facets.

The facet growth dependence to the window oxide was treated by Liu's work [16] and Borgstrom [99]. The shape is predetermined by the growth rate in the orientation perpendicular to the facet. In our case we will deal only with the convex surface case, illustrated in Figure 37.

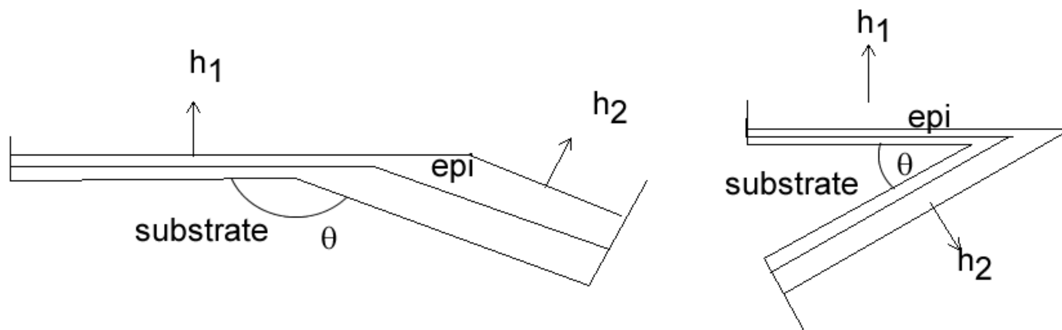

Figure 37.- Schematic showing Borgrstrom construction with a convex surface $0° < \theta < 180°$. In convex structures h_1 is slower than h_2.

In the schematic, for easy comparison, the areas are equal at the beginning, established by the substrate. In convex surfaces, the slowing growing facet consumes the faster growth

facets. In concave surfaces, the opposite effect is found, where the fastest growing facet consumes the slowest one. The construction implicitly assumes that the growth rates of the orientations between the growth directions of two neighboring facets are linearly interpolated.

Another method used is the Wulff construction. Its ability to determine the shape in planar substrates makes it ideal for patterned oxide windows. Wulff constructions take into account the growth rate in all directions, instead of assuming a linearly interpolation. We took this as the method of study to take into account all the possible facets formed.

From observations, the three main facets of growth for Ge are (100), (111) and (311). Knowing their facet speed growth would give us an estimate of the time required to fill a trench. We have studied the growth rate on Ge on Si in <100>,<111> and <311> at different pressures and at different thickness, as shown previously. With the help of the Wulff construction, and using the sidewall angle ϕ, shown in Figure 38, and using cross-sectional SEM a simple expression can be reach, derived from previous known theory. It was shown that filling time would be,

$$t_{fill} = \frac{d_{<>}}{v_{<>}} = \frac{\left(\frac{h}{sin\phi}\right) sin(\phi + \theta_{<>})}{v_{<>}}$$

where $d_{<>}$ is the thickness growth of the facet <>, $v_{<>}$ is the speed of the facet growth, $\theta_{<>}$ is the angle of such facet and h is the thickness at the highest point. This expression is correct for any Ge growth, as long as the width of the mesa is larger than $50\mu m$. At Ge thickness growth over 4 μm , this expression is no longer valid. The growth time might also vary according to pressure and temperature, which are not taken into account in the expression.

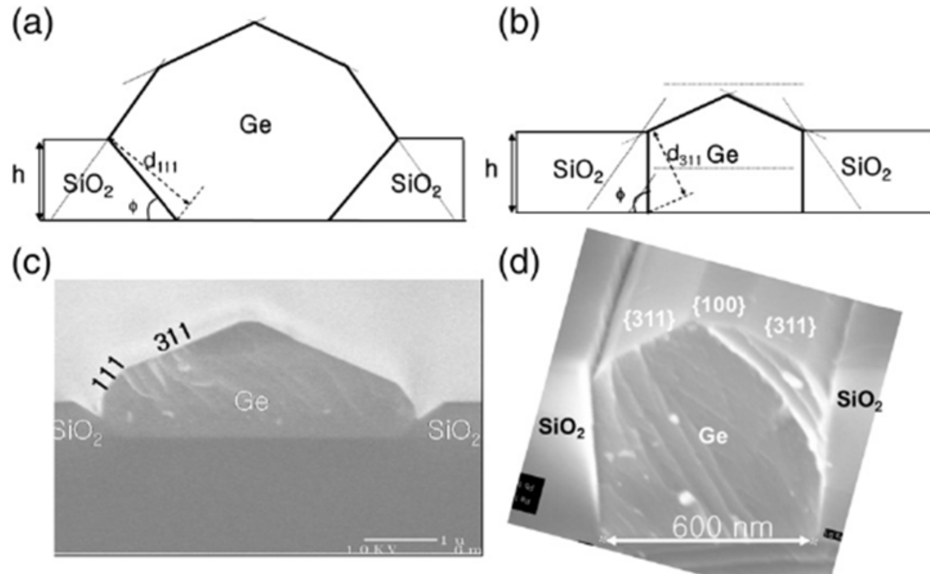

Figure 38.- Wulff construction for cross-sectional morphology of Ge selectively grown in trenches with (a) a sidewall angle (ϕ) close to 45°, and (b) a sidewall angles (ϕ) close to 90°. The dotted lines demonstrate the Wulff construction of (111), (311) and (100) facets. The area enclosed by the dotted lines and the SiO_2 side wall determines the shape of the GeSi crystal (thick black lines). The profiles shown here correspond to the moment when the trench is just filled up. This model is compared to cross-sectional SEM pictures of Ge grown in trenches with ~ 45° sidewall in (c) and ~ 90° sidewall in (d). The Wulff construction model is in good agreement with growth morphology shown in the SEM pictures.[100]

According to the sidewall angle, there is a predominant facet growth [16]. When $\phi < 82.5°$, the (111) facets will be the limiting factor during the growth rate; when $\phi > 82.5°$, the (311) facet will be the limiting factor. As seen in Figure 39, the theory matches observations. However, the growth filling factor is not corrected when two neighbor facets intercede.

Under identical conditions, Ge growth rates changes according to the size of the window oxide. This is due to the (311) colliding with its mirror facet. This is independent of

the angle since growth direction will be dominant by (001) and will always have same neighboring facets. The time it would take to collide is

$$t_{311} = \frac{d_{311}}{v_{311}} = \frac{w}{2v_{311}cos\theta_{311}} = \frac{w}{1.8v_{311}}$$

Where w is the width of the oxide trench width. This time would have to be compared to t_{fill} derived. If t_{311} is smaller than t_{fill}, then the maximum growth possible is

$$h = \frac{t_{311}v_{<>}}{\left(\frac{\sin(\phi + \theta_{<>})}{sin\phi}\right)}$$

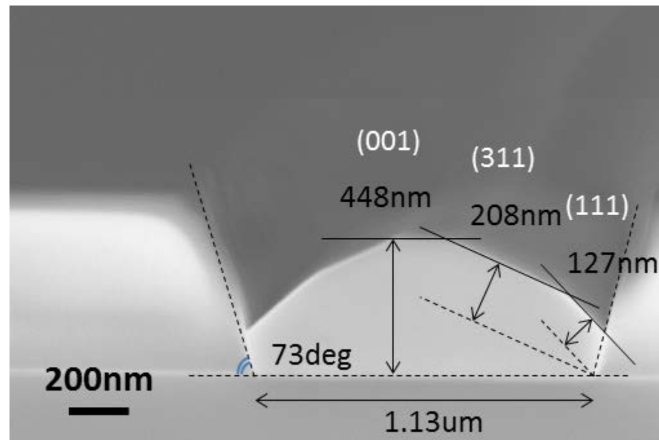

Figure 39.- Ge waveguide SEM growth under 9mtorr for 90min.

In summary, the window oxide permits the growth of complex shapes of Ge while still retaining passivation. Nonetheless, the oxide also becomes a limitation when the structures are reduced. Our point of interest is on waveguide structures under $3\mu m$. Hence, the limitations put another stop into the growth and filling of the trenches.

3.1.3 Pressure dependence on Ge waveguides growth

The growth filling of oxide trenches is vital for device fabrication. During CVD fabrication, it was used a constant temperature and GeH_4 - PH_3 flow. From rate kinetics it can be derived that the only variable is pressure. In this section we demonstrate how a varying pressure has a

strong effect on growth rates of n+Ge. Under UHVCVD, we explored the growth kinetics under higher pressures than 2mTorr [77] and how the growth rates facets and overall thickness in Ge change accordingly. The gas flow was PH_3 at 12sccm and GeH_4 at 3.7sccm. The growth temperature was set at 650°C. Growth time was limited to 90minutes.

It was observed that facet growth rates do not change significantly with different pressures. The most plausible trend needed is reduction of (311) facet growth rate, an increase on (111). As seen in Figure 40, there is no evident increase on rates. From fitting a slight increase is seen in (111) facets under heavy pressures. If a trend is assumed, the shift is greater. Such measurements need to be performed to justify such shift.

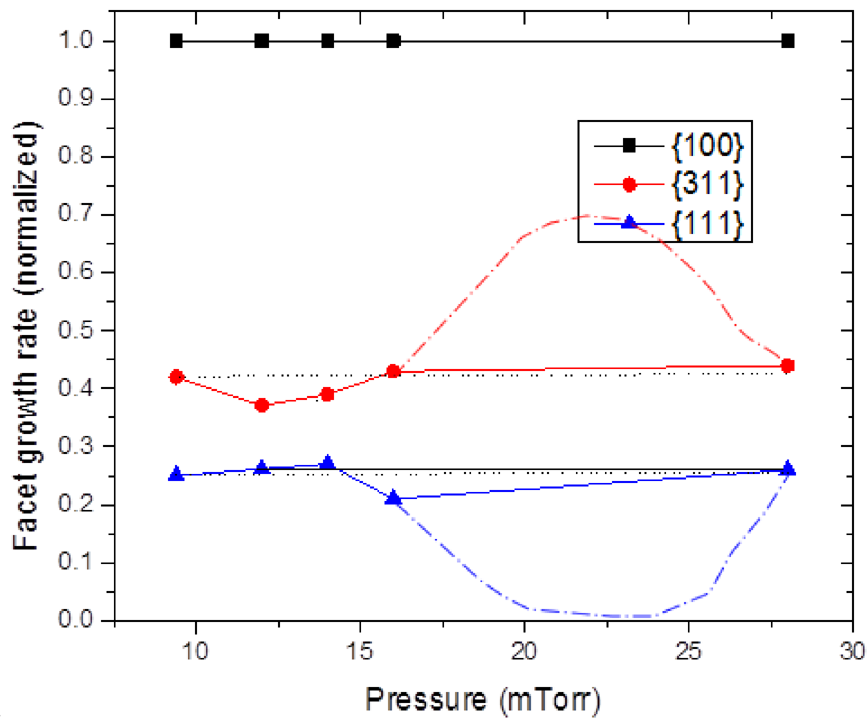

Figure 40.- Growth rates at different pressures under same time and conditions. Dashed line shows predicted growth rates, and dotted line the most possible case where the growth differences are noise on the measurement.

The growth have been normalized to the (100) plane but the overall thickness differ. The fastest growing facet (100) would have to grow enough in order to overcome the t_{311} limit. Under a time frame of 90 min, this limit is not achieved. The growth rates remain approximately constant so further investigations are needed at different angles in the oxide windows.

In Figure 41, we can see the increase in growth speed over different pressures, same temperatures and same oxide trenches width. The final thickness changes significantly. The stronger the pressure the most likely a Ge atom will recombine in the surface since it would be more available. Pressure correlates directly with concentration of atoms from ideal gas law, C_G=p/kT. The increase in thickness is linear which matches with steady state conditions, where flow V is linearly dependent to concentration C_G. The increase in pressure should not increase the defect concentration since Ge mobility is dependent mainly on the temperature of growth, as long as the reaction is reaction limited.

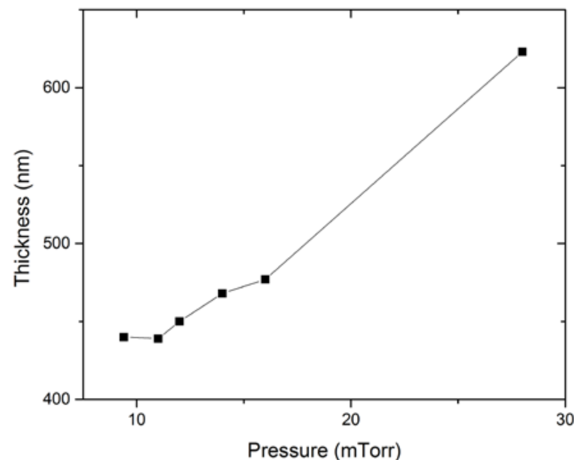

Figure 41.- Final thickness of growths at different pressures, and same temperature and time. Linear dependence to rate of deposition is obtained due to similar growth conditions in time and flow.

In summary, we observed a change in growth rates linearly dependent to pressure. This dependence can give an estimated growth size related to pressure. From these results it would be recommended to grow under heavier pressures, while doing plane-view TEM defect analysis. The following section will discuss how to improve strain in Ge, and the removal of Ge buffer.

In this section we demonstrated,

- Dislocation dependence to width, temperature-time, orientation of the trench, and doping.

- Tensile strain decreases insignificantly despite reduction of dislocation density

-Facet formation rates limit the thickness of the Ge devices

- Total pressure in the system does not change the facet growth speeds.

3.2 Ge Nonbuffer growth

The Ge buffer has been an essential part for the growth of single crystalline low dislocated Ge. The buffer accommodates for the large mismatch between Si and Ge, as explained in previous sections. Ge-on-Si photonic devices typically require a minimum thickness of 50-100nm, so that the buffer can occupy a large portion of the active device. This buffer layer is highly dislocated and therefore has a large number of recombination centers that can degrade the performance of Ge devices, as was seen in the TEM figures. For Ge photodetectors, the recombination centers can reduce responsivity and increase dark current. In the case of on-chip Ge lasers, the Ge buffer reduces gain and acts as a dopant sink. Therefore it is highly desirable to eliminate the buffer in order to improve device quality. In this section, Ge buffer reduction and elimination is explained. It is shown that the excess of dopants and reduction of dimensions provide a path to deposit Ge without a buffer.

Typical Ge growth has a low temperature Ge buffer [24], but as seen Figure 42, it has the drawback of dopant sink. Thicker the Ge buffer, the larger the dopant absorption taken from the active device area. This sink can take concentrations over ~10^{21} cm^{-3} on dopants making them an important part of electrical and optical properties. Electrical since it can form alloys of GeP making it more difficult to conduct to the n+Ge active layer. Optical since it can take part of the dopants in n+Ge, reducing the possible achievable gain. At such dopant absorption, the buffer can be detrimental to achieve high doped Ge for laser devices, which needs >$1x10^{19}cm^{-3}$ P concentration. Once the P reaches the interfaces, those being Si or SiO_2, the P diffuses order of magnitudes slower. It suggests that the main mechanism of dopant loss is outdiffusion to the surface or the sink.

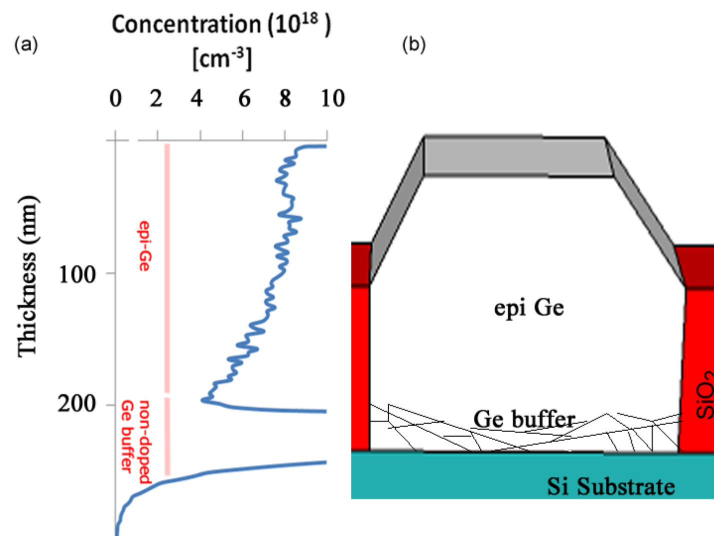

Figure 42.- (a) SIMS results showing P concentration in Ge-on-Si. Notice that the buffer acts as a dopant sink with concentrations above $1x10^{20}cm^{-3}$. (b) schematic shows typical Ge trench growth and where the dopant sink appears, which is in the Ge buffer.

Furthermore, Samaveda reported that bufferless Ge growth has a thickness limitation, where the diameter of a selectively grown area had to be less than the thickness of the Ge film

in order to retain single crystallinity [101, 102]. Since Samaveda's research focused on the growth of dislocation free Ge, it is not clear if his constraints are generally applicable. Ge islands tend to have an average length ~$3\mu m$. If the average diffusion length is shorter, the island growth is expected to be suppressed. It is perceived that a 1-D reduction laterally, to confine in waveguides, should be the mechanism needed to permit the same effect.

This section will cover the general preparation and the particulars of each growth. It is discussed the P, B and combine effects in the growth. The epitaxial Ge layer shows an atomically abrupt interface with Si and still retains its tensile strain compared to identically patterned Ge using a buffer layer. Bufferless Ge can potentially improve the performance of Ge-on-Si photonic devices.

3.2.1 Materials preparation

Epitaxial Ge without buffer was grown on bulk silicon substrates with (100) orientation by UHV-CVD using a low temperature Ge buffer to accommodate for the 4.2% lattice mismatch between Ge and Si. The buffer thickness and growth conditions were varied to determine the minimum thickness of the buffer that still results in single crystalline Ge growth.

Before Ge growth, Si wafers were wet-oxidized to 500nm oxide thickness. The wafers were then patterned to open long rectangular windows of various widths (200-1500nm) spaced 100µm apart and etched using reactive ion etching (RIE) and a buffered oxide etch. Ge was grown in the open windows selectively as previously mentioned [103].

The bufferless growth was performed at 650℃ -720℃ for 2hr with a variety of flows, reported ahead and total pressure during growth at 9.8mTorr.

3.2.2 Bufferless P-doped Ge

Phosphorus is a dopant of choice for n-type Ge due to its high solubility. Moreover, n-type dopants permit a faster movement of threading and misfit dislocations, reducing centers of nucleation during growth. Phosphorus can be considered as a surfactant that provides stress release to Ge deposited, or as a dislocation diffuser. The introduction of a 1-D constrain provides a barrier for island formation, as it will be seen in this section.

While it was not found that any large area growth conditions that yielded a pit free epitaxial layer without the use of a buffer, dimensional constrained growth areas could be used to grow bufferless Ge. Figure 43 shows an example of a 2μm wide Ge layer, selectively grown in an oxide window without the use of a buffer using the same growth recipe as typical n+Ge. The rate is 3.8sccm Ge to 12sccm P at 650°C for 2hr. The Ge layer clearly shows faceting, a sign of single crystal growth. This material was further explored using transmission electron microscopy (TEM). Due to the small size of the sample and the distance between Ge layers, focus ion beam preparation was necessary to obtained a Ge sample. Analysis was performed in the direction of the (100) and (111) planes (Figure 44).

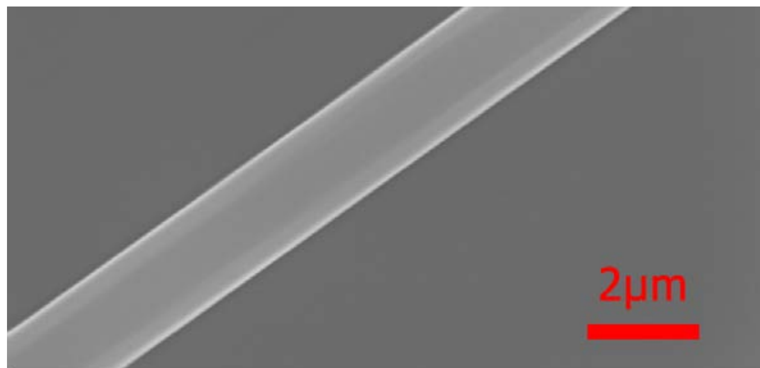

Figure 43.- Bufferless Ge growth upper view SEM in constrained oxide window. A lateral constraint of $<2\mu m$ results in single crystalline epi-Ge growth.

TEM images confirm the single crystal growth, as seen in Figure 44. The misfit dislocations are clearly constrained to the Si-Ge interface, extending less than 5nm in either direction. Analysis was performed in the direction of the (100) and (111) planes. Fourier transformation analysis of the high resolution images confirmed the single crystallinity of the Ge.

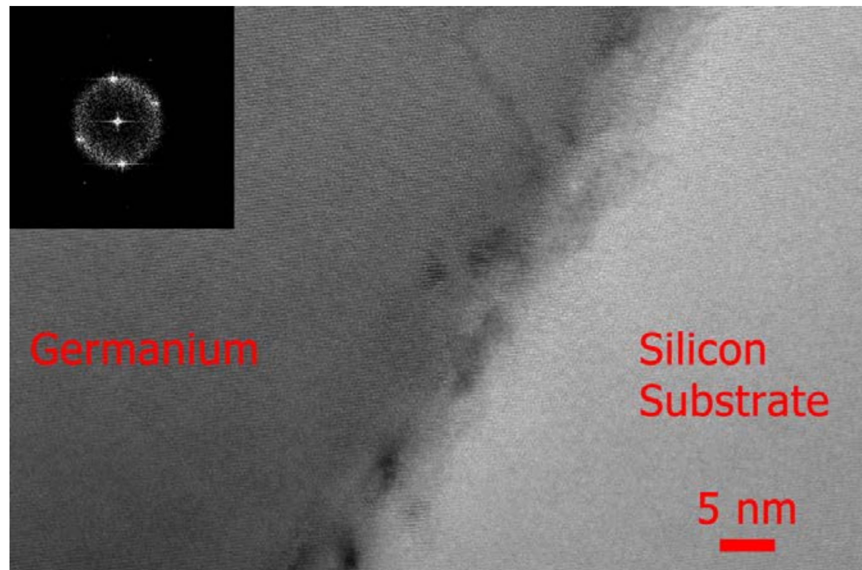

Figure 44 . TEM image of the Si-Ge interface after bufferless growth in a constraint area. The[001] plane matches the lattice in both materials.

TEM plane-view aligned to (220) plane reveals, as seen in Figure 45, a similar quantity of dislocations, ~$5x10^{8}cm^{-2}$. This small concentration of dislocations is only expected with annealed samples.

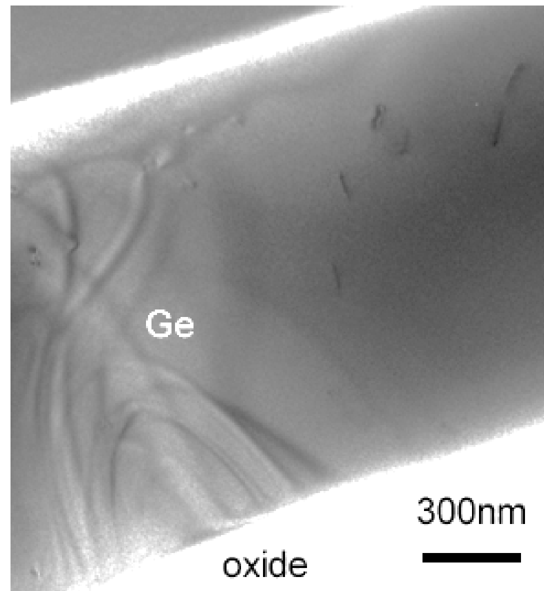

Figure 45.- Ge heavily doped to $1x10^{19}cm^{-3}$ grown without buffer. The dislocation density is $\sim 6x10^{8}cm^{-2}$.

Due to the difference in thermal expansion coefficient between Si and Ge, Ge-on-Si layers typically show a tensile strain of about 0.2-0.3% due to lattice relaxation at growth temperature. In order to determine if bufferless Ge layers retain tensile strain, we evaluated the residual strain in the layers using XRD. We found that the tensile strain of the bufferless Ge waveguides $1\mu m$ on width is ~0.25% as can be seen in Figure 46 in comparison to a Ge layer grown with buffer. This result shows better strain than buffer Ge waveguides, which show a decrease in strain. Full-width-half-max (FHWM) of the Ge XRD peak in both samples is equivalent showing that bufferless Ge has similar tensile strain compared to a Ge film grown with buffer.

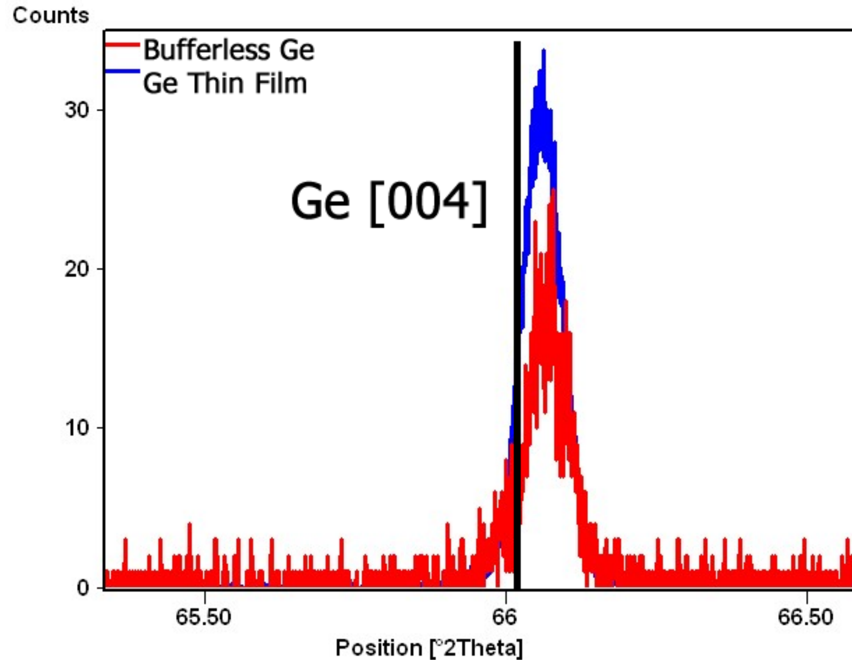

Figure 46. XRD peaks of Germanium (004). Symmetrical measurement shows compressive strain in the z direction, translating into a ~0.25% tensile stress. Distribution of strain is observed through comparison of FHWM.

The increase in tensile strain can be due to reduction in the buffer which prevents heavy relaxation to occur in small trenches. This effect has the potential of increasing emission and gain in Ge light emitters.

Ge was grown, as stated before, in the oxide channels at different thicknesses. Ge grows in trenches of ~2μm width or less exhibiting faceting, as can be seen in Figure 47. Continuity in longitudinal dimension suggests single crystal epitaxial growth, in any sample, and from now on in this analysis it is taken as a condition for crystallinity.

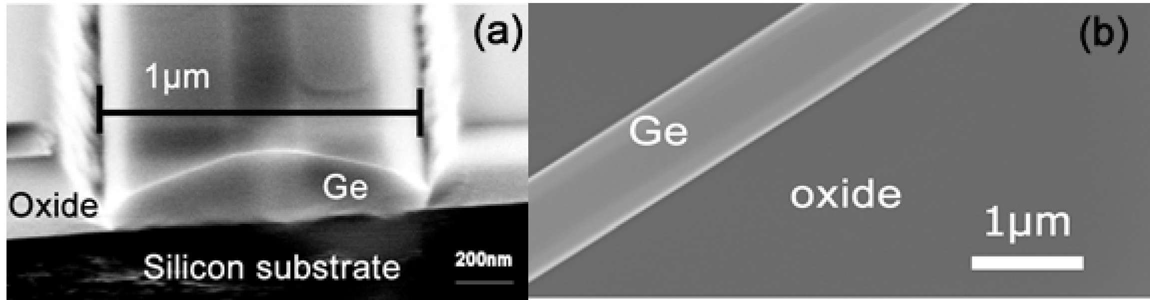

Figure 47. SEM image for Si/Ge interface with dimension constrained bufferless growth. [001] plane matches the lattice in both materials. Cross-section(a) and upperview (b) show faceting and continuity of the Ge channels.

SEM microscopy confirms the polycrystallinity by loss of faceting for oxide openings with widths larger than 2μm, as seen in Figure 48. This loss in faceting suggests a competing mechanism between the P dopant and the nucleation growth controlled by the oxide window width.

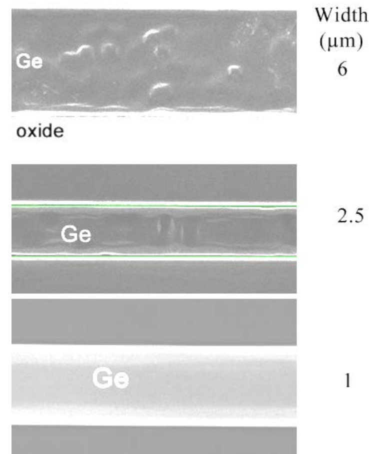

Figure 48. SEMs show top-view of the Ge channel growth and their change in roughness as their width change. Observe that at thicknesses above 1um the faceting is no longer discernible.

Due to the small dimensions of these structures, Hall effect was not used to determine the dopant concentration. In n-type Ge, the crystalline quality can be determined by the photoluminescence (PL) of the direct bandgap transition [49, 104]. Figure 49 shows a

comparison between n-type Ge-on-Si with and without a buffer layer. The figure clearly shows that the PL emission of both samples have similar spectral width, indicating high crystalline quality. The samples PL were normalized to peak intensity to see the peak shift, which is used to determine total active dopant concentration by using BGN. The larger the red shift, the larger the dopant concentration [105]. For more information, please refer to chapter 5. The red shift shows the bufferless method potential to achieve higher doping concentrations with the appropriate growth conditions. The PL demonstrated here, was grown with delta doping. Bufferless Ge grown under same conditions as standard Ge showed identical PL emission.

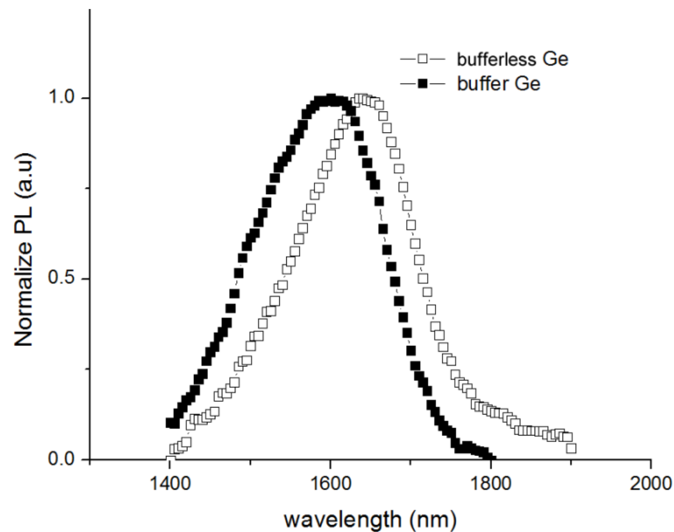

Figure 49.- Normalized to peak intensity PL comparing buffer and bufferless Ge growths, showing the potential of higher doping shown through the red-shift to 1640nm= ~$3x10^{19}cm^{-3}$ n-type active dopant. Both films showed same tensile strain ~0.25%

As the Ge height increased, twinned facets appear on the surface. Twinning occurs for thicknesses larger than 700nm for 1µm wide channels. The Ge crystallinity is highly dependent on the phosphine flow during growth as was observed in further experiments.

Generalizing the effect of P in the surface for epitaxial growth was studied. Through single flows of P at different temperatures, and flowing only Ge afterwards, or at different rates

of P:Ge. From these approaches a combination of P:Ge seemed to accommodate the most defects and permit growth of an almost defect free surface. P was expected to act as a surfactant but with pure P flown for a period of time, and after only Ge flown does not show continuity or crystallinity.

With a rate of 12:1 P:Ge while keeping total pressure in the system at 9.8mtorr at 720°C for 5 min and then growth of intrinsic Ge showed heavy twining while still keeping the crystallinity. As seen in Figure 50, faceting is clear but twinning occurs through the length of the waveguide.

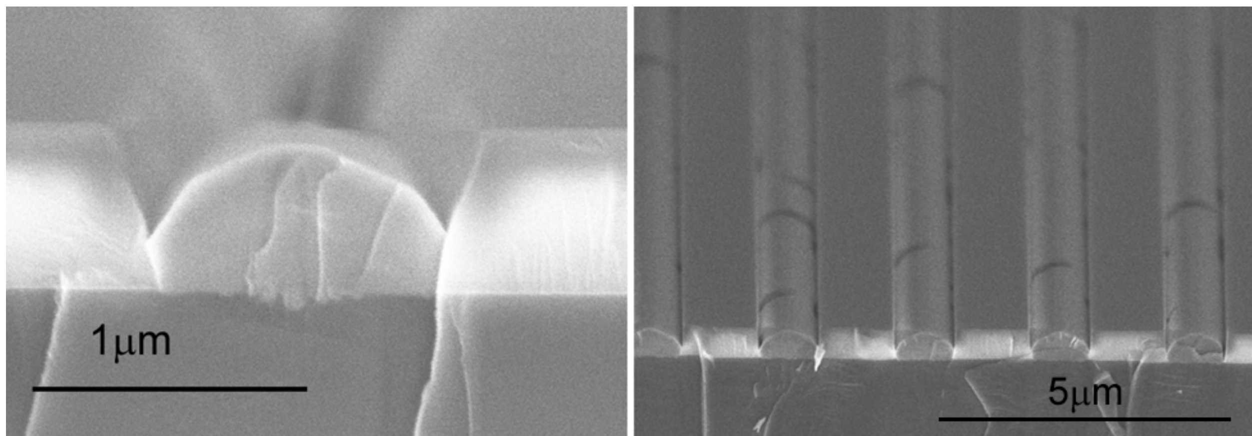

Figure 50.- Ge growth with rate of 12:1 P:Ge flow for 5min and intrinsic growth for 90min. Heavy twinning is observed, prevented the continuity but keeping single crystalline body.

Further TEM analysis revealed and increase in defect concentration. The dislocation density in the interface with the substrate was close $>10^9 cm^{-2}$, while the body remained around $\sim10^9 cm^{-2}$, and the upper surface $\sim10^9 cm^{-2}$. It suggests that the threading dislocations glide easily through the body of the device at 720°C.

Under the same conditions at 650°C growth temperature a different result is obtained. As seen in Figure 51, the waveguide structures possess less elastic relaxation in the surface, and show a more uniform grow facet. The increase in P incorporation permits faster diffusion of the

Ge atoms that are being deposited. The dislocations, as well, are faster to lock or distribute through the surface due to the dopant enhancement, as explained in previous sections.

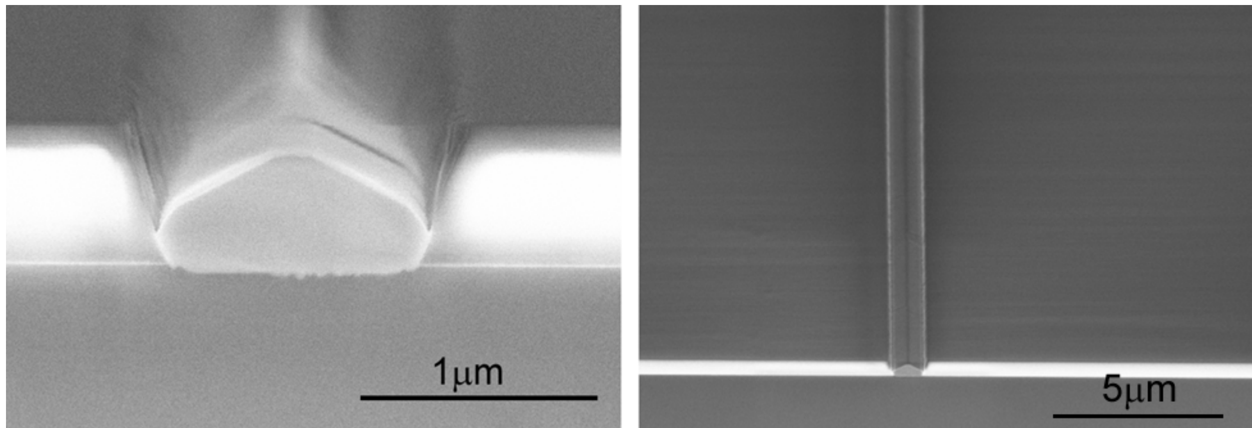

Figure 51.- Ge growth with rate of 12:1 P:Ge flow for 5min and intrinsic growth for 90min. Continuity is observed throughout the surface of the Ge waveguide.

TEM Plane-view analysis showed that even though the continuity was preserved, dislocations were still high, as seen in figure Figure 52. The dislocation densities were between 10^8-10^9cm^{-2} through the intrinsic grown Ge, while the misfit dislocations and most of the threading dislocations were buried during the initial layer, which acted as a buffer. The results show that P acts as a both a surfactant and an increase of threading dislocation speed. The existence of epitaxial growth with the single layer of P suggests the surfactant effect. The threading dislocation density difference between a Ge body fully growth with P and a single layer shows the increase on speed of annihilation of dislocations.

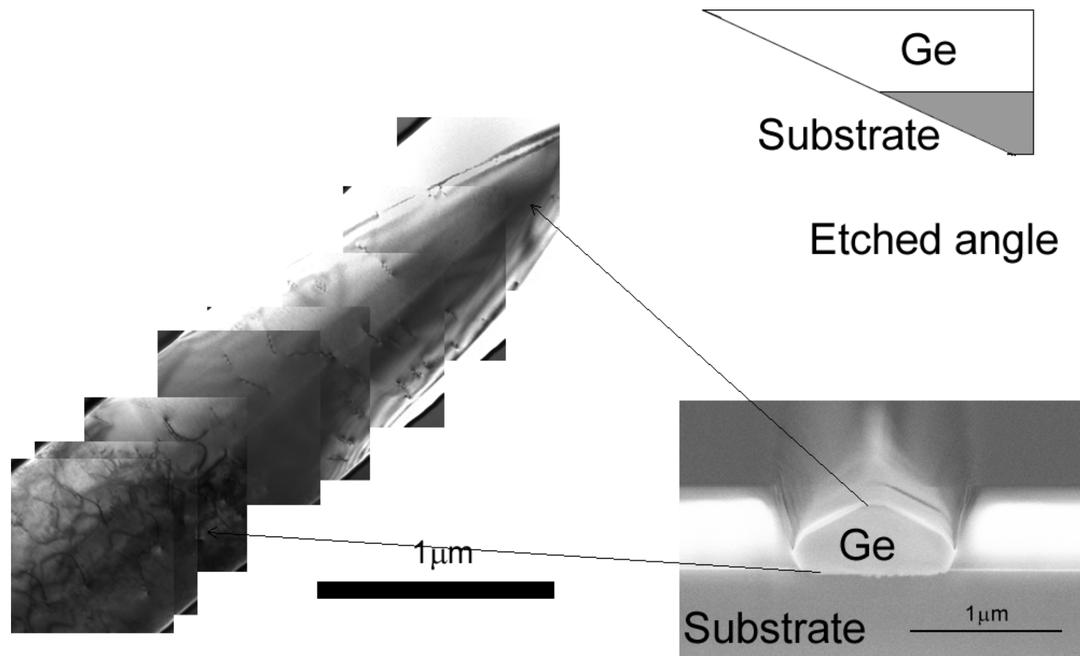

Figure 52.- Plane-view TEM aligned to (220) plane to quantify the threading dislocations. It shows a variation from >10^9cm^{-2} to ~10^8cm^{-2} in the upper surfaces.

In summary, it was demonstrated epitaxial growth of Ge without the use of a buffer to accommodate for the large lattice mismatch between Ge and Si. These films retain all misfit dislocations at the Si-Ge interface and show similar strain when compared with Ge-on-Si epitaxial films grown with buffer. P mechanism reduces the total threading dislocation in the body of the Ge growth. P effect is a combination of surfactant and threading dislocation speed increase. Oxide 1-D trench permits to control the epitaxial growth areas. Bufferless Ge epitaxial films can therefore mitigate issues like carrier recombination and dopant accumulation that has limited the performance of Ge films grown with buffer.

3.2.3 Bufferless B doped Ge

Boron is a p-type dopant that has been used in Ge devices to produce good ohmic contacts for MSMs[106], pin photodectectors and modulators [101] and even pnn light emitters[49, 107]. It is explored the possibility of using B as a surfactant or stress reliever in the same form as P. It

will be demonstrated that the same concept of s dopant surfactant and 1-D oxide constrain can be used with p-type dopants.

The conditions for the started growth were 12:1 B:Ge flow. Boron is not well represented since it is diluted to 1% with He. The total pressure remained at 9.8mTorr. After a period of 5min grown at 720°C, the growth was changed to intrinsic growth at the same temperature. SEM analysis shows faceting but lack of continuity, as seen in Figure 53.

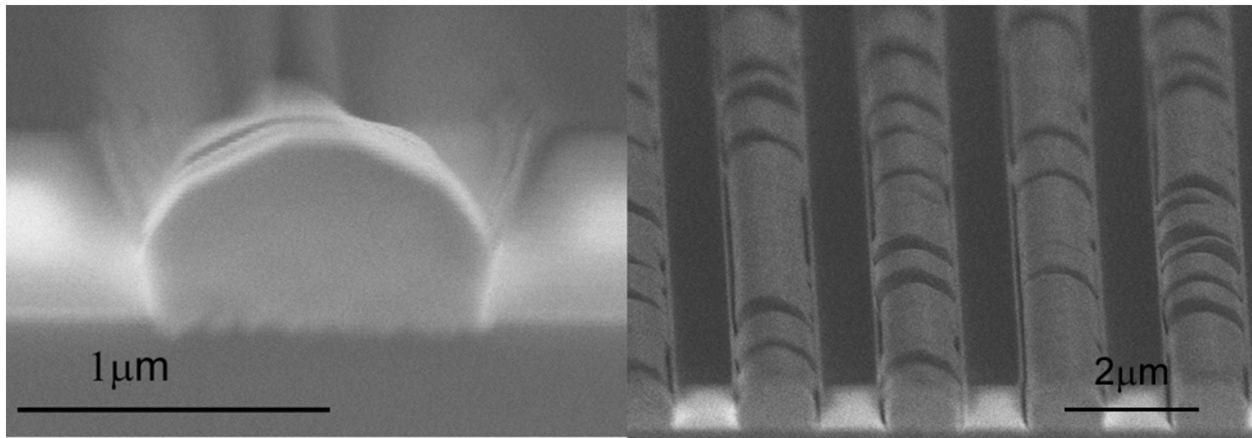

Figure 53.- Ge growth with rate of 12:1 B:Ge flow for 5min and intrinsic Ge growth after that. Ge waveguides show heavy twinning and the possibility of columnar bamboo growth.

Comparison with TEM showed that system is crystalline but heavily dislocated, >$10^9 cm^{-2}$. P-type dopants reduce the speed of annihilation of dislocations, such that the increase in dislocation density is expected. The performance for photodetector devices is doubted due to heavy amount of dislocations and possible grain boundaries, which are known to increase the dark current.

It is believed that these grain boundaries are due to the nature of bufferless growth with a mixture of 2:1 B:Ge at same pressures and temperatures throughout the entire growth. The morphology, as seen in Figure 54, is disrupted. This result confirms that the growth is mediated

by surfactant effect rather than dislocations. B decreases speed of dislocations, which would produce same result under heavier B concentration.

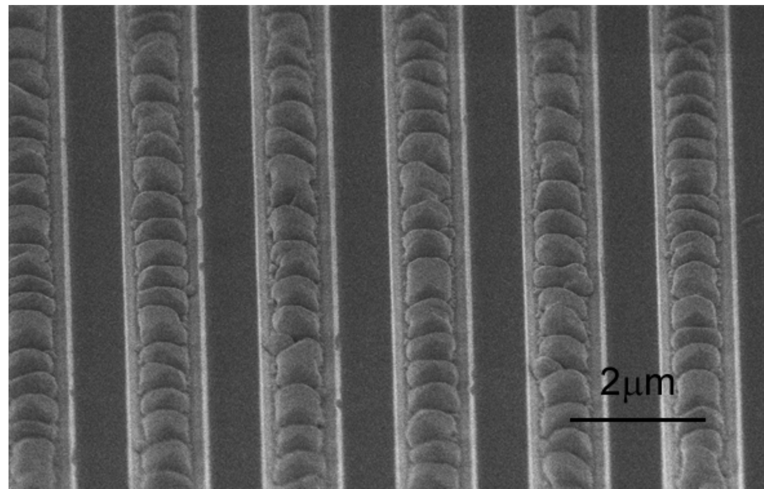

Figure 54.- 2:1 B:Ge growth at 9.8mTorr. Multiple grains are formed showing evidence of bamboo formation.

With 4:1 B:Ge, under same pressure of 9.8mTorr at 650°C, the material showed continuity and slight twinning, as observed in Figure 55. The effect of Boron through the entire Ge matrix acts more as a stress reliever, otherwise previously described waveguides would have been single crystal as well. This result confirms the surfactant effect of Boron on Ge growth.

It was demonstrated that B can also be used under the same condition of 1-D oxide trench constrain, despite the increase in dislocation density. B is confirmed to act as a purely surfactant material for Ge.

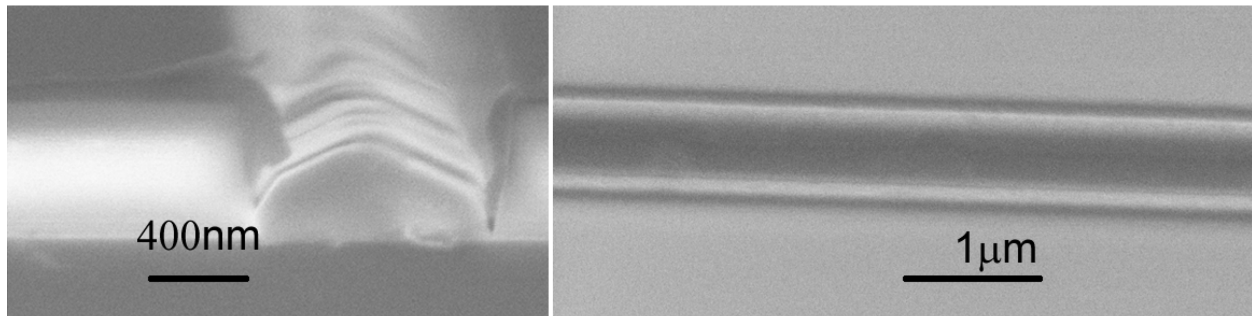

Figure 55.- 4:1 B:Ge SEM cross-section and plane-view. Continuity and slight twinning is observed. Faceting indicates single crystal.

Further experimentation is needed at lower temperatures were Diboron gas is reactive, and both, Ge and Si, surfaces are more reactive to addition of the dopant.

In summary, we have demonstrated bufferless growth of epitaxial Ge-on-Si. Controlling 1D in oxide windows provides larger single crystalline Ge on features under 1.2µm width. This effect is partially controlled by dimensions since the nature of the dopant plays as important of an effect. As the dimensions increase above ~1 µm, the surfactant effect , and formation of several nucleation points appear, creating a polycrystalline material. We conceived that the addition of B, relaxes the Ge matrix, permitting any dimension to be growth due to the combine effect of both dopants. We show evidence that a growth combining both dopants relaxes dimension constrains, providing a wider dimensional range of epitaxial growth. Further investigation on lower temperatures and more equivalent rates with less diluted solutions are required. Notice that both P and B were diluted with He to 10% and 1% respectively. Even though He does not interrupt the reaction, the possible maximum concentration is constrained, as well as the effects achieved for the bufferless growth.

In this chapter, we covered:

- Advantages of a heavily doped n-type Ge for dislocation reduction
- Advantages of confined growth, and its implications to strain and threading dislocations
- Defined the maximum possible height in a constrained 1-D structure
- Pressure independence to facet growth, and linear dependence to rate of total growth thickness
- Feasibility of non-buffer growth through used of confinement and heavy doping n-type

The following chapter deals with doping in Ge and the approaches taken in order to increase the n-type dopant content.

Chapter 4. n-type Doping

Ge heavy doping processes have been explored with limited success. The maximum doping concentration achieved through UHV-CVD is limited to ~$1x10^{19}cm^{-3}$ [27], since it is reaction and diffusion limited as seen in Figure 56. This maximum dopant concentration represents the starting dopants for all the diffusion methods analyzed.

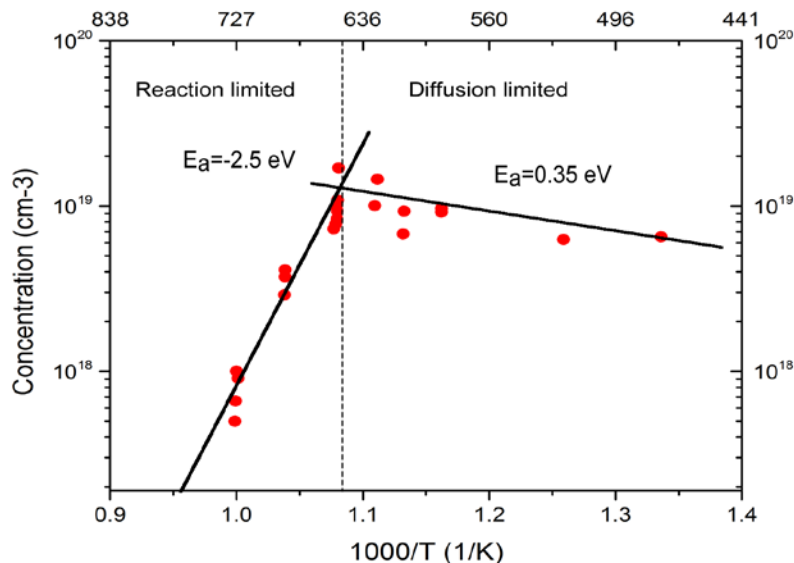

Figure 56.- Comparison of total active concentration of growth at different temperatures. Limits to the maximum active concentration are set at $1x10^{19}cm^{-3}$. [88]

The active carrier concentration needed for carrier inversion in Ge is >$1x10^{19}cm^{-3}$ [56], and the evidence presented in this chapter suggests that achieving higher level doping is feasible.

In this chapter, we present the challenges around doping Ge on Si. A brief explanation of the theory and challenges will follow. Then, an approach to solve the dopant issue is shown through a source of concentrated dopants. This approach follows three different schemes: Spin-

on-dopant (SOD), overlay implantation and delta doping. Each of these approaches is Si CMOS compatible and is applicable to Si-based electronic-photonic integrated circuits.

4.1 Doping Germanium

Doping in Germanium, especially n-type doping, is challenging in Germanium for a variety of reasons.

- N-type dopants pose a high diffusivity difference within the chemical solubility limit. The slowest diffuser with higher solubility is Phosphorus, estimated approximately at $2x10^{20}cm^{-3}$ at 600°C and the electrical activation, reported at $6x10^{19}cm^{-3}$ at 600°C or $7x10^{19}cm^{-3}$ at 800°C.
- Growth of n-type Ge through *in situ* process is limited, unless using physical deposition techniques. Physical techniques, such as molecular beam epitaxy (MBE), implantation and others, portray limitations on scalability and reliability of the devices. Through chemical techniques, as CVD, there is an inherent limitation as mentioned previously, to $1x10^{19}cm^{-3}$.
- Diffusion through the boundaries occurs through all the different dopants. The severe dopant loss during annealing has been reported even with P [108] . Diffusion through the body of Ge is usually anchored by charged defects and kinks, permitting a one-path outdiffusion to the boundaries.
- Long anneals can induce Si-Ge interdiffusion, as low as 700℃, as was demonstrated by Xia [109]. Time constrain on diffusion suggests that a fast diffuser and short anneal times are the best way to increase the doping concentration without Si-Ge compound formation.

P has been chosen as the dopant most studied in this research due to the high solid solubility in Ge, $>1x10^{20}cm^{-3}$. Moreover, the diffusion constants of Ge are well-known, as those for P on

other materials such as Si and oxide, which are typical boundaries. Moreover, P is the slowest n-type diffuser in Ge, diminishing outdiffusion during annealing cycles.

The active doping for P is ~mid $10^{19}cm^{-3}$, however, as can be seen in Figure 57, the value is below the solid solubility of the material. Other n-type dopants, such as As and Sb could be used for such high doping. The limit is due to kinetic effects that come into play during the chemical reactions in the epitaxial growth of Ge or during recrystallization.

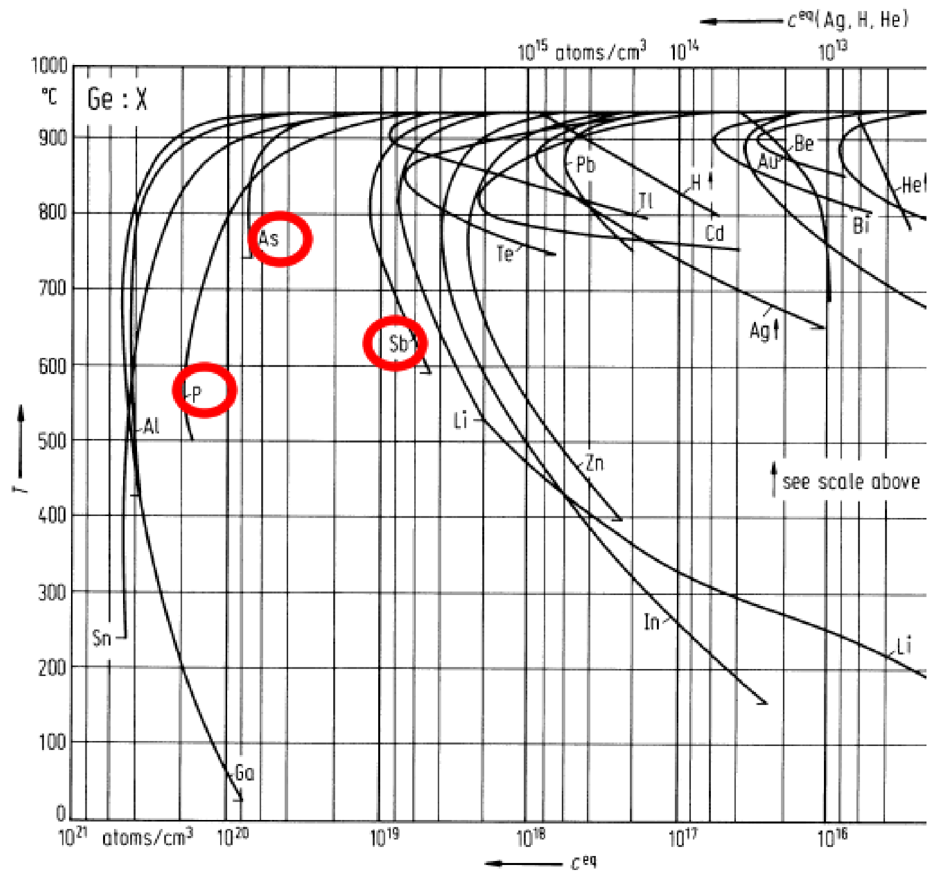

Figure 57.- Solid Solubility of P, As and Sb in Ge[110, 111]. These lines represent single measurements taken. Solid solubility might differ from author to author.[112]

The solubility of an impurity in a solid phase is the maximum concentration of such impurity with another phase. Such behavior is usually explained in the liquid phase; however, the thermodynamic equilibrium between the crystal and the melt is defined by the segregation

coefficient[113]. This coefficient is dependent on temperature, and has an intrinsic relationship to the radius of the impurity added. As can be seen in Table 5, the trend of radius and solubility follows. As the impurities increase in size, the segregation coefficient decreases. The solubility of most elements in Ge exhibits a retrograde behavior[113], which is related also to the segregation. The elements with smaller segregation coefficient reach the maximum solubility near the melting point of Ge, hence, P has the smallest retrograde effect for n-type dopants, and lowest temperature maximum solubility.

The temperature for these effects varies due to a variety of reasons from charged mobility of defects to redistribution through crystalline structure. The faster element to analyze is the sheet resistance of the semiconductor. It can be calculated as,

$$R_s = \frac{\rho}{t} = \frac{1}{\int_0^t \mu(T,N) q N(x) dx}$$

where ρ is the average resistivity of the material, t is the thickness of the analyzed layer, μ(T,N) is the mobility of the majority carrier as a function of temperature and concentration, *q* is the carrier charge, and *N(x)* is the concentration as a function of depth in the material. In heavily doped materials, the mobility and the concentration dominates the function, minimizing the effect of thickness. R_s is easily measured through Hall effect measurements, a common technique used for calculating total active dopant concentration throughout the entirety of the semiconductor volume. It is seen that of all n-type dopants, P would have the lowest R_s in Ge, making it a good candidate for electrical devices as we intended.

Table 5.- Doping maximum equilibrium for n-type and p-type doping in Ge, and diffusion.

Doping element	Maximum equilibrium solid solubility (at./cm^3)	Temperature for max solubility (°C)	Expected Sheet resistance, R_s (Ohm/sq)	Diffusion coefficient constant, D_0 (cm^{2}s^{-1})	Activated Energy, E_a (eV)
B	5.5 x 10^{18}	~940	315	-	-
Ga	4.9 x 10^{20}	724	34	-	-
P	2.0 x 10^{20}	~600	42	9.1	2.85
As	8.1 x 10^{19}	~800	79	32	2.71
Sb	1.2 x 10^{19}	815	163	16.7	2.55

As and Sb have not been used in our *in situ* experiments due to in-situ doping constrains and maximum solid solubility. Another limitation is that both have higher diffusivity than P and have a tendency to out diffuse from Ge body [113]. The control of dopant diffusion permits the use of new techniques to increase the dopant concentration in Ge.

Higher doping concentrations for *in-situ* doped Ge films are possible when using non-equilibrium growth methods like MBE. For MBE growth a n-type doping concentration of $1x10^{20}cm^{-3}$ has been demonstrated [49]. However, it is very challenging to integrate MBE grown Ge films into a CMOS process flow due to high capital cost and low throughput. Ion implantation, another commonly used method to introduce dopants into Ge, causes significant lattice damage such that, after the implantation, samples have to be annealed at temperatures above 600°C. The lattice damage increases vacancies and other defect concentrations that act as recombination centers and cause increased optical absorption as well as donor compensation, decreasing the active dopant concentration. High diffusivity of the dopants prohibits anneals at higher temperatures to remove the implantation related defects. In order to slow down the dopant loss, diffusion barriers of silicon oxide or silicon nitride have been used [114, 115].

Active carrier concentration is not equivalent to dopant concentration, therefore, is not equivalent to the solid solubility. Several groups have shown results with high-doping, even

higher than $1.2x10^{19}$ cm^{-3} [116-118], but active doping remains at $1x10^{19}cm^{-3}$. The difficulty comes from keeping the lattice undamaged to provide the lowest scattering effects, which translates in inefficient optical material; and minimizing dopant compensation by vacancies and defects. These diverse groups are encountering that optical PL is highly reduced even if the dopant concentration is high. [119]

Reduction of defects is accompanied by annealing, which enables diffusion of the dopants. The self-diffusion in Ge is mainly monovacancy mechanism, where the vacancy acts as an acceptor[113]. No evidence on a contribution of self-interstitials in self-diffusion has been found on n-type dopants in Ge. The diffusion of foreign atoms like B and Si in Ge is lower than Ge self-diffusion. This would provide less diffusivity of the Ge into the Si interface, but enhanced the diffusion of other dopants. The trend can be seen in diffusion constant calculation,

$$D_{Ge} = D_{Ge}^{0} + D_{Ge}^{-}(n_i/n) + D_{Ge}^{=}(n_i/n)^2.$$

As the dopant concentration increases, the diffusion keeps increasing. It is important to remark that for a tensile strained Ge, the diffusion coefficient decreases for Si. P and As are heavily affected by strain, due to the interstalcy mechanism, while Sb shows small dependence because it is a vacancy dominated diffuser [120]. The effect can be explained through sizes of the dopants. P and As atoms are relatively smaller or about the same size as Ge, vacancy or interstalcy mechanism is most likely to occur. However, the major effect at high doping concentrations is the double charged diffusivity as proved by Brotzmann, et al [115], and experimentally proven that the effect will be majorly lead by vacancy diffusion. This formalism is based on the direct consideration of the physical phenomena involved in the equilibrium formation of point defects: for a vacancy to form, an atom is taken out from the crystal to the surface. This atom increases the total volume of the crystal by an atomic volume Ω equal to 20 Å for Si. Neighboring atoms

around the created vacant site relax and decrease the total volume by V_r. The exact opposite phenomenon is supposed for the formation of an interstitial where an atom of the surface is introduced in the crystal. The effect of the stress on the equilibrium concentrations of point defects is determined by the work against the external stress field [115]. Sb slow diffusion can be understood from the large size of the dopant allowing diffusion only through vacancies. Strain in the lattice will not improve as much as the inherent strain provided by the dopant.

Results relevant to the dopant diffusion and concentration of Ge are dated back to 50 years ago, mainly due to sheet resistance measurements. P experiments show discrepancies in diffusion constants and maximum concentration of active dopant [115]. The confusing results on dopant diffusion in Ge show the need to understand their diffusion behavior more accurately, in particular P. A picture of the spectrum of diffusion constants is seen in Figure 58. As can be seen, there is not a single consensus of the diffusivity of P on Ge, changing orders of magnitude from study to study. However, Cai, etal [121],showed that there is a discrepancy between extrinsic and intrinsic diffusivity. This discrepancy is due to dopant enhanced diffusion caused by the double negative vacancy mechanism.

The high concentration of dopants and its common use in diffusion calculations made it the most suitable [115, 122]. The extrinsic diffusivity $D_{(DV)}^{-}$, defined as the dopants diffusion, is quadratic carrier concentration dependent and can be expressed as follows:

$$D_n = D_{(DV)^-} = D_0(\frac{n}{n_i})^2,$$

where D_0 is the intrinsic diffusivity, n is the equilibrium carrier concentration in the Ge, and n_i is the intrinsic carrier concentration in tensile strained Ge at the diffusion temperature. The reduction in n_i has been discussed in previous sections. In our case n is the carrier concentration

for P concentration in the Ge matrix. This trend shows that under heavier doping the diffusivity increases, as has been observed in Figure 58.

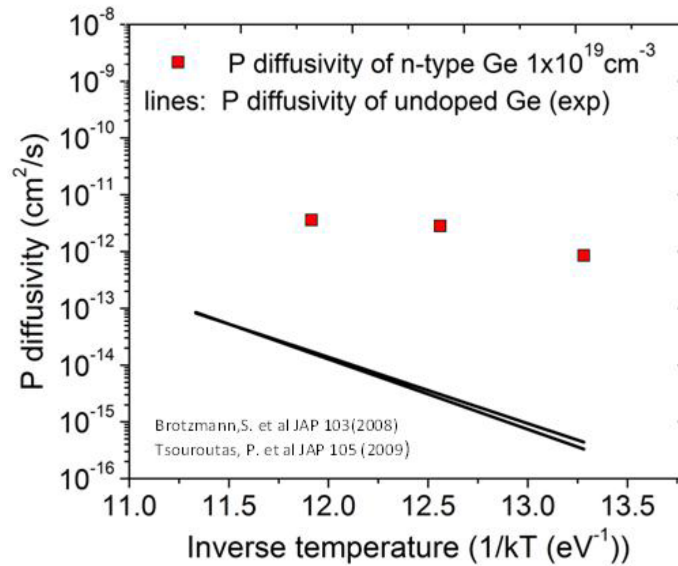

Figure 58.- Doubly charged diffusivities from extrapolated diffusivities [115, 123-125] for temperatures ranging between 600 to 750 °C. The diffusivity for heavy doped materials is up to two orders of magnitude higher than undoped and implanted samples. [125]

The difference in the diffusion behavior of foreign atoms in Si and Ge is consistent with the general accepted view that both vacancies and self-interstitials mediate atomic mass transport in Si, whereas vacancies are the main important diffusion vehicles in Ge. The slightly lower diffusivity and slightly higher diffusion activation enthalpy of Si in Ge compared to Ge self-diffusion, indicate a repulsive interaction between Si and vacancies [115]. Notice that the diffusion of all n-type dopants P, As and Sb, exceeds Ge self-diffusion[126]. In a previous investigation it has been theorized that this might induce an attractive interaction between the dopants and the vacancies leading to the formation of dopant-vacancy pairs [115].

The problem with heavy doping resides in the assumptions made usually for low doping levels. Such assumptions, as the host crystal is not seriously perturbed and the band edges states are still described by simple parabolic bands [127], no longer applies. There has been evidence of BGN in Ge is dopant dependent, due to the different nature of the heavy doping and lattice strain caused by them. Dopants P and Sb have been studied. P has not shown any band shrinking or BGN [30, 39], though recently clear BGN has been seen in Ge doped heavily with Sb [128]. BGN and its relation to doping is further explored in Chapter 5.

4.2 Dopant Solid Sources

The doping diffusivity in Ge is strong enough and larger than its own self diffusivity. Dopant diffusion is large enough than it becomes a limiting factor, as seen in chapter 3. However with the use of diffusion barriers, such as SiO_2 or SiN_x, the out-diffusion of the dopants can be retarded. This section will cover the different approaches followed through the use of a dopant source using the mechanism of enhanced diffusion, as seen in Figure 59. First, we will show Spin-on-Dopant (SOD) increasing the active doping concentration up to ~$1x10^{20}cm^{-3}$, but not consistently. We then follow through implantation techniques of different sources to act as dopant sources. Si dopant sources and self-dopant sources were experimented and showed increases up to $4x10^{19}cm^{-3}$, with addition of increment of point defects. Further sections will show the work done in delta doping in Ge and P. Each of the techniques presented are suitable for Ge light emitter.

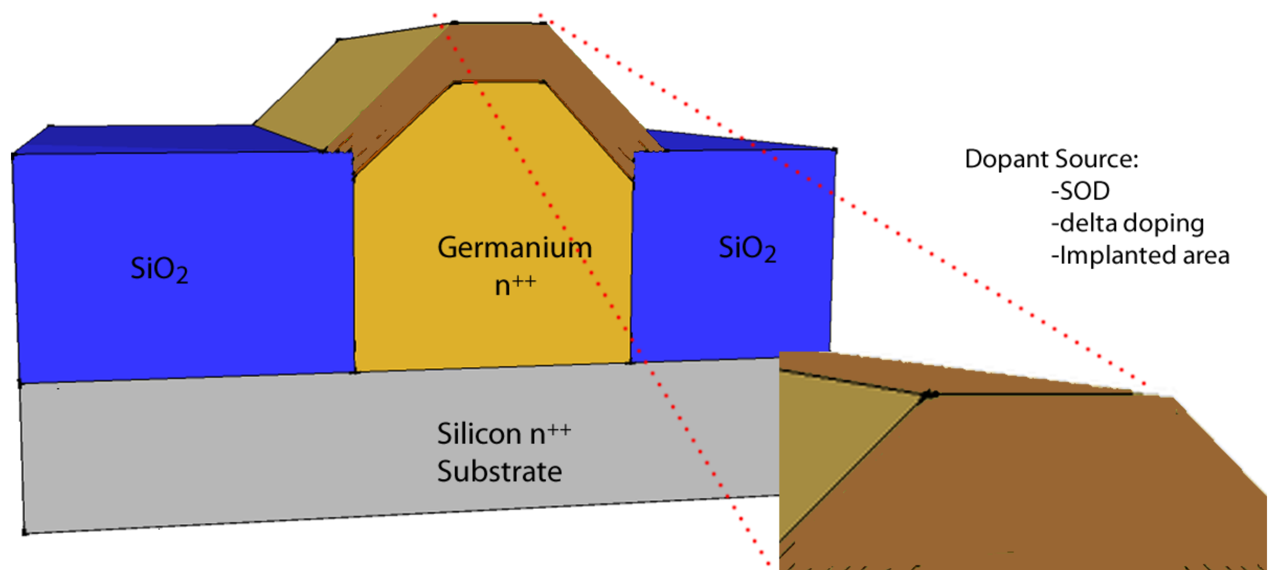

Figure 59.- Depiction of the strategy for doping Ge through dopant sources.

4.2.1 Spin-on-Dopant

Spin-on Glass doped with P or Spin-on-Dopant (SOD) is a mixture of SiO_2 and dopants (either boron or phosphorous) that is suspended in a solvent solution. Phosphorus content of these solutions is over $10^{22}cm^{-3}$. The high concentration of potential dopants makes this solution a good candidate for dopant diffusion source.

SOD is applied to a clean silicon wafer by spin-coating just like photoresist. The SOD is the dopant source. To get the dopant out of the SOD and into the silicon wafer requires two steps. The first is a "pre-dep" in which the dopant leaves the SOD and saturates the silicon surface. After, the SOD is removed in an HF dip. Finally a "drive-in" step is performed in order to diffuse the dopant into the silicon. This process is mostly used in thin Si films. Due to the higher dopant diffusion in Ge, the SOD was expected to contribute to higher doping.

Silicon wafers were used as substrate material for grown of intrinsic highly dopant Ge. The sample is heated to 100°C for 30min in a chamber to remove the water vapor. Then, 5ml of

SOD Phosphorus PDC1-2000 are spin-on the substrate. The sample is baked for 3min at 200℃ in a hotplate. Ashing the organic components through oxygen plasma, leaves the sample pristine with only P and SiO_2. The thickness of the SOD is 1um to 2um after this step. A nitride cap or SiO_2 cap were used as a diffusion layer. Different combinations of tension of these upper films result in a protection for out-diffusion of the dopants. Driving annealing from 550-850℃ from 30sec to 5 min results in an effective increase in dopant concentration. Removal of the diffusion layer is done with a solution of 1:5 HF: H_2O. Reaching temperatures above 800℃ increased the possibility of Si/Ge interdiffusion[109]. The results were characterized through SIMS, PL and Hall effect measurements.

As seen in Figure 60, non-uniformities after application of the SOD on large surfaces can occur. Depending on the area, the samples emit at different intensities and wavelengths suggesting random increases in active dopant concentration and increase in point defects. In small areas, such as waveguides, these anomalies are not observed.

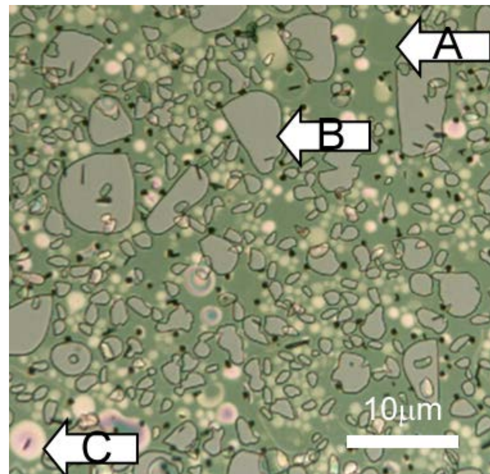

Figure 60.- Microscopy of SOD sample after annealing and removal of diffusion barrier. (A-C) represent different points where PL was performed. (C) shows the highest PL photoluminescence. SOD is not uniform as observed.

SOD presents an unusual matrix that is defined by post-processing and diffusion barriers. In Figure 61, it is seen the distribution of dopant behavior acts in a random pattern caused, most likely by the matrix of the system and the control in the dopant layers. SOD dopants do not form SiGe compounds. The random nature of the glass matrix makes the results random, having 1/10 chance of getting the desire result. This matter leads to small yields of the desired dopant concentration. Nevertheless, starting with a heavily doped Ge substrate leads to higher probability of obtaining heavy doped concentrations due to the increase in dopant diffusion, discussed in previous sections.

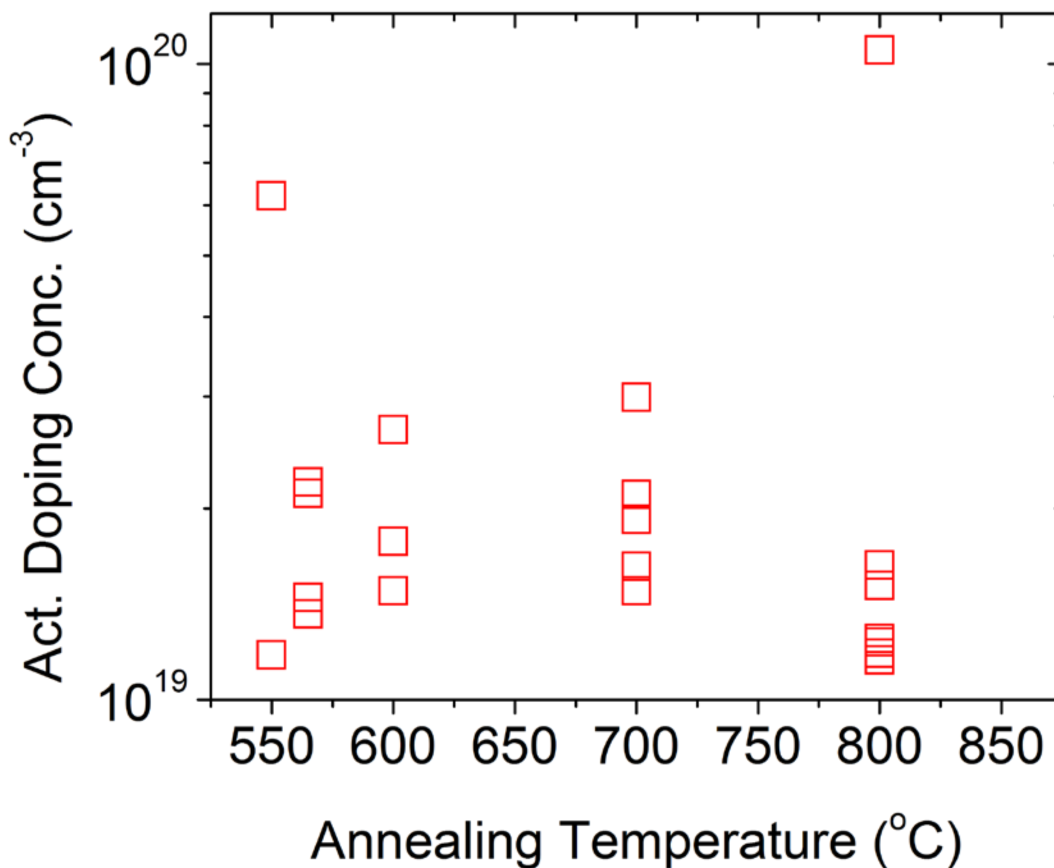

Figure 61.- Hall effect active dopant concentration measurements from SOD Ge samples under different annealing temperature (Celsius). Random active doping of SOD matrix is observed.

Despite the randomness of the procedure, SOD provides results agreeing with concentration in the system and PL emission. In Figure 62, the increasing PL matches with the increasing annealing temperature. This increase in PL emission suggests an increase of dopant while keeping point defects constant.

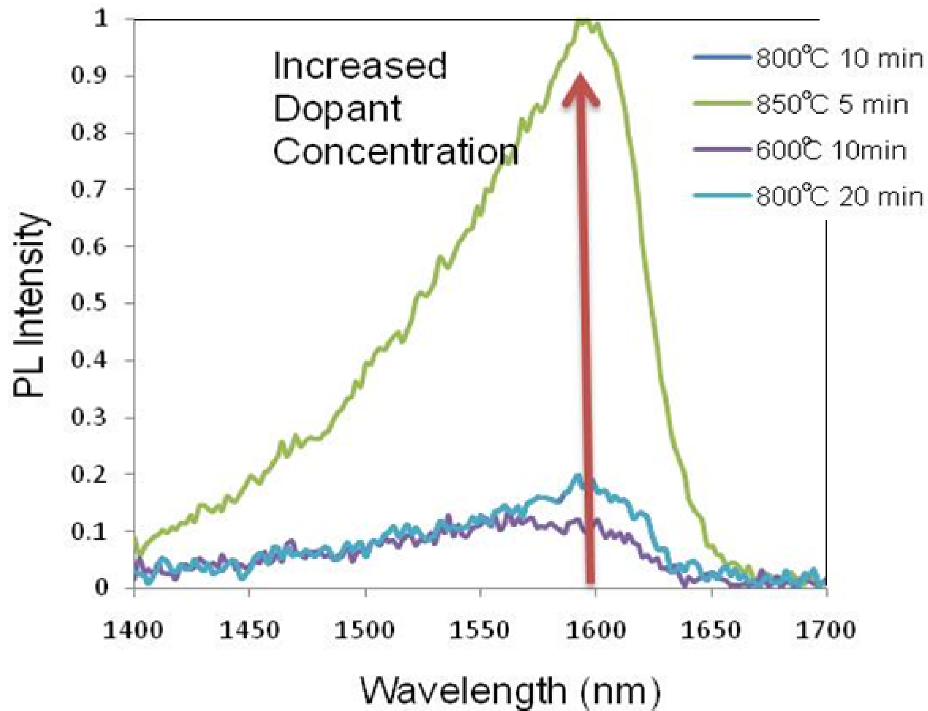

Figure 62.-PL of different annealing times and temperatures for same SOD. PL intensity has been normalized to max emission. Under similar conditions emission peak slightly shifts to 1600nm, caused only by dopant.

Peak emission in PL remains around 1600nm, which shows an increase in doping from BGN as explained in previous sections. High temperatures between 700-800˚C enter the regime of Ge/Si interdiffusion, which was confirmed in later measurements with SIMS analysis, as seen in Figure 63.

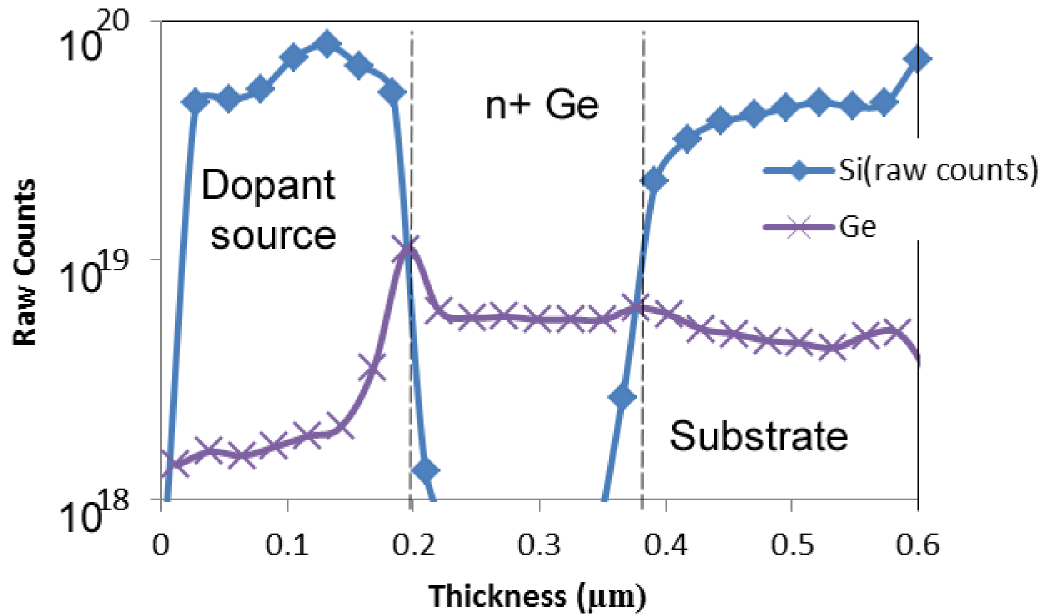

Figure 63.- Ge/Si interdiffusion on the substrate after 800˚C 20min . The substrate/Ge contact shows a heavy increase in Ge concentration that extends 200nm into the substrate.

SOD represents a powerful dopant source, but due to the SiO2 matrix, they don't diffuse well with materials that have not been previously doped. In Figure 64, it is observed that the concentration of P still remains mostly in the SOD/Ge interface. The concentration near the interfaces is ~$10^{20}cm^{-3}$ but it drops rapidly through the substrate due to the slow diffusion. A secondary source of dopant loses becomes the un-doped substrate. Dopants accumulate between the Ge buffer and the substrate, creating a well of inactive dopants, as explained in previous sections.

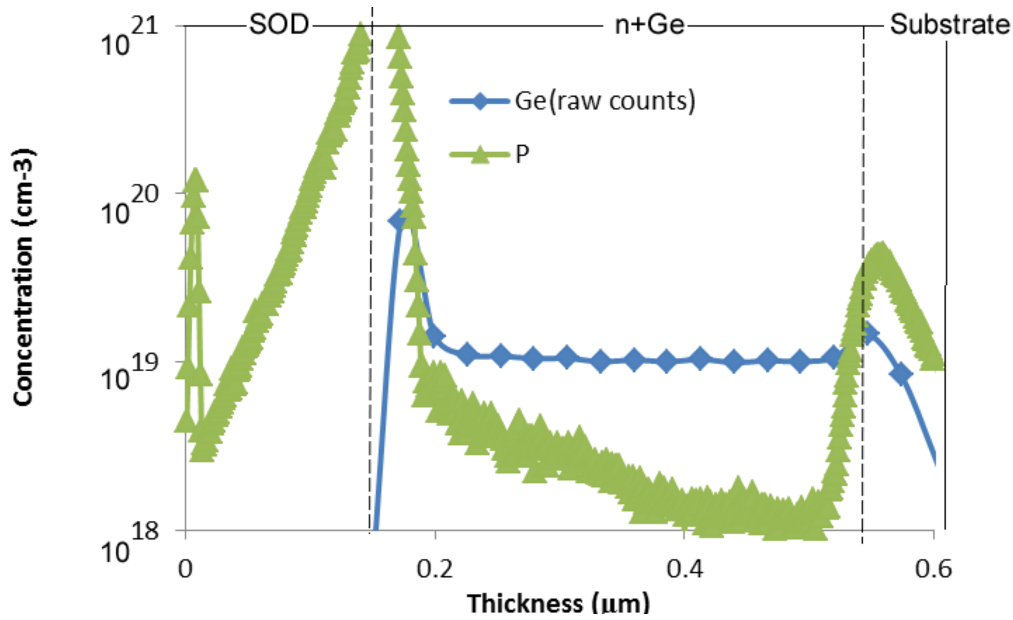

Figure 64.- SIMS of interface accumulation of P dopants in the interfaces. Not uniform doping throughout the Ge body is caused by the slower diffusion due to the dopant concentration. Accumulation of the dopants in the substrate represents a secondary source of dopant loss.

A substrate with highly doped Ge (~$1x10^{19}cm^{-3}$), followed by SOD deposition showed a significant increase in the average concentration of the dopant. The SOD concentration matches to the Hall effect measurements performed.

SOD results show that we are capable of depositing high levels of dopants into the Ge material without adding extra defects in the upper layers. The type of barriers and treatments of the SODs have to be tuned to optimization in order to avoid barrier sinks where the dopants will flow in the opposite direction, instead that into the Ge.

Carbon contamination due to the organic compounds in the SOD is a major barrier for implementation on CMOS machinery. Excess carbon can short circuit the system and contaminate other devices in the chip making it non appropriate for electrical injection.

Despite the nature of this compound, a consistent result was achieved getting a PL equivalent to that of *in situ* dopants. The quality of the Ge was not compromised and the level of dopants was increased, as seen in Figure 65. Implanted samples showed similar BGN but decrease in emission which can be attributed for the increase in point defects.

The SOD diffusion source was successfully used in optically pumped Ge laser as will be described in later chapters.

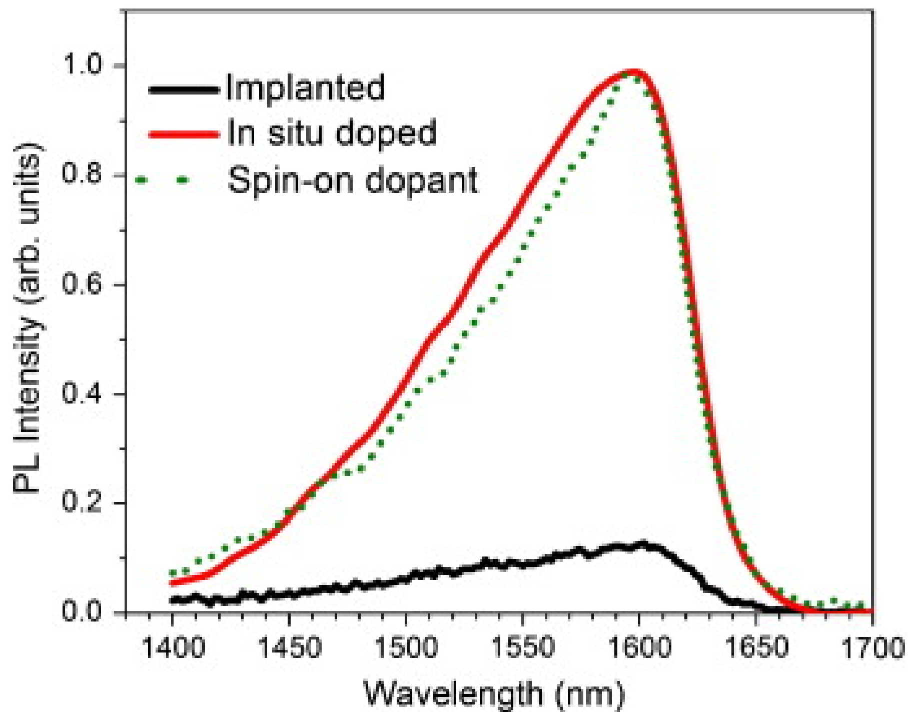

Figure 65.- Comparison of room temperature PL spectra of n+Ge doped with $1x10^{19}cm^{-3}$ P, fabricated by in-situ doping, diffusion doping from spin-on dopants, and ion implantation. (Courtesy from J.Liu)

It was demonstrated that SOD as a dopant source can increase the dopant concentration to the dopant level required for lasing devices. The low level of defects introduced makes it a suitable technique for doping Ge. The maximum dopant diffuse is limited by the homogeneity of the source and the diffusion time. SOD is appropriate for final stage doping. Due to the

contamination of carbon of this technique, it is only appropriate for optically pumped devices. For more details in the SOD process, please refer to Appendix.

4.2.2 Implantation

Implantation is a well-known technique to increase doping concentration in Si. It is often misunderstood that the theorized maximum concentration is the maximum active concentration[129], assuming that every dopant in the system would act as an active donor. Unfortunately, the information regarding the activation is mostly for surface concentration, since there is an interest for shallow trench Ge transistors, due to the high carrier mobility [123, 130, 131] .

In Ge optical devices, any defect is a source of optical losses, reducing the overall efficiency in light emission. The gradient of dopants in the bulk differs in the electrical design since an optical device requires uniform doping and a shallow transistor, as its name marks it, works under shallow highly doped trenches. Despite the differences, both devices shared common threads as in the dopant diffusion and the defect formation.

Germanium n-type dopants usually used are P, As and Sb. The maximum concentrations of these dopants are limited by their solid solubility, P at $2x10^{20}cm^{-3}$ [110, 132], As at $8x10^{19}cm^{-3}$ [133]and Sb at $1x10^{19}cm^{-3}$ [134]. High doping concentrations above $5x10^{19}cm^{-3}$, and diffusion studies exist for ion implantation [108, 135, 136]. The trend in diffusion speeds is $D_P<D_{As}<D_{Sb}$ [113], making P the most attractive dopant due to slow diffusion and high solid solubility. However, it has been theorized that the maximum level of *in situ* or implanted active doping is ~$2x10^{19}cm^{-3}$[115].

Ion implantation is used for doping insertion in most studies, but severe dopant loss observed during annealing [115, 123, 130] has lead toward alternatives. Coimplantation is a

promising technique that has managed to achieve high concentrations with P+As [108] and P+Sb [137]. Due to slow diffusion into the bulk and high out-diffusion, the active carriers remain in the first 100nm, but the concentrations of active carriers reach $1x10^{20}cm^{-3}$. This total concentration does not take into account defect formation. Dopant activation depends in both level of doping concentration and level of defects; the higher the latter, the smaller the first. Defects are also created through implantation, creating interstitial point defects [138] that can damage the Ge structure by adding extra optical losses or becoming dopant diffusion retardants. The latter would be desired but it has shown to be ineffective[139] , although at high doping levels enhanced diffusion can be considered.

Semiconductor materials at high concentrations have enhanced dopant diffusion.[140] Nevertheless, this is the first time that high concentrations in Ge are studied for increased doping. Previous studies focus with bulk Ge doped to high levels and observed the dopant diffusion trend. The implanted area, due to a high level of defects, has retarded diffusion, while the bulk Ge is non-doped avoiding any evidence of enhanced dopant diffusion. For a proper demonstration it is necessary to start with a highly doped Germanium with small defect concentration and a highly doped implanted area.

For our studies, standard n+Ge growth was performed, described in previous sections[2]. The samples were divided into 2 categories, Si-source and self-source.

The first, Si-source is a dopant source made of Si. LPCVD a-Si was deposited at temperatures around 560-600C. These temperatures are high enough to cause outdiffusion of the initial dopant concentration in the Ge. A thickness of 100nm was chosen, and the samples were implanted with As and P.

The second, self-source depends on implanted Ge. The samples were implanted with different doses, as can be seen in the Table 6. The aim is to achieve average (P+As+Sb) concentration of $1 \times 10^{20}\mathrm{cm}^{-3}$ over 700nm range of Ge; to get (P+As+Sb) concentration $> 1 \times 10^{19}\mathrm{cm}^{-3}$ around 200nm deep Ge from the top.

Table 6.- Implantation conditions for different single target and multiple target dopant implantation.

#	Tilt angle (°)	ions	Energy(keV)	Dose(cm^{-2})	ions	Energy(keV)	Dose(cm^{-2})
1	7	P	100	7.3×10^{15}	-	-	-
2	7	P	100	3.5×10^{15}	As	250	3.8×10^{15}
3	7	P	100	3.5×10^{15}	Sb	375	4.1×10^{15}

Assuming $\mathrm{N(x)} = \mathrm{peak\,x\,dose\,x\,exp}[-\frac{1}{2}(\frac{\mathrm{x}-\mathrm{R_P}}{\Delta\mathrm{R_P}})^2]$, and that the average carrier concentration in 700nm thick Ge is: $\mathrm{n} = \frac{\int_0^{700}\mathrm{N(x)dx}}{700}$, leading to a total average dopant concentration of $1.04 \times 10^{20}\ \mathrm{cm}^{-3}$ and the 200nm-deep concentration is 5.5-5.8x$10^{19}\mathrm{cm}^{-3}$. The implantations are designed such that the upper part of the structure is sacrificial, and the highly crystalline Ge remains intact (Figure 66).

After implantation, samples were annealed to drive diffusion from the damage area into the single crystal Ge. Temperature ranged 650-800℃ and between 30-180 seconds. After analysis, chemical mechanical polishing is used to remove the damage implanted zone. Removal is important to decrease the point defects added through implantation, the poly-Ge formed and to reduce lose mechanisms of the optical devices.

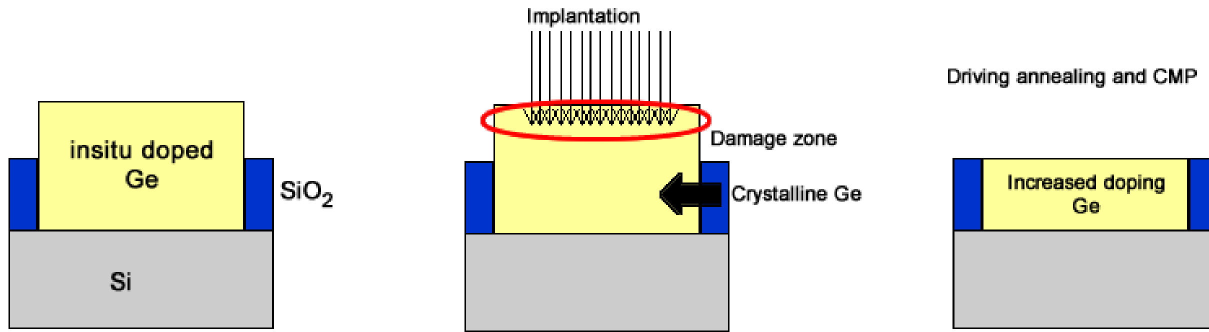

Figure 66.- Concept to prevent damaged germanium in the final structure.

Samples were further analyzed through secondary ion mass spectroscopy (SIMS), Hall effect and photoluminescence (PL).

Doped Si with P source on Ge was growth, following a similar approach to SOD. At high temperatures, the diffusivity of P is matched with that of the Si, as seen in Figure 67. The presence of grain boundaries also leads to increase diffusion from upper polySi. As we increased the temperature or time, the interdiffusion effect increases.

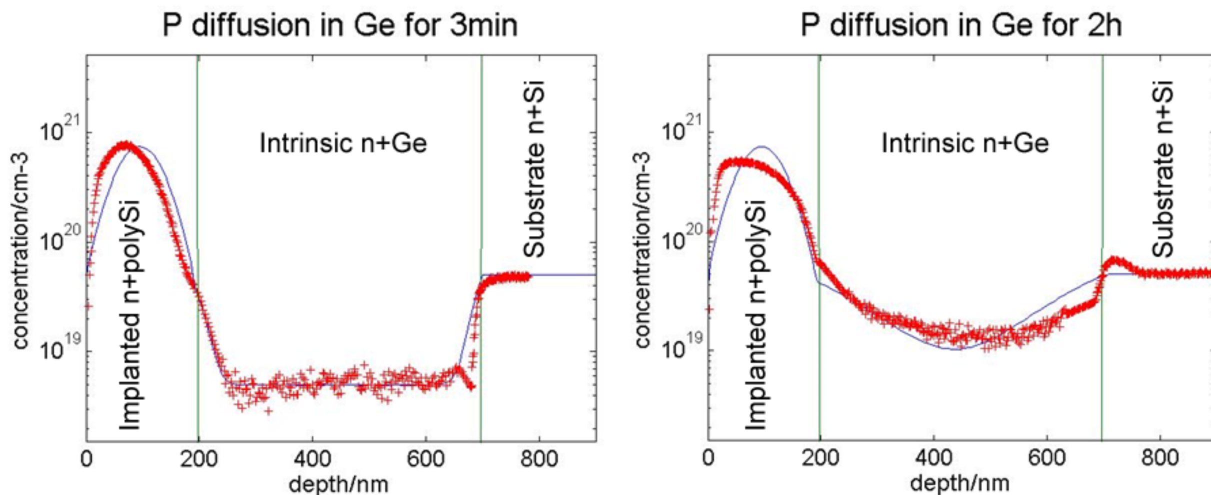

Figure 67.- Si implanted wafers. RTA for 3 min and slow annealing for 2 hrs are shown. Theoretical simulation matches the diffusion profiles.

Ge solid sources showed better results, since there is no Si interdiffusion, the fast diffusion in Ge prevented long anneals; the use of the same material, avoiding extraneous defects; and easily removed, since CMP is known for the Ge. PL results showed the increase on active dopants.

Photoluminescence has the property to analyze no-invasively the dopant concentration. By correlating band gap narrowing (BGN) to active doping, a relation is form [41] .This effect can be used to tabulate the total active carrier concentration since optically active dopants are equivalent to electrically active. More details of the calculation and theory behind BGN can be found in Chapter 5. A simple relation between peak emission and doping shows that,

$$\lambda = 2.2 \times 10^{-18} n + 1600$$

for high doping concentrations, where n is the doping concentration. Since the maximum doping level was being analyzed, closed focus was given to PL measurements.

The implanted samples showed a significant shift in photoluminescence emission (PL), shifting above 1650nm that is equivalent to the values above $3\text{x}10^{19}\text{cm}^{-3}$ n-type dopant. As seen in Figure 68, all the different dopants caused BGN. Nonetheless, since the samples were implanted, the implanted zone is considered damaged, and hence, not appropriate for optical devices due to high defect concentration.

The samples were compared to a standard sample which is doped to $1\text{x}10^{19}\text{cm}^{-3}$ [P]. (Figure 68). Change in PL intensity leads to believe that different annealing temperatures would radically change the BGN.

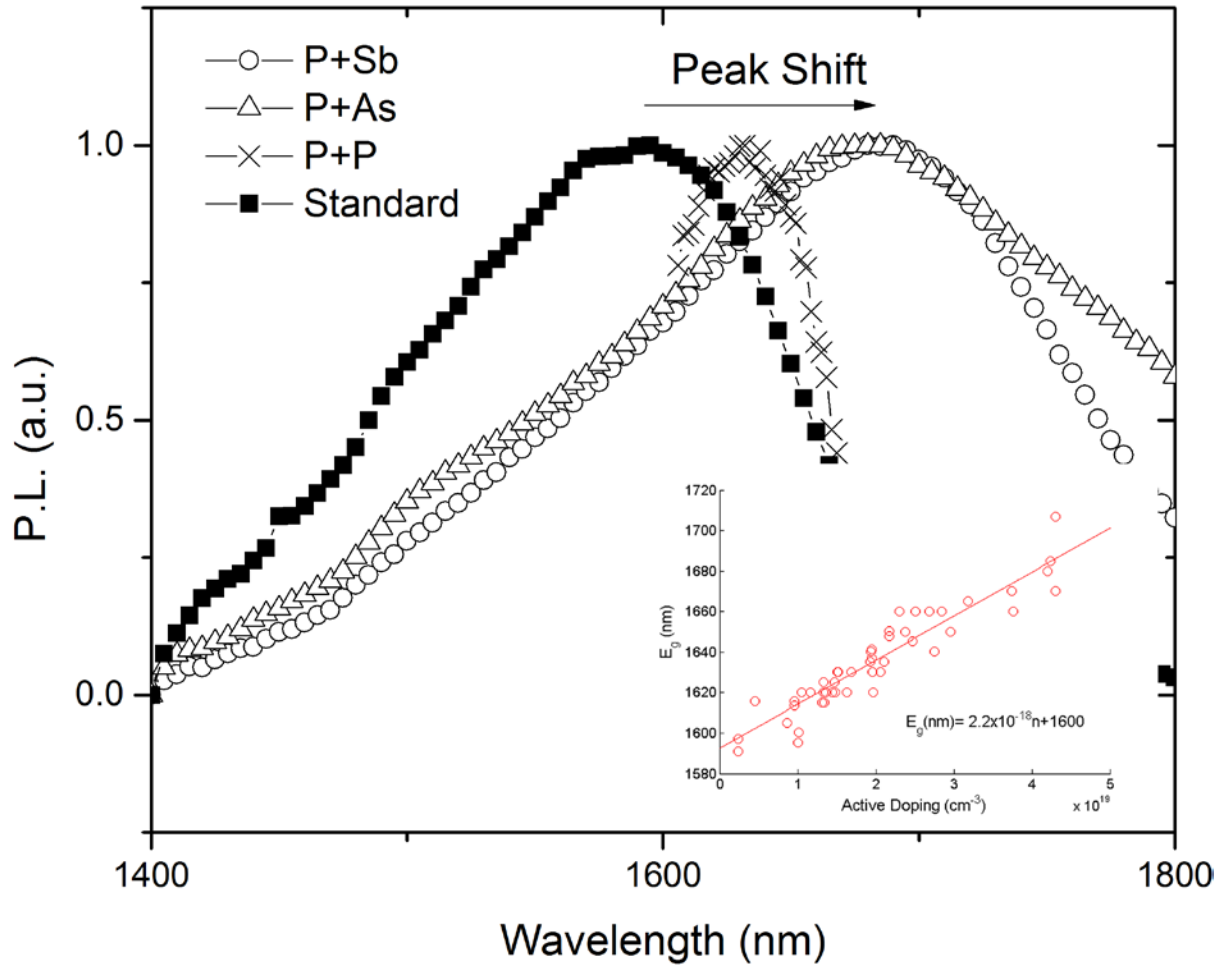

Figure 68.- 750°C 30sec anneal without CMP. Band gap shift in implanted samples is larger than *in situ* material. The active dopant concentrations reach <5.5x10^{19}cm^{-3}. BGN relation is shown as the parameter to relate active doping to peak shift.

The transition in BGN changes according to annealing temperature is meaningless when observing at different annealing temperatures at the range of 650 to 800°C. The range of temperatures was selected based on the diffusion of the dopants on Ge, and necessary energy required to activate dopants on a-Si. Diffusivities of the different dopants at 750°C, correspond to $D_P = 8.29x10^{-14}cm^2/s$, $D_{As} = 1.4269x10^{-12}cm^2/s$ and $D_{Sb} = 4.5731x10^{-12}cm^2/s$. As seen, P diffusivity is 3 orders of magnitude faster, and similar behavior was expected from the other dopants.

As can be seen in Figure 69 and Figure 70, BGN from As and P codoped samples matches with expected increased in integral PL and FHWM. Even though BGN did not change appreciably, PL intensity did. The concentrations in P and P+As are between 2 - $4x10^{19}cm^{-3}$. Although there is some outdiffusion, the nonimplanted Ge has higher diffusion rates than the upper implanted area. The high concentration of defects on the implanted surface acts as a diffusion retarder.

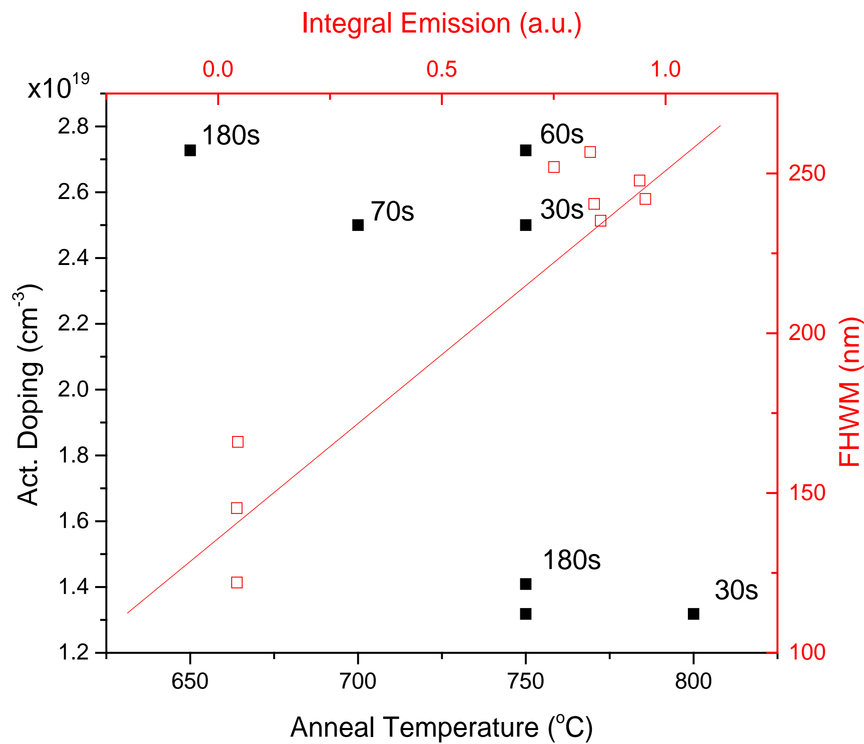

Figure 69.-Ge implantated P PL after different annealing temperatures (°C). Max peak shift observed at 1660nm~$2.7x10^{19}cm^{-3}$ active doping under 60 sec anneal.

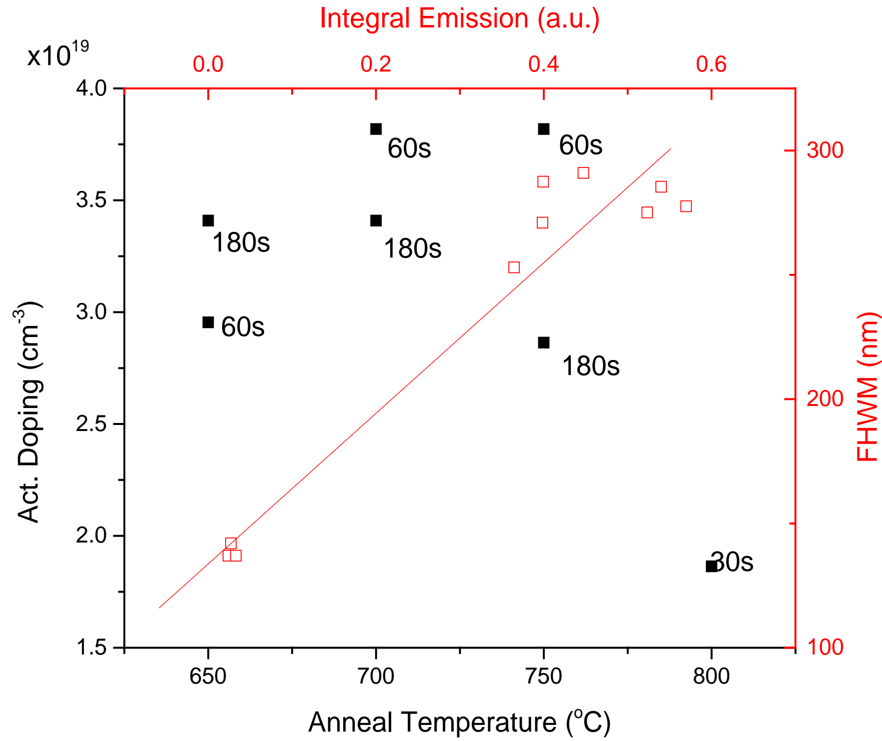

Figure 70.- P and As PL after different annealing temperatures and times. Peak at 1685 nm ~ $3.75X10^{19}cm^{-3}$ active doping under 60 sec anneal.

FHWM changes with integral PL as expected, and the higher doping concentrations show the largest shift on FHWM, which goes in accordance with spectral width.

In the case of P+Sb samples, it is seen that the differences in total peak emission changed $\Delta\lambda\approx20nm$, as seen in Figure 71. This 20nm in the range of 1700 are equivalent to over $\Delta n>5x10^{19}cm^{-3}$, which is significant for Ge emitting devices. In all cases, the dopant concentration was increased above the *in situ* doping concentration ~ $1x10^{19}cm^{-3}$. The defect concentration was also reduced by increasing the temperature during anneals, but higher temperatures represent, additionally, larger outdiffusion.

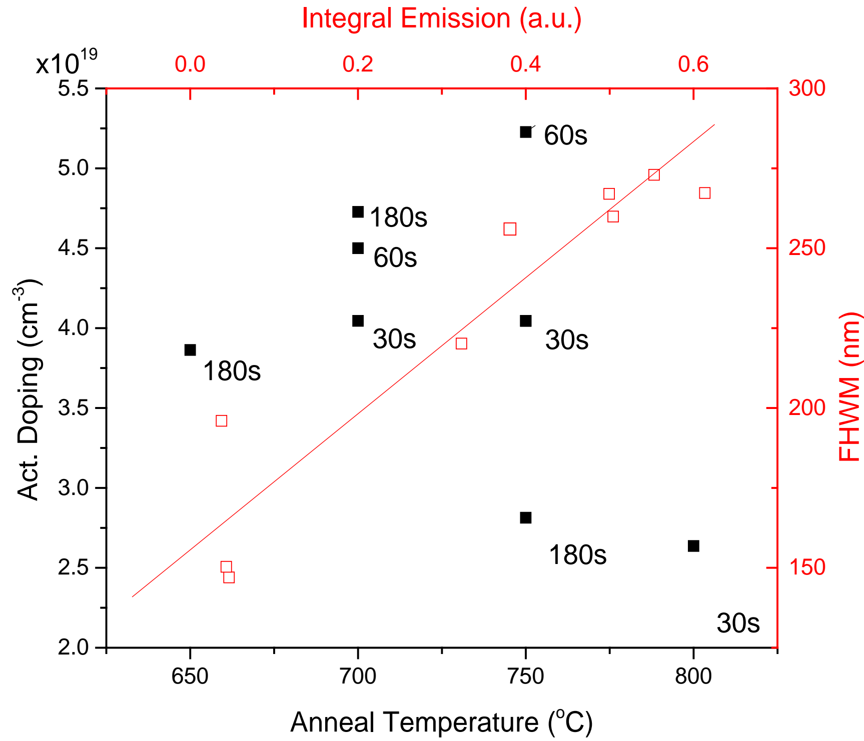

Figure 71.-P and Sb coimplantation PL after different annealing temperatures and times. Peak at 1714nm ~5.4x10^{19}cm^{-3} under 60 sec anneal

It was considered that the peak emission did not change significantly, but that the damaged area of the samples would affect the overall efficiency as a light emitter. Consequently, the samples were treated with CMP to reduce the damaged area and flatten the surface for electrical injection. As can be seen in Figure 72 and Figure 73, there is a discrepancy in BGN after CMP according to the type of dopant. The discrepancy is expected since not all dopants were supposed to diffuse through, as the nature of each dopant having a different diffusion rate.

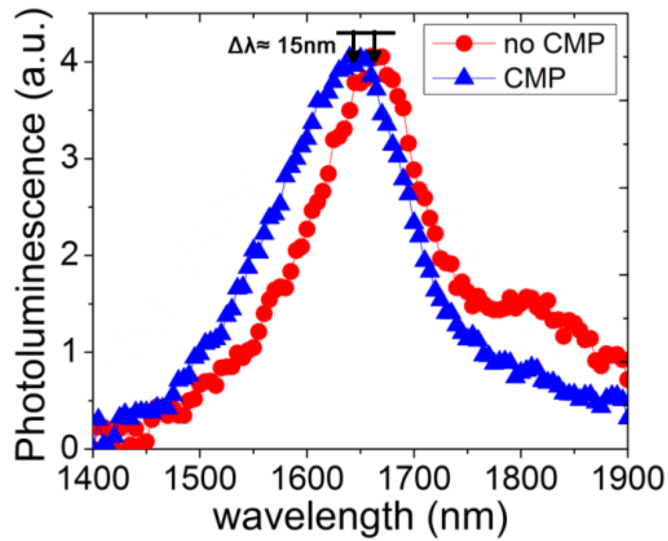

Figure 72.- P implantation sample pre- and post- CMP. Small transition is observed

P only doped samples showed a relative low change, with total concentration varying by less than $5x10^{18}cm^{-3}$. Assuming that the level of doping concentration is the main reason for the small shift, a similar result was expected in the coimplanted samples. According to the activation obtained in previous work [108], the level is superior since it reaches levels around $4.5x10^{19}cm^{-3}$ active doping.

Coimplanted samples (Figure 73) did not show the small change but rather concentration changes around $2x10^{19}cm^{-3}$. The difference in doping level cannot be attributed to the level of doping or annealing temperatures, since they were treated all at 700C for 180 seconds. Hence, the change in BGN is assumed to be caused due to the dopant type. It is noteworthy to state that the level of active doping is higher than was expected theoretically[115]. Coimplanted samples do not seem to benefit from CMP but rather loss a high amount of material. Using two donor types retards the diffusion of the dopants, resulting in lower doping concentration after CMP.

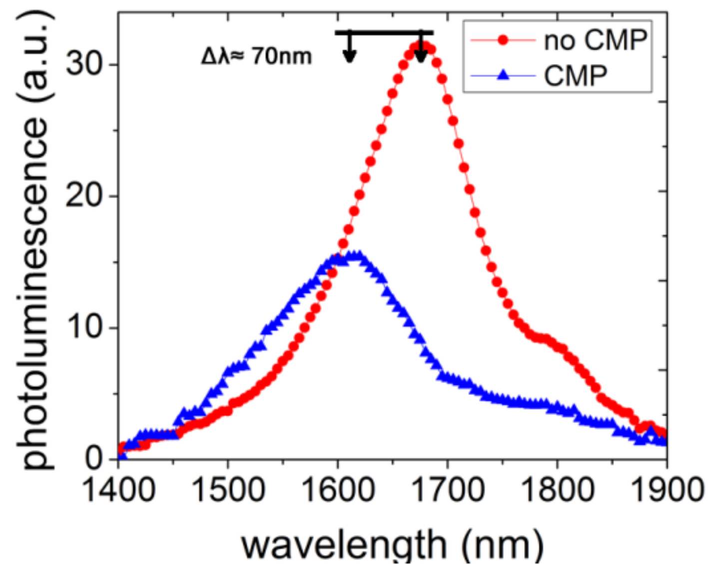

Figure 73.- P and Sb coimplantation sample pre- and post- CMP. Difference in emission is due to slow diffusion of the dopants, causing nonuniform redistribution. Similar is observed in P and As coimplantation.

The decrease in emission suggests not complete redistribution of the dopants. From diffusion equation with known diffusivities, it is seen that the maximum diffusion permitted is 150nm. To confirm such behavior, SIMS analysis was performed.

When looking at the total dopants in P+As implantations through SIMS, we see that the As does not diffuse thoroughly (Figure 74), and seems to retard the P outdiffusion, agreeing with our theory. However, increased in doping level above $6x10^{19}cm^{-3}$ in the body of intrinsic growth Ge, shows a steep increase in the diffusion rate for P. Arsenic is absorbed by the oxide diffusion barrier suggesting diffusivity smaller than known. The steep increase in dopant concentration in depth through Ge, and the clear PL proof enhanced dopant diffusion in Ge. The total doping concentration is larger than observed through PL or Hall effect suggesting that more than half of the dopants are inactive. Since the dopants do not uniformly distributed, most of the dopants will be removed with CMP, as was observed in PL measurements.

.

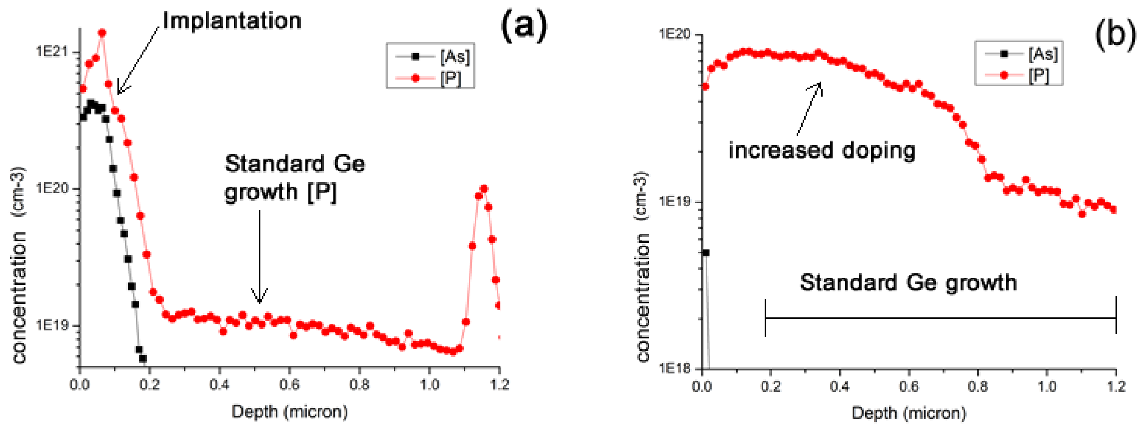

Figure 74.- SIMS analysis of P and As sample (a) before annealing, (b) after annealing at 700 C for 3min.

Difference in diffusion speeds is possibly related to the mechanism of diffusion. It is thought that P diffuses through substitutional and interstitial diffusion, permitting higher speeds that its counterparts. As on the other hand only diffuses through substitutional diffusion.

The difference between the total concentration levels obtained in As, P and Sb are related by how much of the lattice remains damaged and the nature of each dopant. Further research is needed to understand the mechanisms for retardation, rejection and enhanced diffusion.

In this section it is demonstrated that the implantation technique can be used with the damaged source approach. . The steep increase in doping concentration makes this material a potential candidate for light emitters.

4.3 Delta Doping [141]

The approach succeeded in achieving doping concentrations up to $4.2x10^{19}cm^{-3}$ and a theoretical limit based on the solid solubility. Delta doping samples were used for all our PL and EL

experiments due to the large variety of dopants, the reliability of the process and the low addition of point defects

Crystalline quality of the Ge affects absorption and recombination paths for carriers and photons in a light emitter. When using ultra high vacuum chemical vapor deposition (UHV-CVD) to grow Ge epi-layers, n-type doping during growth is concentration limited [27] in order to maintain low defect densities. The maximum theoretically expected active dopant concentration for UHV-CVD n-type Ge is $2x10^{19}cm^{-3}$ [115] and experimentally a phosphorus (P) doping concentration of $1.2x10^{19}cm^{-3}$ was demonstrated [25]. CVD in-situ doping concentrations are limited by a delicate balance between P out-diffusion and Ge growth temperature for high quality films. We presented delta doping which could overcome the limitations of CVD, while using the same CMOS tools and steps.

Delta doping has been used in compound semiconductors[142, 143], Si[144], and MBE grown Ge [145, 146] to significantly increase doping levels locally. Scappucci et al. [145, 146] showed that delta doping was possible through low temperature deposition of Ge. Here we present a similar process to increase the P-doping concentration in Ge to above 4 $x10^{19}cm^{-3}$, while retaining single crystallinity and utilizing a CMOS process. In order to reach high doping levels we utilized dopant enhanced diffusion of P in already P-doped Ge films. The enhanced diffusivity is necessary to limit P out-diffusion while increasing the P concentration in the active device area. A detailed description of the diffusion mechanism can be found elsewhere [125]. We achieved a growth process that yields P concentrations in Ge in the mid $10^{19}cm^{-3}$.

Ge films were grown epitaxially on bulk silicon substrates with (100) orientation by UHV-CVD. Here we use the same growth process as has been described previously[25, 77] . The films were deposited in a two-step process beginning with a low-temperature deposition of a thin, but

highly defective Ge buffer epitaxy layer. On top of the buffer layer, a high-temperature (650°C) growth of P doped Ge creates a thick layer of high quality crystalline n^+ Ge with an activated P concentration of up to 1.2×10^{19} cm^{-3} [125]. To retain the high quality n^+Ge layer, a higher concentration P diffusion source is deposited on top of this active device layer. Since higher than 1.2×10^{19}cm^{-3} doping levels of P cannot be achieved with in-situ doping of Ge using UHV-CVD, a new growth process was developed that would increase the activated P doping level without introducing additional defects in the active device layer. The dopant source can be created by introducing mono-layers of P on Ge (delta layers). P adheres to Ge at low temperatures without growing epitaxially. Due to the accommodation coefficient of Ge-P, only mono-atomic P delta layers are allowed on the Ge surface.

The dopant source concentration depends on the amount of deposited layers. A single monolayer surface concentration of ~5×10^{14}cm^{-2} is equivalent to ~1×10^{19}cm^{-3} P if fully incorporated into a 500nm layer. The process demonstrated here shows a multilayer structure with an expected concentration of ~4×10^{19}cm^{-3}. During deposition of the monolayers, or delta layers, surfactant poisoning effect is observed on the Ge surface stemming from P, decreasing the growth rate of any subsequent Ge layer[147]. This effect has been observed before in Si and Si:Ge alloys [27]. Ge atoms cannot interchange the positions taken by P on the Ge surface, leading to growth stop. A schematic of the complete growth process is illustrated in Fig. 1 where the dopant reservoir depicts several P delta layers.

Intrinsic undoped Ge growth rate is higher than P-doped Ge growth rate and its slower P diffusion rate in Ge retains the P delta layers. Hence, the P delta layers are encapsulated by intrinsic undoped Ge to form a P diffusion source for the active device layer. The delta doped source layer exhibits a higher P diffusivity compared to undoped Ge due to dopant enhanced

diffusion[125] caused by the high P concentration. The delta doped Ge-P layers act as dopant source, not affecting the crystallinity or defect concentration of the active device layer of high temperature growth crystalline Ge.

The multilayer structure is fabricated from a series of 4 alternating layers of undoped Ge and P deposited at 400°C and 450°C, respectively, so as to obtain P concentrations close to $5x10^{19}cm^{-3}$. A schematic of this process is shown in Figure 75 , comparing P concentration desired on each layer.

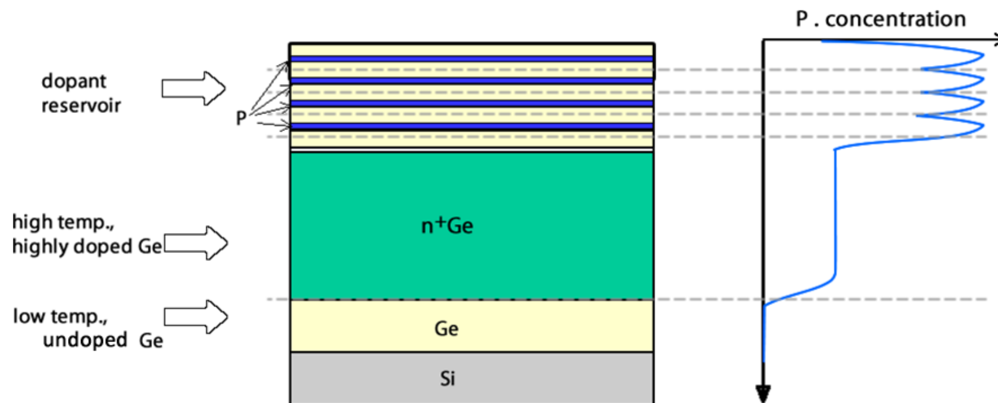

Figure 75.- Schematic of grown layers. The dopant reservoir are alternating layers of Ge and P. Dopant concentration in Ge increases dramatically in the dopant reservoir without being linear due to slow diffusion into the intrinsic undoped Ge used in the layers.

Although the P concentration in the Ge film is significantly increased using this modified growth process, Hall Effect measurements on as-grown samples, presented in the following section, suggest that the P dopants are not fully activated. Similarly, photoluminescence (PL) measurements show that the direct bandgap Ge light emission from these samples, absent further processing, is less efficient than that from reference samples without P delta doping. Therefore, low PL from delta doped samples indicates that thermal treatment after deposition can activate the dopants.

The samples were thermally annealed under Nitrogen flow by rapid thermal annealing (RTA) using an AG Associates Heatpulse 410. The temperature ranged from 550 to 800°C with annealing times in the range of 30 to 300 seconds. In order to prevent dopant out-diffusion and oxidation, a thin 100nm SiO_2 was deposited by plasma enhanced chemical vapor deposition (PE-CVD) using an Applied Materials Centura 5300 DCVD system.

Surface morphology changes with growth process and annealing times were observed. Figure 76a and b show Ge films grown using a standard in-situ P doped epi-growth [77] and a delta doped growth. The doping concentration of the delta doped films varies, ranging from 2 to $4.5x10^{19}cm^{-3}$. Comparing these results with standard epi-growth shows a significant increase in roughness after delta doping due to the arrest in epitaxial growth in the delta doped growth. Nevertheless, the roughness does not change the active carrier concentration but only increases the light scattering at the surface, as can be seen in PL intensity measurements.

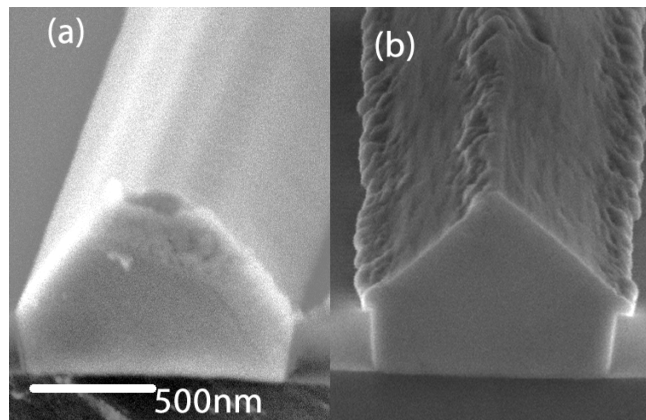

Figure 76.- SEM images of (a) in-situ doped Ge and (b) delta doped Ge grown with source grown at 400C. Notice difference in surface roughness which indicates the arrest of epitaxial growth.

Surface roughness of 35-50nm root-mean-square (RMS) is measured in all samples after delta-doping. In comparison, an atomically flat Ge surface has a roughness of ~5nm RMS.

Annealing conditions above 600˚C will decrease the surface roughness. As seen in Figure 77, the RMS does not change dramatically over different dimensions or times, but temperature decreases in higher magnitude the surface roughness. However, in order to obtain atomically flat surfaces the required temperatures are close to the melting point of Ge. Such high temperatures would have an adverse effect in the dopant concentration.

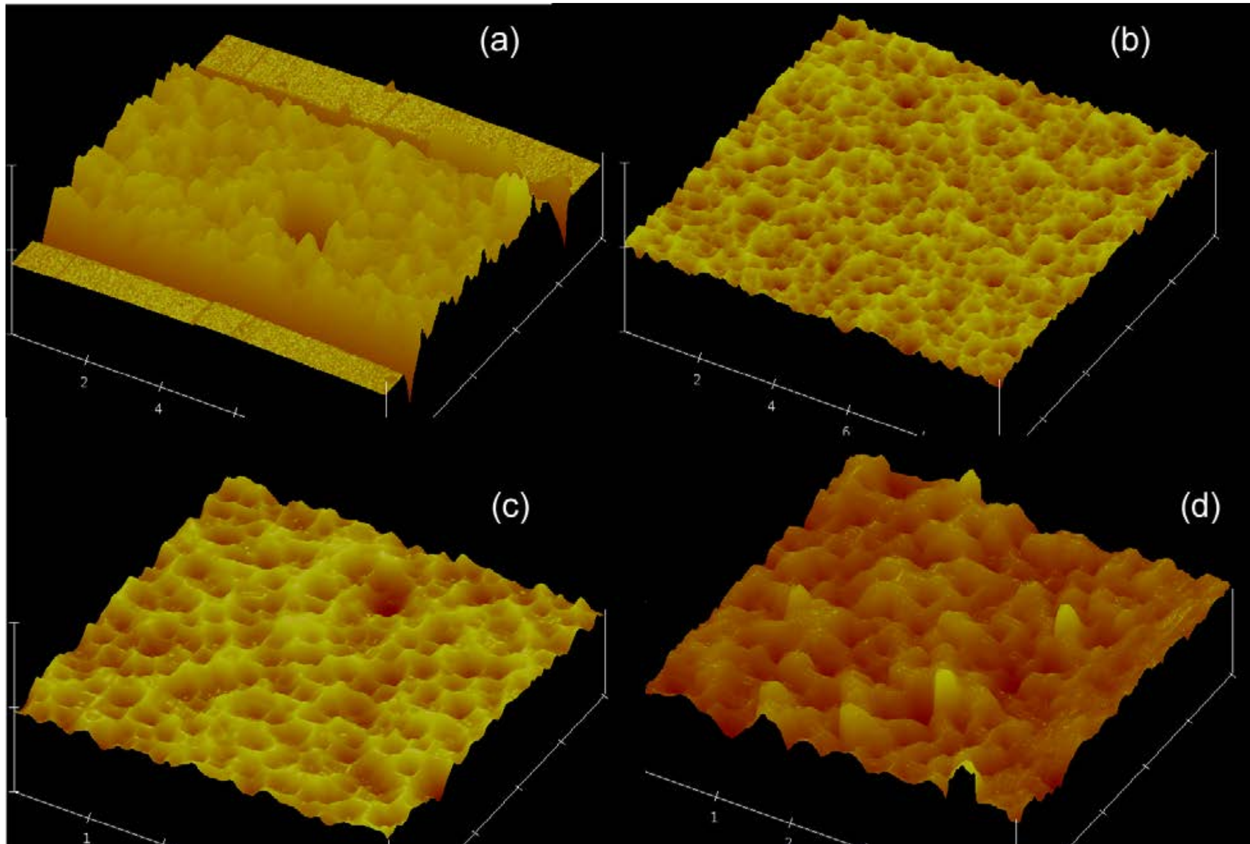

Figure 77.- AFM measurements showing the progression in roughness with different annealing temperatures. (a) waveguide anneal at 600°C for 2min RMS of 38nm, (b) film anneal at 600°C for 30sec RMS of 42nm, (c) film anneal at 600°C for 60sec RMS of 37nm, and (d) film anneal at 700°C for 30 sec RMS of 35nm.

XRD measurements confirmed that all the samples are strained 0.2-0.3% and that the heavy doping does not contribute to release or increase the strain. As seen in Figure 78, the

different peak shapes FWHM show that the upper layer (delta zone) is highly defective and most likely poly. CMP procedure after annealing can remove this layer and make it atomically flat.

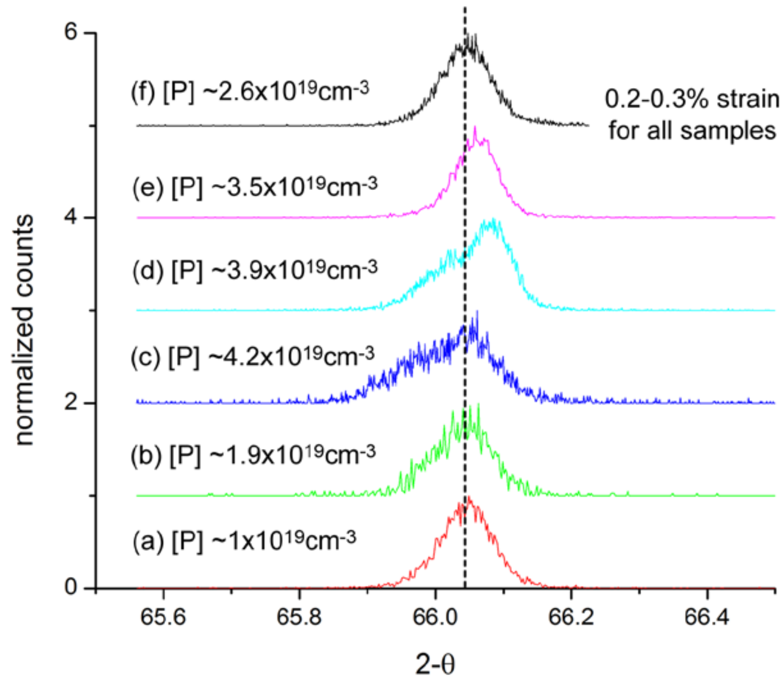

Figure 78.- XRD of Ge doped samples. All samples indicate an average 0.2-0.3% strain. The difference in shapes strives from the upper layer of defective Ge; broadening the X-ray emission.

TEM measurements confirmed that the layer is highly defective, as seen in Figure 79. It shows heavy amount of dislocations through the device. The average dislocation density of a delta is above $10^9 cm^{-2}$, which is of the same order as the buffer layer. The core of the n+Ge tends to be in mid $10^8 cm^{-2}$. Annealing these samples for longer period would represent and increment of the dopant loses, even though it could remove the high dislocation density. A secondary problem is the gliding of the dislocation into the low dislocated area. This problem was unforeseen due to the quick annealing times during RTA, but it shows a clear trend of increase. The core of most Ge samples is $<10^8 cm^{-2}$, as seen previously, but the area close to the delta

growth shows a significant increase. This is suggested to be due to gliding of the heavy dislocated neighbor.

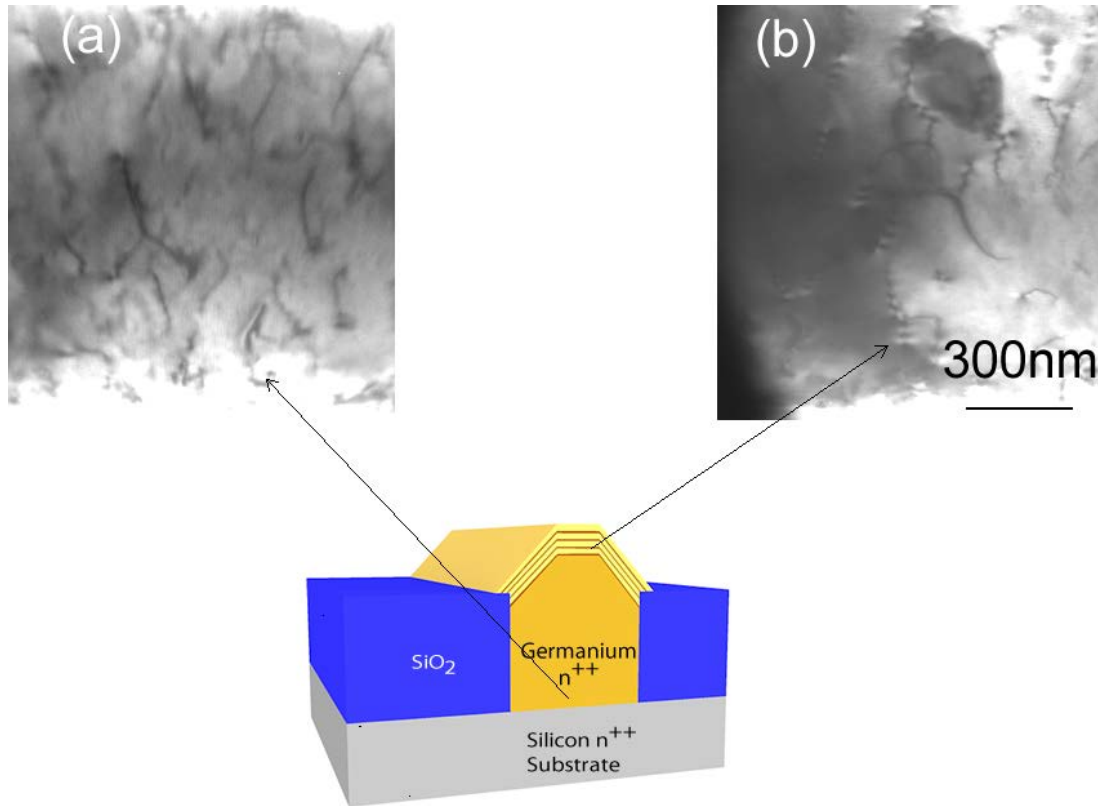

Figure 79.- TEM measurements of different sections of a delta sample after annealed at 700°C for 30sec. (a) shows the buffer with a dislocation density >$10^9 cm^{-2}$, (b) shows the delta layer with dislocation density around $2x10^9 cm^{-2}$.

In order to evaluate if the active P doping can be increased in the high quality Ge film secondary ion mass spectrometry (SIMS) was used to determine the total P concentration in the Ge films and Hall Effect measurements were used to determine the activated P concentration. SIMS profiles for delta doping at 360, 400 and 450°C are shown in Figure 80. The total P concentration in the delta doped region is above the predicted maximum P concentration [115] and is significantly higher than in-situ doped, UHVCVD grown Ge. Adhesion of P increases as

temperature decreases obtaining largest P accumulation at 360°C. The figure also shows that P diffusion already occurs at the growth temperature. At 450°C, P has diffused from the delta layer further into the in-situ doped Ge region than at 400°C, obtaining a uniform P concentration dopant source. The SIMS profiles furthermore highlight the dopant accumulation at the Ge-Si interface at the bottom of the Ge layer. Due to the growth process, the initial 60nm thick Ge buffer layer is highly dislocated, providing a sink for fast diffusing dopant atoms. The average active carrier concentrations for the 400°C and 450°C growths were determined by Hall Effect measurements to be $1.5x10^{19}cm^{-3}$ and $1.8x10^{19}cm^{-3}$, respectively. The discrepancy between active carrier concentration and total dopant concentration clearly shows that defects limit the dopant activation. It confirms as well that with lower temperatures, the addition of P on Ge is intensified.

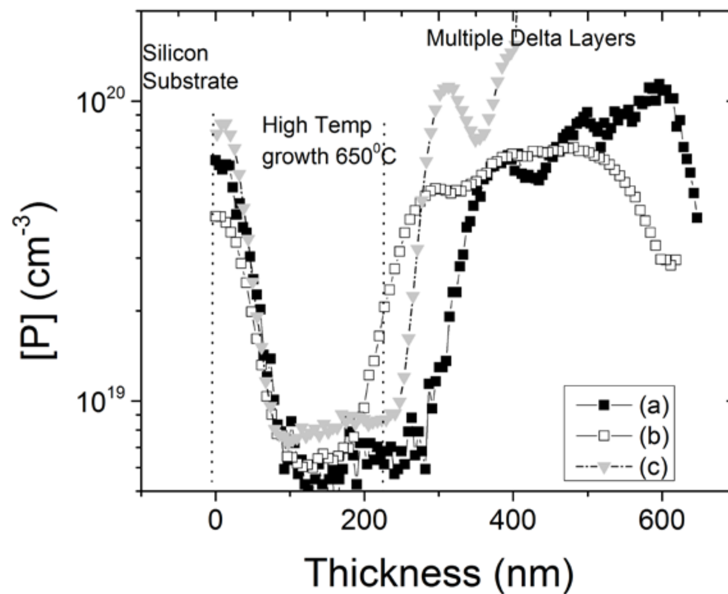

Figure 80.- SIMS profiles of as-grown P delta doped Ge, with P deltas grown at (a) 400°C , (b) 450°C and (c) 360°C. Dopant diffusion from delta source increases the concentration of P in the underlying high temperature Ge region.

An example for the P redistribution due to annealing is shown in Fig. 4 SIMS results. A 400°C delta doped Ge films were annealed at 600°C for 30 and 60 seconds, and 700°C for 30 seconds. A fairly even distribution of P in the in-situ doped Ge region due to P out-diffusion from the delta doped range can be observed. The average P concentration in the in-situ doped region is about $4x10^{19}cm^{-3}$ after 30sec at 700°C annealing. Annealing improves the P concentration by at least a factor of 3 as seen in Figure 81 Since P is diffused into Ge of high crystalline quality, it is expected that the in-diffused P is completely activated.

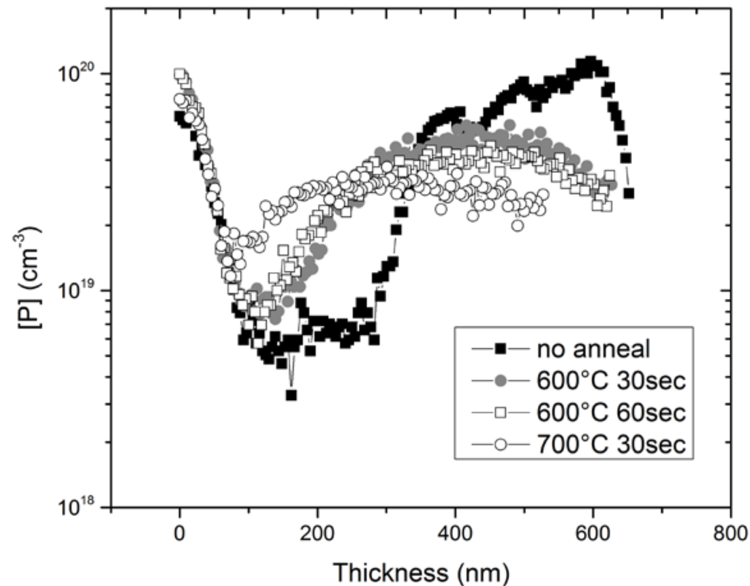

Figure 81.- SIMS profiles of dopant redistribution from delta doped Ge grown at 400°C. The diffusion of the dopant is time and temperature dependent, becoming more uniform at higher temperatures but limited by outdiffusion at longer times.

It is observed that the active carrier concentration increases with annealing, however, the active carrier concentration typically increases up to a certain annealing temperature and then decreases. Agglomeration of dopants on the Si interface due to misfit dislocations and the lower dopant concentration on the Ge surface after extended anneals prove that out-diffusion is the mechanism for dopant lose. This leads to each temperature having an optimal time for

maximizing active carrier concentration, preventing out-diffusion loses. The PL intensity increases as the active carrier concentration achieves the maximum capable per annealing temperature and time. Since Hall Effect measures the integrated carrier concentration of the delta doped region as well as the in-situ doped region, it is very difficult to determine the optimal annealing conditions from these data.

It was therefore important to find an additional indicator of the quality and active doping level of the Ge films. It was found that band gap narrowing in Ge correlates to the active n-type doping. As the active doping level increases the direct band gap of Ge narrows, which is observable in PL measurements. More details can be found in Camacho-Aguilera et al [148]. An example of the highest PL intensities and the accompanying shifts is shown in Table 7. The emission intensities are not normalized for Ge thickness. It is obvious that the samples with the largest red-shift show the highest PL intensity. PL intensity depends heavily on dopant concentration and crystal quality[147]. At low annealing temperatures, the dopant concentration is high while the PL intensity is low. One possible explanation of this effect is that annealing at high temperatures reduces defects, resulting in lower loses from the Ge crystal matrix.

Table 7.- Photoluminescence at RT of delta doped Ge samples under different RTA conditions

Anneal (°C)	no anneal	600		700		standard epi-Ge
Time (sec)	-	30	60	30	60	-
Peak emission (nm)	1640	1659	1662	1642	1650	1603
Hall effect active carrier concentration ($x10^{19}cm^{-3}$)	1.9	3.8	4.3	4.2	3.4	1.1
PL integrated Intensity (a.u. $x10^{-2}$)	0.742	2.04	1.73	1.5	1.3	1.18

As seen in

Table 7, PL decreases with increasing annealing time even though the active carrier concentration increases, suggesting that doping decreases with increasing annealing times. Out-diffusion is the mechanism governing the PL intensity loss at longer annealing times. However, the active carrier concentration does not increase past a certain value that is given by the solid solubility. Olesinski et al.[110]determined that the solid solubility of P in Ge at 775°C is $8x10^{19}cm^{-3}$. Fig. 5 shows the maximum active carrier concentration that was found for different temperatures and annealing times and compares the concentrations to the solid solubility of P in Ge. As can be seen from Figure 82, P reaches near solid solubility at temperatures below 550°C. Above 550°C, the maximum active carrier concentration is always smaller that the solid solubility of P, decreasing above 600°C despite the increase of the solid solubility. The disparity is caused by the competition of P dopant loss due to out-diffusion and defect annealed, which permits active dopants. P incorporation is also limited by the diffusion source, which contained $\sim 4x10^{19}cm^{-3}$. Maximum dopant activation was almost reached for the quantity available in the delta doped source. Hence, short annealing times at higher temperatures, coupled with an effective diffusion barrier and a higher doped diffusion source, are expected to yield better P incorporation overcoming dopant loss.

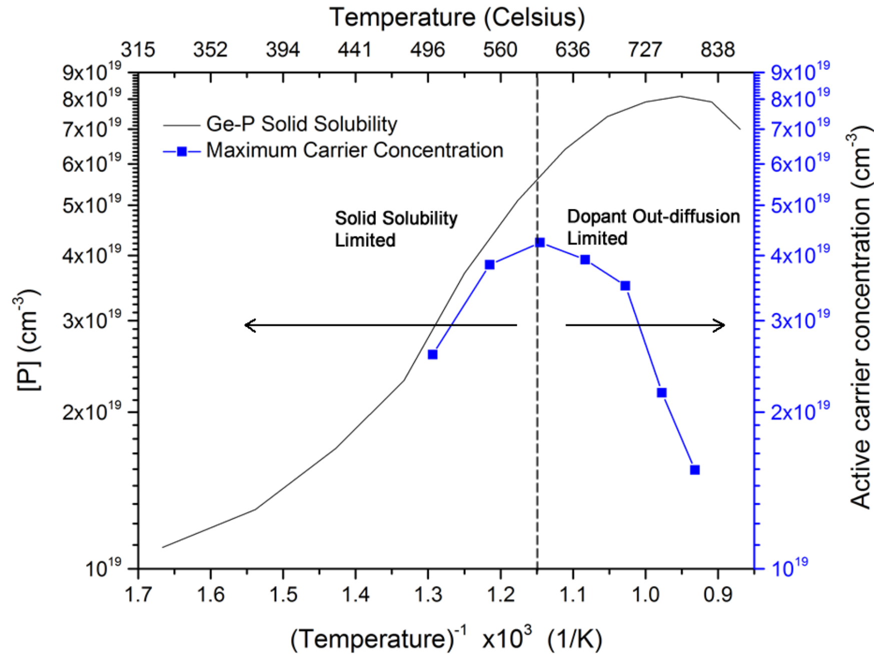

Figure 82.- Comparison of P solid solubility[110] in Ge and observed maximum active carrier concentration of delta doping at different temperatures.

The increase in dopant concentration is made possible by a dopant source with concentrations of >$2x10^{20}cm^{-3}$ and enhanced dopant diffusion [125]. The diffusion source can be removed from the active device layer through chemical mechanical polishing (CMP) for use in active light emitting devices [22].

Fully incorporated multi-layered delta doping provides a high chemical activity source for achieving active carrier concentrations above $4x10^{19}cm^{-3}$. The main mechanism limiting the maximum carrier concentration is the out-diffusion of the dopants. The multi-layered dopant diffusion source is a critical element of the diffusion design to solve the main issues in high dopant concentrations in Ge, while sustaining a low defect concentration. At higher dopant concentrations this trend might change.

Selective growth of the delta doped Ge grown films makes them a suitable candidate for CMOS compatible Ge diode lasers.

In this chapter we have demonstrated:

- High doping enhanced diffusion in Ge for used in secondary dopant diffusion
- Three methods of doping through extrinsic or intrinsic sources
- The limitations of SOD due to Si and SiO_2 diffusion of dopants
- The potential of implanted Ge for devices after anneal and CMP is performed
- Delta-doping >$4x10^{19}cm^{-3}$ without the introduction of external defects
- The main limitations for any method are : solubility of the dopants, diffusion of the dopants on extrinsic or intrinsic sources, source concentration of dopants, and Si-Ge interdiffusion

Delta-doping was selected for the use of the highly doped devices due to the low insertion of defects and uniformity of the doping achieved. The following chapters will covered the results of such highly doped samples.

Chapter 5. Bandgap Modifiers

Germanium band structure has been studied since the advent of semiconductors. Data has been collected about Ge electrical and optical properties at a variety of temperatures. The vast amount of information has focused on its properties under low doping, or heavy doping at low temperatures [149-155]. This has led to understanding openings on Ge band gap on the level of interested for lasers. On Ge devices, as it has been mentioned, the need of room temperature operation to high temperatures (300K- 500K), heavy doping and high injection of carriers are expected. The combination of these events causes a series of band gap changes and multi-body carrier interactions. As shown in Figure 83, Ge bandgap effects can be summarized into temperature dependent and carrier dependent. Each of these effects is considered as bandgap modifiers, and change the Ge laser behavior, ergo, altering efficiency predictions. In this chapter, we will overview heavy doping effect on BGN under desired gain spectrum; and temperature effect on electron-phonon intervalley interactions under operation temperatures.

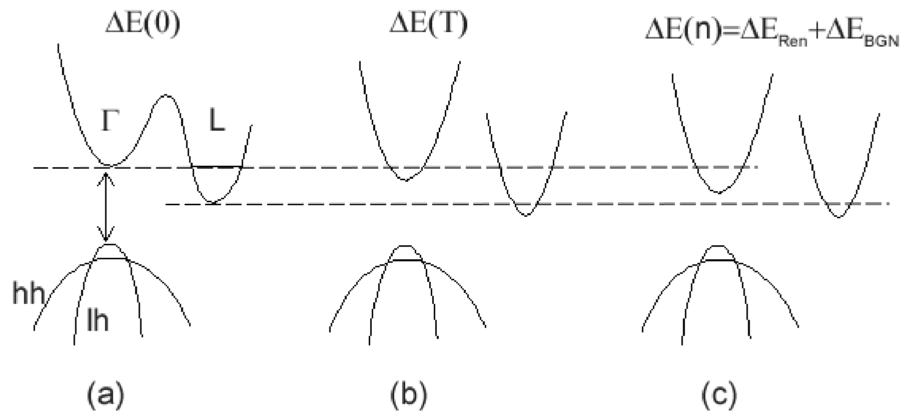

Figure 83.- Schematic representing doped strained Ge band structure under (a) no effects, (b) temperature increase, and (c) renormalization (BGR) and bandgap narrowing (BGN)

5.1 Band Gap Narrowing [156]

Tensile strained n^+ doped Germanium shows promise as a light emitting material for fully integrated silicon photonic applications. The combination of modest tensile strain and n-type doping makes epitaxial Ge-on-Si a pseudo-direct band gap emitter, but the emission efficiency for electrically pumped devices is projected to be practical only if doping levels greater than mid 10^{19} cm^{-3} can be achieved [24, 30, 56]. Furthermore, the incorporation of dopants must not introduce defects into the Ge crystal structure, since these significantly reduce emission efficiency [50, 51]. Unfortunately, implantation techniques, which can raise the dopant concentration, generally introduce defects. Therefore, the total dopant concentration does not equal the total *active* dopant concentration [30, 41, 115].

The most common process for determining dopant concentrations is secondary ion mass spectroscopy (SIMS). However, SIMS is disadvantageous because active dopant concentrations cannot be determined. Furthermore, this technique is destructive as material is removed during the measurement. Other techniques such as Hall Effect measurement, which can determine an average concentration of dopants, are limited by the sample size needed. It is proposed in this section a technique using photoluminescence (PL) to determine average active doping based on band gap narrowing (BGN).

A shift in absorbed or emitted wavelength due to doping is known as BGN and has been observed in many semiconductor materials. BGN has also been observed in unstrained Ge [157-160] through infrared absorption measurements. Tensile stressed Ge-on-Si has been known to emit at ~1550nm at dopant concentration up to $1x10^{19}cm^{-3}$ with unidentifiable changes in the peak emission wavelength [24, 30, 48]. Under degenerate doping, $n > 1x10^{19}cm^{-3}$, a clear

shift in emission wavelength is observed [161]. The effect of BGN should not be confused with band gap renormalization (BGR).

BGR is analogous to BGN, as it will shrink the band gaps as carriers are injected, obtaining a similar behavior to BGN. Moreover, BGR is usually compared to potential screening where $\Delta E \propto N^{1/3}$, in accordance to heavy doped materials [162, 163]. BGR evidence suggests that, in Ge, BGR will follow similar trend as BGN as will be seen in Chapter 6.

Burstein-Moss (BM) shift is another effect occurring on degenerate semiconductors. BM translates into a blue shift on the band emission. BM has a dependence of $n^{2/3}$, and is overcome by the BGN effect under low injections. A summary of these effects can be seen in Figure 84.

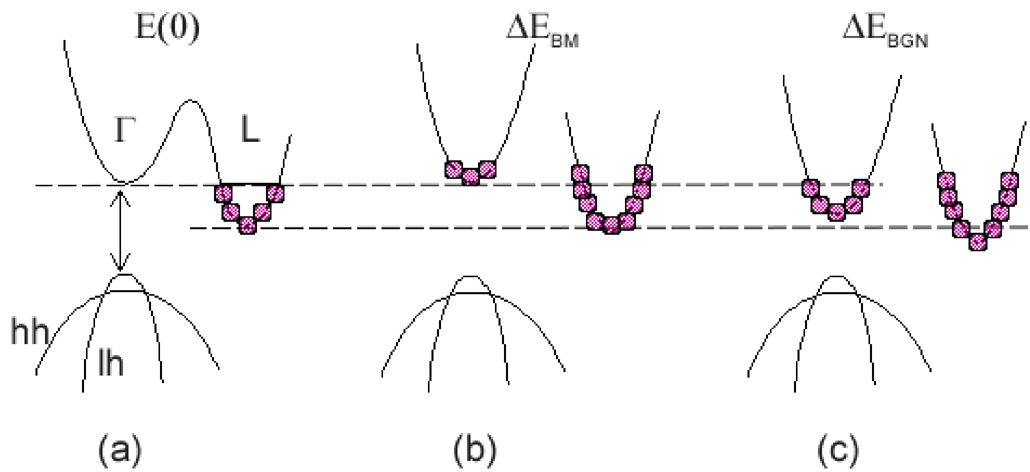

Figure 84.- Schematic showing the differences between Ge doped under (a) no effect, (b) Burstein-Moss shift, and (c) BGN shift.

A present BGN model presented by Jain et al. [41, 45] assumes a bandgap shrinkage due to carrier concentration in the L valley and temperatures <77K. The expression for Ge does not include strain, which also narrows the band gap, hence, shifting the PL emission peak. Furthermost, the present model fails to address high doping level band gap emission shift at high temperatures and direct band gap shift.

Here, it is presented a study on BGN at 300K for Phosphorus-doping concentrations of $5x10^{18}$ cm^{-3} to 4.5x 10^{19} cm^{-3} in Ge. Our observations utilize BGN to determine effective active carrier concentrations. Comparison with present's BGN preliminary results showed that the previous theory is only appropriate for low temperatures (< 77K) and for the indirect L band gap BGN effect in Ge.

Germanium films were grown epitaxially on bulk silicon substrates with (100) orientation by ultra-high vacuum chemical vapor deposition (UHVCVD). Details of the deposition process have been described previously [30, 125, 164]. Ge films were deposited in a two-step process, beginning with a low-temperature deposition of a thin but highly defective Ge buffer epitaxial layer. This buffer layer relaxes the strain induced by lattice mismatch of 4.2% between Si and Ge at the substrate interface and serves as a sink for dislocations. On top of the buffer layer, a high-temperature co-deposition of Ge and P creates a thick layer of high quality crystalline n^+ Ge with a carrier concentration of 1×10^{19} cm^{-3}. Then, delta doped Ge layers are deposited. They consist of monolayers of P encapsulated by intrinsic Ge [164]. The upper cladding of the material is provided by a PECVD SiO_2 layer. P is diffused into the n^+ Ge film by rapid thermal anneal (RTA). The oxide layer acts as a diffusion barrier. Details of the P diffusion can be found in [125]. The Ge threading dislocation density is $\sim 3x10^8$ cm^{-3} from TEM measurements, and the point defect is assumed $\sim 10^7$ cm^{-3} from the law of mass action.

Blanket films and waveguides were made and compared in x-ray diffraction (XRD) and PL. The different dopant concentrations were analyzed using Hall Effect and PL measurements. A Horiba MicroPL system with a 1064nm laser and an EOS InGaAs IGA1.9 photodetector were used at RT to measure the photoluminescence spectra of the Ge samples.

Samples with P concentrations ranging from $5x10^{18}$ to $4.5x10^{19}$ cm^{-3} were studied. XRD measurements showed that both blanket films and waveguides have similar tensile strain of ~0.25%

It has been shown, that an increase in PL intensity in Ge is equivalent to higher active carrier concentrations in Ge while retaining low defect concentration [20, 41]. The total integrated emission also increases, showing low defect density in Ge and that the dopants are contributing to emission. In addition to such increase of PL intensity, we also observe a redshift of the peak wavelength for the direct band gap emission with higher doping concentration, as seen in Figure 85. The emission is from the band-edge of direct gap from the Γ valley. Hence, the PL peak emission is equivalent to the energy gap, E_{Γ}. The wavelength shift indicates BGN of the Ge Γ valley transition. Although change of strain may also result in a shift of the bandgap, cross-analysis with XRD shows that even at these high doping levels, dopants are not sufficient to relax the lattice strain. We therefore consider a model only based on carrier interactions to explain such BGN effects. BGN also provides a simple, non-destructive measurement to determine doping concentrations of samples smaller than permitted for standard methods. Since the Fermi level is still below the Γ valley, Boltzmann distribution is used to interpret the emission spectrum. The energy of the peak emission is kT/2 higher than the direct bandgap. The band gap without BGN is calculated by adding kT/2 to the energy difference between valence band and Γ. The difference between the peak emission and the base band provides the BGN in the Γ valley.

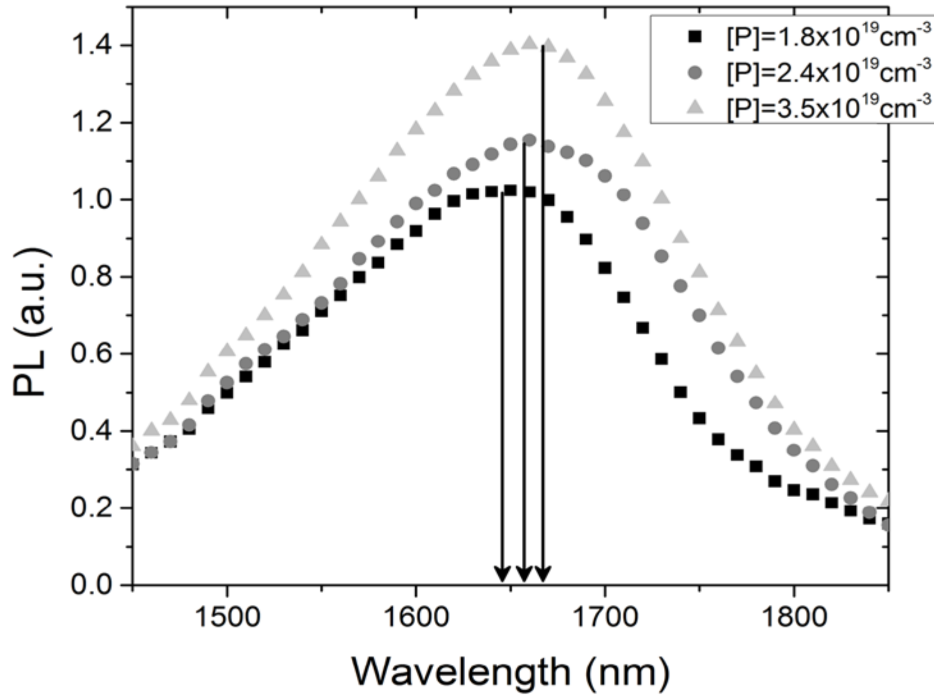

Figure 85.- PL intensity for heavily n-type doped Ge. BGN shift in emission compares to doping concentration of samples analyzed. Arrows show peak shift from the different doping concentrations, red shifting with increasing active dopant.

Haas presented his observation of direct BGN of Ge by analyzing the absorption spectrum [45]. This method takes into account recombination of carriers from valence band to L valley band edge. Both absorption and emission mechanisms show equivalent results for Γ valley at 300K, as shown in Figure 86. Our data fit Hass's 300K data [13] and suggests a lower limit for BGN, as will be discussed. The extensive experiments in this work show a linear dependence of Γ-point band gap shrinkage with heavy n-doping.

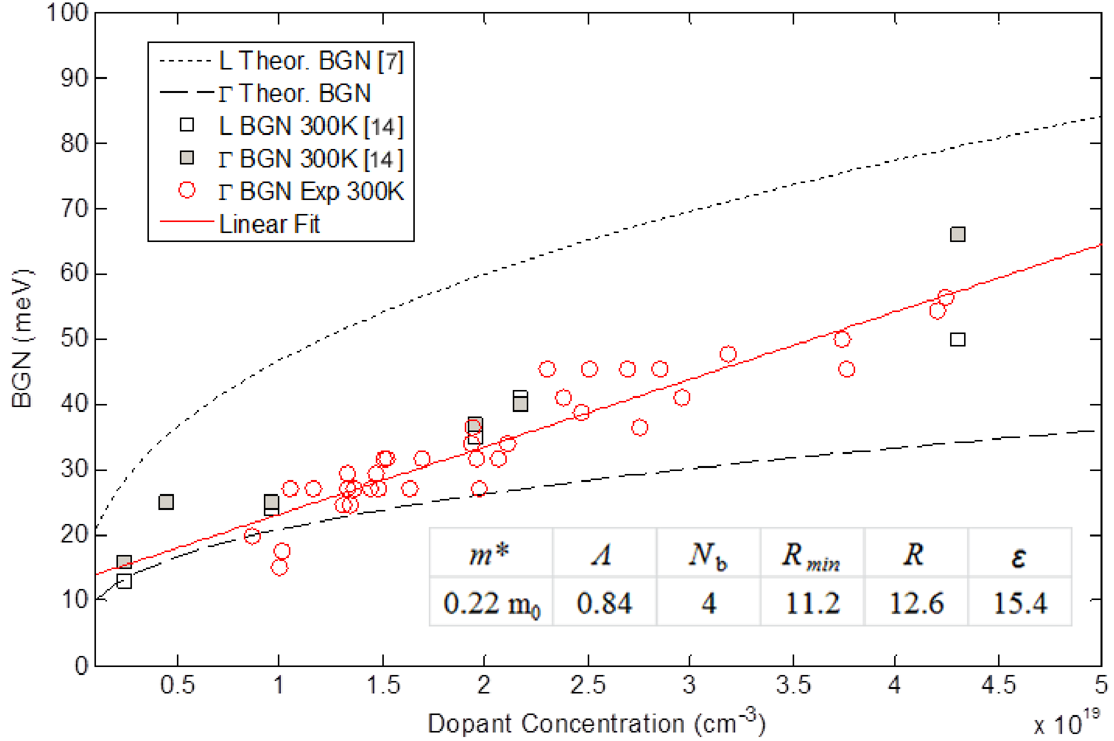

Figure 86.- Experimental observations of BGN as a function of n-type doping concentrations at 300K. A linear relationship is observed. The data falls between Jain's theory (L band) and equation 4 of this work for the minimum change (**Γ** band).Table shows parameters used for equation 3 and 4.

From first principles, theoretical treatment of the experiments in this work may need to consider two distinguishing features: i) the experiments are at 300K, and ii) the system is tensile strained Ge where the quasi-Fermi levels at the L- and Γ- minima overlap in energy.

This approach might be generalized for Ge according to equation,

$$E_g(N_D = 0) - E_g = E_{BGN} + \Delta_{BGN} N_D (cm^{-3})$$

where N_D is the dopant concentration, E_{BGN} is BGN turn-on offset energy reduction (intercept of the linear relationship at N_D=0); and Δ_{BGN} is the BGN coupling parameter (slope of the linear

dependence of E_g reduction with N_D). The data of this work yield the parameters: E_{BGN}=0.013eV and Δ_{BGN}=10^{-21} eV/cm^{-3}.

It is proposed that the linear dependence can be regarded as the dominant first order term of a BGN phenomenological model. This linear dependence can be evidence of the effect of an impurity band created under heavy doping [165]. The linear fit, therefore, can be used to predict with reasonable accuracy the spontaneous emission wavelength of doped Ge and to measure through such emission, the doping level of the Ge.

FHWM shows a linear trend fits with the narrowing. As the band narrows, FWHM should increase in a linear fashion from intensity calculations. The calculation should match with BGN, and it does as shown in Figure 87.

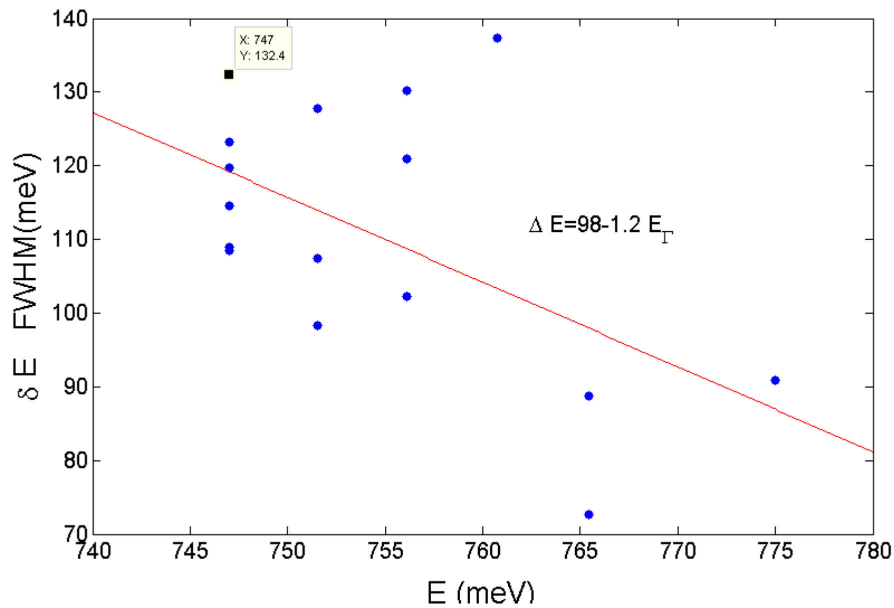

Figure 87.- FWHM comparison with Peak energy . The linear fitting just shows that there's an increase in FHWM with shift in BGN.

A calculation of the FHWM to doping concentration shows same linear dependency, as seen in Figure 88. It shows that the exchange in between bands is justified. The dopant

contribution is isotropic, hence, it affects the conduction bands equally. At the degenerate level, the effect is clearly observed as an emission of only the Γ band.

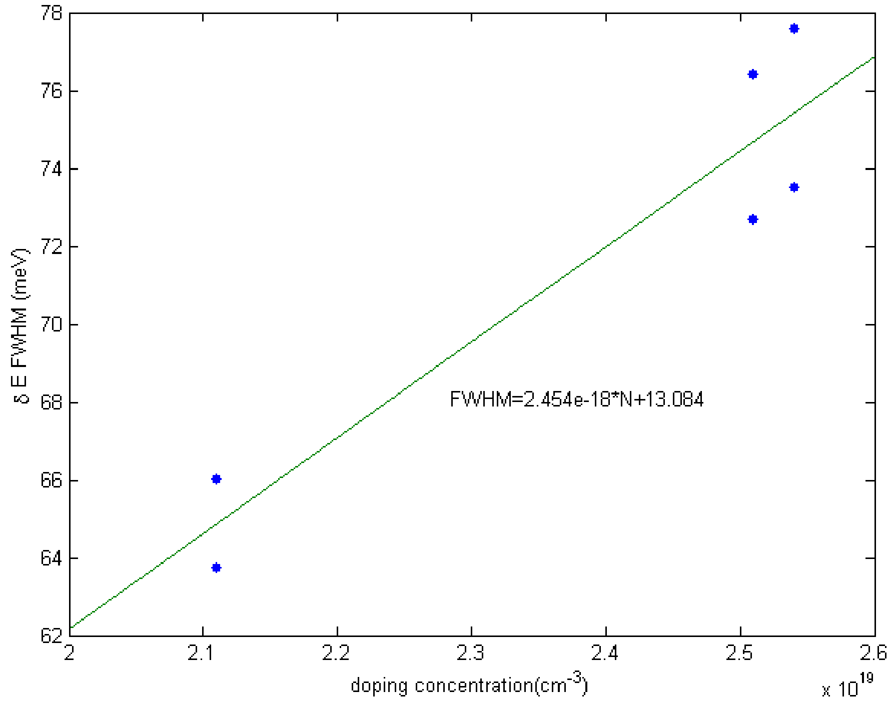

Figure 88.- FHWM comparison to doping concentration.

This functional dependence contrasts with predictions of the Jain model[41] for the L-point and of the simplified lower-limit model further discussed in this work. However, the experimental values of all observations fall between the predictions of the two models.

The present model for BGN assumes a static lattice model under temperatures <77K. It has four components [41]:

$$\Delta E_g = \Delta E_x + \Delta E_{cor(min)} + (\Delta E_{i(maj)} + \Delta E_{i(min)})$$

In n-type semiconductors, the exchange interaction, ΔE_x, is defined by the electron interactions in the different sub-bands, which is described by Hartree-Fock potentials [166]. The shift of the holes is considered in the electron-hole correlation energy, $\Delta E_{cor(min)}$; and the shift of electrons (*maj*) and holes (*min*) due to carrier impurity interactions is represented by,

ΔE_{imp}=$\Delta E_{i(maj)} + \Delta E_{i(min)}$. If the shift of the L valley is considered, the equation has the following form [41],

$$\frac{\Delta E_g}{R} = 1.83\frac{\Lambda}{N_b^{1/3}}\frac{\delta}{r_s} + \frac{0.95}{{r_s}^{3/4}} + \left[\delta + \frac{R_{(min)}}{R}\right]\frac{1.57}{N_b r_s^{3/2}}$$

where N_b is the number of interacting sub-bands, Λ is the correction factor due to anisotropy in the conduction band; R is the effective Rydberg energy for both majority (R) and minority carriers (R_{min}); and r_s is an dimensionless unit from the half average distance between impurities, r_a, under the effective Bohr radius, a. After substituting the appropriate values, L-band fit is observed.

In the classic low-temperature model, inter-valley interaction is limited and electrons can only have exchange and scattering effects within their own sub-valley. Such effect in the L valleys is much larger than that for the Γ valley, reducing ΔE_x and $\Delta E_{i(maj)}$ for Γ. Thus for Γ only the correlation energy $\Delta E_{cor(min)}$ and the impurities interaction of valence band $\Delta E_{i(min)}$ are left in the equation. Since $\Delta E_{cor(min)}$ and $\Delta E_{i(min)}$reflect only changes on the energy of states in the valence band, the same values can be used for L and Γ. The equation becomes,

$$\boldsymbol{\Delta E_\Gamma = 8.15\left(\frac{N}{10^{18}}\right)^{\frac{1}{4}} + 2.03\left(\frac{N}{10^{18}}\right)^{\frac{1}{2}}}$$

This equation expresses the unique contribution of carrier concentration to the shrinkage of the band gap at *Γ* point in Ge. This expression should be regarded as the minimum band gap shrinkage because carrier redistribution due to higher temperatures will further reduce the band gap. As seen in Figure 2, the ΔE_Γ prediction is undervalued at 300K.

At 300K an increase of doping concentration clearly narrows the band gap, and the energy reduction follows a linear relationship with doping. It is significant to observe that Hass's data [45] for both L and Γ BGN, and our data follow the same linear relationship at 300K, as

seen from Figure 86. In this context, similar BGN effects observed by Hass for the Γ-point and L-point conflicts with Pankove's k-space, modified theory [44]. One possible reason is that more electrons will go into the Γ valley at high doping and that temperature may generate a larger exchange interaction, ΔE_x. Another possible reason is the effect of impurity band formation at high doping. An impurity band would enhance the interaction between electrons in L and Γ valleys, weaken momentum conservation, and may average the energy shift in different valleys. Thermal energy can also increase interaction between Γ and L valleys by providing energy for intervalley scattering transitions [165].

From PL results, the peak emission shift will be equivalent to the active dopants, ergo, free carriers. By using Equation 1, we can determine the active dopant concentration by analysis of the PL spectrum, and vice versa. Within the tensile strain values studied in our Ge films of 0-0.3%, we find no evidence that the degree of doping induced BGN is modified by strain.

This work shows that BGN measured from a PL spectrum can be used as a nondestructive technique to determine active carrier concentrations in heavily doped Ge. This technique could be extended to other semiconductors with similar behavior.

5.1.2 Conclusions

In summary, it was measured a significant red-shifts in the photoluminescence spectra of degenerately n-doped, tensile strained Ge. The red-shift exhibits a linear dependence on doping level that we have interpreted as band gap narrowing, BGN. This linear dependence is interpreted as an impurity band dependence. It is proposed a first order phenomenological model for BGN based on two parameters whose values for Ge are E_{BGN} = 0.013eV and Δ_{BGN} = 10^{-21} eV/cm^{-3}. BGN can be a powerful non-destructive method for determining the total active dopant

concentration in Ge-on-Si devices. This method was used to non-invasively determine the dopant concentration of Ge laser devices.

5.2 Temperature effect

Temperature effects deal with lattice expansion and multi-body interactions between electrons, holes, photons and phonons. In Ge, and any semiconductor, bandgap energy is dependent on temperature due to: thermal expansion and renormalization of band energies by multi-body interactions (Figure 89). In Group III-V semiconductor lasers degrade emission efficiencies with temperature. As temperature increases non-radiative recombinations, such as Auger, increase. This effect in Ge results on contributions of indirect bands to Ge light emission, as was demonstrated with CCCH Auger indirect recombination. Moreover, the low energy difference between conduction bands permits for thermalization of carriers through intervalley interactions.

Band-to-band transitions from L to valence band have been the major focus, as low temperature effects, dividing the areas of interest into: Debye-Walter [150] terms for intravalley interactions between carriers; and Bose-Einstein statics regime, where carrier-carrier/phonon-carrier states interact as well intervalley. The latter usually treats with temperatures above to 300 K and ignores the high temperature regimes, and it is the main point of interest for Ge laser devices. This section will cover such interactions and review the high temperature regime and what are the implications in highly doped strained Ge on Si.

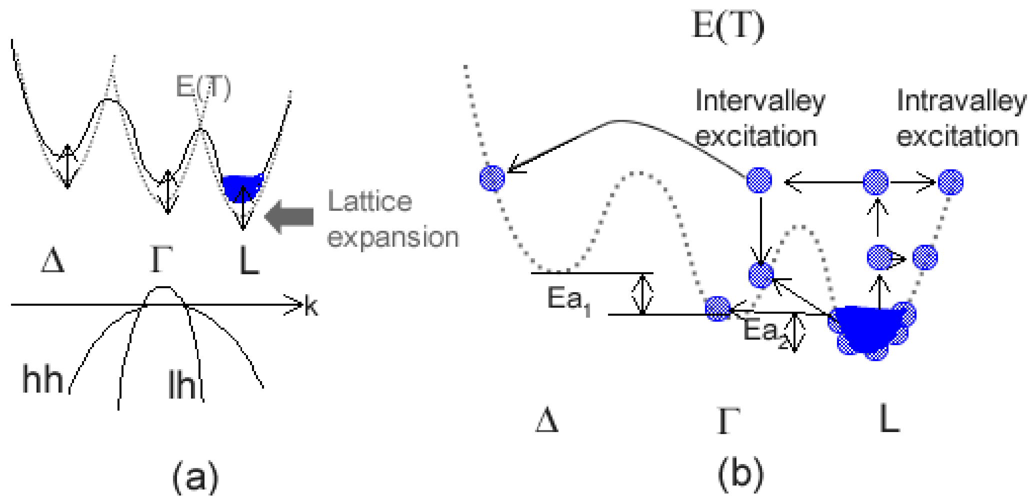

Figure 89.- Schematic of temperature effects shown as (a) lattice expansion described by Varshni, equation, and (b) multi-body interactions resulting on intravalley and intervalley carrier interactions.

The purpose of this section is to show the presence of intervalley scattering caused by electron-phonon/electron-electron interaction. First, we cover the band shape and shift expected at low temperatures, and its effects on emission. Then, band shift according to previous theories is discussed as portraying the complications to perform similar analysis with Ge. Conduction bands contribution to direct emission is then discussed in terms of carrier density and thermalization, as cause of intervalley scattering. Finally, it is shown how the scattering can provide further occupation of carriers on higher energy gaps, such as the direct gap Γ under high temperatures under different doping concentrations in Ge.

5.2.1 Band gap Shift

The effects of temperature on carriers require understanding their nature in the shape formation during PL emission. To calculate the shape of any band-to-band PL spectra, a direct bandgap semiconductor with gap E_g is used. In Ge, E_g is the energy gap between the heavy holes

$E_{\Gamma-\mathrm{hh}} = 0.7795$, and for the light holes $E_{\Gamma-\mathrm{lh}} = 0.7607$ [30]. Combining E_g in the joint density of states D,

$$D = \frac{2^{\frac{1}{2}}\mu^{\frac{3}{2}}}{\pi^2\hbar^3}(E - E_g)^{1/2}$$

and using the quasi-equilibrium distribution functions for electrons and holes, f_e and f_h, we can come with a solution to the shape of PL. Under low excitation f_e and f_h can be approximated to Boltzmann distribution $\propto \exp[-\frac{E}{kT}]$ [167]. Substituting into the emission rate of transition, it becomes,

$$I_{PL}(hv) \propto n^2\left(hv - E_g\right)^{\frac{1}{2}}\exp[-\frac{hv - E_g}{kT}]$$

where *hv* is the emitted photon energy, and *n* is the carrier density. As seen in figure Figure 90, the Ge PL emission follows normal Gaussian shape as other semiconductors. Ge PL has contributions from both direct band gap Γ and indirect band gap L. Total FWHM of Ge PL has to be considered as the sum of lh and hh interacting with Γ, and each changing differently with temperature.

Even though occupation of electrons is higher in L band, due to indirect recombination, the mechanism lifetime is longer than the direct recombination. The longer lifetime leads to smaller emission, as the radiative recombination has a relation of $1/\tau$. PL agrees with Γ having larger emission, hence, shorter lifetime. Studies on band-edge emission in Ge will differ from absorption experiments under different temperatures, as will be shown.

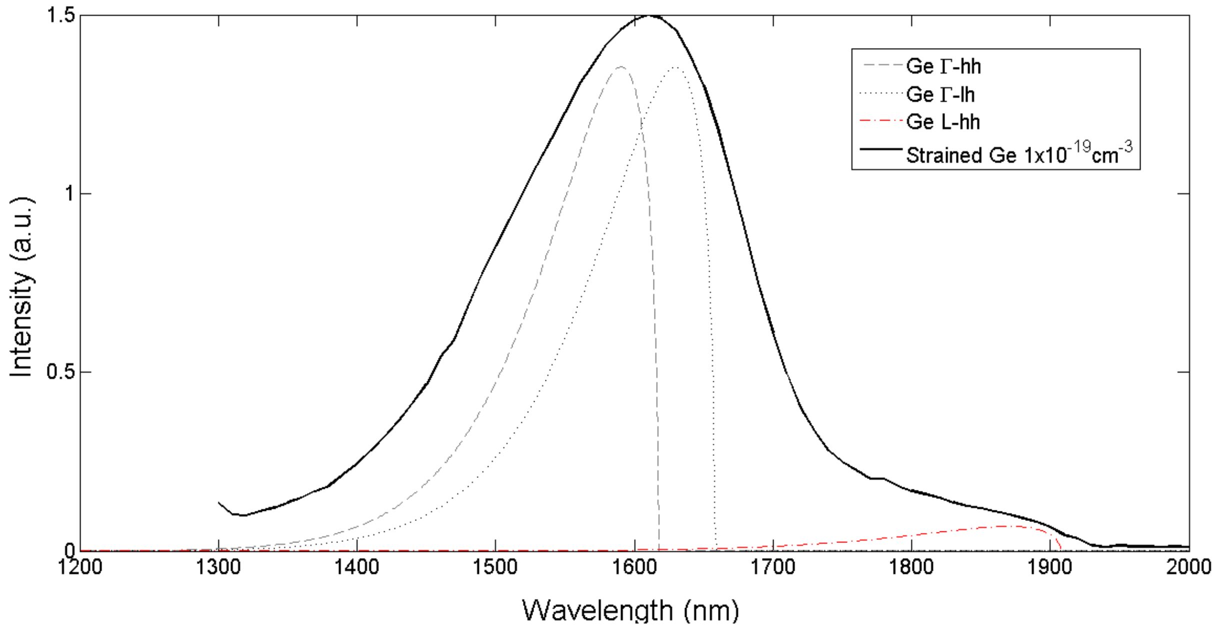

Figure 90.- Ge waveguide PL showing the shape of Ge emission at 300K.

The temperature dependence on the shape of emission is important since in semiconductors the temperature on chip remains ~ 60℃ [168] and locally up to 150℃. These high temperatures are not suitable for group III-V materials light emitters. Lattice and phonon scattering increase with temperature, increasing non-radiative recombinations. Ge increases in PL intensity with higher temperatures due to its unusual band gap energy structure.

Shifts on band gap energy have been studied on the indirect bap L, and empirical models have been developed, such as Varshni relation[153]

$$\Delta E = \alpha T^2/(T+\beta)$$

where α [eV/K]and β [K] are fitting parameters which in Ge intrinsic L-valley are 4.774x10^{-4}eV/K and 235 K, respectively. This expression relates Debye temperature from β, and the lattice bond energy from α. Varshni relation is weak at low-temperatures, and heavy doping; furthermore, it has been calculated through absorption only to L valley. The direct band Γ has not been calculated and electron-phonon interactions have been ignored. At high temperatures

electron-phonon and electron-electron interactions need to be considered. A relation describing the interactions for any semiconductors is described by

$$\Delta E = S < hv > [\coth\left(\frac{< hv >}{2kT}\right) - 1]$$

where S is a dimensionless coupling constant, and <*hv*>is an average phonon energy. This method describes more accurately describes the intravalley interactions between carrier-carrier interactions. Under any of these two formulas, an increase on temperature increases the band gap until saturation. Only in Ge BGN is accompanied by increase PL; other semiconductors non-radiative recombinations increase faster than the increase dependence with temperature. Since absorption is also temperature dependent, the mechanisms behind it rule the behavior of emission rate in most semiconductors.

Temperature increase changes as well the tensile strain on the Ge films. As grown, the Ge films possess an average biaxial strain of ~0.25%. This strain is reduced as the substrate temperature increases, as seen in Figure 91. The change in strain modifies the energy band gap in Γ, changing the emission photon wavelength. The reduction of biaxial strain with increasing temperature will shift the emission to shorter wavelengths. The theoretical blue shift under a change of 200˚C is of 25nm. Other effects counterbalance this blue shift, as will be shown.

As temperatures increases, other mechanisms could occur such as: lattice expansion, counteracting with strain causing blue shifting; Auger recombination, which increases at a rate of ~ $T^{3/2}$; and free carrier-absorption, which increases exponentially. Lattice expansion will be shown experimentally to not affect significantly. Auger recombination might interact under high temperatures, but under regular temperatures CCCH indirect Auger is the dominant mechanism. FCA was demonstrated by Wang, et al[57] to follow thermalization in the range observed in this experiment, hence not providing a source of loss.

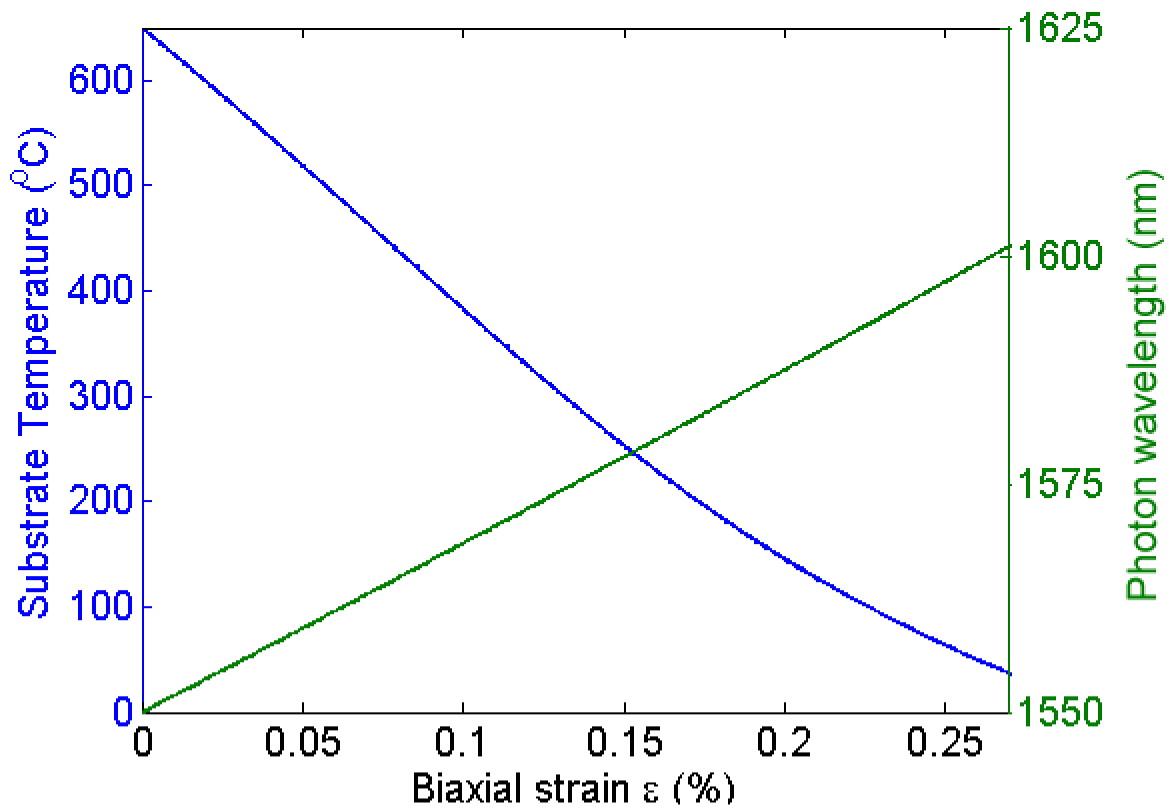

Figure 91.-Simulation of biaxial Strain change with substrate temperature and photon wavelength energy. As temperature increases, the bandgap increases, producing an effective blue shift in theory.

The reason for the higher emission in Ge is due to increase interactions between Γ and L valley. These interactions have been theorized, and usually are consider insignificant in bulk Ge. In heavily doped tensile strain Ge, due to closing in energies and the decreasing activation energy between the bands, effects such as impact ionization, carrier-phonon and carrier-carrier intervalley interaction become more important. Impact ionization occurs due to the increase of available ionized dopants. Phonon interactions increase due to increase in temperature. Carrier interactions increase due to the heavy doping and injection, being particularly important for laser operation. The importance of these multi-body interactions are shown.

5.2.2 Conduction Bands contribution

Intervalley phonon interactions are particular kind of phonon interactions that are, in Ge, $\Gamma - L$ or $\Gamma - \Delta$, being these valleys the three lowest energies, and the main contributors to emission. A brief description of these interactions was seen in Figure 89 (b).

In Ge, the phonon interactions are mainly lead through Longitudinal Acoustic (LA) and Optical (LO) phonons in $\Gamma - L$ [169]. The other interactions between valleys are transversal optical (TO), and acoustic (TA). Acoustic phonons are the most affected by strain in the system, and their interactions will be highly dependent on the direction of the stress [167]. The absorption and emission of phonons follow density of states with the energy of the observed phonon. It is observed that both emission and absorption of phonons is weak on Γ compared to L or Δ -due to the low effective mass of Γ electrons. This makes the interactions between phonons with Γ extremely weak in comparison to indirect bands, causing intervalley thermal scattering from indirect to direct bands. A similar effect has been observed as well in Si [170] where intervalley interactions caused by carrier-phonon and impurity scattering changes the mobility of the carriers.

The importance of intervalley phonon interaction is the intervalley scattering that occurs. It consists of a zone-edge phonon scattering an electron from a band minimum at the zone edge to another band minimum at the zone edge. The effect has been observed at high temperature (>300K) in other semiconductors [171].

The absorption can be increased or decreased in the Γ valley through addition of L or Δ valley electrons interacting with the phonons. As the temperature is increased more phonons are in the matrix, providing higher probability for intervalley scattering, which is beneficial in

Ge. Joint density of states can explain the number of carriers interacting with each other, and how they contribute to the phonon interaction.

The occupancy of states- electron density - on the bands is dependent on temperature, as described in the following equation,

$$n = \int_{E_c}^{\infty} \frac{2m_c(2m_r)^{\frac{1}{2}}}{2\pi^2\hbar^3}(E_p - E_{band})^{1/2} \frac{1}{\exp(\left(\frac{E_{band}}{2} + \frac{m_r}{m_c}\left(E_p - E_{band}\right) - E_{fc}\right)/kT) + 1} dE$$

where $1/m_r=1/m_c+1/m_v$, E_{band} is the energy gap between chosen conduction band and valence band; E_{fc} is the conduction band quasi-fermi level; E_p is the energy of the wavelength *hv*. The last term of the equation comes from the Fermi-Dirac distribution, related to the distribution of the electrons on the conduction bands, those being Γ, L or Δ valley. As the temperature increases, the dopants become more available in the bands due to thermalization of the carriers and available states. Interestingly, the free electron distribution increases faster in the indirect bands than in the direct band due to the low effective mass of electrons in the Γ valley. Results of these calculations can be seen in Figure 92. The Δ valley becomes degenerate at ~$1x10^{18}$, at temperatures around 450K, using Pankove’s expression [44] for degeneracy. The calculation is an approximation assuming X valley is identical in behavior to Δ valley, and using the degeneracy of 4, assuming the biaxial stress only contributes positively to 4 of the 6 points of symmetry on the k-space (100). Importantly, the free electron density does not explain the step increase in PL on Ge, and shows that even under high temperatures, the effect of temperature on Γ is at the minimum. The effect causes indirect bands contributions of carriers on Γ valley.

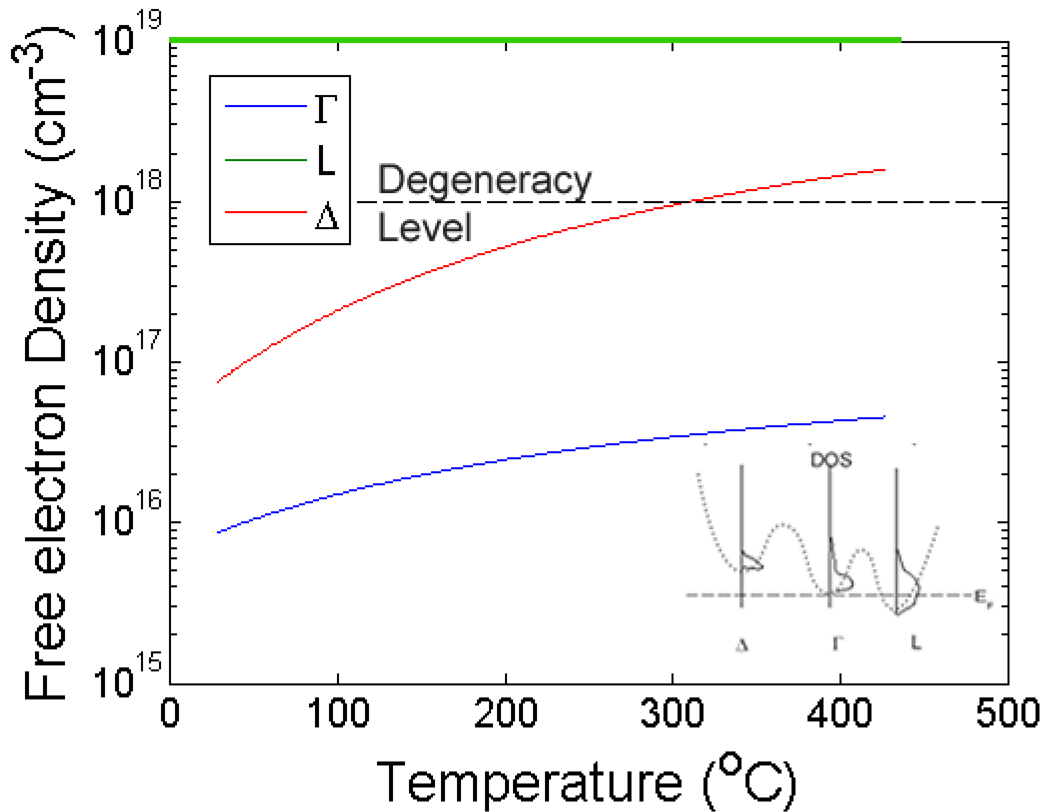

Figure 92.- Theoretical calculation comparing free electron density to temperature on the different conduction bands. As the temperature increases, the redistribution of electrons increases on the different conduction bands, achieving degeneracy on the Δ band.

Contributions of carriers to Γ require surpassing the activation energy in between bands, E_a, as depicted in Figure 93. E_a is the energy difference between the band-edge of CB and the Fermi Level. Phonon absorption in Ge is high at temperatures above 300K [150], assuming an unlimited source. E_a is dependent on the initial Fermi energy, E_F, which depends with the doping concentration, as has been explained. For E_a L-Γ was to be 0.102eV, as seen in Figure 93. This was observed as well in our measurements, and we found E_a ~0.120, 0.101 and 0.74 eV at dopant concentrations: intrinsic, ~1x10^{19} and ~3.5x10^{19}cm^{-3} respectively. These

correspond to the increase in Fermi level, as depicted. Furthermore, the activation energy is of the order of Indirect Auger recombination allowing for increase PL, as explained in Chapter 2.

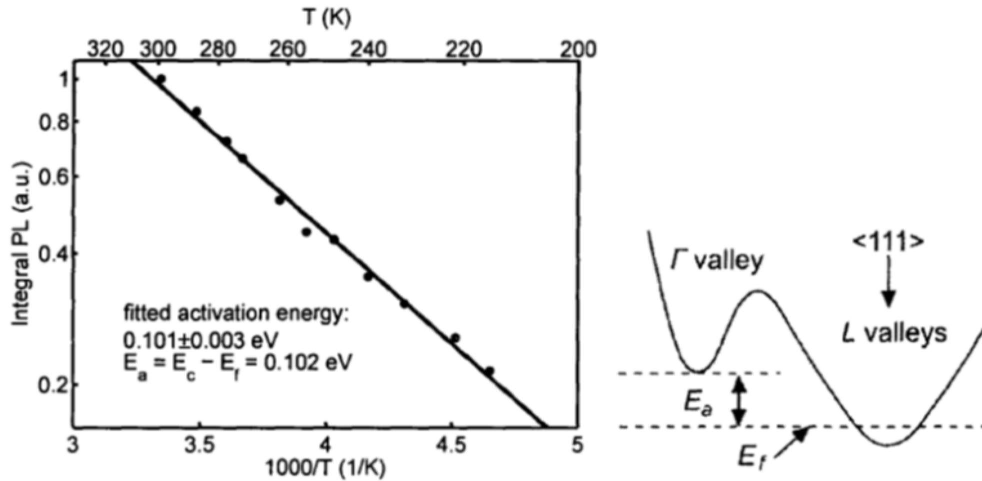

Figure 93.- Comparison of integral PL intensity respect to temperature on n+Ge tensile strained at ~1x$10^{19}$$cm^{-3}$. An activation energy of ~0.102eV corresponds to Arrhenius calculations. [27]

In order to understand this mechanism, a temperature dependent PL study was performed in Ge substrates with 0.2% tensile strained and under different doping conditions. The temperature spectra range covered 120-730K to explore the spectrum of band gap interactions. In order to understand the temperature contributions, edge information for Γ valley from peak and integrated PL intensity was extracted. The former was used to explain the band-edge behavior. The latter was used to explain r^{spon} behavior and band-to-band transitions.

5.2.3 Experimental Results

PL was performed with Horiba MicroPL with photoexcitation at 1064nm under an Instec hot stage temperature control above 400°C. The detector cutoff is ~ 2000nm, and the responsivity of the detector was taken into account in the measurements ranging from 1400-1900nm. Figure 94 shows the characteristic emission of Ge under two different dopings at high temperatures.

Under temperature and wavelength detection range chosen, PL information is presumed to portray accurately the behavior of the Ge direct band edge.

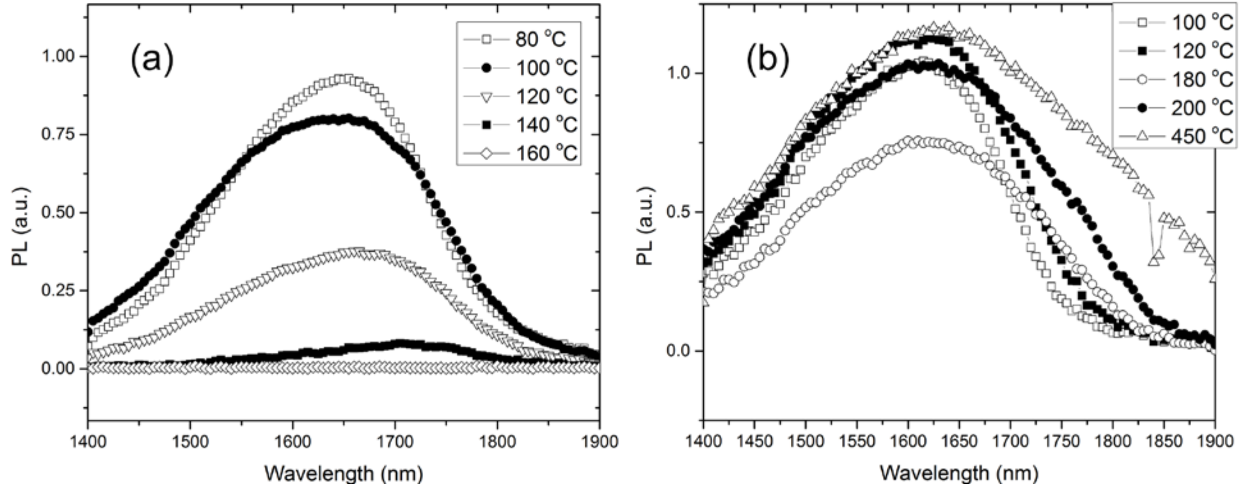

Figure 94.- PL at high temperatures of Ge n+type (a) ~3.5x10^{19}cm^{-3} and (b) ~1x10^{19}cm^{-3}.

A relation between the peak emissions, the integrated intensity and the temperature is shown in Figure 95. The peak emission is almost independent of the dopant concentration in a regime between 200-400K, $\frac{\partial E_{g\Gamma}}{\partial T} \sim 2.05 \times 10^{-4} eV/K$, which has been observed previously [150]. It was observed to be smaller than the standard ~4 x 10^{-4} eV/K in this temperature range [172]. This difference was thought to be due to the increased thermally induced tensile strain in Ge upon cooling, reducing the band gap to partially compensate the temperature-induced energy gap increase. The discrepancy comes at higher or lower temperatures. In both cases $\frac{\partial E_{g\Gamma}}{\partial T}$ is larger than what was previously known. The experiment suggests stronger contributions of both $\Gamma \leftarrow L$ -phonons intervalley interactions.

The plateau occurs since Γ electron density remains constant, avoiding shrinkage. This comes from carriers exchanging as $\Gamma \rightarrow \Delta$, occupying the states. As temperature increases,

Γ ⇠ Δ restarts since the free electron density on Γ changes slowly with temperature, while Δ increases faster as was seen. In order to confirm this effect, the integral intensity of each state has to be analyzed. Furthermore, indirect CCCH Auger recombination works as well in Δ.

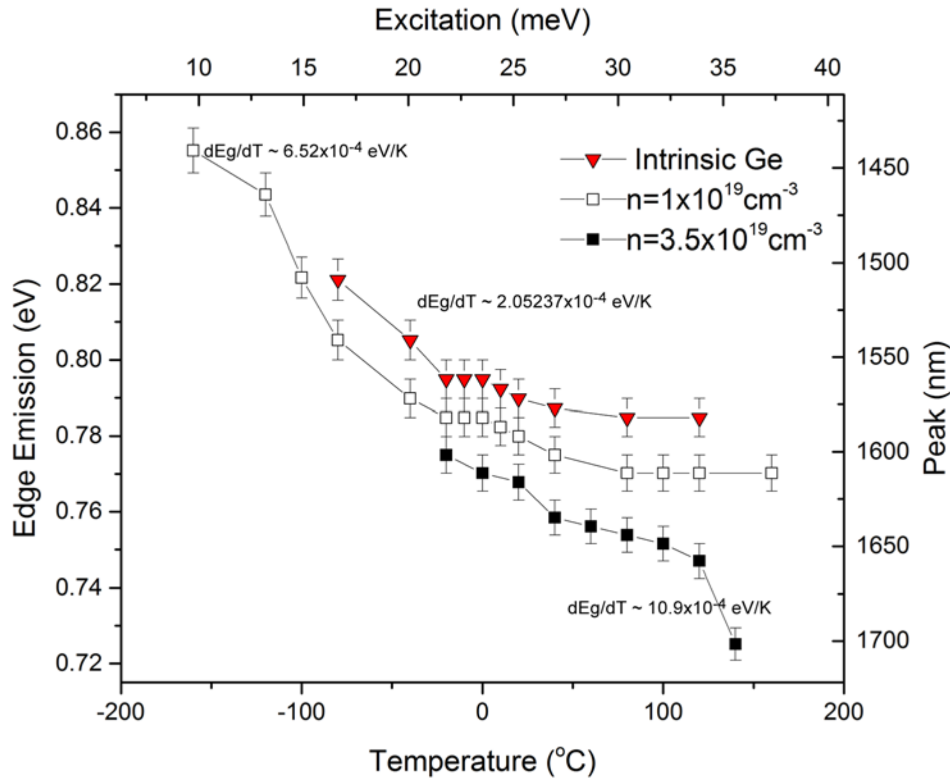

Figure 95.-Peak energy representing of $\boldsymbol{E_{g\Gamma}}$ versus temperature of observed PL. There are three regimes observed corresponding to the different points of L and Δ interactions.

Auger recombination increases as temperatures increases, and heavily doped material is known to be more susceptible to the loss of emission due to it. As demonstrated in chapter 2, CCCH Auger recombination does occur in an indirect way. In both L and Δ occur, at lower energies than direct Auger recombinations, having energy thresholds equivalent to $\mathrm{E}_{th} = 0.0299$ and 0.0364eV, respectively. This permits increase in emission with increase temperature since more carriers are available in the direct band. Both transitions require a minimum energy for activation, that being at ~350K and ~425K. Edge emission measurements

show increase in band gap shrinkage, suggesting that the mechanisms are in play. From integral PL the effects of both mechanisms on radiative recombination are observed.

When comparing different temperatures integral PL versus peak emission, it can be seen that the shift of peak emission matches the PL emission, as seen in Figure 96. On an intrinsic strained Ge, BGN is slightly seen, and contribution of carriers plateau ~400K or 120℃, corresponding to Auger CCCH energy. BGN is difficult to see since the material is not degenerate and requires filling L valley before contributing heavier to Γ. The matching trend matches that LA phonons are interacting for intervalley interaction between $L \dashrightarrow \Gamma$. If the contribution was to happen on opposite direction, the band would not narrow, hence no peak shift; and the emission integral would decrease.

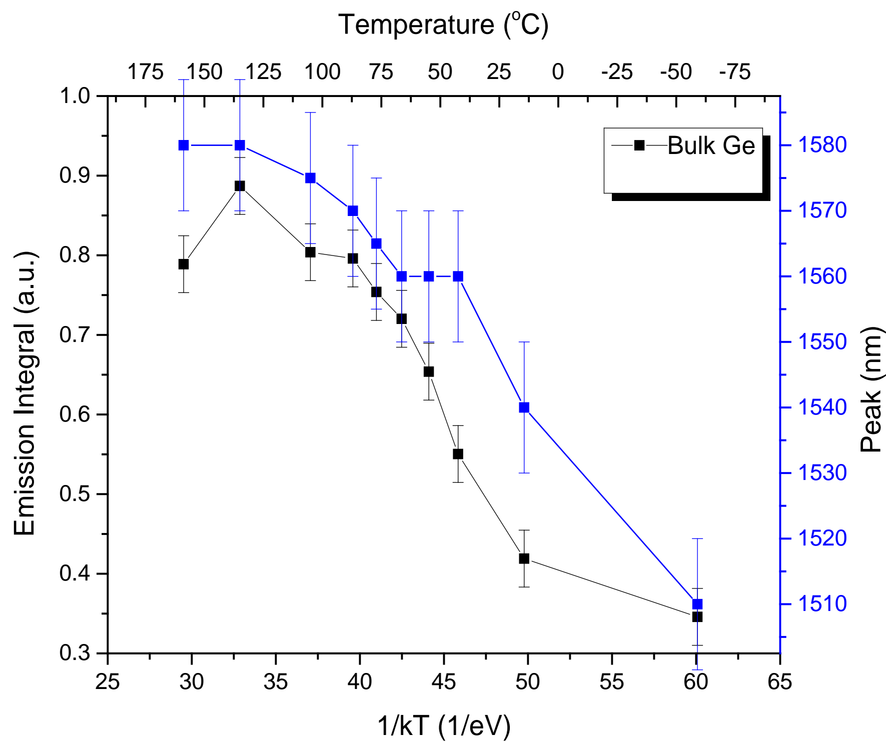

Figure 96.- Integral PL and Peak energy plots against 1/kT of undoped strained Ge. Increase in PL and edge emission show both **Γ** BGN and L –valley contribution on **Γ.**

The dopant concentration has the major role on differences between Ge light emission. As the bands fill at different dopant concentrations, available carriers are more or less readily for interactions. As the dopant concentration increases, the Fermi level increases as well, as the non-radiative transitions. It is known that with increasing dopant concentration, the PL intensity increases, due to the increase of available carriers in Γ valley. The trend is observed, but the beneficial effect of temperature decreases with increasing doping after $1x10^{19}cm^{-3}$, as seen in Figure 97. At heavier doping, as with ~$3.5x10^{19}cm^{-3}$, after ~393 K a clear decrease in integral emission is observed. This is expected since the Fermi level is higher, and the energy required to have $\Gamma - \Delta$ intervalley interactions is decreased. The carriers from Γ contribute more readily to the Δ valley. Moreover, the increase in Γ BGN considers lattice expansion, and decrease of L carrier contribution.

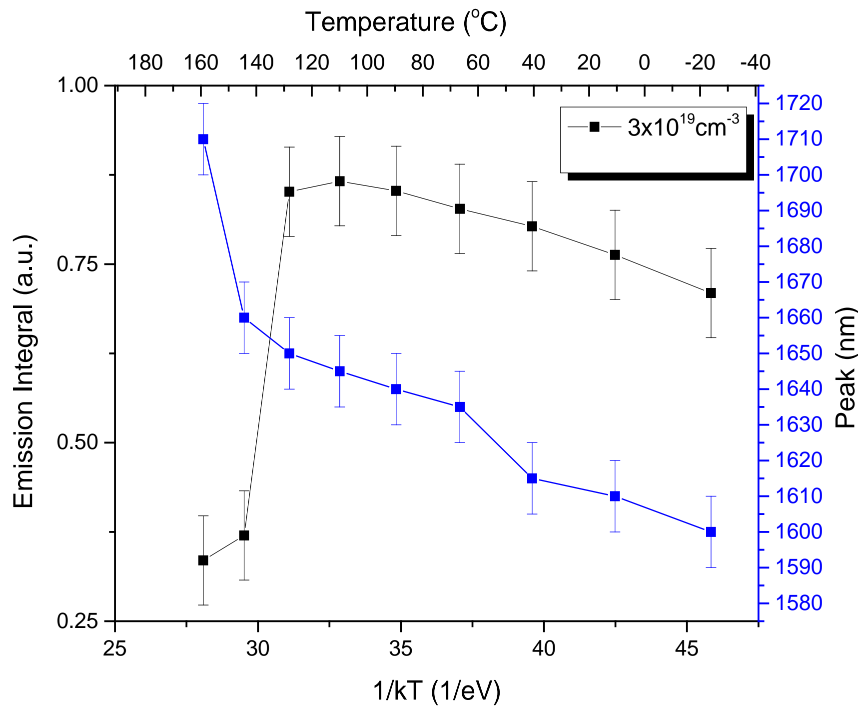

Figure 97.- Integral PL and Peak energy plots against 1/kT of degenerate doped strained Ge. Increase in PL and edge emission show both Γ BGN and L –valley contribution on Γ.

Degenerate doping shows a larger BGN in the peak emission and faster drop in emission with increase in temperature.

Using the standard condition of ~1x10^{19}cm^{-3} dopant concentration, and observing the peak shift, a trend is noted. As seen in Figure 98, the values for $\frac{\partial E_{g\Gamma}}{\partial T}$ are about -1.64x10^{-4}eV/K and -1.88x10^{-5} eV/K. It suggests that the intervalley interaction when L→ Γ and Δ→ Γ is stronger, they become ~ - 1.5-2x10^{-4}eV/K. This trends matched observations for Γ and L [150] , and suggest the present of electron-phonon interactions in the total lattice. It was seen as well, that the presence of lattice expansion has little to no effect on the contribution under non degeneracy of dopants in Γ.

When the interaction is L→ Δ or Γ → Δ , it is more likely to decrease the peak shift, since available carriers are more readily interacting into the Δ valley. This happens since the overlapped density of states observed empty states on Δ valley, making it a thermodynamically stable transfer of energy. Moreover, the mechanisms of thermalization are competing with Auger CCCH transitions, which are less probable to occur at Δ valley at low temperatures, due to low density of states and available carriers in Δ. As temperature increases, all CCCH transitions contribute to radiative recombination by contributing carriers to Γ valley. This is a suggested mechanism but further research is needed to understand such mechanisms.

The shifts on energy show that lattice expansion never occurs without contribution from another band, as was the case in degenerate doped Ge. The important point of these results is that Ge can emit light, potentially increase on gain, well over temperatures >600K. Ge lasers benefit from these interactions by utilizing both the temperature effects noted, BGN and BGR. The latter will be treated in further chapters.

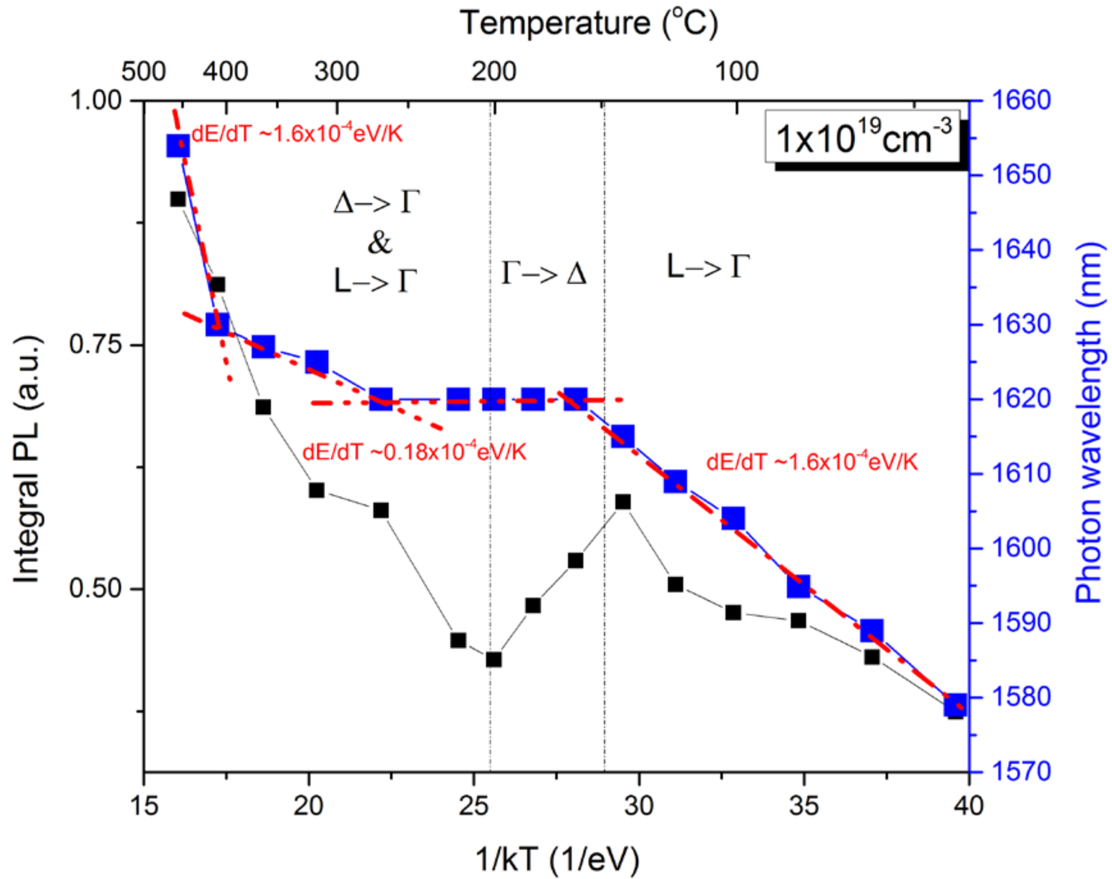

Figure 98.- Peak energy of n+Ge ~1x10^{19}cm^{-3} at high temperatures different regimes exist at high temperatures.

5.2.4 Conclusions

In summary the effects observed over the band can be divided in 4 regimes:

1) $L \to \Gamma$ Interaction where LA phonons contribute to electron-phonon interactions and intervalley exchanges between the bands. Furthermore, overlap of unoccupied density of states of Γ with filled L band permits a thermodynamically stable exchange. Increase in BGN Γ proves this trend.

2) $\Gamma \to \Delta$ or $L \to \Delta$ due to overlap of density of states under same reasoning. Decrease in PL and saturation of BGN Γ proof that both conditions might be occurring at

once. The nonradiative recombinations, such as direct Auger recombinations, decrease PL, as the temperature is high enough for activation

3) $\Delta \rightarrow \Gamma$ and $L \rightarrow \Gamma$ interactions increase, as the energy required for activation is reach. As the difference in activation energy $E_{\Gamma} - E_{\Delta}$ increases, PL increases and BGN Γ increases.

4) Γ Free carrier excitation contribution through excitation temperature increases exponentially through Fermi-statistics and BGN Γ increases exponentially until saturation.

It is suggested that electron-phonon/electron-electron – thermalization and Auger recombination- interactions keep contributing to Ge radiative recombinations under high temperatures through intervalley scattering. The shift on peak energy shows the change on band tail due to thermal expansion and the existence of plateau proof the multi-body interactions reducing the positive effect. Further studies are necessary to understand the activation energy, and the gain contribution of temperature and increase dopant.

Chapter 6. pnn Ge LED

It is demonstrated functional Ge on Si LEDs, in the form of FP cavities, hence, polished waveguides. The structure tested was selected for simplicity and to allow the greatest surface area to be exposed. The enhanced surface area permits an analysis on the upper and lateral facets of the devices. This chapter is divided into low Ge n-type doping ($<1x10^{19}cm^{-3}$) and high n-type doping ($>1x10^{19}cm^{-3}$). It is demonstrated that the enhancement on doping permits to reach bleaching on the devices.

First, the theory behind the low doping Ge LEDs is covered, and the difficulties on processing. After the electric and optical characteristics of these devices are shown and how they perform as diodes, lateral and upper light emission is demonstrated.

Finally, the advantage of using a highly doped n-type substrate and low temperature Si deposition to avoid dopant outdiffusion is presented. The highly doped devices show better emission and a stronger BGN. Through pulsed current, reduced degradation of the metal contacts is demonstrated. The temperature effect matches normal performance of high current injection on lasers. It is demonstrated the onset of bleaching and hot carriers proved aiding the recombination.

This chapter presents the work performed to achieve the electrically pumped Ge laser, as it follows similar principles.

6.1 Introduction

In order to fulfill a totally integrated laser on chip, electrical pumping on chip is necessary. To achieve such task, Ge-on-Si light emitting diodes (LED) where designed. Hence, electroluminescence (EL) through pnn-heterostructures has been explored, and LED behavior

characterized. The pseudo-direct band gap of Ge allows a more efficient radiative recombination, than expected from its counterpart in bulk, non-strain and non-doped format. EL results from spontaneous radiative recombination, and has a linear relation to the doping concentration. Through this process, we can relate the total injected carriers of both electrons, Δn, and holes, Δp. The photon flux, or intensity, expected has to have the form,

$$\Phi = \eta_i \frac{V \Delta n}{\tau_r}$$

where η_i is the internal quantum efficiency, V is the volume, and τ_r is the radiative lifetime of the carriers which is <10^{-10}s observed from previous theories [26]. The linearity of the photon flux can be confirmed through our EL experiments. Ge-η_i was observed in previous work[173] showing Ge pnn structure capable of achieving 10% external quantum efficiencies, η_e . The efficiency is limited by the injection from Si to Ge contacts, and the confinement of the barrier from p-Si contact. The confinement prevents a large leakage current, and an effective high current density on the device. Alignment of lower energy bands under heavy doping becomes the most important constrain improving the efficiency, as will be shown.

The internal efficiencies will be dependent primarily in the Ge core doping concentration. As the doping concentration increases, Ge Γ valley presents more radiative recombination. Both efficiencies, η_e and η_i, depend in the total number of carriers passing the Si/Ge junction, explaining the concern with high crystal quality and minimum boundary mismatch. Notice that η_i depends on doping, temperature and defect concentration of the material since it shows the electron-to-photon transducer capacity of the material.

Double-heterojunction, as will be shown, provides an improved carrier confinement and provides the higher carrier densities required for an efficient injection. Since the devices are using single crystal Si for substrate and poly-Si as an upper contact, other adverse effects have

to be considered. Both contacts are heavily doped, and causing an increment in absorption in both contacts. Furthermore, the contacts under heavy carrier injection will diverge from their established index of refraction. The increment in absorption has adverse effects on the allowed possible modes, reducing to a maximum of 7 modes with losses up to $900cm^{-1}$, with x-z dimensions 800x1000nm waveguide. The increase in losses makes the device unsuitable for lasing, as will be shown. Doping and carrier injection, as was noted in Chapter 2, are the main limits for net gain.

The doping is reduced through appropriate control of annealing temperatures and increment of deposition temperatures, as shown in the following sections. The doping concentration is $3\text{-}7x10^{18}cm^{-3}$, reducing to a fraction of the original doping of $1x10^{19}cm^{-3}$. Nevertheless, as confirmed in Figure 99, the pnn diode provided enough confinement for spontaneous emission, and appropriate injection of carriers. Moreover, as the dopant concentration increased, signs of bleaching were observed. Each of these details is covered on detail in the following sections.

The work is divided in the two main ranges:

- Doping concentration $<1x10^{19}cm^{-3}$:
    - Diode I-V behavior with resistance as low as 5ohms.
    - Diode electroluminescence from all directions.
    - Outdiffusion of dopants through high temperatures during processing
- Doping concentration $>1x10^{19}cm^{-3}$
    - Delta-doping for electrical devices
    - N-type Si substrate maintains total doping post-processing to $>1x10^{19}cm^{-3}$
    - Diode I-V behavior of highly doped materials, showing lower resistivity

- Temperature effects calculated with an impedance ~27W/K.
- Non-linear effects, as hot carriers, confirmed
- First demonstration of bleaching on electrically pumped Ge
- Identify flaws for Laser LD

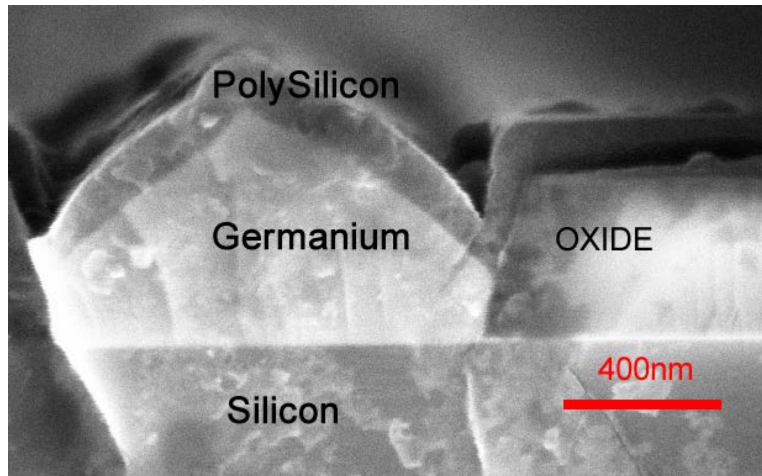

Figure 99.- Si/Ge/Si pnn heterojunction LED migrograph cross section showing all the elements of the device.

6.2 Low doped Ge-LED <1x10^{19}cm^{-3}

LEDs were design with *in situ* P doping 1x10^{19}cm^{-3}.The behavior of these devices and the effective active doping concentration is discussed in this section. It is shown that the lower emission is dependent to the doping concentration, and no evidence of BGN permits to determine doping concentration below growth conditions. In this section, we explored the behavior of the pnn Ge LED made and the overall electrical and optical efficiency.

6.2.1 Materials Preparation

Starting with a p+Si substrate 6"(100) with an edge perpendicular to (110), a thin film wet oxide was grown ~ 400nm. Boron doping concentration was $1x10^{20}cm^{-3}$. Photolithography defined the oxide trench. n+Ge was grown on the oxide trenches with single crystallinity and defect concentration ~mid-$10^{8}cm^{-2}$ dislocation density, and *in situ* doped, as described in Chapters 3 and 4. No further anneals were explored to avoid the loss of doping through outdiffusion. For more details on the deposition procedure, please refer to Appendix.

Ge waveguides were treated with Ge-RCA, to avoid any secondary contaminants in between processing steps. For details on RCA bath, refer to Appendix. Ge waveguides were covered with a-Si grown at 560°C for 2hrs through low-pressure chemical vapor deposition (LPCVD). The technique has the advantage of covering uniformly through the entire sample and avoiding electrical shortages. The thickness of the a-Si was measured ~180nm. LPCVD technique has the disadvantage of a peak temperature of 620°C for 5 min in the initial steps, to remove native oxides with H_2 flow. Amorphous material has poor conductivity and no-doping, requiring an implantation procedure with P.

Implantation of the a-Si layer was predicted through a Monte Carlo Simulation tool, SRIM/TRIM, that predicts the implantation damage, lateral straggle, and depth of implantation. As seen in Figure 100, the simulation predicted with a 50keV, 7 degrees inclination, and a dose of ~$1x10^{16}$ for the donor dopant, P, the material would be thoroughly implanted. Substituting in the equations used in Chapter 4, we obtained a total dopant concentration of >~$1x10^{20}cm^{-3}$. Implantation process was executed by Innovion, Corp.

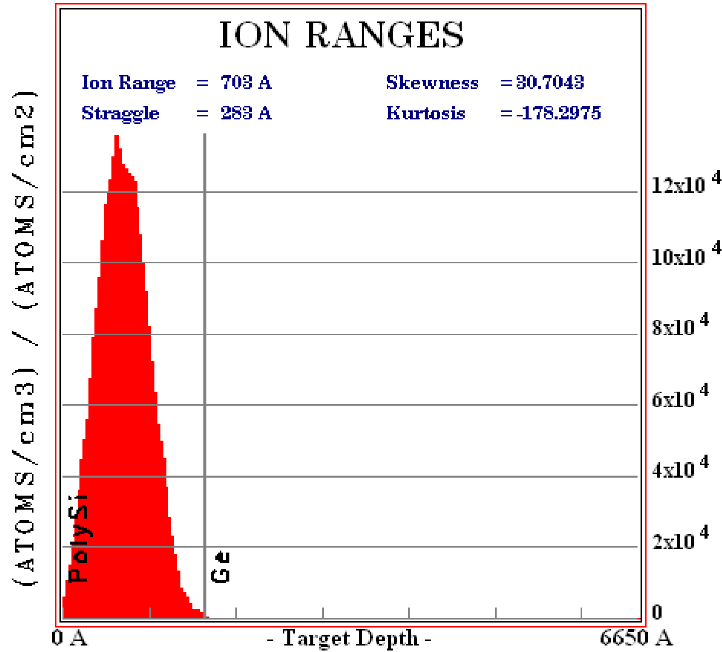

Figure 100.- Monte Carlo Simulation of implanted poly-Si with P at 50keV, dose of $1x10^{16}$ and 7 degrees angle.

The resulting sample was further annealed to activate the dopants and change the structure from a-Si to poly-Si. Annealing step was divided in temperature and time, due to the importance in the outdiffusion and redistribution of the dopants. It was determined that under our conditions the minimum temperature required was ~685±5°C, and a minimum time of 30 seconds. For full activation of the dopants, the temperature required is 700°C with 30 seconds. Poly-Si grain size and surface diffusion is left for future studies.

Poly-Si was photolithographically defined to expose the oxide. Metal was further on deposited through metal sputtering using Applied Materials Endura tool. The metals of choice were Ti, Ti/Al, and TiN/Al. The metals were selected since they are standards on the CMOS technology industry and their availability during process. It was important to deposit the metals immediately after activation and cleaning of the surface had been performed to avoid any oxide

formation in the poly-Si surface. This would reduce the total resistivity from the contacts and allow for better injection of carriers.

The devices were characterized through fiber coupling while being injected through bottom and upper contacts, as described in Figure 101. The injection point is through a W-tip of $50\mu m$ diameter and substrate connected to the current. The devices were measured through optical diodes for power emission and through OSA spectrometer to determine the PL emission.

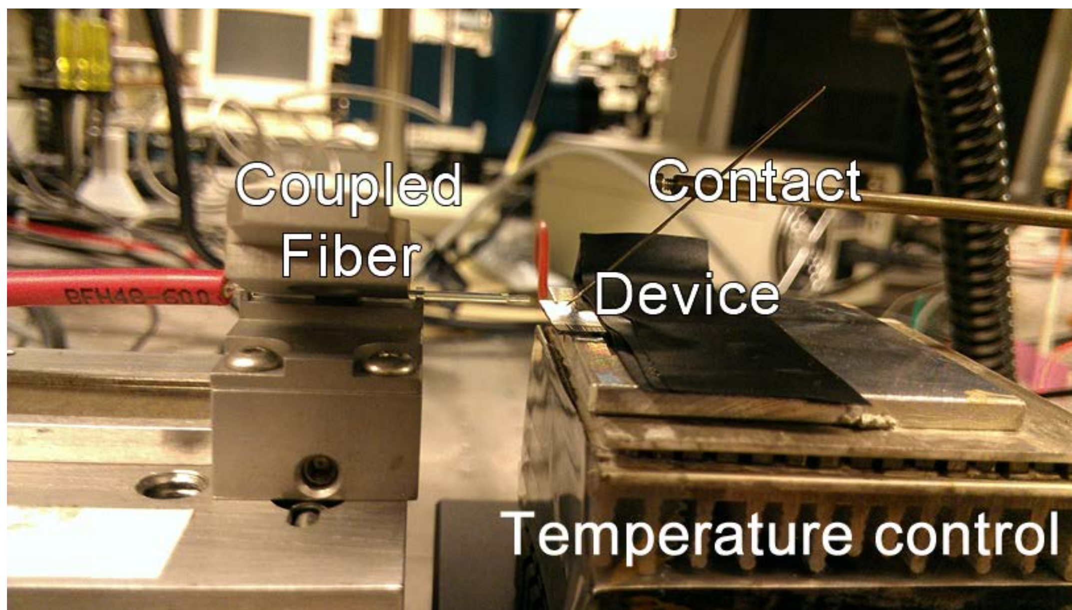

Figure 101.-Device setup for characterizing through fiber coupling.

The devices presented LED optical and electrical behavior. To determine their response, characterization was performed, as well, in the upper surface. As depicted in Figure 102, the fiber couples were in both directions to determine the response of the devices.

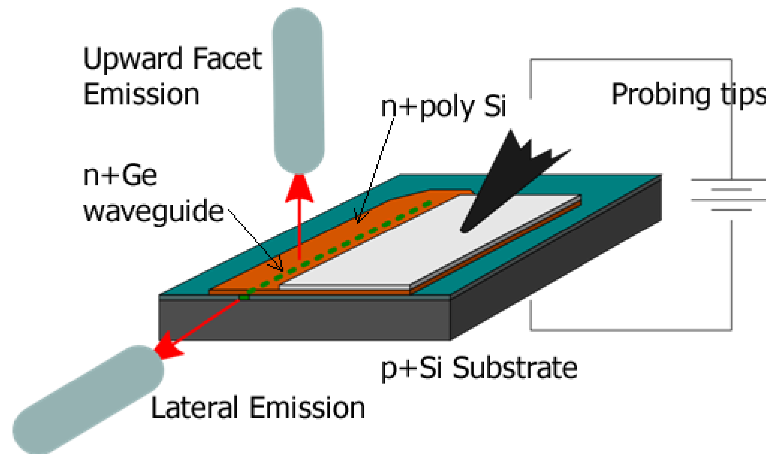

Figure 102.- Experimental setup diagram to determine the emission characteristics and behavior of the devices. (Courtesy from J. Bessette)

In the following sections the results are described, and the devices analyzed.

6.2.2. Post-growth temperatures effect

Ge has a fast diffusion constant. The speed of diffusion of most n-type dopants in Ge is orders of magnitude higher than those of Si. Post-growth processing showed to increase above 580°C. At growth temperatures, 650°C, D_{Ge}~10^{-3}-10^{-5} cm^2/s and D_{Si} ~$7.6x10^{-20}$ [174]. The disparity in diffusion permits Ge dopant to get displaced to the boundaries. Growth time constrains are limited to the final thickness desired and preparation of the chamber. Both steps add to a 90 minutes process minimum with temperatures allowing P outdiffusion in Ge boundaries. As seen in Figure 103, SIMS confirms the loss of dopants. The dopant loss can be identified in both the Ge buffer and the body of n+Ge. The former has been explained in Chapter 3. The latter is confirmation of the dopant loss during processing.

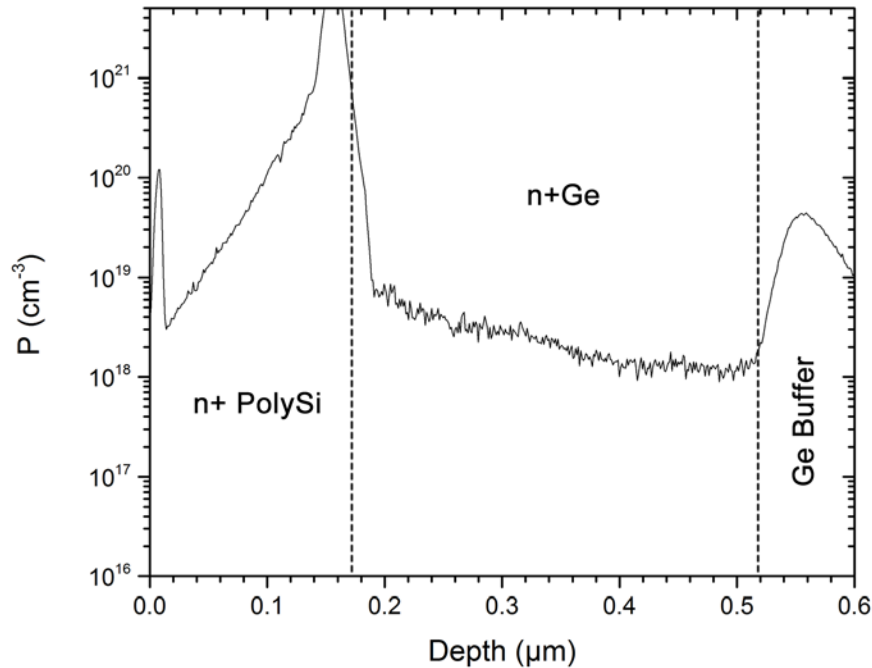

Figure 103.-Ge pnn-low doped SIMS analysis. Processing post-growth temperatures increase affects the overall device quality due to dopant loss. Both buffer and upper layer lose dopant. The buffer acts like a sink, as mentioned. The upper layer deposition temperature (<580°C) is high enough to lose the dopant concentration.

A secondary effect not expected was the dopant distribution that prevents proper behavior of the dopants. The dopant concentration difference prevents from loss Electrical effects of the device response. This will be shown in the following section.

6.2.3 I-V Diode Characteristic of Low doped-Ge

I-V characteristic in LEDS have normal pnn behavior after injection. As seen in Figure 104, the I-V characteristics show normal diode behavior under forward and reverse bias. It shows a resistance like,

$$\frac{\partial V}{\partial I} \sim 10 \pm 4\Omega$$

with 4 Ω intrinsic from the measurement setup. The current density, J, can also be expressed in heterojunctions as,

$$J = J_0[exp\left(\frac{qV}{kT}\right) - 1]$$

where J_0 is a variable dependent on temperature which includes the working function between Si-Ge contacts, ~ 9.24x10^{15}A/cm^2. It can be seen that the structure follows perfectly the diode behavior. The diode was made with Ti-Al contacts. Similar pnn devices with half the doping were fabricated and showed an increase on resistance of one magnitude, ~100 Ω. It permits a fast way of determining the dopant concentration of the devices.

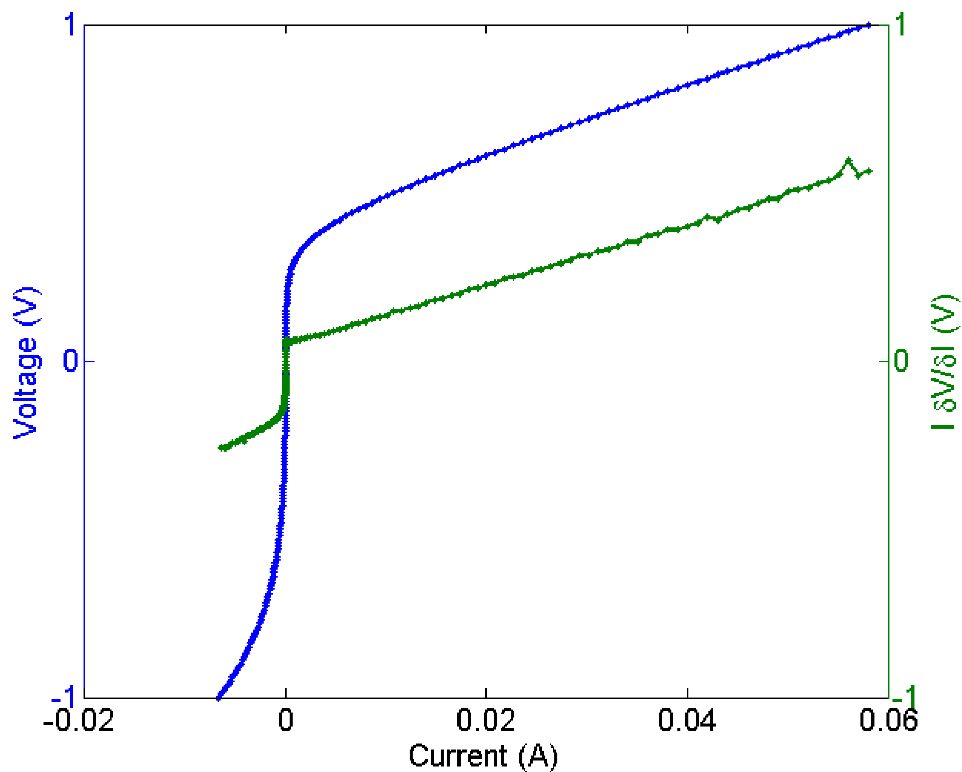

Figure 104.- I-V characteristics of low doped diode ~7x$10^{18}$$cm^{-3}$

The other outcome to consider was how the metal behaved under continuous current conditions. For that the mean time to failure for the metal layer can be calculated with Black's formula,

$$ttf_x = A_x w t J^{-n} e^{(\frac{E_a}{kT})}$$

Where A_x is a constant that for Al is 3x10^{12}-1.5x10^{14}, w and t are the dimensions of the contact, n is the current density exponent 1-3, and E_a is the activation energy of diffusion that for Al is 0.4-0.6eV. It calculates that ttfx is around 1hrs under continuous operation and 100mA. Due to the concentration of current density of Ge surface, electromigration can decrease to only >10min under same current. This change in ttfx can be seen in Figure 105, where the electromigration stop the device. The currents used during this electromigration are of <30kA/cm^2 on the upper point of the Ge contact.

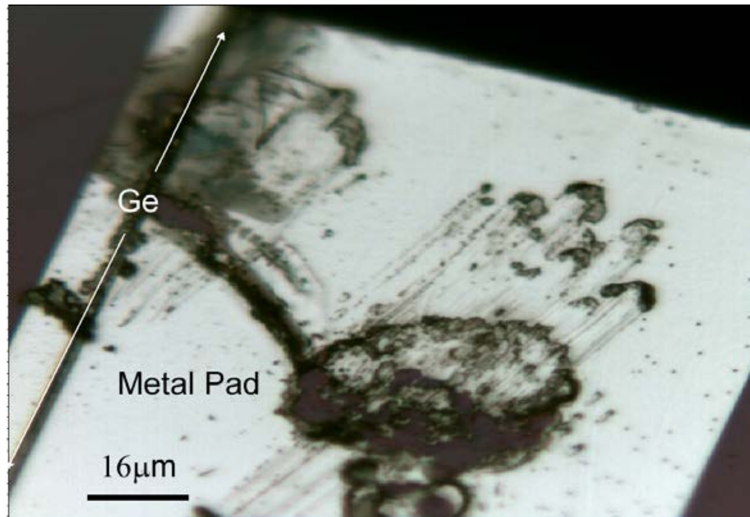

Figure 105.- Ge pnn Metal pads damage. It is theorized due to electromigration. (Courtesy from J. Bessette)

Even though the performance of the first generation devices was not optimal, the devices showed appropriate PL emission, as it is shown in further sections.

6.2.4 Photoluminescence and Electroluminescence of low doped-Ge

Emission of the devices was characterized through three different core fibers to identify the optimal core for coupling. As seen in

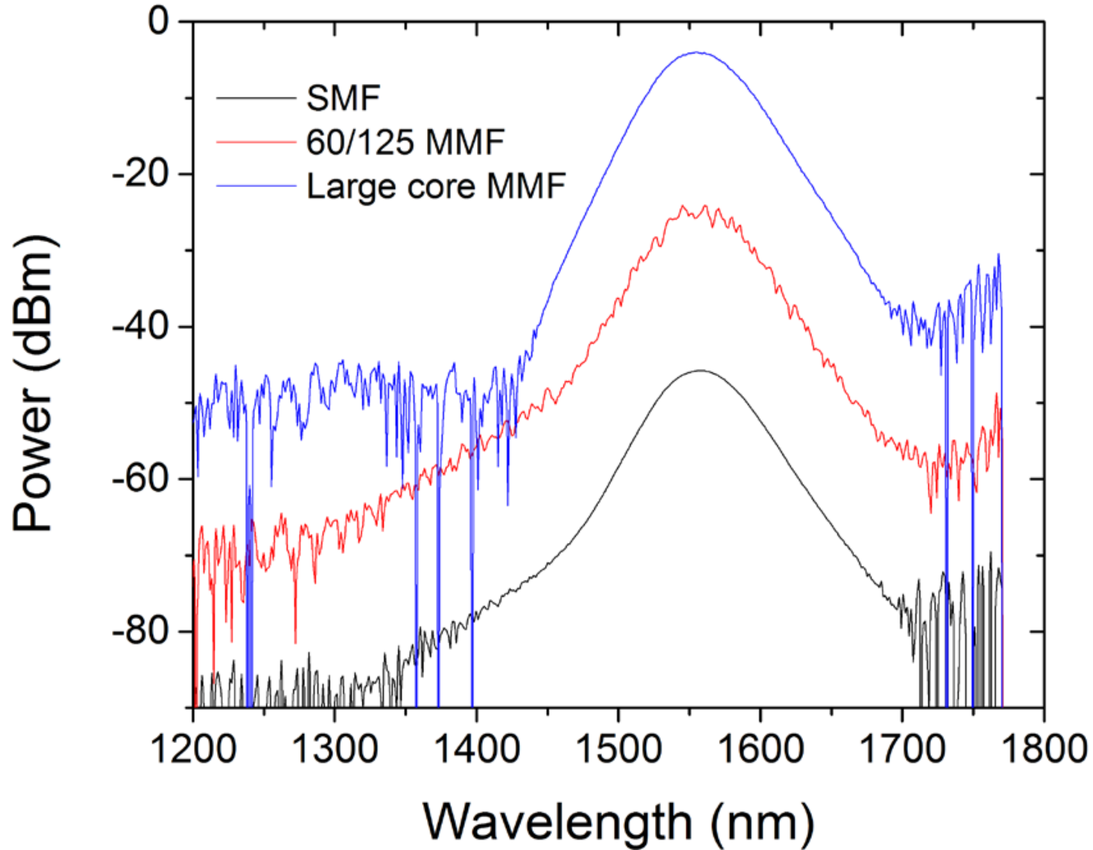

Figure 106, fiber coupling showed to be insignificant in emission change. To increase the alignment and prevent non-linear effects, multi-mode fiber (MMF) large core was used. Single-mode fiber (SMF) has the disadvantage of cutting off the light, and portrays a cleaner signal, when in reality it is not. Hence, electroluminescence was measured using a MMF coupled to an optical spectral analyzer.

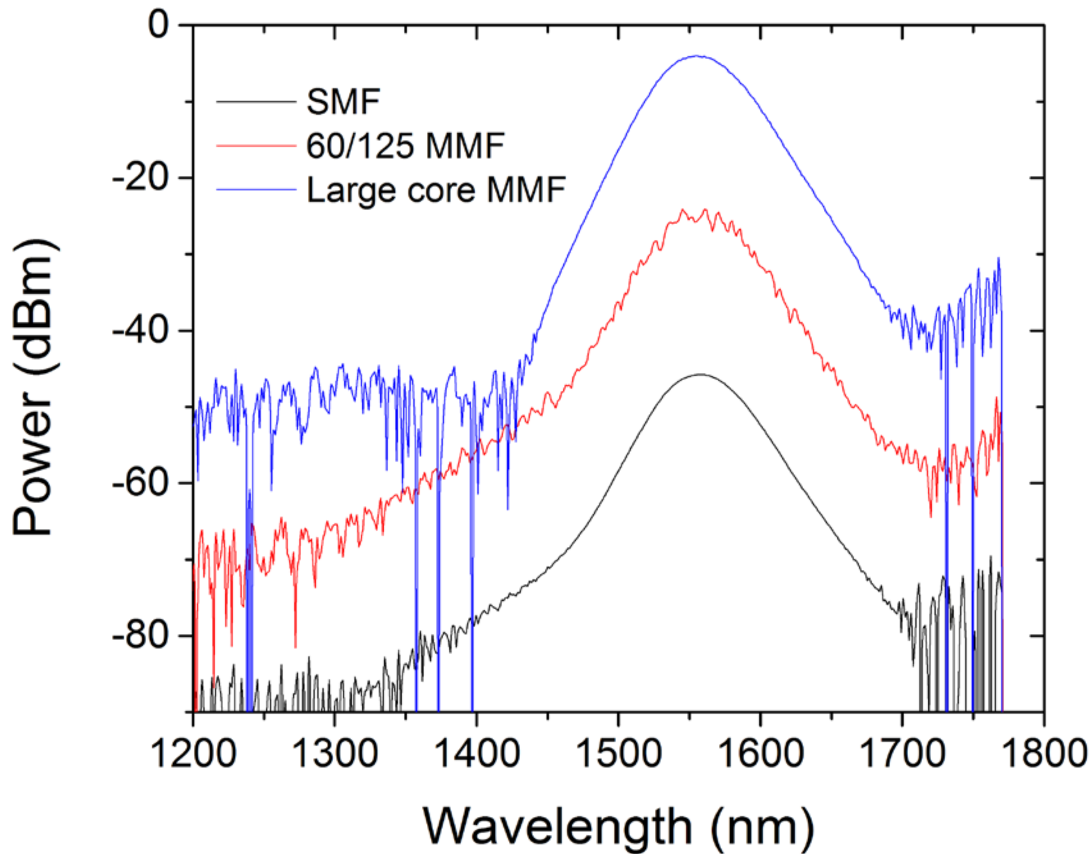

Figure 106.- Fiber coupling through different waveguides. (Courtesy of J.Bessette)

The spectral width, $\Delta\lambda$, was ~95nm from

$$\Delta\lambda \approx 1.45\lambda_p^2 kT$$

where λ_p is the emission peak corresponding to the band-edge of Γ to HH and LH. The spectral width matches well with the measuring temperature and with the measurements. As $\Delta\lambda$ increases, the temperature is expected to increase. Furthermore, the contribution of both HH and LH expands $\Delta\lambda$ which its valence band contribution, as seen in Chapter 5. A measurement of the device establishes $\Delta\lambda$ ~150nm, showing that the contribution is asymmetrical. FHWM, which should be identical to $\Delta\lambda$, is the normalized variable employed to determine extraneous effects due to temperature or carriers redistribution.

Since the waveguide design serves as a template for a diode laser, emission from the edge of a cleaved facet was of particular interest. Figure 107 shows EL spectra as a function of increasing diode bias, V. The spectrum shows the evolution of the spectrum under heavy current. It can be seen that the FHWM expands with temperature, and the peak shifts to 1650nm. The change in peak emission is not due to BGN. BGR and temperature are the main culprits in the change in peak emission. As the excess carriers get injected, band bending occurs, as with BGN. The difference here is the presence of the quasi Fermi levels in both bands, reducing the emission.

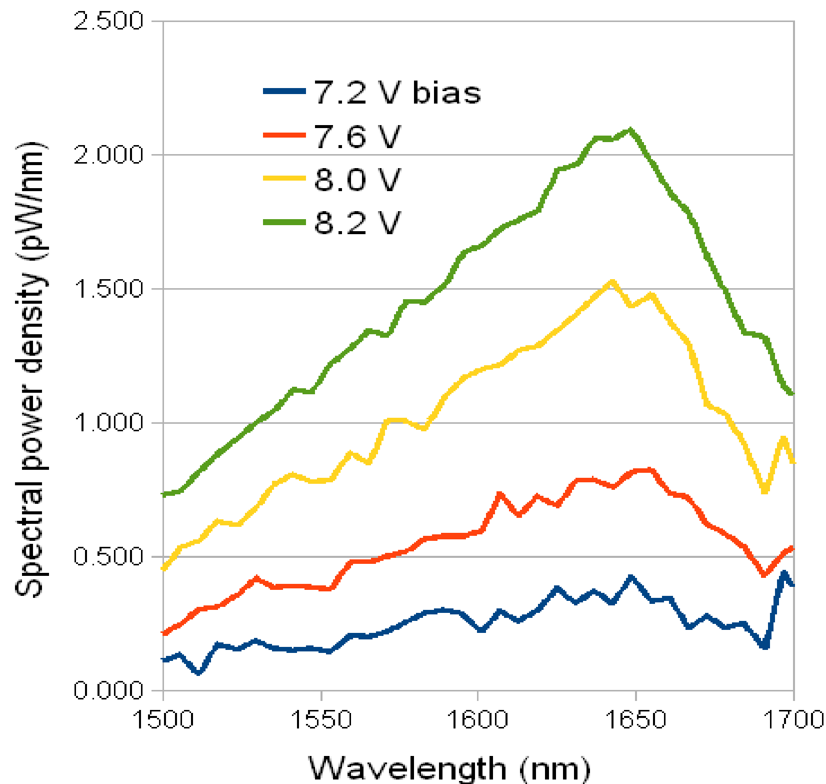

Figure 107.-Electroluminescence spectra of edge emission from cleaved pnn diode cross-section. Peak shift is attributed to high voltage. (Courtesy of J.Bessette)

Significant electroluminescence was detected from these devices showing a significant red shift in the bandgap. This shift can be attributed to an increase in temperature [30] due to heating effects during electrical pumping [9]. Temperature also changes the peak emission but

a shift of this magnitude would represent an increase of temperature up to ~800K or 450°C, as seen in Chapter 5. Further temperature measurements confirmed that the temperature change was <20°C. Furthermore, an increase in strain can be ruled out from XRD measurements. It is obvious that BGR can contribute the most under these parameters.

Comparing previous results reported in pin[20, 49] and pnn[23] heterostructure, it is demonstrated normal pnn behavior and emission from Ge LEDs. The emission intensity of the diode increases superlinearly with respect to voltage owing to an indirect valley filling effect which scatters more electrons to the direct valley under injection. Additionally, LED behavior is confirmed by comparing edge and top emission, as seen in Figure 108, where both results are consistent with Ge emission, and possess identical FHWM under same pumping conditions.

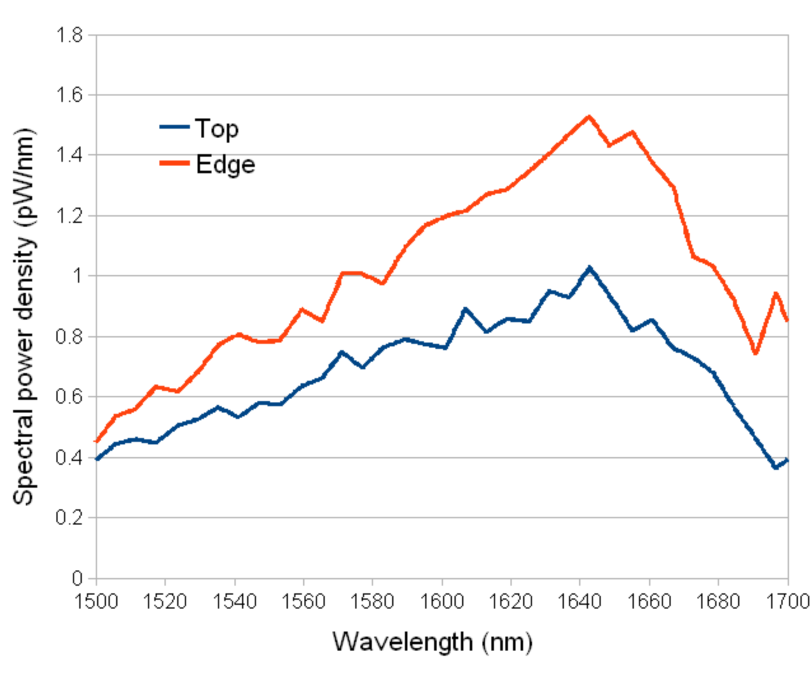

Figure 108.-Comparison of EL emission from top and edge emission from same device. (Courtesy of J.Bessette)

In this section, it is demonstrated:

- Edge emission electroluminescence in waveguide pnn Ge heterojunction diode structures

- Strong light emission from an edge and upper emitting LED is observed
- Red shifted Ge direct bandgap emission at 1650nm matches BGR
- Low resistance from <10Ohms. Doping concentration is the major factor controlling the resistance and effective injection of the devices before degenerate level ($1x10^{19}cm^{-3}$)

In the following section results of the highly doped LEDs with comparisons with the first generation are portrayed.

6.3 Highly doped Ge-LED >$1x10^{19}cm^{-3}$

Ge pnn LEDs heterojunctions showed difficult behaviors to overcome in doping, metal contacts and overall efficiencies. Different approaches were pursued at once to reduce dopant loss in the Ge buffer, the metal contacts electromigration, efficient carrier injection and temperature control.

Process variations and the use of delta-doping in the growth step, n+Ge was doped up to $3.5x10^{19}cm^{-3}$ P. The increase in doping did not reduce the quality of the device but introduced poly-Ge on the surface of the active material, as is discussed. Higher efficiencies and larger optical power is observed.

Finally, Ge LEDs show evidence of bleaching, or onset of lasing. The presence of hot carriers and bleaching is treated, as EL and PL behavior are shown describing the behavior of the devices.

6.3.1 Materials Preparation

Ge pnn heterostucture was made in similar manner to the lower doped LEDs. Modifications are the order of the contacts and injection direction, as the doping procedure for Ge. Starting

material was n+ Si (100) doped with Red Phosphorus to ~5-7x$10^{19}$$cm^{-3}$. A doped wafer was selected to avoid losses of the dopants on the interfaces as was seen in the previous section. By having a large doping source, it was expected to overcome Ge buffer dopants absorption.

Ge growth was performed over oxide trenches for selective growth. Ge *insitu* process was grown with delta-doping, as described in Chapter 4. Delta doping allowed for an increase in dopant concentration. Amorphous Si was deposited through plasma-enhanced chemical vapor deposition (PECVD). The tool used was DECVD Applied materials with SiH_4 as chemical reactant. The technique permits to grow a-Si under temperatures of <400℃, avoiding dopant diffusion. This tool has the disadvantage of excess hydrogen, or creation of a-Si-H.

Hydrogenated a-Si is common in the solar industry, but the excess hydrogen tends to outdiffuse during postprocessing, breaking film uniformity, and being a cause of shortage. To overcome H outdiffusion, a long-time diffusion technique was developed to minimize stress on the a-Si and other surface morphological changes which all can have a detrimental effect on injection and absorption. The maximum temperature through this process is 420℃ corresponding to peak of diffusion of H on Si, with smallest P diffuse from Ge. The details of a-Si long annealing can be found in the Appendix.

Si thickness deposited was ~180nm, and after the long annealing it reduced to 140nm due to densification and loss of hydrogen. Si is acting as well as a diffusion barrier for P dopants in Ge.

The material was further implanted with Boron with 23keV at a dose of 1x10^{16} at 7° degrees tilt. This permitted to create a dopant injection as shown in Figure 109. The dopant injection was designed to avoid damaging Ge upper surface.

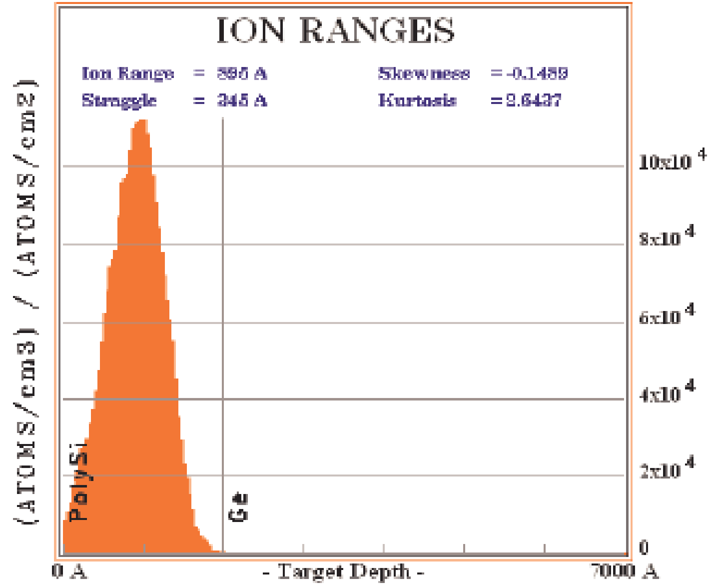

Figure 109.- Doping implantation on poly-Si for B at 23keV 7° degrees tilt. Notice the Gaussian formed to permit proper doping throughout the contact.

Rapid thermal annealing is used to activate the dopants on a-Si and move dopants on Ge delta region. The delta doped area is not diffused in previous steps to avoid higher losses of dopant on the interfaces.

Metal contacts were selected in terms of their resistivity. Kelvin Bridge, as shown in Figure 110, was used to determine the best metal for contact resistance. It is used a measurement tool to detect resistance under <1Ω and it has repeatedly shown to be an accurate measurement technique [175]. It consists of a metal connection to a semiconductor through a single piece of square dimensions size, ℓ. When applying voltage through the semiconductor and metal, and reading the current through the other two contacts, a simple relation is achieved,

$$R = \frac{V_{14}}{I_{32}} = \frac{\rho_c}{\ell}$$

where ρ_c is the resistivity of the metal with the surface exposed, that being p+polySi, in our case.

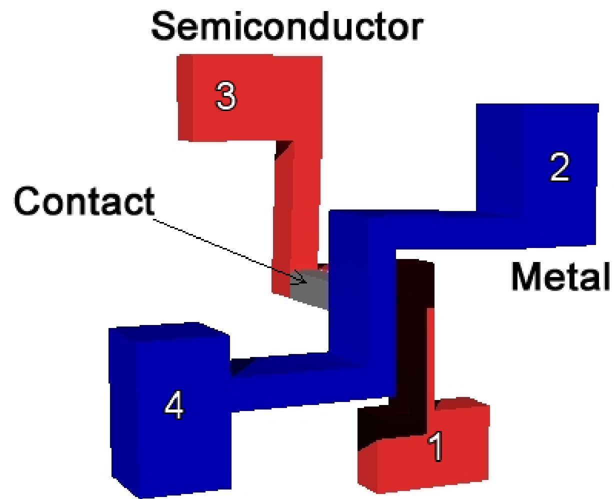

Figure 110.- Kelvin Bridge resistor schematic.

The results of the different metals are shown in Table 8. It shows that Ti and TiN are the best contacts for the heterojunction with a $\sim 60\ \Omega\mu m^2$, while most other materials showed orders of magnitude larger resistivity ranging from 400-1000 $\Omega\mu m^2$. The difference resides from the work function of the different materials and B-doped Si, and the processing. The former reason is clear when seeing other similar results from other groups, with better contacts with the same metal but different dopant for Si[175]. The latter is more likely due to formation of oxide on the polySi before implantation of oxidation of the metal. Notice that Ti, TiN and Al are deposited under 30minutes after the final oxide cleaning and they are deposited using a sputtering chamber with high-vacuum and temperature control. The other metals were deposited with electron beam, where the deposition lasts over 3 hours, the temperature increases the heavier the metal - as is the case with W – and the material cross contamination from other devices is more likely.

Table 8.- Metal resistance of different devices

Metal	**ρ_c ($\Omega\mu m^2$)**
Ti	57
Ti-anneal	81
TiN	45.35
Ni anneal 350C	2280
Ni anneal 450C	423
Pt	890
W	1300

The device was finalized with Ti 100nm / Al 500nm and etch to exposed the polySi and avoid further optical losses from the metal on Ge, as seen in Figure 111. The double layer is an old standard at industry. The metal was not on top of the Ge substrate to avoid metal optical losses. The contacts were set both in the upper face of the device to minimize the distance for the current and bias.

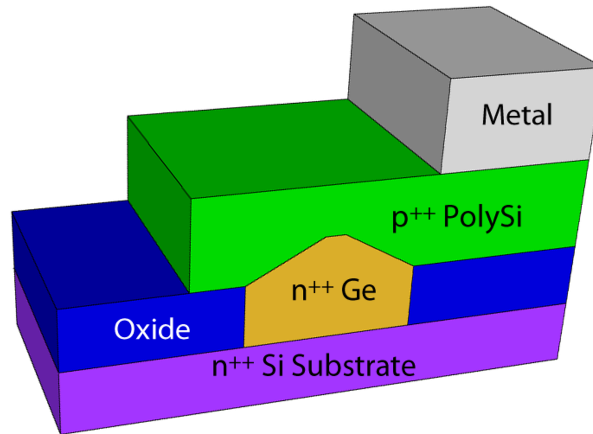

Figure 111.-pnn Ge heterostructure LED design for higher dopant above >$1x10^{19}cm^{-3}$.

6.3.2 IV Diode characteristic and Electroluminescence

Measurement of highly doped materials, as seen in Figure 112, shows normal behavior of degenerate materials. Under reverse bias, the voltage and current are linear, as expected from Zener breakdown. This happens due to heavy bending of the bands and quantum tunneling.

Furthermore, the increase in Fermi levels easier exchange of the carriers. For the type band I alignment, for carriers confinement, forward bias is needed, as will be seen.

Decrease on resistance is observed under heavy doping. Resistance difference is dV/dI~5±4Ω for heavy doping and 10±4Ω for the low doped. The limitation between the doping stages comes from the leakage current, or leakage bias, that the any device has to overcome. Furthermore, at the values measured for resistivity, we are limited by our experimental setup since they are on the order of the intrinsic resistance of the setup.

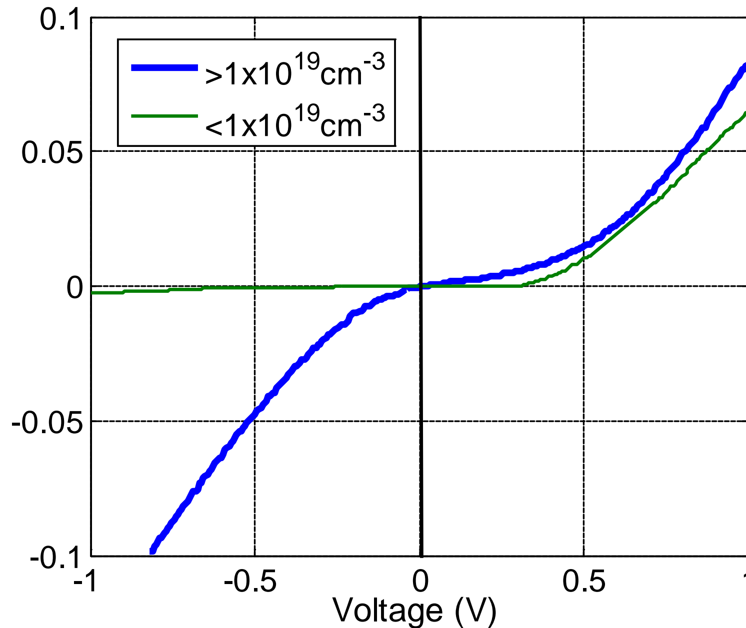

Figure 112.- I-V comparison of two different dopant concentration LEDs. Highly doped LED shows typical degenerate system under inversion.

When comparing luminescence of highly doped devices, we see that both EL and PL match, as seen in Figure 113. The emission shows full activation of the dopants in the material and heavy shifting due to BGN, and not due to temperature. The comparison shows that an injection of 1kA/cm^2 is equivalent to few μJ without having adverse temperature effects. PL

depends on the absorption of the material, preventing BGR from happening. Use of current injection, instead of bias, permits to reduce the level of carriers injected, and prevent BGR.

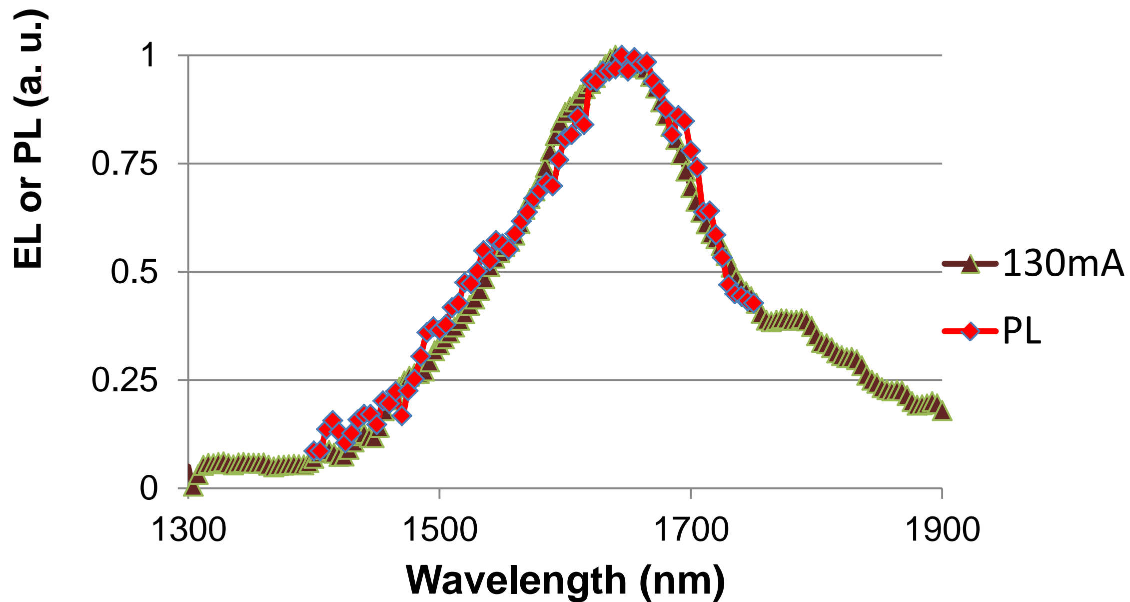

Figure 113.- pnn Ge diode PL and EL at 130mA continuous current normalized spectra with temperature control to 300K. (Courtesy of J.Bessette)

The diode was tested under pulsed current to minimize metal electro-migration observed in the low doped devices. Pulsed current prevents overexerting the metal contacts and extends the lifetime of the metal, as was observed. By maintaining a 50% duty cycle, the material was capable of sustaining up to ~45 kA/cm^2.

Additional study of the temperature change with peak emission, showed that under heavy injection the temperature plays a role on devices, as observed in Figure 114. The dopant peak shift is large enough to suggest the presence of hot carriers due to the linearity between power and temperature shift. A hot carrier is present when the electrons or holes are at higher temperatures than the lattice, which effectively excites the carriers as observed on lasers.

Silvaco Simulations of these devices predict a maximum temperature shift of 10°C. Due to the large shift, such small temperature change does not have a significant contribution to peak shift, as seen in Chapter 5. However, the difference between stage temperature control, suggests that carrier temperature might still have an important effect. Excited carriers through hot carriers could contribute to BGR, and the effect would be reduced under a cold stage, as observed. The spectrum of non-temperature control emissions are shown in Figure 115.

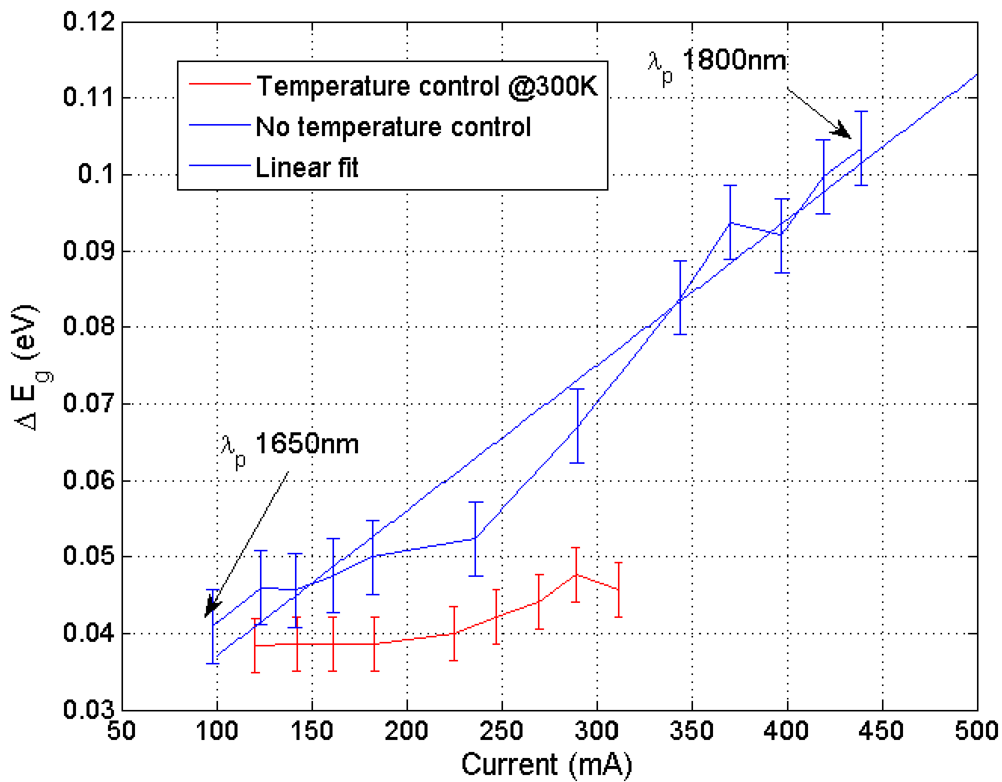

Figure 114.- pnn Ge diode emission difference on peak emission (λ_p) with injected current. The maximum peak shift is equivalent to a temperature increase up to ~500˚C

In terms of BGR, the effect would have a 1/3 power relation between dopant and peak emission. The electron-holes interactions have been seen before on different work[166, 176] to cause BGR, and it assumes that the interaction energies are proportional to the carrier-carrier

distance. Under degenerate doping or heavy injection, above Mott criteria, the relation would be lost and follow a linear relationship with change in energy as follows,

$$\Delta E_g \propto N$$

where N is the number of carriers injected under heavy injection. The difference in injection matches the injected carriers and follows similar criteria to BGN, as discussed in Chapter 5.

The increase in EL with the increment of carrier injection follows the superlinearity common in LEDs, as seen in Figure 115. The shape indicates common LED behavior and kT relation with FWHM. The peak at high current show new peak formation, though this is due to lag on detection and the peaks height are under experimental error.

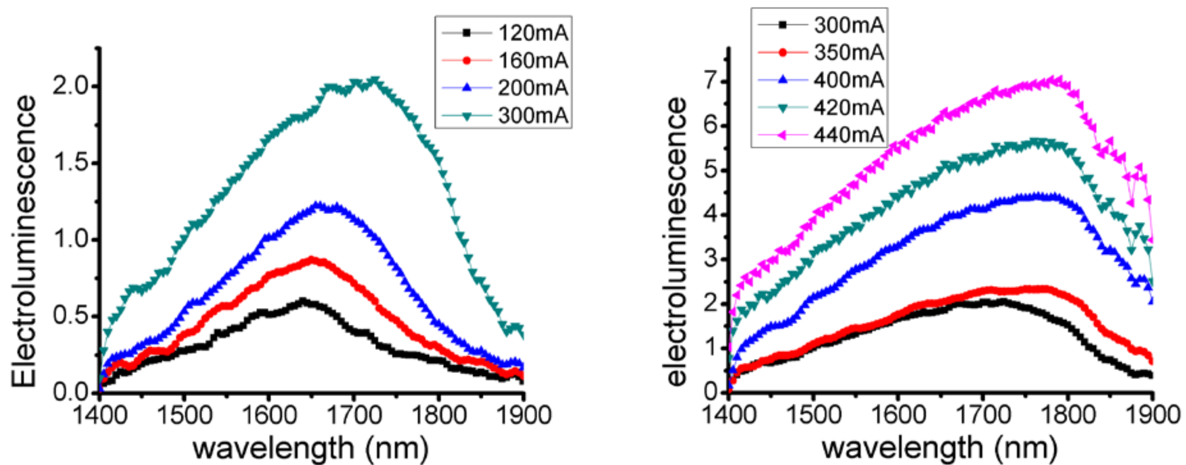

Figure 115.- Low injection and high injection of highly doped Ge pnn LEDs. Emission and peak emission match with calculations.

Under high injection, the amount of holes injected is comparable to the doping level of P, leading to strong BGR and possibility of hot carriers, as mentioned. Under the conditions in Ge LEDs, we observed resonance and change in peak morphology. The peak formation at long wavelengths is thought to be a resonance within device, and could be interpreted as nonlinear effects being introduced.

The lack of narrowing, characteristic of lasing, denied the possibility of inversion but the bleaching is a possibility, as observed in Figure 116. The elbow formation is characteristic of lasers, but the spectrum does not have the requirements for it. FHWM does not decrease; however, due to the spectrum acquired, the accuracy of the measurements is faulty. At long wavelengths, the peaks anomalies suggest changes in sensitivity, and might be an artifact.

We predict bleaching through the device in different sections, having an increment in light emission as more sections go under transparency. The EL measurement is an average of the different mechanisms occurring at once in the device. When the entire waveguide goes under transparency, resonance can be achieved and inversion of the carriers, ergo, lasing.

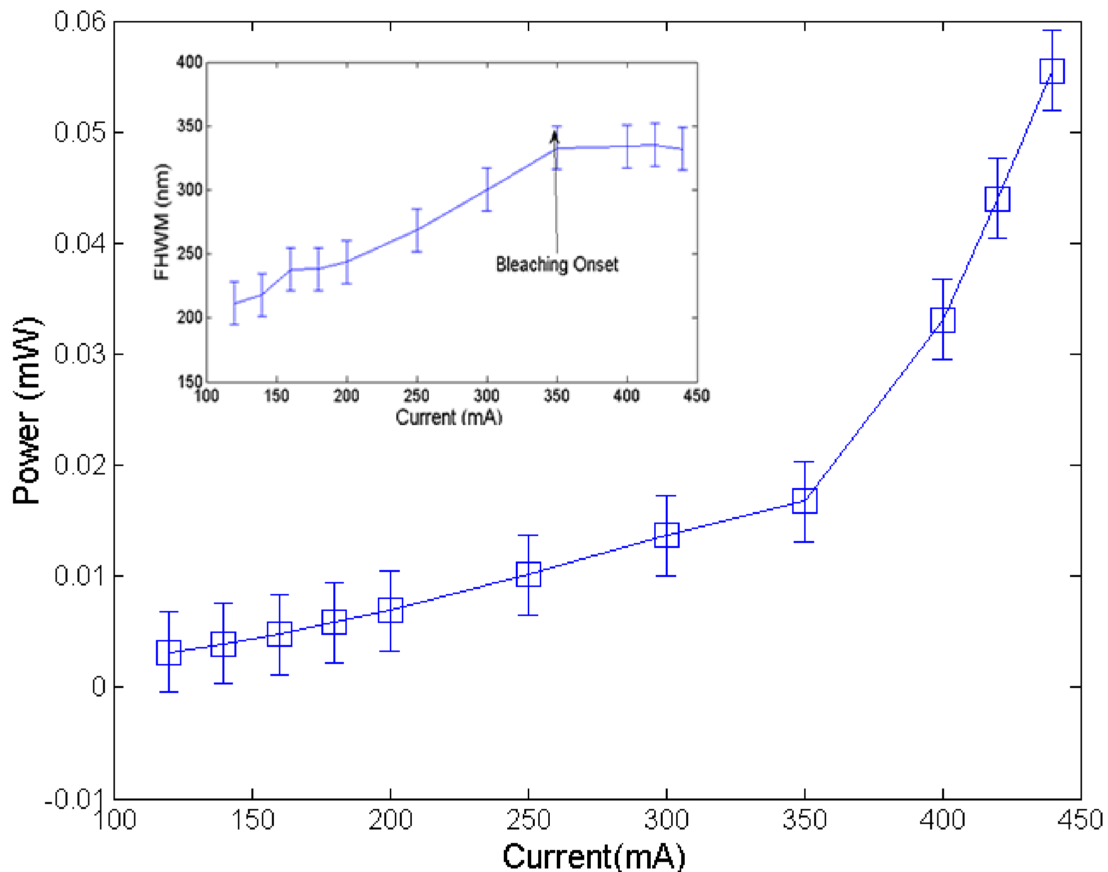

Figure 116.- Ge LEDs power emission to injected current, comparing FHWM to current. Bleaching onset is observed at 350mA corresponding to a current density ~35kA/cm^2.

Bleaching observed suggests that the material used for LED and the processing is not ideal. Calculating the internal efficiency of the device, η_i, as seen in Figure 117,shows that the photon flux increases dramatically, reinforcing the theory of partial bleaching of the device.

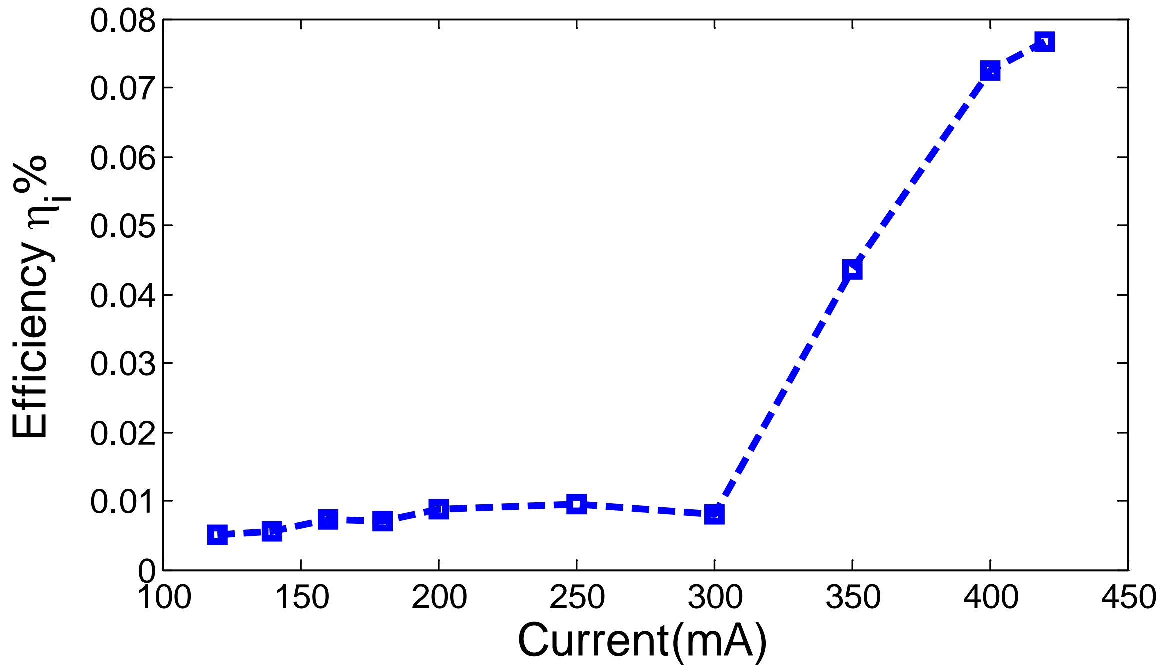

Figure 117.- Internal quantum efficiency of pnn Ge LED compared at different current.

Moreover, if we consider the best result for external efficiency and internal efficiency, at different lengths of the device, it shows that to reach 0.08% efficiency, it requires several sections working together so the absorption can be close to zero, and obtain the efficiency stated. The simulation of such result can be seen in Figure 118, aiding to support the evidence of bleaching.

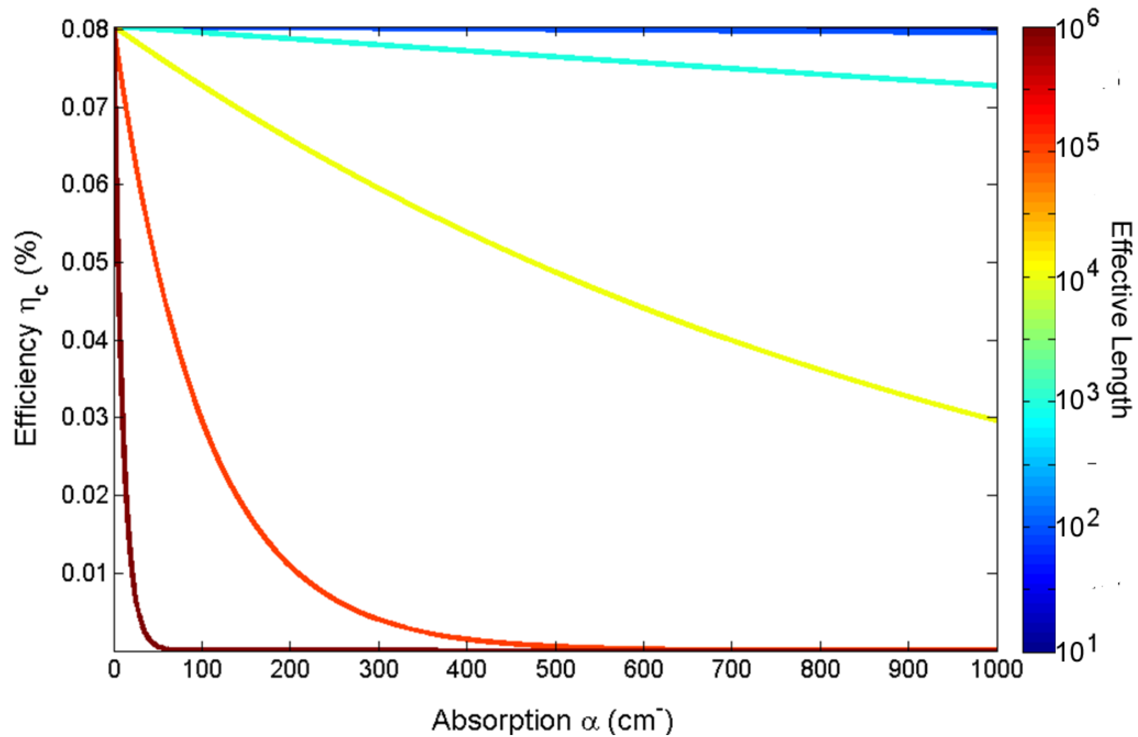

Figure 118.- Simulation of pnn Ge diode efficiency at different lengths comparing how the absorption changes the efficiency of the device.

6.3.3 Comparison of heavy and low doping

Comparison of the power output with high and low doping provides the information required for improvements of extraction, efficiency and injection. While analyzing power to voltage characteristics of these devices, it shows a clear increase in the response from highly doped LED in comparison to their predecessor, as seen in Figure 119. It shows that the heavier doping would aid for larger injection current.

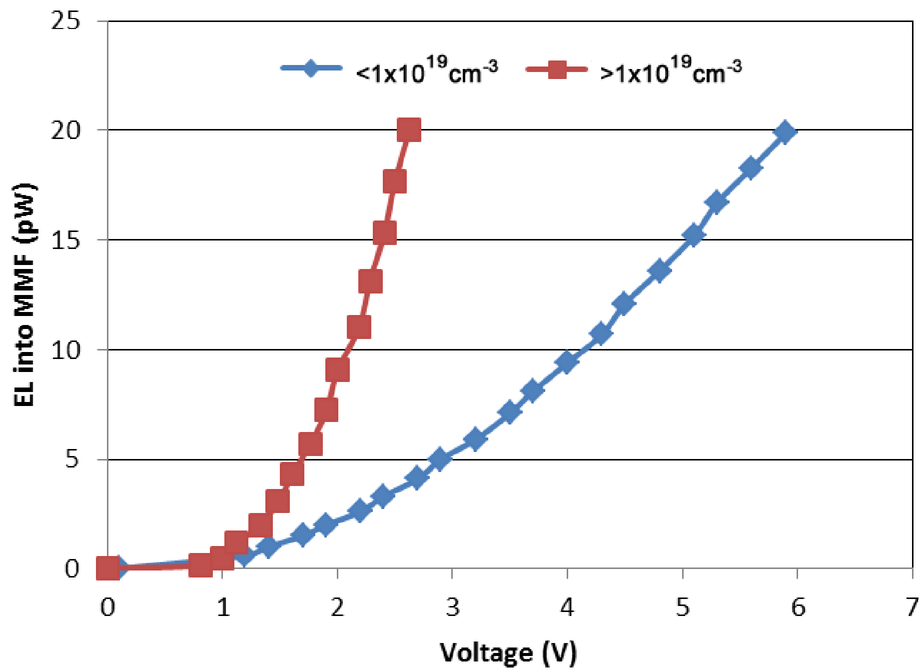

Figure 119.- Comparing low and high dopant concentration devices due to their power according to different biases. (Courtesy of J. Bessette)

This increment in voltage response suggested an increase in responsivity. Responsivity of an LED is the ratio of optical power to injected current[62]

$$\Re = \frac{P_o}{i} = \eta_{ex}\frac{1.24}{\lambda_o}$$

Despite the differences on dopant concentration, $\Re$ ranges from 68.8-72.8 pW/A, as shown in Figure 120, establishing an external efficiency of ~ 10^{-4}%. This is to be expected due to the low extraction efficiencies, the edges made by cleaving, and the extremely dispersive polySi above the Ge. Better quality Si, mirrors and minor losses in Ge active area would increase the external efficiency. The discrepancy between power output in these measurements and the previously shown comes from the setup allowing for better extraction under HoribaPL setup

compared to the fiber coupled setup depicted in these results. The losses per setup are added in our calculations.

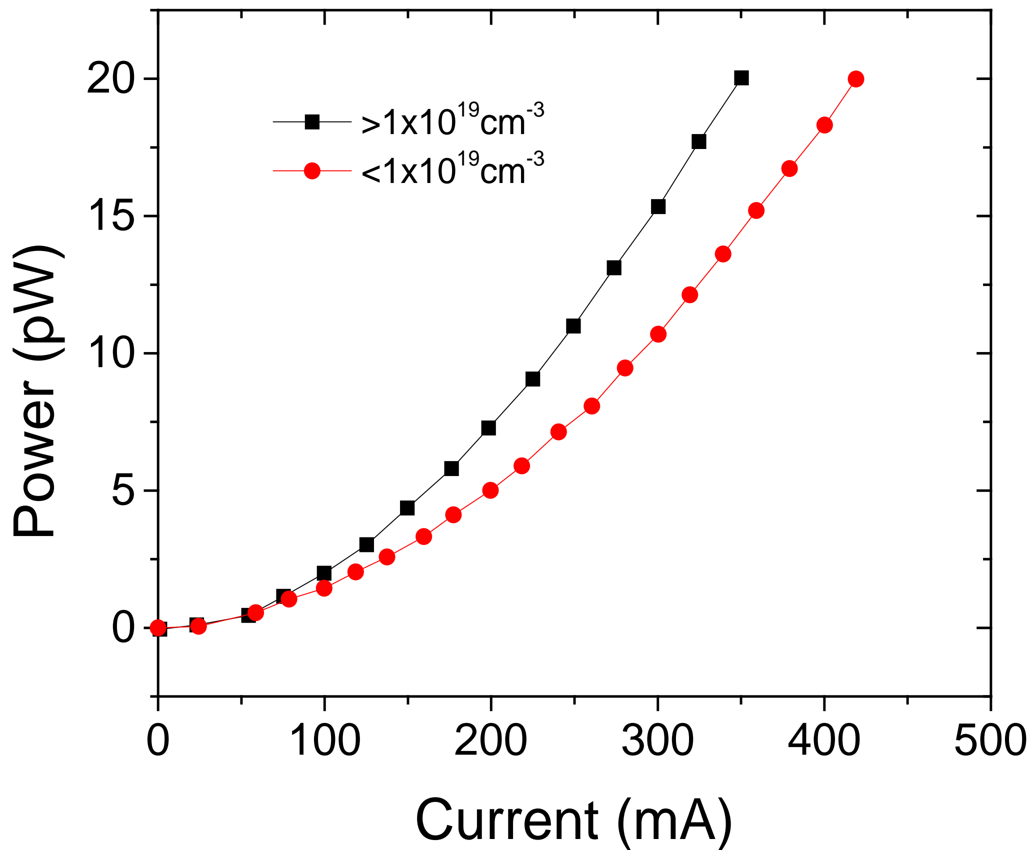

Figure 120.- Comparing low and high dopant concentration devices due to their power output according to different currents, use to determine responsivity.

The same design and material, under heavy injection, shows a different behavior in $\Re$. The drastic change can be due to bleaching or hot carriers, as seen in Figure 121. Theoretical simulation includes all the values measured, extracting the current and power outputs from it. As seen, at low current densities both experimental and theoretical models match. At high currents, the discrepancy is large, and this cannot be attributed solely to bleaching, since its effect is also included in the theoretical model. Hot carriers are a possibility considering that

the voltage used is >10^3V/cm [167] which is a typical voltage temperature for diode to exhibit hot carriers. Hot carriers could contribute to larger power emissions from the direct band gap, without the aid of larger parts of the device, and achieving larger responsivity on Ge LEDs. More experiments have to be done to determine the discrepancy between theoretical and experimental work.

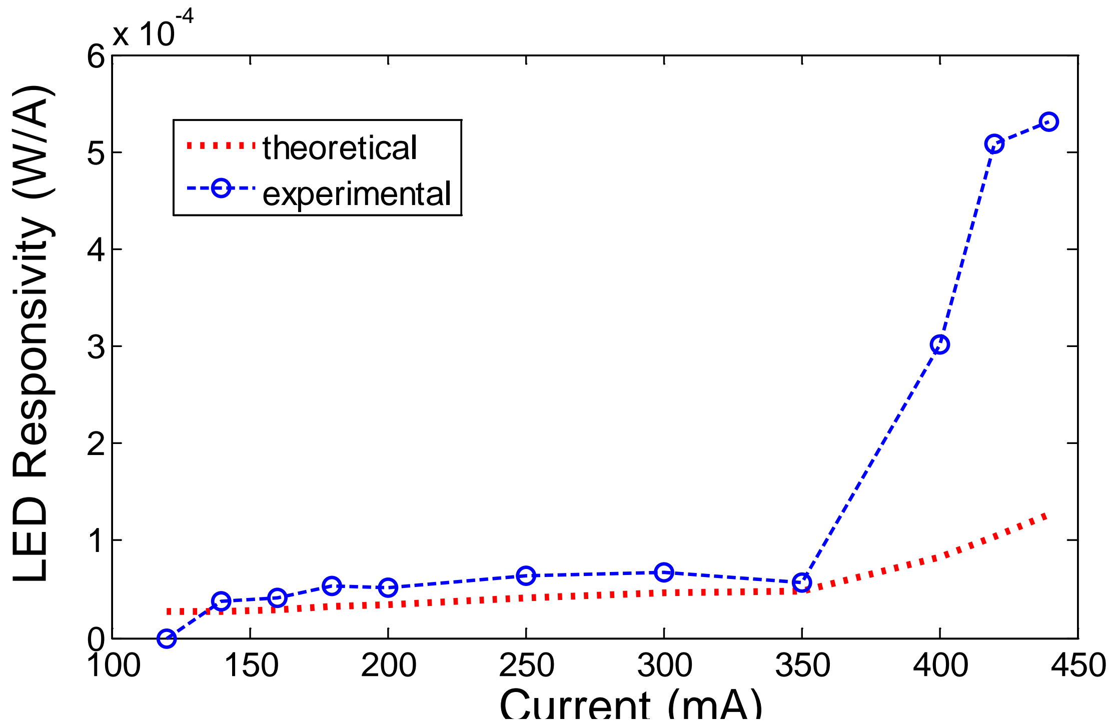

Figure 121.- Measured responsivity (R) of pnn Ge LED under heavy doping ~$3.5x10^{19}cm^{-3}$.

6.4 Conclusions

The results in Ge pnn-heterojunction show increase in emission, as expected. The area of emission belongs to a waveguide of 1μmx500nm . The area of emission of the pin diode first tested was a 10μmx50μmx500nm prisms. The measurements comparisons of PL and EL in Ge show correlation between doping concentrations with electrical behavior. Due to

electromigration, higher power concentrations were not explored, and state the need of better injection paths for carriers. Secondary nonlinear effects are observed under heavy injection.

Ge LEDs show evidence of bleaching. Further studies will confirm the secondary effects in the injection of the bands. Presence of BGR and hot carriers are left for further study. It is demonstrated the first evidence of bleaching in any Ge LED under heavy doping and complete activation of the carriers through appropriate process.

A combined effect of higher temperatures and increased electrical injection leads to the inversion of the carriers. This approach and some others will be discussed in the final section.

Chapter 7. Ge-on-Si Laser

We demonstrated a fully CMOS compatible process for development of Ge-on-Si laser diodes. The demonstration of the electrically pumped Ge laser was based on the work done on the optical pumped laser[177]. The basis of this work required to overcome the extrinsic losses on the laser cavity.

Further, we show the materials development and simulations for structure design and FP laser limitations. We then show the experimental results and analysis common to all laser diodes. We finalize showing the implications of the result and possible improvements for the laser diode.

7.1 Optical pump Lasers

We demonstrated stimulated emission from Ge and, hence, carrier inversion[177]. Stimulated emission, as established in chapter 2, is the main radiative mechanism for lasing. Optical bleaching was previously demonstrated in Ge, with gain ~$50 \pm 25 cm^{-}$. The gain was limited by carrier injection and doping in the material. By increasing the doping concentration to 1.5-2x10^{19}cm^{-3}, larger gains are obtained and clear lasing emission was recorded. In this section we show a multiple-mode Ge laser with a Fabry-Perot (FP) cavity through optical excitation. This work was fundamental for demonstration of the concept of injection for gain and lasing.

7.1.1 Materials Setup

Ge material was *in situ* doped with ~1x10^{19}cm^{-3} phosphorous during the growth to further compensate the energy difference between the direct Γ and indirect L conduction. A cross-sectional scanning electron microscopy (SEM) picture of the Ge waveguide is shown in the inset of Figure 122. The width of the Ge waveguide is ~$1.03 \mu m$, and the height is ~600 nm. In order for valleys to enhance the direct gap light emission [30, 58], and overcome the low gain

expected, a secondary doping process was performed with spin-on dopant (SOD). The total dopant concentration obtained was ~1.3-2.5x10^{19}cm^{-3}, with a calculated gain of >60cm^{-1} at carrier injection ~5x10^{19}cm^{-3}. The waveguide was further cover with oxide to passivate the surface and reduce scattering losses.

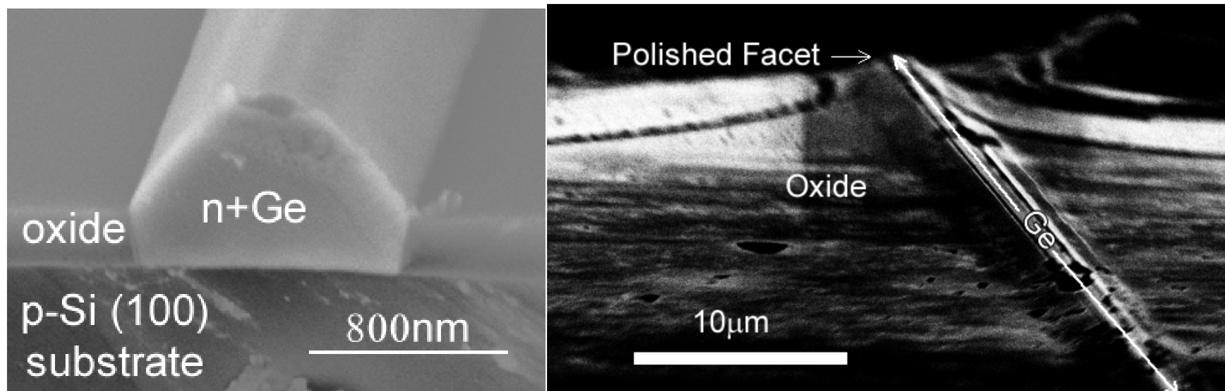

Figure 122.- n+Ge waveguides SEM micropraphs showing facet and structure, acting as a FP resonator.

The relatively large cross-sectional dimensions were selected conservatively to guarantee >90% optical confinement in the Ge gain medium for demonstration of lasing, without optimization for the minimal threshold.

On typical III-V material this can be easily achieved by cleaving [178]. Due to the large index of refraction difference between air and most laser emitting semiconductors, the reflection on the facets is ~30% with perpendicular mirrors. Moreover, the difference on index between substrate and active material can maintain a guided mode. Hence, simple cavity is formed with an in-plane waveguide and perpendicular mirrors, forming a Fabry-Perot (FP) cavity.

The edges of the samples were cleaved and further mirror polished to obtain vertical facets for reflection mirrors on both ends of the waveguides. The polishing step is performed since Si (100) wafers will break on the [110] direction, 60°, preventing maximum reflection R.

Slurry chosen was ethanol glycol due to the inert properties it presents. Etchants based on water corrode Ge as pH increases[179]. The slurry gets filtered and recirculated, while changing the diamond grids from 30μm to 0.5 μm. The decrease in diamond grid allows formation of an atomically smooth surface with maximum reflection of 37% in Ge.

The length of the waveguides is ~ 4.8-7 mm. Such a long waveguide was chosen to guarantee a mirror loss of <<10 cm^{-1}, which is much smaller than the optical gain of Ge [58]. The reflectivity at an ideal facet is estimated to be 37%, considering the index contrast between Ge and air, corresponding to a mirror loss of ~2 cm^{-1}. The mirror loss, α_m, from the cavity is

$$\alpha_m = \frac{1}{L}\ln\left(\frac{1}{R}\right) \sim 2 - 10.2 cm^{-},$$

where L is the length of the cavity, and R is the facet reflection. The approximation of the mirror loss comes from the different lengths and reflection.

Other fabrication losses in the Ge waveguide are the modal losses As seen in Figure 123, Ge waveguide simulations show confinement of up to 7 modes, intermix both TE-TM fields, defined by the total thickness of the device. The total modal losses α_{sc} account for <4cm^{-}. As the substrate is lowly doped p-type Si, the total absorption is less than 2cm^{-}. The largest loss is through injection determined by free carrier absorption, α_{FCA}, which is ~42-63cm^{-} in the wavelength range 1500-1700nm. Adding up α_m, α_{sc}, and α_{FCA}, it follows that the gain has to overcome the minimum loss of,

$$g_{net} \geq \frac{\alpha_s + \alpha_m}{\Gamma} \sim \alpha_{sc} + \alpha_{FCA} + \frac{2}{L}\ln\left(\frac{1}{R_1 R_2}\right) \approx 48 - 83 cm^{-1},$$

which is achievable with the doping concentration and previously observed gain of 50cm^{-}.

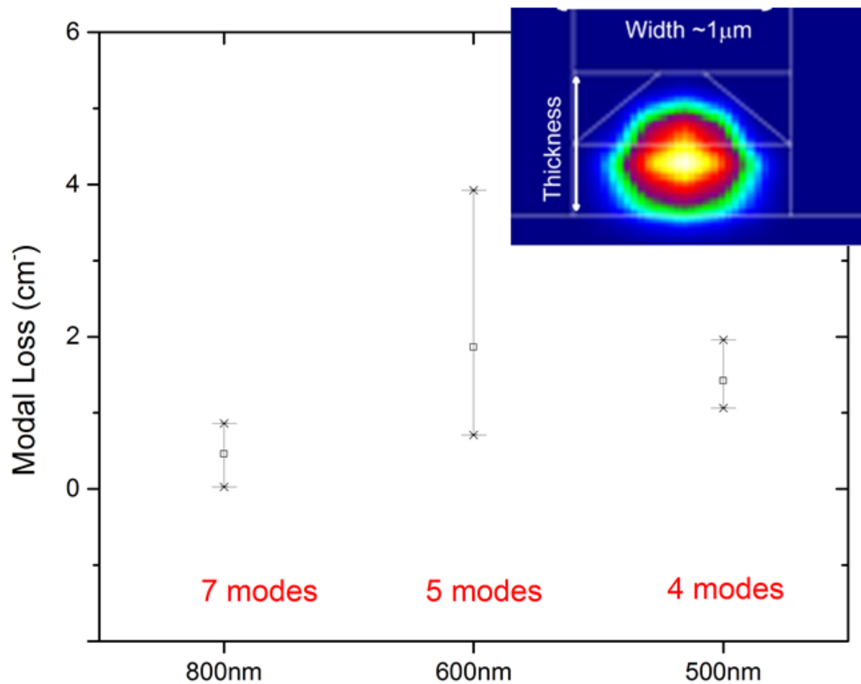

Figure 123.- Ge waveguide 2-D simulation showing modal loss and number modes different thickness.

The entire waveguide was excited by a 1064 nm Q-switched laser with a pulse duration of 1.5 ns and a maximum output of 50 μJ/pulse operating at a repetition rate of 1 kHz. The pump laser was focused into a line of ~7 mm long and ~0.5 mm wide by a cylindrical lens and vertically incident on top of a Ge waveguide, as schematically shown in Figure 124.

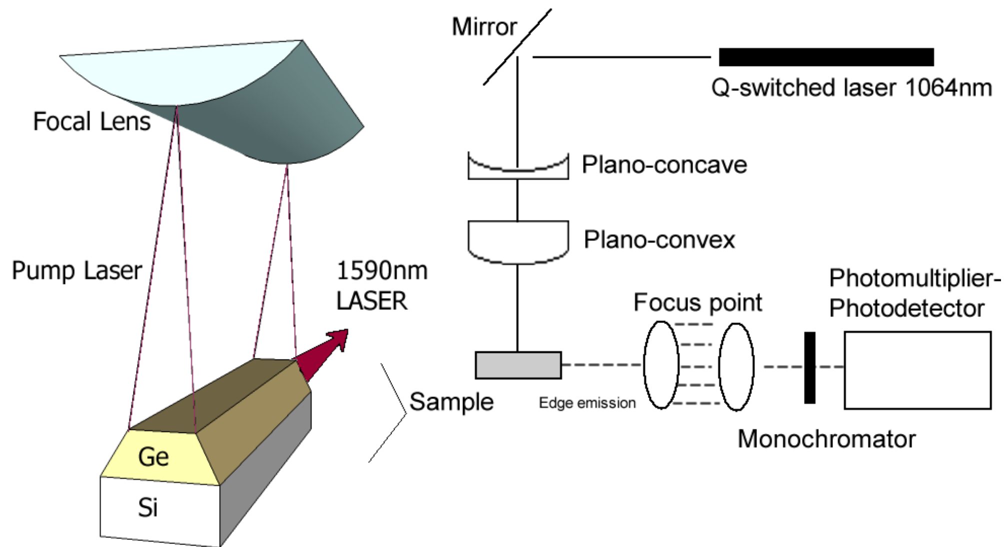

Figure 124.- Schematic of the setup used for testing and probing n+Ge waveguides. *Q*-switched laser with pulse duration of 1.5 ns and a repetition rate of 1 kHz was used with a photomultiplier/photodetector.

Through SOD doping method, as described in chapter 4, the material compensated the low gain and low carrier injection. We reported the first (to our knowledge) observation of lasing from the direct-gap transition of Ge-on-Si at room temperature using an edge-emitting waveguide device. We demonstrated that the emission exhibited a gain spectrum in the wavelength range of 1590–1610 nm, line narrowing and polarization evolution from a mixed TE/TM to predominantly TE with increasing gain, and a clear threshold behavior.

7.1.2 Optical Photoluminescence

Photoluminescence (PL) was performed Ge FP samples. Figure 125 shows the light emission spectra of a Ge waveguide under different pumping levels with a spectral resolution of 2 nm. At low carrier densities, the emission from the waveguide shows a broad band with a maximum around 1600 nm, consistent with PL and EL spectra of ~0.2% tensile strained Ge reported

earlier [20, 30]. The broadening of the peaks confirms the emission of both heavy holes and light holes, as normal spontaneous emission.

As the pump power increases, emission peaks emerge at 1599, 1606, and 1612 nm. This shift in wavelength is due to the increase in carriers in the system leading to BGR due to the excess carriers. As power increases pass the onset of lasing, multiple peaks become clear in accordance with resonance in the FP cavity.

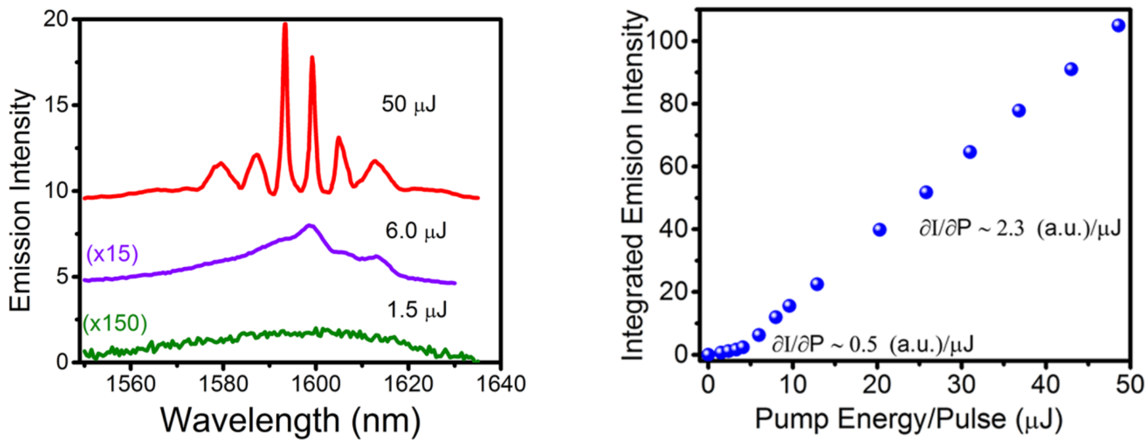

Figure 125.- PL emission progression of n+Ge waveguides under different probing conditions from Q-switch laser, and L-I curve showing the threshold of lasing. [177].

As pump power increases to 50 μJ/pulse, the widths of the emission peaks at 1594, 1599, and 1605 nm significantly decrease, due to peak narrowing; while the polarization evolved from a mixed TE/TM to predominantly TE with a contrast ratio of 10:1 owing to the increase of optical gain. This polarization of the laser shows the coherency of emission; a typical characteristic in lasing.

The strongest emission peak blue-shifts from 1600 nm to 1594 nm, and two new peaks appear at shorter wavelengths, with a separation of $\partial\lambda$~6nm. The blue-shift is consistent with Burstein-Moss shift, such that the gain spectrum shifts to shorter wavelengths with the increase of carrier injection due to occupation, or band filling, of higher energy states in the direct Γ

valley [24]. The shift expected is ~9.05 nm, compensating BGR from excess dopants and carriers, matching our observations.

The change in the emission spectrum occurs at the pump power corresponding to the threshold behavior, marking the onset of transparency larger than 50 cm^{-1} gain [24], and closer to ~80 to overcome all fabrication losses in Ge, as was demonstrated. This aspect is of outmost importance since a slight increase in losses would quench the gain, and make it non-observable.

F, finesse, and Q are according to the resolution measured ~40 $x10^3$ being much better FP resonator than expected. Q is calculated as ~790, and F of ~265 calculated from the emission observed. The low theoretical Q suggests the presence of multimodes, transversal and longitudinal, in order with simulations.

7.1.3 Other resonators

Microdisks were analyzed to observe gain in WGM, as previously observed [58]. PL was analyzed, as seen in Figure 126, showing an increase in PL compared to films or waveguides. The increase in spectral width, and the presence of resonances was unexpected. The spacing between resonances suggests a cavity of Q~110, and a radius of ~200nm, which indicates resonance from the fiber instead of the cavity. The resonant frequency is not determined since the detector used, OSA analyzer, cuts-off at longer wavelengths. As well, the resolution of the detector prevents clear determination of the effect of these resonators.

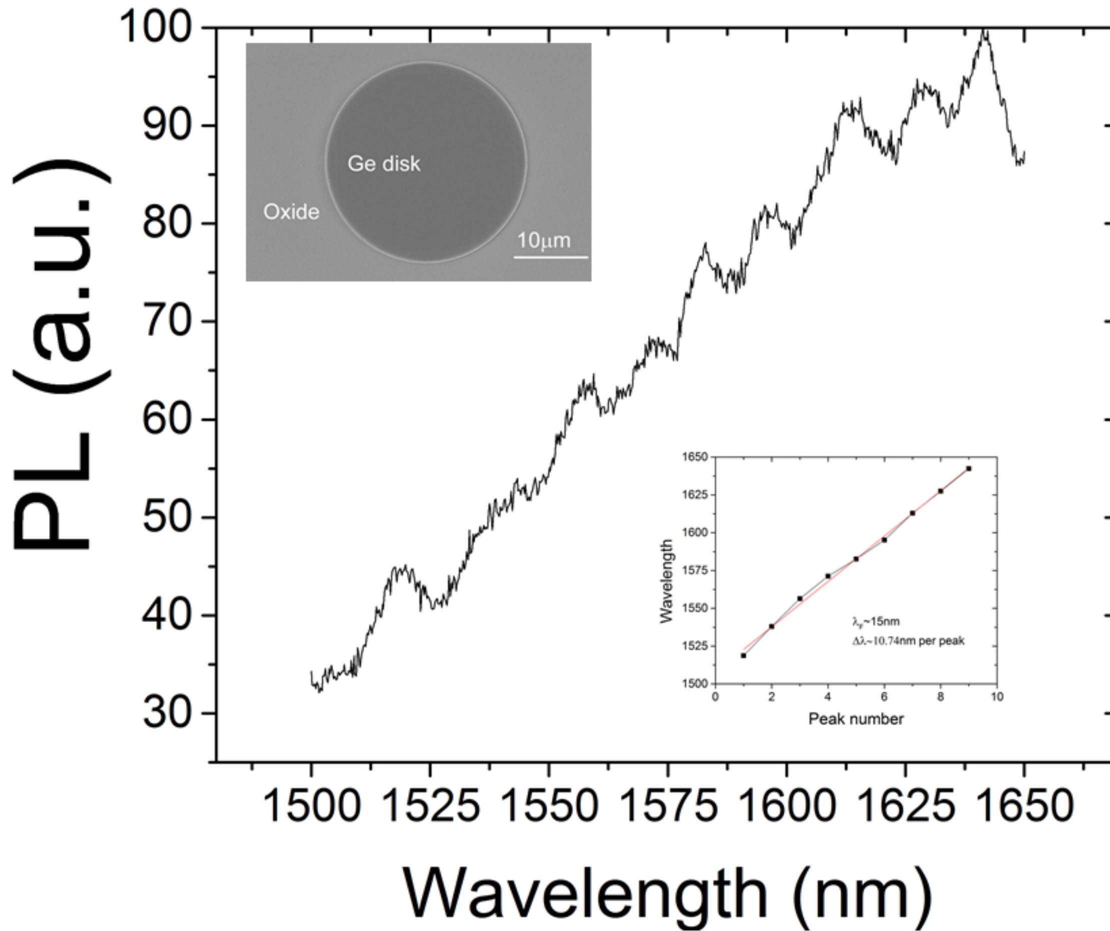

Figure 126.- PL emission from n+Ge microdisk. The value extends to the high 1650nm with a resonance distance of 300nm. The peaks are seen as an artifact between the separation of microdisk and the optical fiber.

These resonators were explored for further optical injection. The low extraction and angle dependence of the extraction prevented from observing lasing. Furthermore, the injection was done through a method that prevented to uniformly inject the material. The facets in Ge disks become scattering points, likewise, the multiple resonances with limited reflections of 37% prevented perfectly getting the mode. This losses add to higher than >500cm^{-1} for the TE_0 in a 20μm diameter disk. In order to simplify extraction and reduce losses, toroids were built.

Ge toroids were Ge disks in a pedestal of p-Si, surrounded by SiO_2, as seen in Figure 127. Formation of these structures is through an oxide mask protecting Ge, and the use of TmAH to etched underlayers of Si. TmAH etch rate is an order of magnitude slower in Ge than in Si, but in order to avoid etching scattering surfaces, the oxide cover was necessary. The structures showed similar PL behavior to disks and with similar complications of extraction. Further research is necessary to learn to couple the light out of these devices.

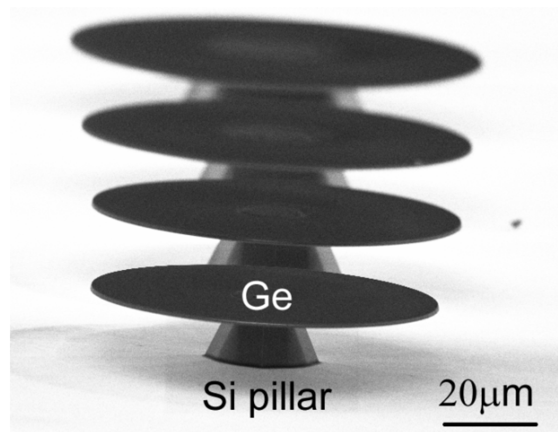

Figure 127.- Micrograph of Ge toroids .

Due to the difficulties of emission extraction of these devices, and to uniformly inject carriers, the study of the pnn Ge disks was omitted. The electrical study of Ge was continued under FP measurements.

7.1.4 Conclusions

In this section it was demonstrated a room temperature optically injected laser with concentrations as low as $1.5x10^{19}cm^{-3}$. The difference in gain due to the increase in doping is significant enough to overcome external losses as the non-radiative recombinations.

- FP multimode Ge laser on Si with doping concentration $1.5\text{-}2.5x10^{19}cm^{-3}$ at 300K.

- A polishing method to avoid corrosion on facets and permit atomically smooth surfaces, maximizing R.
- Thickness influence in total modal losses.
- Importance of cladding surface for optical confinement.
- Total loss is dominated by FCA.
- Under high injection, non radiative recombination Auger should dominate. Nevertheless, no observation of decrease on emission is observed.
- Lifetime carrier of Ge laser stimulated emission comparable to III-V materials

7.2 Double Heterostructure Ge Laser Diode [22]

Through this document, it has been shown evidence of Ge gain, and its ability to luminesce through electrical injection, LEDS; and optical gain capable of carriers inversion, optical injected Laser. Also, it has been shown that using a combination of tensile strain and n-type doping, efficient direct bandgap emission of Ge can be achieved [180], optimizing the effects under larger doping concentrations. Using the previous work as a basis, a FP Ge-on-Si laser diode was approached.

In this chapter, it is presented an electrically pumped pnn Ge diode laser on Si that can be monolithically integrated into a CMOS process. These first laser devices produce more than 1mW of output power and exhibit a Ge gain spectrum of over 200nm.

7.2.1 Materials Preparation

Ge waveguides of 1µm width were fabricated by selective growth of n-type Ge-on-Si in silicon oxide trenches using UHVCVD [3], using a similar procedure as for Ge LEDs on previous chapter. Details of the growth can be found in the Appendix. A delta-doped Ge layer

was grown on top of the n-type Ge to serve as a phosphorous diffusion source [181, 182]. The delta-doping technique inserts monolayers of P in the Ge film at low temperatures by alternating the phosphine and germane gas flow in the CVD reactor, as mentioned in previous chapters. After thermal annealing to drive the phosphorous into the n-type Ge layer, the delta-doped Ge layer was removed during planarization using chemical mechanical polishing (CMP), to reach a uniform doping concentration in the gain medium. Slurry was water based with no pH control, being prompt to changes from badge to badge. CMP was performed by Entrepix under device wafers covered with 400nm oxide. Figure 128 shows a successful batch. Characterization through AFM showed atomically flat surfaces. Further clean under Piranha bath clean the surface with a small rate etching on the surface of Ge of < 2nm/min.

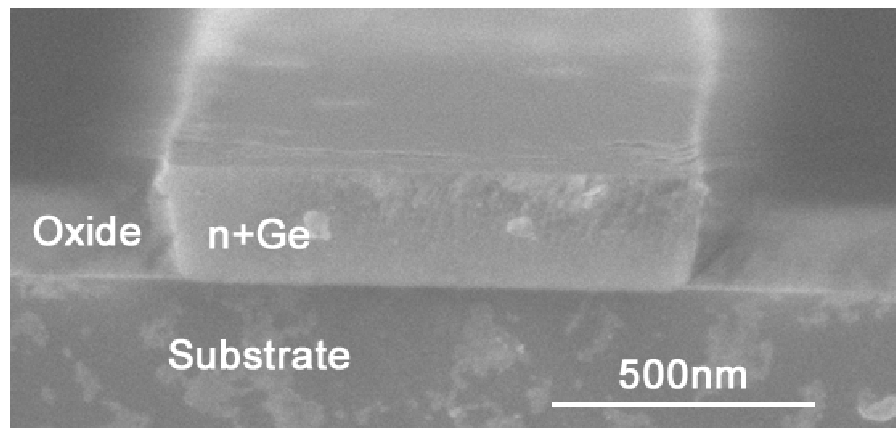

Figure 128.- Ge device CMP after Piranha clean .

The remaining thickness of the Ge waveguide after CMP varied between 100 and 300nm depending on wafer and location on the wafer. The variance on heights on the wafer was not planned but rather a mistake through manufacturing. Due to severe dishing of the waveguides, as seen Figure 129, in after CMP the supported optical modes in the waveguides could not be determined exactly. The modes were simulated to hold 2 TE modes. Up to six TE cavity modes can be supported in the largest waveguides.

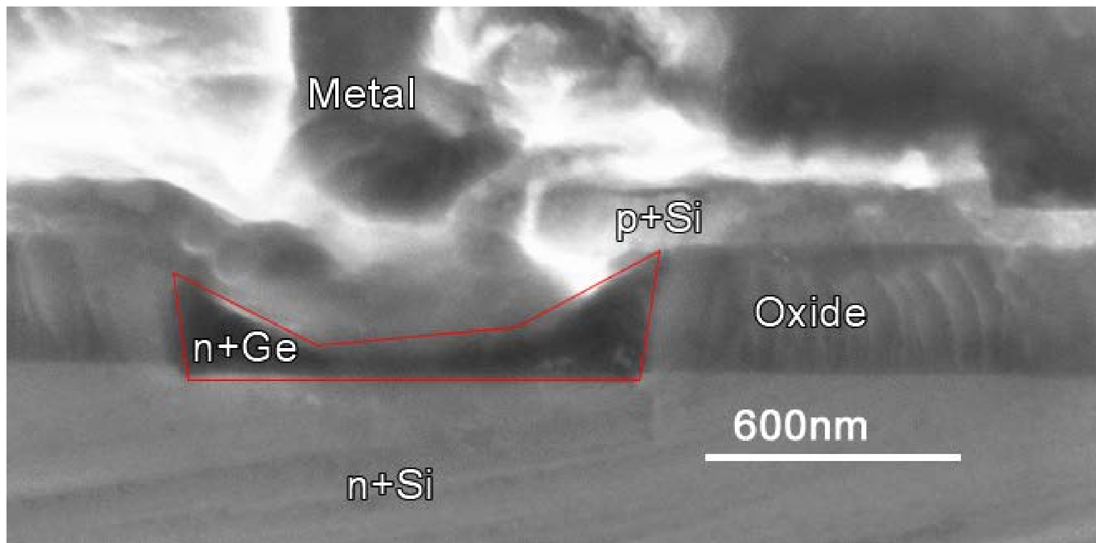

Figure 129.- pnn Ge LD device cross-section of the final device.

A 180nm thick amorphous-Si film was deposited via a Plasma-Enhanced CVD process. Long annealing technique removed excess hydrogen from amorphous Si. More details in the Appendix. Subsequently phosphorus was implanted to a doping level of ~$10^{20}cm^{-3}$ using the set described in the previous chapter. After dopant activation anneal at 750˚C for 30 seconds, a metal stack, consisting of Ti 100nm and Al 1 micron was deposited for top and bottom contacts. Al was surrounded by Ti in both upper and lower surfaces to reduce electromigration. This permitted increasing the current densities above $600kA/cm^2$.

The oxide trench provides excellent current and optical confinement. In order to assure even carrier injection into the n-type Ge, the top contact metal was deposited on top of the waveguide. The increase in carriers injection brings losses in optical confinement bringing the mode closer to the metal and reducing the total amount of possible modes.

After dicing, the waveguides were cleaved to expose the Ge waveguide facets. The devices were polished with Ethyl Glycol slurry to avoid etching of the facets, and to permit a perpendicular interface. A thin oxide layer of ~15nm was deposited on the facets to protect

against contamination and catastrophic optical mirror damage which was observed in devices that did not have oxide protection.

The waveguide emission was measured using a Horiba Micro PL system equipped with a cooled InGaAs detector with lock-in detection. The emission power measurement was calibrated using light from a commercial 1550nm laser that was coupled into a single mode optical fiber with the fiber end at the sample location. In the calibration we verified that the detection was linear with input power. The electrical pumping was supplied by a pulse generator with current pulse widths in the range of 20 μs to 100 ms. The duty cycle was varied between 2 and 50%, typically 4%, to reduce electrical current heating effects and metal failure. The laser was contacted with metal probes and the current was measured using an inductive sensor placed directly in the biasing circuit. The samples were set over a temperature control to keep samples at RT and avoid extraneous effects. The experimental set-up is shown in Figure 130.

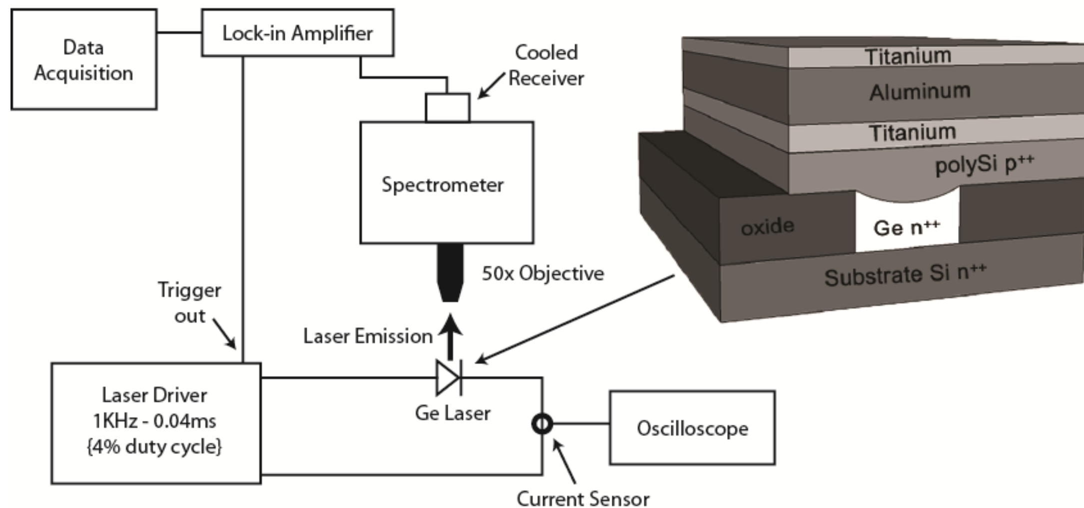

Figure 130.- Schematic of the measurement set-up

Simulations showed that the devices could perform with electrical and optical properties. Furthermore, the values calculated approximate the efficiencies of the final devices.

7.2.2 Simulation

Initial estimates of gain in n-type Ge based on experimental results showed that an n-type doping level of $1x10^{19}cm^{-3}$ would yield a gain of about 50 cm^{-1} [58]. Such a gain can lead to lasing when pumped optically because optical losses are mainly limited to facet losses and free carrier losses in Ge. For electrical pumping, additional losses due to the electrical contacts, free carrier losses in doped poly Si and losses due to the interaction with the contact metal, have to be overcome. Modeling of mode propagation in Ge waveguides with electrical contacts shows that these additional losses are >100 cm^{-1}, as seen in Figure 131. With an estimated thickness ~300nm and width ~ $1\mu m$, only 3 available modes are possible. The losses for TM are large due to metal contacts, as observed. The highly doped Si contacts also increase in absorption under heavy doping. The thickness of the poly contact cannot be reduced since a loss on thickness means an increase on absorption loss to the metal contacts. TE modes are the most likely modes due to low losses.

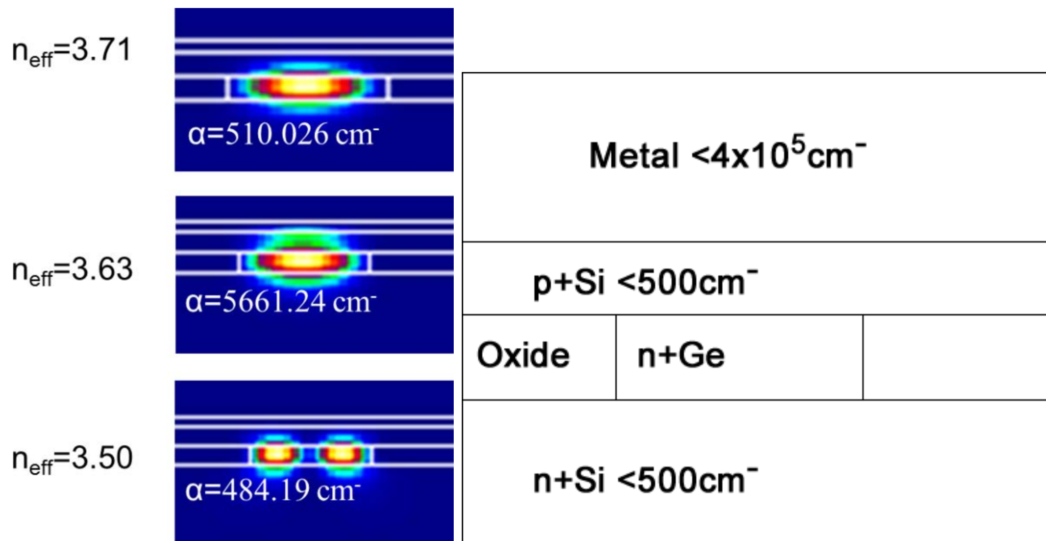

Figure 131- Simulation of Ge modal gain on 300nm thick Ge, permitting only 3 modes. Only TE modes have low enough losses for light emission.

By varying the thickness the total losses can be control, as seen in Figure 132. The expected losses from 100-500nm waveguides change from ~160cm^{-} to 1100cm^{-} from modal losses, not including free carrier absorption of Ge under this doping level. Ge FCA is calculated ~340cm^{-} at 4x10^{19}cm^{-3} doping. On degenerate Ge, calculations from first principles show that FCA <100cm^{-} under high carrier injection [57].

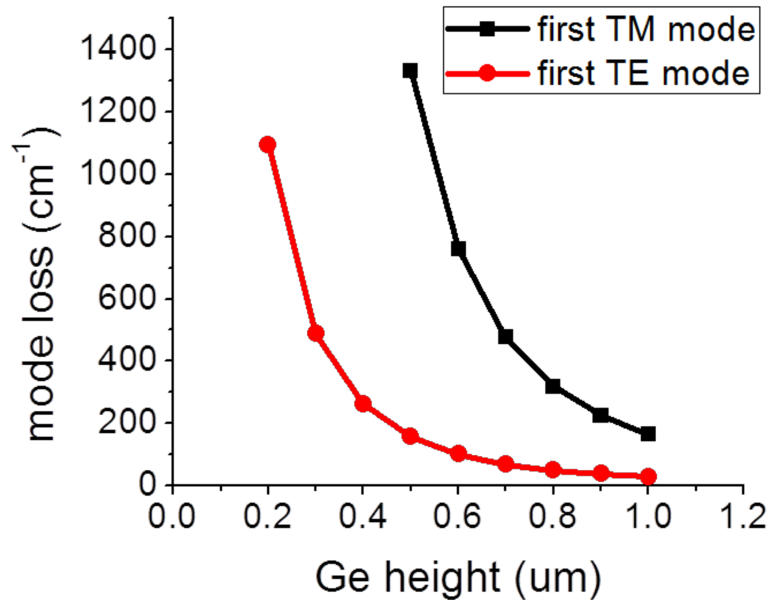

Figure 132.-Simulation of total modal losses in Ge waveguides according from thickness of Ge. (Courtesy of Y.Cai)

To overcome these losses, the Ge gain must be increased by increasing the n-type doping to a level of 3 - 5x10^{19} cm^{-3} [2]. Recently, we achieved n-type doping levels of >4x10^{19}cm^{-3} by using a delta-doping technique during epitaxial growth of Ge [182]. By correlation of photoluminescence (PL) intensity, n-type doping level, and measured material gain, we have determined that an n-type doping level of ~4.2x10^{19}cm^{-3} corresponding to a material gain of >400cm^{-1}, enough to overcome the losses in an electrically pumped laser device.

The electrical simulations were done with Silvaco to establish the effects on optical properties and injection of the carriers. The simulation limits were chosen to reduce processing time and establish the electrical and optical changes on the material over long ranges. We assumed a thickness of 100nm on Ge and poly thickness is ~800nm, and substrate of ~1200nm. The dopant concentrations were limited to similar conditions observed on Ge LEDs. Previous simulations assumed constant index of refraction throughout the different parts of the device. Under forward bias, increased in total carriers in the device can change the index of refraction. As seen in Figure 133, under forward bias of 1.2V, polySi upper contact increases on index of refraction. The increase on *n* pulls the mode up, closer to the metal contact. The increase on index in Ge provides better confinement of the modes, decreasing the modal losses on 100nm to <500cm^{-1}.

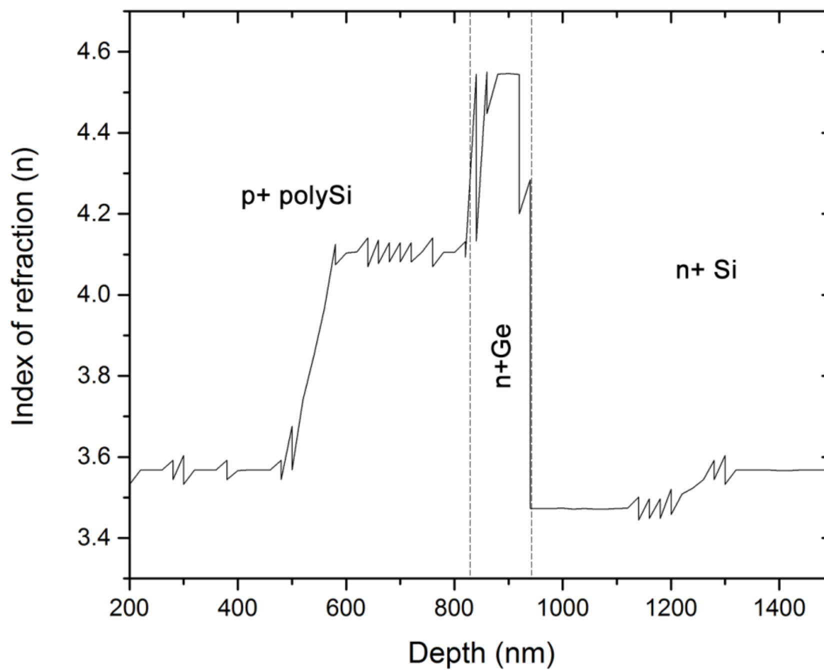

Figure 133.-pnn Ge diode index of refraction change under 1.2V

It is observed that total current density under 1.2V is ~10kA/cm^2 on the interfaces, assuming saturation close to the Ge buffer/n+Si contact. The change in current density of $\Delta J \sim 2kA/cm^2$ is not large enough to limit the performance of the device

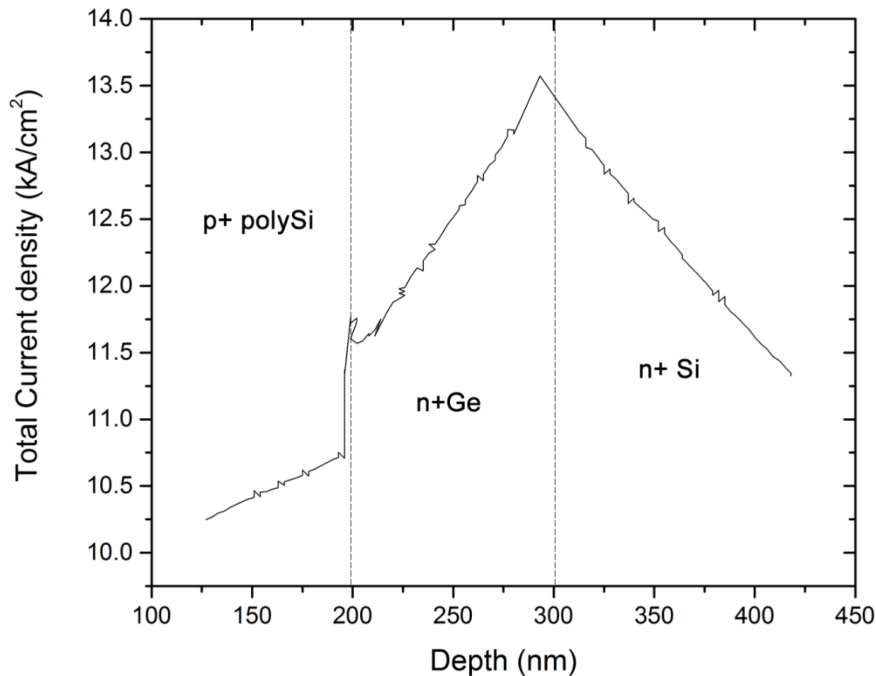

Figure 134.- Carrier density simulation in pnn Ge diode, showing that the maximum current is concentrated on the interface.

The heat of recombination and Joule heating are mostly observed in the Ge body and the interfaces, as seen in Figure 135. The total energy is low enough that under heavy injection $\Delta T \sim 20°C$. The small change in temperature is not enough to justify the large change in peak emission from LEDs, and further justify hot carriers and impact recombination as mechanisms of increasing peak shift.

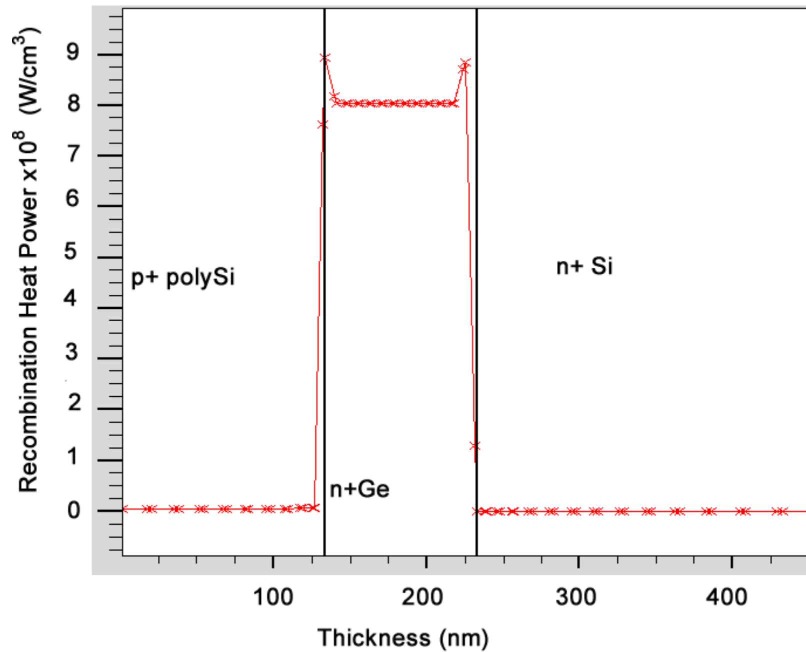

Figure 135.- Heat Generation and Joule heat is concentrated in Ge body.

Ge pnn diodes bands seemed to properly confine the carriers as in Figure 136. Under 1.2V, band bending the material shows proper type I confinement of the carriers. Nevertheless the behavior changes as higher bias is applied.

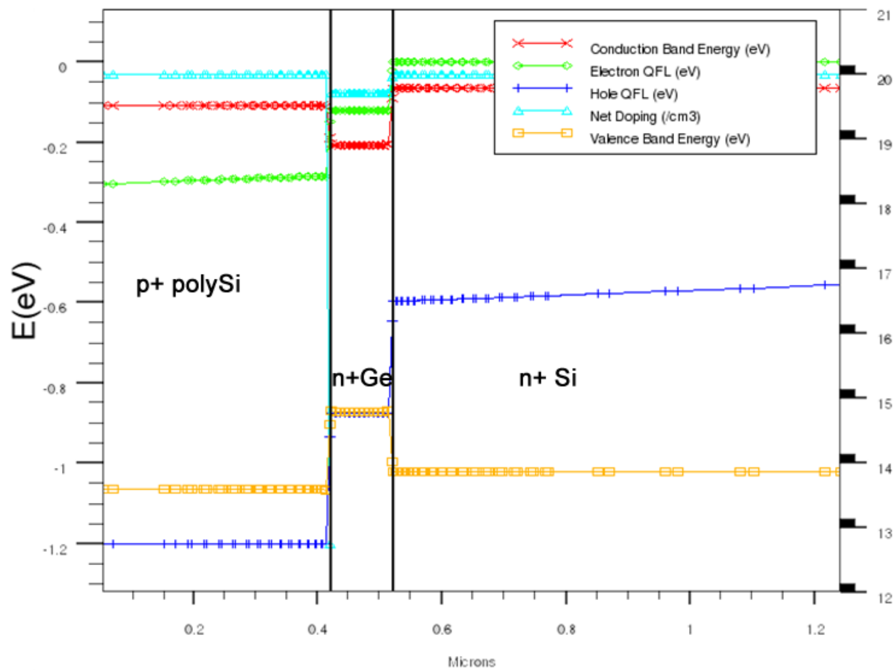

Figure 136.- Simulation of band gap behavior under 1.2V on pnn Ge diode.

The advantage of double heterostructures is the carrier confinement. The increase in doping concentration bends the bands enough that for n+type Si contact the confinement is reduced. As forward bias is applied the carriers confinement changes radically from type II to type I and then to presudo-type I, as seen in Figure 137.

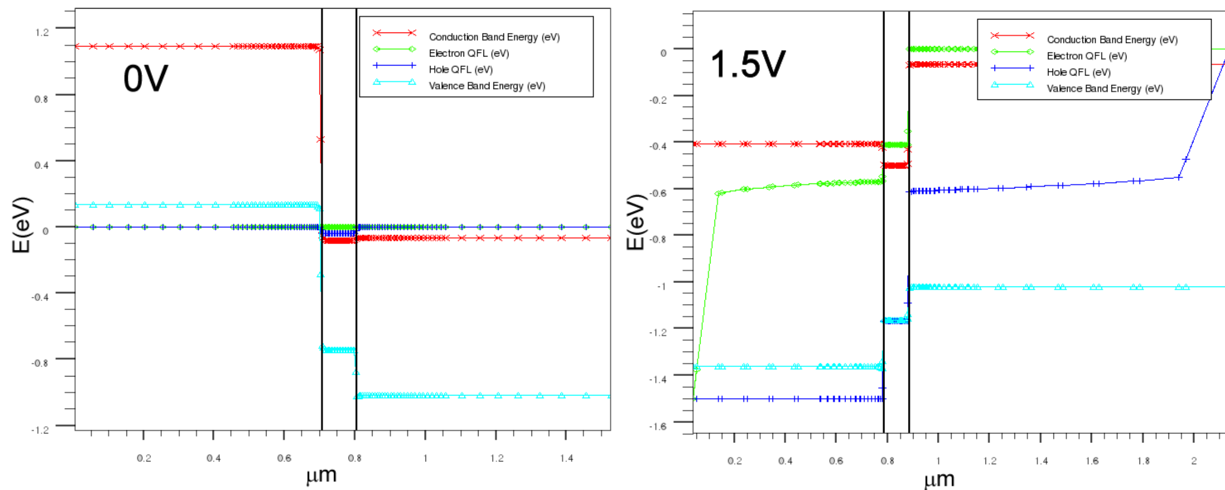

Figure 137.-pnn Ge band bending change from type II to pseudo I under heavy bias.

The change in confinement changes the IV characteristics expected from the device, dividing the emission into the three areas defined by the confinement of the carriers. As seen from Figure 138, from 1V to 1.3V, the type I behavior provides the best confinement, and higher possibility of recombination. Other effects that might help the injection of the device are momentum conservation of the carriers changing from Si to Ge, hot carriers and stronger intravalley interactions.

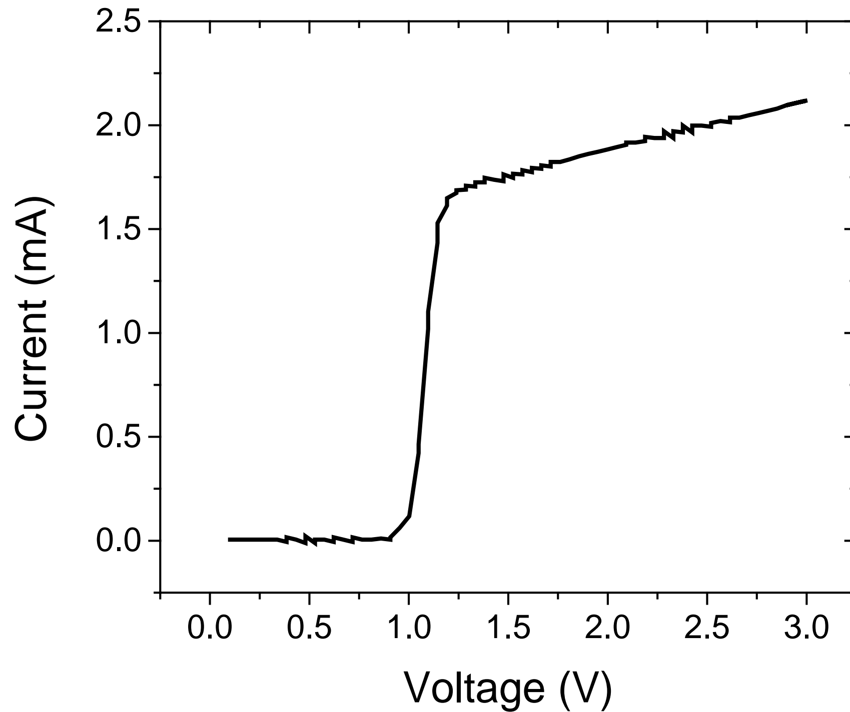

Figure 138.- pnn Ge diode simulation of current input at different voltages. Two different behaviors are consistent with band bending in Ge device

7.2.3 Electrical Luminescence

Electrical characterization of the device showed a different behavior than expected from simulations. The decrease in resistance is observed in IV measurements, as seen in Figure 139.

The I-V behavior is similar do other semiconductor diodes, as expected, but a decrease in resistance is observed as injected carriers is increase. I-V measurement shows low resistance <1Ω, with sudden decrease on resistance. Spike anomalies are considered as noise in the measurement. Such low resistance, and step-like behavior, is expected from heavily doped Ge acting as a laser.

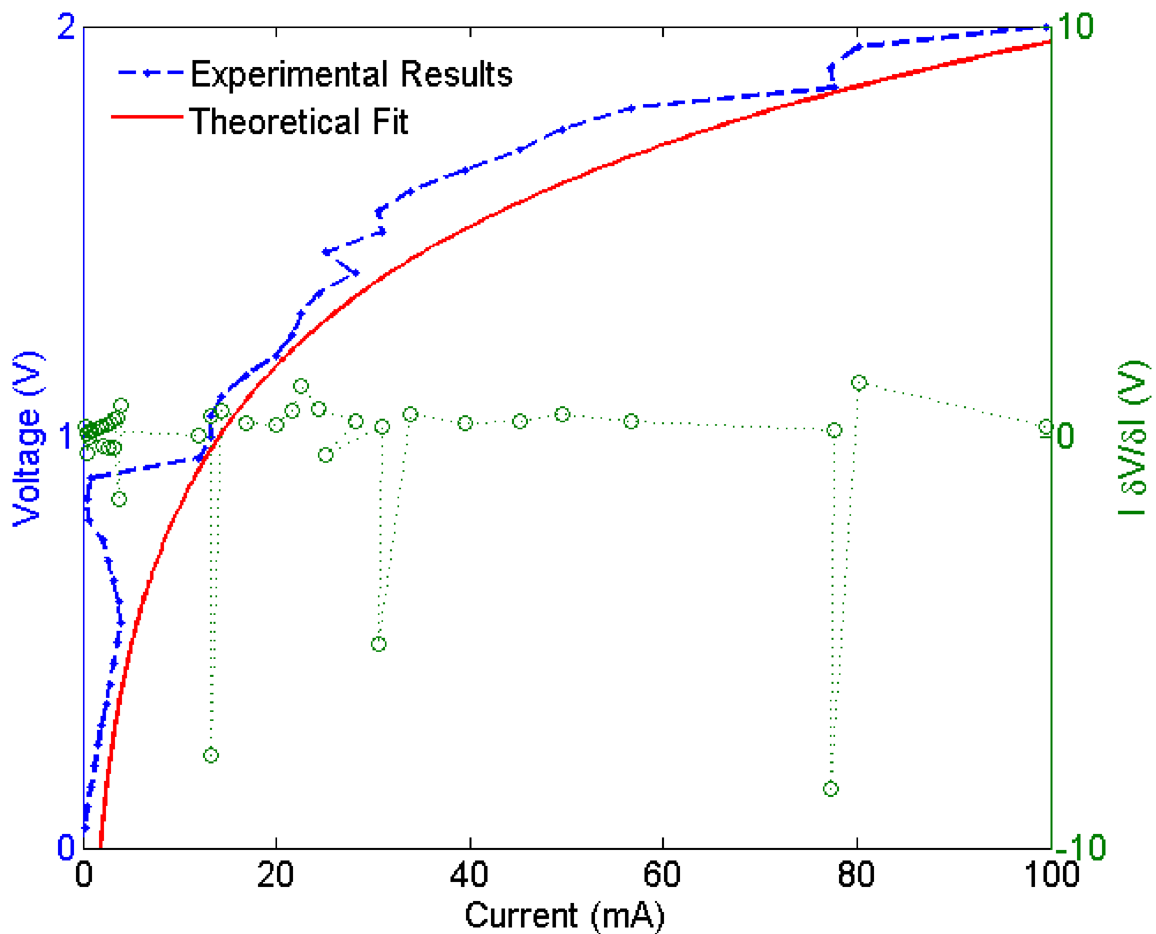

Figure 139.- pnn Ge diode IV characteristics. The ideality factor used is 2, and leakage current is 95% applied bias. Resistance is <1Ω reaching limits of the characterization tool. Shoulder at 5mA is expected from laser behavior.

The device shows a large leakage current equivalent to ~88% of the bias applied. The leakage current is derived from the diode formula and the applied bias V, with the equality

$$V=V_D-I_LR$$

where I_L is the leakage current, V_D bias applied on the device, and R is the series resistance. Assuming an ideality of n~2 – common in LEDs and LDs – the leakage current is calculated.

The high leakage voltage is expected from the band formation and the large carrier density injected. The change in Voltage response close to 1V matches theoretical work.

Emission follows expected effect of confinement and loss. Mirror losses are estimated ~15.14 - 50.4cm^{-1}, assuming SiO_2 interfaces and lengths from 150μm-300 μm. Short integration times assured wide spectrum analyses. Measurement time for these large laser devices is ultimately limited by metal contact breakdown due to the high current flow. Figure 140 shows the spectrum of an electrically pumped Ge laser below and above threshold. Below threshold, Figure 140 (a), no emission can be detected due to the heavy modal losses. When the injection current density is increased above threshold, sharp laser lines appear, as shown in Figure 140 (b).

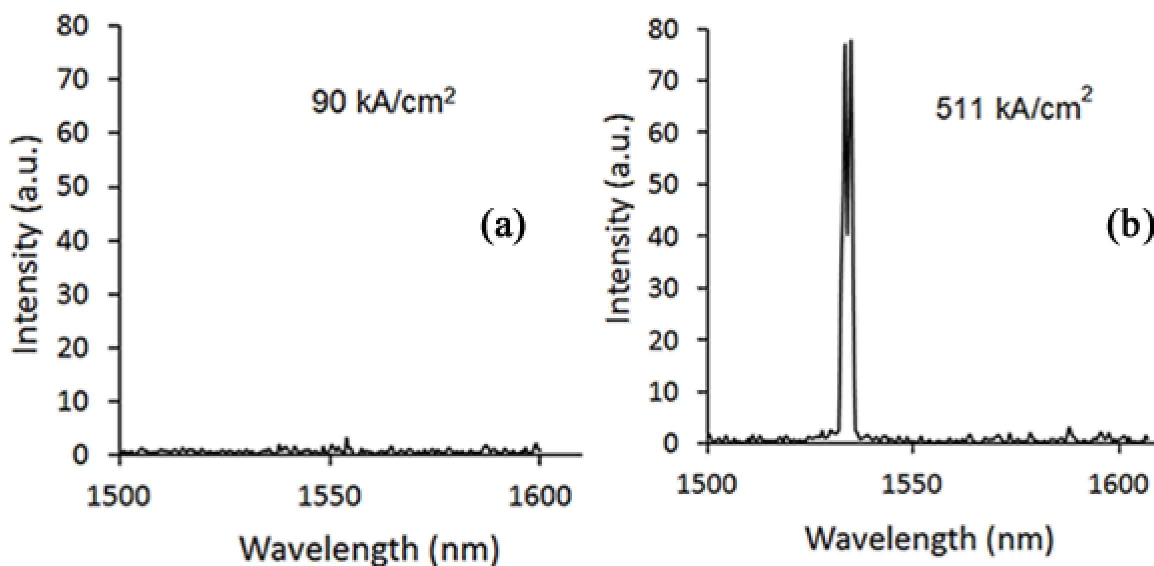

Figure 140.- Ge laser emission spectrum before (a) and after (b) threshold. The cavity length of the waveguide is 333μm and the waveguide height about 100nm. Current injection employed pulse widths of 50μs at 800Hz and 15°C. The detector spectral resolution was 1.2nm

The spectrum shows two lines. The estimate of the cavity free spectral range is 1nm, and the line spacing, 3nm, is a possible multiple of the FSR. Quality factor, Q, of these devices is

>540, which is expected from FP cavities. This can be due to absence of multiple transversal mode, allowing for a better estimation.

Local device temperatures are likely higher due to the high current injection, as was the case with Ge LEDs. Moreover, the temperatures could not be established with certainty, with a measured value of $\Delta T\sim 4K$. Observed linewidth of the individual lines is below 1.2nm -the spectral resolution of the measurement set-up. It suggests a lifetime of the carriers is smaller $<10^{-9}$s on the Γ valley.

Other devices showed similar emission without control of temperature, nevertheless, the metal contact failure stops the device. SEM analysis through FIB cross-section (Figure 141) shows that Si/Ge/Si heterostructure does not see any major changes in morphology. The metal failure shows to be the main constrain during the analysis due to the heavy injection. Used of Ti/Al/Ti permit to increase current densities 1 order of magnitude.

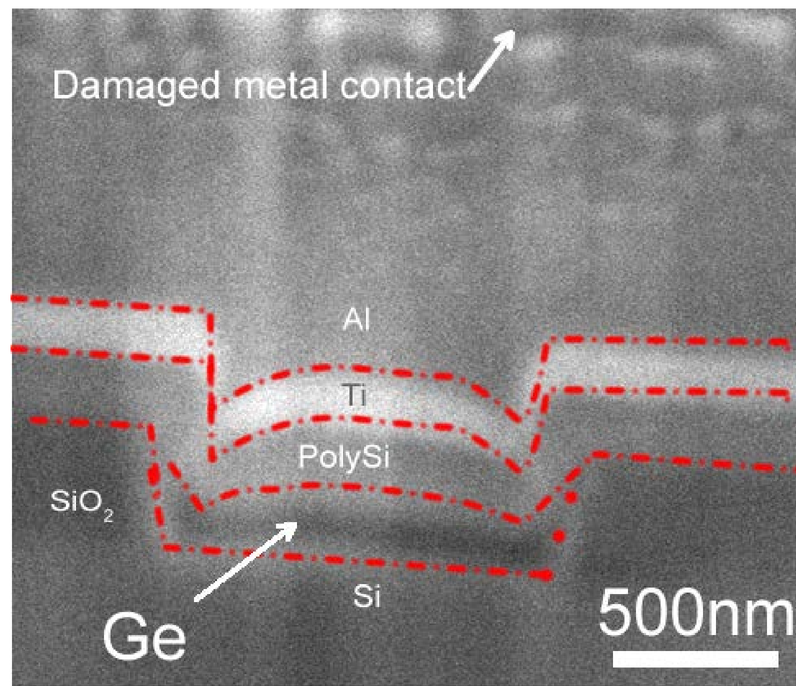

Figure 141.- Cross-section FIB of Ge pnn diode after failure mode occurs. Notice that Ge and Si present no extra defects.

Power spectrum, L-I curve, shows a typical behavior for laser diodes, as seen in Figure 142. The measurement was taken using a wide instrumental spectral resolution of 10nm, at a wavelength of 1650nm, monitoring a single laser line. The lasing threshold at about 280kA/cm^2 is clearly visible. Optical emission power of this device is not representative of the maximum power observed. The maximum power observed was up to 8 mW on ~1680nm. From the L-I curve, η_i~9.8%, being in order with the calculations for intrinsic efficiencies. It was shown that the maximum possible $\eta_i$was limited by the Si contacts, with a value of~10% [173], due to defficiency of injection of carriers. From possible maximum power, threshold and efficiency is back calculated from,

$$P_{out} = \eta_i \frac{hv}{q} \frac{\alpha_m}{\alpha_i + \alpha_m} (I - I_{th}).$$

If intrinsic losses are reduce, the maximum output power doubles to ~20mW. Mirror losses are going to be expected, but the losses can be reduced through use of distributed feedback gratings, or Bragg gratings. More efficient mirrors will increase the wall-plug efficiency another order of magnitude

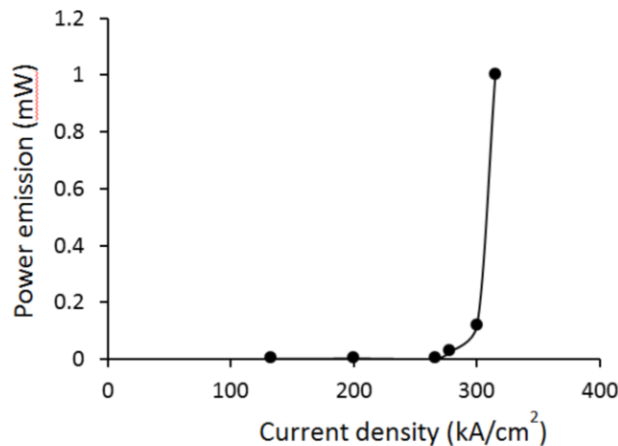

Figure 142.- L-I curve for a 270μm long waveguide device. 40μs electrical pulses were used at 1000Hz. Measurement temperature was 25°C.

The wall-plug efficiency of these devices is calculated as P_{out}/P_{in}~0.5-4%. The range is determined through analysis of I-V and L-I characteristics. The plug-wall efficiency is large when both leakage current, hot carriers, and optical losses are taken into account.

The differential quantum efficiency can be extracted from these results [183]:

$$\eta_d = \eta_i \frac{\alpha_m}{\alpha_m + \alpha_i},$$

where α_i is the intrinsic losses depending on the non-radiative recombination rate, spontaneous radiative or stimulated radiative recombination rate and Auger recombination rate. Using the stated assumptions for losses, the differential quantum efficiency is ~2.3%. This is relatively small compare to other III-V lasers [184], but comparable to first bulk DH GaAs laser demonstrated in Ref. [185]. Additionally, the extraction efficiency, η_e, of the device is calculated ~53%, as expected from a double facet system.

The devices showed a lasing range from 1520nm to 1700nm. Figure 143 shows selected laser lines between 1576nm and 1656nm for different Fabry-Perot cavities of the same gain material. Different devices show a dependence on emission wavelength with threshold current density, which is expected from the modal loss variation and confirms the theoretical conclusions that the gain spectrum of Ge for the given doping level and strain reaches over more than 100nm spectral width [186]. The shorter wavelengths show larger threshold current, as was expected from theoretical work.

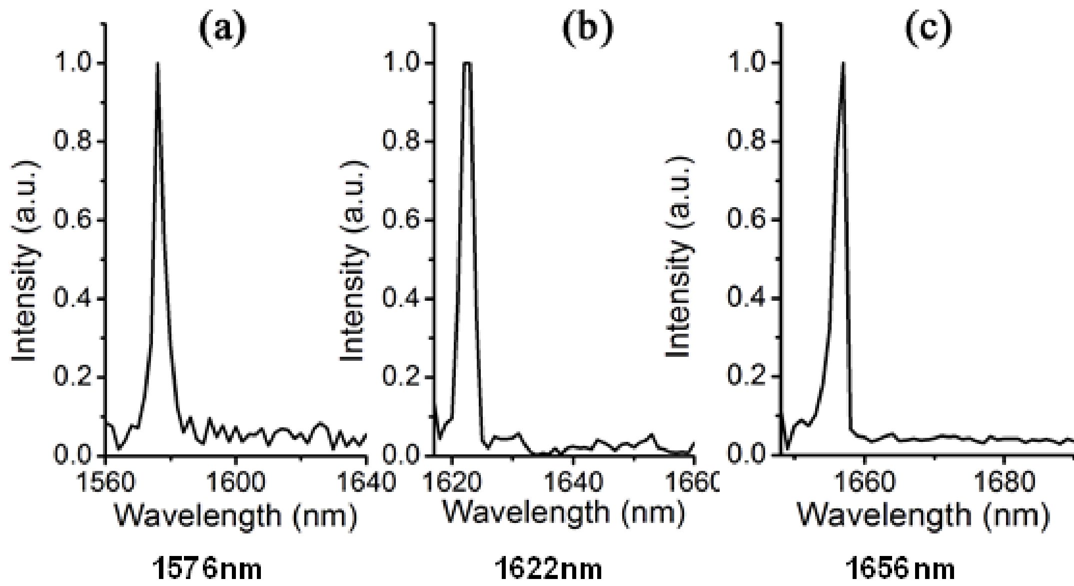

Figure 143.- Spectra of Ge lasers with different Ge waveguide heights. The measured laser line wavelengths are (a)1576nm, (b)1622nm, and (c) 1656nm.

Moreover, the device shows wider spectrum emission due to the BGN and BGR effect caused by the degenerate band and the injection of excess carriers, as seen in Figure 144. Theoretical work suggests a gain bandwidth of >300nm. The shorter wavelengths require larger carrier density to obtain a net gain large to overcome losses, matching observed experimental threshold current behavior. Experimental results show emissions wavelengths range is from 1520-1700nm, falling inside the range of theoretically calculated gain under $5x10^{19}cm^{-3}$ carrier injection. Dimensions of Ge waveguide – $1\mu m$ width - permit different modes to be excited, and coexist. Furthermore, CMP non-uniformities contribute to thickness variations, therefore changing gain clamping conditions, preferentially selecting certain wavelengths according to loss.

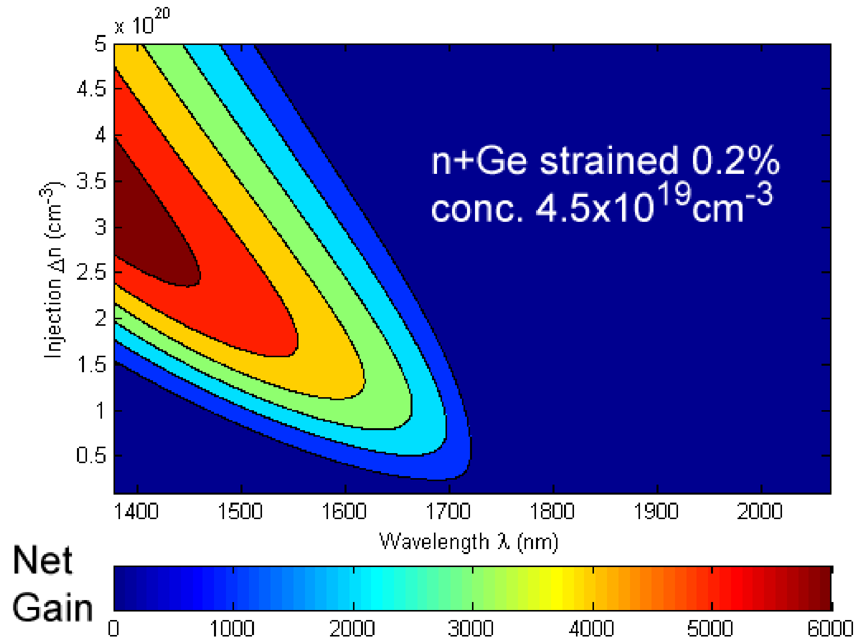

Figure 144.- Calculated net gain in 4.5x10^{19}cm^{-3} n-type strained Ge. Bandwidth of emission is >300nm.

The gain clamping conditions for the different devices were related to the thickness variation. The cavity under lasing action optical gain can be approximated to a waveguide; it is clamped at exactly the value of the resonant cavity losses. Furthermore, Ge thickness changes the amount of mode leak into the metal. As Ge becomes thinner, resonant modes are leaked into the highly-doped poly-Si cladding and into the lossy metal contacts.

Since the modal loss is the main source of losses, the facet light spectrum clamps will be strongly modified by this loss. G_n is the net modal gain equal to $\Gamma g - \alpha_i - \alpha_m$. Since α_i and α_m depend on thickness of the device, and its length, the spectrum lines with larger gain are correlated with the waveguides with smaller loss.

The wavelength corresponding to the Ge gain peak (the threshold injection level) and the cavity loss is the expected emission wavelength of the device. As the modal confinement

decreases with decreasing Ge layer thickness, modal loss and correspondingly threshold current increases and the emission wavelength blue shifts. Burst-Moss blue shift is not significant in these calculations. In Figure 145, we show spectral threshold conditions for two different modal cavity losses using a parabolic band model, showing match with theory.

A Ge waveguide of 500nm thickness has a modal loss of about 90 cm^{-1} due to losses in the doped poly Si and the metal electrode (solid line). A Ge waveguide of 100nm thickness, however, has a modal loss of ~1000cm^{-1} due to the closer proximity of the mode to the electrode (dashed line). To overcome the high losses of the thin Ge waveguide, a relatively high carrier injection level is needed. Lasing is therefore expected at < 1520nm. For lower loss waveguides we expect lasing to occur at longer wavelengths as shown in Figure 145.

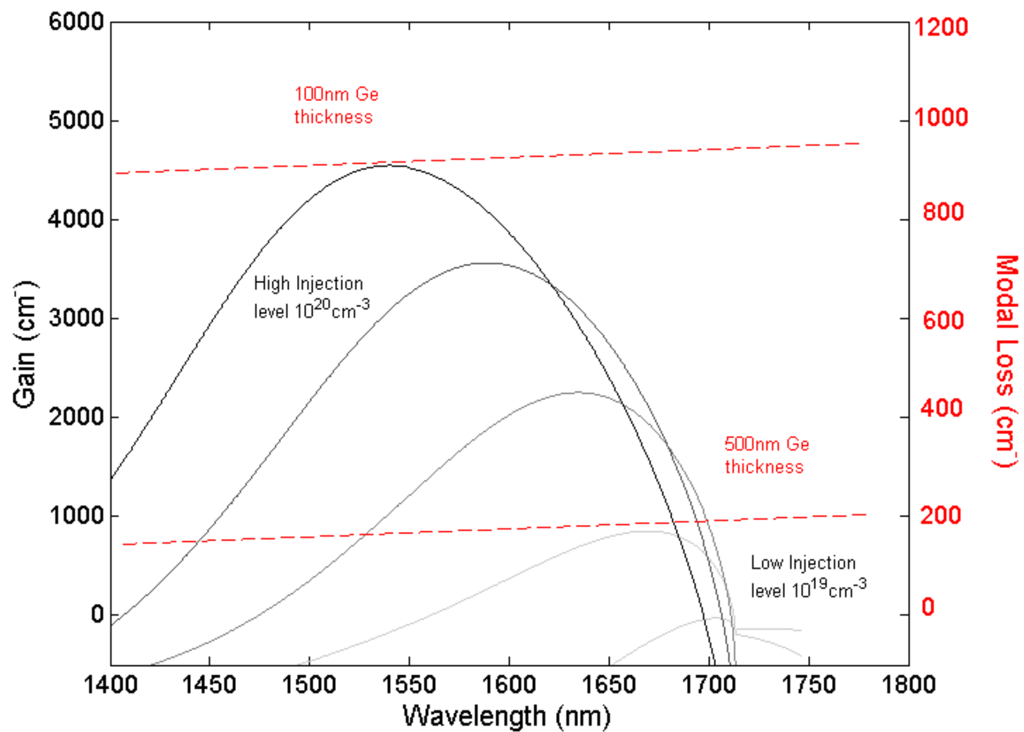

Figure 145.- Simulation of gain clamping condition for two different Ge waveguide thicknesses (100nm: solid line; 300nm: dashed line). The axes plot the corresponding modal loss and gain

spectrum for the two different injection levels that are needed to overcome the respective modal losses and to achieve lasing.

From the calculations, it is possible to extract the radiative lifetime of the carriers in the device. When calculating the threshold current density for a laser device, we obtain [187]:

$$\tau_r = (\frac{n_0 ed}{\eta_i} + \frac{\alpha_i}{\Gamma A} + \frac{1}{\Gamma AL}\ln\left(\frac{1}{R}\right))/\, J_{th}(d)$$

where $= a\frac{\eta_i}{ed}$,τ_r is the minority carrier lifetime or recombination lifetime in n-type Ge; d is the Germanium thickness; Γ is the confinement factor which extracted from simulations; L is the cavity length; R is the front and back mirror reflectivity calculated as 23%; *a* is the differential gain ~$2.44\mathrm{x}10^{-17}$ cm^{-2}; and n_0 is the injected carrier density at transparency which is ~0.5-$2.7\mathrm{x}10^{20}cm^{-3}$. Notice that the current density has a linear relation with thickness of the material. This is because thicker the material, the more carriers are required to achieve transparency. The result for the radiative lifetime is less than <10^{-9}s being orders of magnitude lower than previously measured.

The calculation does not take into account BGN or BGR, which change a(n) and n_0(n), as a function of carriers. This would induce a smaller radiative lifetime, causing larger radiative stimulated recombination.

The total losses in the waveguides suggest a total gain larger than $1000cm^{-}$, as was calculated by Cai, et al [56]. The gain under $4.2\mathrm{x}10^{19}cm^{-3}$ dopant concentration exceeds previous theoretical expectations [58], showing the need to add BGN to BGR for a complete picture of gain behavior and light emission in Ge.

7.2.4 Conclusion

We have observed lasing from electrically pumped n-type Ge Fabry-Perot cavities. The threshold current densities decrease with increased modal confinement. The emission linewidth is less than the 1.2nm resolution of our measurement set-up. Laser emission wavelengths were observed between 1520nm and 1700nm with a variation consistent with the gain clamping condition for each device. Measured output powers greater than 8 mW at room temperature were measured. Internal quantum efficiency of 9.8% is close to theoretical calculated. A wall plug-efficiency of 0.5-4% is calculated as a first generation Ge laser diode.

In summary,

- First demonstration of Ge-on-Si DH laser diode
- Linewidth emission < 1.2nm
- Bandwidth emission larger than 200nm, matching theoretical expectation
- Correlation of modal losses with mode clamping according to Ge thickness
- Clear laser threshold behavior under high injection
- Output power up to 8mW, with plug-wall efficiency as high as 4%

Improvements in Ge growth, electrical contacts, and in modal loss reduction will decrease the lasing threshold to values comparable with Fabry-Perot diode lasers. The high power and observed gain spectrum of nearly 200nm indicate that the Ge laser could be used for WDM applications. Since the laser can be monolithically integrated into any CMOS process flow, novel device applications and systems can be developed.

Chapter 8. Summary and future work

Epitaxial Ge-on-Si has a pseudo-direct band gap and compatibility with Si technology. Our theoretical and experimental analysis has shown that Ge can be band-engineered to behave like a direct gap material by using tensile strain and n-type doping; moreover, it can provide optical gain, and inversion of carriers. We reported the first observation of direct band gap lasing through photo- and electro-luminescence, showing the onset of optical gain of n+ tensile-strained Ge-on-Si at room temperature.

We have shown a growth process that permits the formation of devices while retaining <0.2% tensile strain in Ge. The need of a Ge buffer is questioned, and shown to be unnecessary for heavily doped n-type narrowed waveguides of Ge under $2\mu m$ width. Through different growth techniques, we have shown a proper technique to measure the final thickness of the devices grown in oxide trenches. We have also shown the Ge-P reaction depends linearly with total pressure, affecting minimally the facet formation, which is partial pressure dependent. Future work would confirm the effects under lower and higher total and partial pressures of the active gases.

We showed effective methods of doping using CMOS compatible techniques. SOD would be recommended for sample and optical material analysis. For electrical injection, implantation and delta doping hold the best promise to increase the total active dopant concentration, as observed. At the moment, the maximum dopant concentration is ~4.2-$5.5\times10^{19}cm^{-3}$ achieved through delta doping and implantation. It is recommended to further explored implantation technique samples due to the larger increase in active dopants that was observed.

We have demonstrated new understanding of Ge conduction bands under heavy doping. The positive effects of temperature on Ge are more evident with increasing doping concentration. Indirect Auger recombination and thermalization interactions present a plausible explanation for the increase luminescence behavior. Both interactions represent a condition where the non-radiative recombinations increase slower, or at the same rate, than radiative recombinations with added dopant or increase temperature, differing from establish semiconductor theory.

We have validated the device concept with a monolithically integrated, Ge-on-Si LED and LD that shows room temperature direct band gap electroluminescence in Ge. Ge-on-Si LEDs have shown bleaching effect and appropriate temperature stability with Ge n-type doping increase >$1x10^{19}cm^{-3}$. We verified Ge-on-Si optically pumped laser with a gain >$50cm^{-1}$; and Ge-on-Si Laser with gain >$1000cm^{-}$. Ge laser shows a bandwidth of >200nm, in accordance with theory. Linewidths <1.2nm Further studies of the latter will confirmed the assumptions made in modal losses and the impact on threshold current.

Ge-on-Si laser emits in the telecomm window; it is stable under high temperatures; its maximum output power is similar than III-V hybrid lasers at RT; and it is CMOS compatible. It is our hope that this device can provide the technology for a new boom in opto-electronic integration.

8.1 Applications

Germanium as a full integrated device has been explored along this thesis work. Ge as a laser can be used for a full monolithically integrated laser emitting in the telecom range. Such bandwidth emission permits a larger wavelength range than any previously known semiconductor laser, making it ideal for wavelength division multiplexing applications (WDM).

WDM applications can be divided into on-chip and out-chip applications. On-chip applications are more suitable for computing. Growth of Ge on Si can be done parallel to electronic chip applications, or as a back-end process. Ge thermal properties permits using it on servers, databases and other high data applications in which cooling is a power drain. Substituting Ge for III-V lasers, which down perform at high temperatures, can alleviate the cooling cost.

Evidence of emission up to 450℃, suggest that Ge LEDs can be used for extreme environments. It is the only semiconductor, known to date, which has such behavior. This out-chip application can be generalized to other areas such as a semiconductor optical amplifier (SOA), fiber optics, etc.

Focus on high temperature semiconductors for light emission and detection research could start with the use an implementation of Ge devices.

8.2 Future Work

The support of indirect band gaps on emission has provided the possibility of using Ge LDs for high temperature applications, making it the only semiconductor capable of such feat. High temperature studies are recommended for future work and analyze the effects on LEDs and LDs. Further analysis of the defect concentration effects on luminescence is required to improve processing of the devices.

It should be self-evident that a less lossy metal or upper semiconductor contact will enhance the efficiency of the devices. However, using the same material as an upper contact, Ge/Ge/Si diode will not work. Ge is highly absorbent. Since the upper contact would not achieve transparency, the material will always absorb, as shown in Figure 146. The material will have higher losses from optical modes.

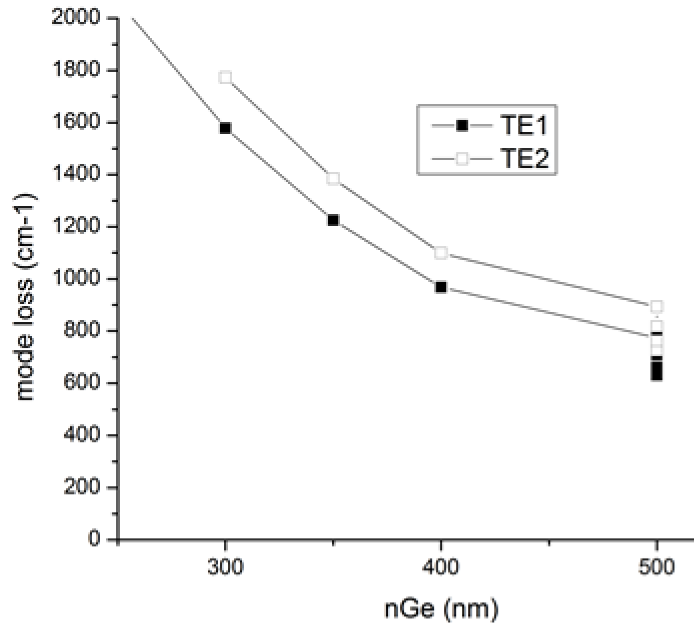

Figure 146.- Absorption of p+Ge/n+Ge/n+Si diode under different thicknesses of n+Ge

Internal Quantum efficiency limitation through the p+Si cladding could be solve with a better hole injector, as Ge. III-V materials might portray same problem as Si due to low hole mobilities.

In p+Ge/n+Ge/n+Si device, alignment of the bands provides appropriate type I confinement for the carriers for a certain biases. As bias increases, same problem observe with Si is observe (Figure 147).

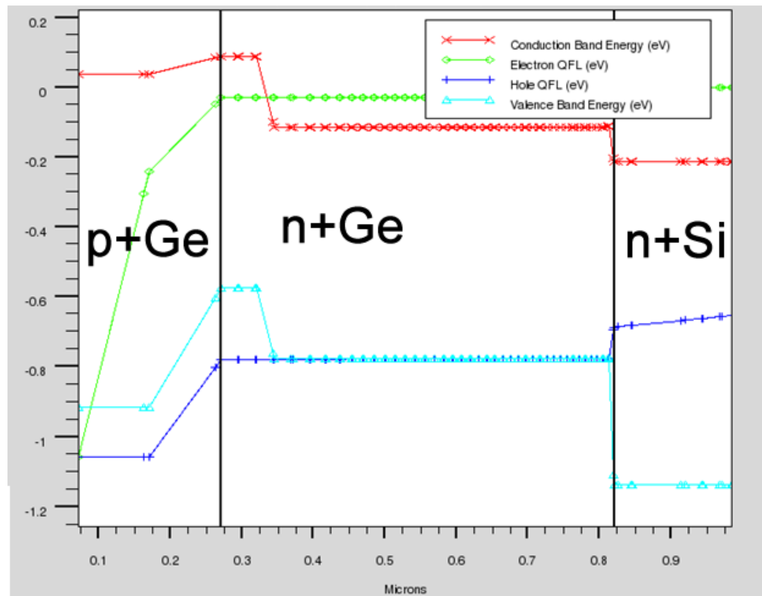

Figure 147.- Band alignment of Ge/Ge/Si diode under heavy bias.

Change of n+Si cladding into larger bandgap will provide a stable type I carrier confinement. A change of the substrate will lead to further difficulties in processing.

Research on implanted samples should be analyzed more carefully. The use of recrystalline Sb or As coimplanted with P showed potential. However, heavy damage imparted by the ions causes vacancy compensation and prevents observing doping enhanced diffusion. The diffusion of the ions becomes slower than bulk P in Ge, resulting in a net loss of P instead of an increase. This method should be analyzed more carefully with deeper implantation of ions.

Delta doping as a method for doping Ge has shown to be the best method by enhancing the dopant concentration, preventing defect compensation and keeping the process in situ. It is recommended to pursue this method in depth, and pursue multiple layers, instead of the maximum of four layers of P treated in our study.

Further research on carriers lifetimes is necessary to confirm the interactions theorized in this thesis. Using minority carrier lifetimes published in the past, does not account for the different band gap we are using neither the possibility of increase radiative efficiency by increase

carrier density in the direct band. Careful analysis of minority lifetimes is required to complete the view in Ge.

Dopant diffusion behavior and mechanisms required further study. Available data only involves heavily implanted material, which introduces a large amount of defects. As proven in this thesis, active doping is not equivalent to total doping in the material. Defect compensation of the total doping has to be study furthermore, as how the increase defect interactions prevent or enhance the dopant diffusion.

It is recommended to explore further architectures of Ge devices cavities such as DBR, DFB and coupled microdisks to observe better results of the devices. Lateral injection of the devices also will hold better injection through the device, and provide less TM losses. Part of the design future work is summarized in Cai et al. [56]. Uniform carrier injection is necessary in any of the new designs to avoid lossy scattering points in Ge.

Using III-V materials growth selectively on Ge would be the best option for lower index and bandgap difference. Furthermore, III-V materials might provide a surface with variable tensile strain capable of improving the direct band. GaAs or InP would provide less leakage current increasing the total wall-plug efficiency.

Better architectures improving confinement of carriers, better cavities and higher doping in Ge will provide a better option to improve the overall efficiency of the laser devices. Ge paved the way to Si electronics, now we can see Si paving the way for Ge opto-electronics.

Appendix

Appendix. I RCA cleaning

The original RCA is based on a two-step oxidizing and etching treatment using hydrogen peroxide solutions[122]. The first is rinse is in a high-pH solution in which the wafers are placed at 80℃ . On this condition a thin layer oxide is created and dissolve continuously in the Si surface. This combination helps remove particles still on the wafer. The second solution is low-pH which function is removing alkali ions and cations insoluble in the previous rinse. Typical "Si RCA clean" steps for Ge growths are:

1) tank 1: H_2O:NH4OH:H_2O_2 (5:1:1) - 10 min- 80℃

2) rinse - rinser1

3) H_2O:HF (50:1) - 60 sec - RT

4) rinse - rinser1

5) tank 2 : H_2O:HCl:H_2O_2 (6:1:1) – 15 min - 80℃

6) rinse – rinser2

7) H_2O:HF (50:1) - 30 sec - RT

8) rinse – rinser1

9) Spin dry

The second HF dip is to functionalize the Si substrate with H bonds. In typical Si growths, this step is not necessary.

Due to the high concentrations of peroxide, and with the knowledge that high-pH with peroxide etches Ge, a different RCA clean has been developed.

For the steps called "Ge RCA clean":

1) tank 1: NH4OH:H2O (1:4) - 5 min

2) rinse - rinser1

3) tank 1: H2O2:H2O (1:6) - 30 sec

4) rinse - rinser1

5) HF - 15 sec

6) rinse - rinser1

7) tank 2: HCl:H2O (1:4) - 30 sec

8) rinse - rinser2

9) spin dry

This sequence minimizes Ge etched through the peroxide.

Appendix II. Standard Ge growth

Ge growth consists of UHVCVD epitaxial growth on bulk silicon substrates with (100) orientation and flats perpendicular to the [110] direction. Here we use the same growth process as has been described in other works [25, 77].

The substrates are clean through a Piranha and RCA clean, described in Appendix I. A thermal wet-oxide is created over the Si substrate. The thickness depends on the function of the devices pursued. The final thickness of the Ge has to be considered when the oxide thickness is chosen to permit the sidewalls of devices to be passivated with the oxide. The oxide growth rate is described in Table 9.

Table 9.- Oxidation time versus thickness (Agmstrongs) chart. These are approximations and should always be checked every 6 months.

	Time (minutes)					
Thickness	Dry				Wet	
(A)	800 C	900 C	950 C	1000 C	1000 C	1050 C
40	30					
50	45					
100		25				
200		70	30			
500			130	60		
1000				180	5:45	
2000					22	
3000					40	
4000					60	
5000					90	
6000						75
7000						95
8000						122
9000						150
10000						200

It follows a lithographical step. Using the SSI 150 Coater prevents human errors and reproducibility since this tool permits both coating and development of the photoresist. The

usual thickness of the photoresist is 1 micron with PDC-1 photoresist. The steeper used for lithography is the Nikon NSR-2005i9 which has the minimum resolution of 700nm. It allows using a single mask to do different die exposures. It also allows further exposures aligned with a resolution under 500nm. This is ideal for multiple lithographical steps such as for the design of pnn devices.

After development of the resist, a reactive ion etching (RIE) is used through AME Model P5000 or Lam Research Model 590. In both cases, a mixtures of gases of CHF_3 and CF_4 as can be seen in Table 10.

Table 10.- Etch rates under different conditions (courtesy of E.Lim, MTL MIT)

	Initialization	Stabilization	Etching			
	Step 1	Step 2	Step 3			
Gas CHF_3	10	10	10	10	20	40
Gas CF_4	40	40	40	40	30	10
Pressure	20	20	20	20	20	25
ECR	0	50	200	400	200	200
RF	0	20	20	20	20	20
Temp.	25	25	25	25	25	25
Rate (A/sec)			10	20	10	10
Angle on under 700nm oxide			~77	~75	~82	~85

Removal of the photoresist followed through oxygen plasma etched with the Matrix 106 Plasma Asher. This process avoids damage of the Si substrate while removing most of the photoresist.

A BOE etch removes any residual oxide in the prepared wafer. This has to be short to avoid changing the angle etched through RIE. The expected etch is from 20-50nm oxide, succeeding on leaving a pristine surface. Piranha cleaning, consisting of H_2SO_4:H_2O_2 3:1 for 15 min, is used to clean any particles and photoresist left.

To functionalize and clean the surface, a Si RCA clean is used, as shown in Appendix I. Ge growth in Sirius UHVCVD happens immediately.

The wafers are heated to 750°C and H_2 flow to remove any native oxide and water vapor in the surface. The temperature is decreased to 360°C to grow a buffer layer. The Ge flow is 10sccm at a pressure of ~4mtorr. This low-temperature deposition permits a thin, but highly defective Ge buffer epitaxy layer.

On top of the buffer layer, a high-temperature (650°C) growth of P doped Ge creates a thick layer of high quality crystalline n+ Ge with an activated P concentration of up to $\sim 1 \times 10^{19}$ cm^{-3} [125]. P was flown at 12 sccm and Ge at 3.8sccm at a 9.8mTorr. The growth rate is ~5.55mTorr. The wafers are left to rest under high vacuum while cooling down, to avoid P desorption and GeO_x formation.

Any modifications *a posteriori* from this step are discussed in chapter 3.

Appendix III. Highly doped Ge through Spin on Dopant

Starting with purchase 6" Si prime wafers (100) .

Step	Lab	Machine	Action
1	ICL	Acid-hood	Piranha
2	ICL	RCA	RCA cleaning
3	SEL[1]	UHVCVD	Ge growth[2]
4	ICL	RCA	Ge recipe[3] [With old wafers a bath of 5min in HF would be succinct]
5	TRL	PMMA Spinner	Spin PDC1-2000 (P Spin-on-dopant)
6	TRL	Hot Plate	Hot plate bake (200C for 20min) [This procedure is intending to remove the organics]
7	TRL	STSCVD	SiO2 50nm and SiN 200nm growth (preventing outgasing of P)
8	TRL	RTA	5min 800C
9	TRL	Acid-Hood	HF/H2O baths to remove excess dopant and SiN

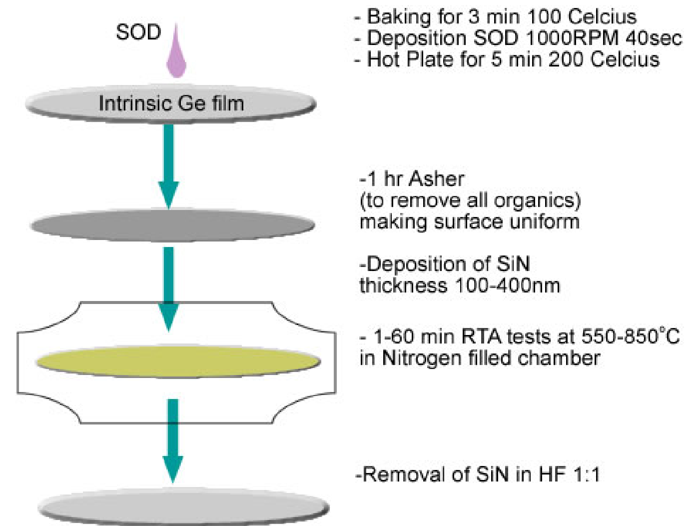

Figure 148.- Schematic describing process for increasing dopant concentration through Spin on dopant.

[1] Surface Engineering Lab in 13-1150
[2] previously approved out-of-MTL process
[3] previously approved recipe

Appendix IV. n-Ge diodes

Purpose: To selectively growth nGe and fabricate isolated devices

Process Step:

Starting with 6” wafers

Step	Lab	Machine	Action
1	ICL	RCA	RCA cleaning
2	ICL	Tube 5D	thermal oxide deposition
3	TRL	EV1	patterning #1
4	ICL	AME5000 Ch. A	oxide etching, two alternatives: 1) RIE + BOE (for last 10nm oxide) 2) RIE only (Fig. 1)
5	ICL	Asher	photo resist strip
6	ICL		Piranha
7	ICL	RCA	RCA cleaning
8	SEL[4]	UHVCVD	Ge selectively growth[5] with phosphorus in-situ doping. (Fig. 2)
9	ICL	RCA	Ge recipe[6]
10	ICL	DCVD	PECVD oxide deposition (Fig. 3)
11	TRL	acid-hood	etch backside Ge by H_2O_2

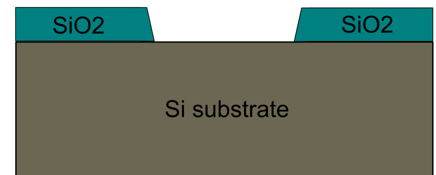

Fig. 1

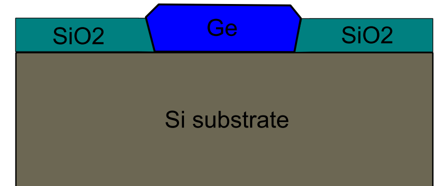

Fig. 2

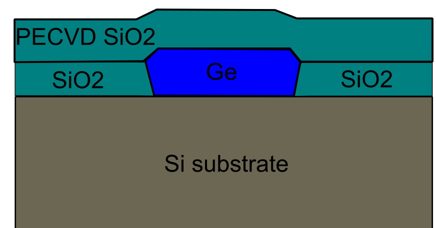

Fig. 3

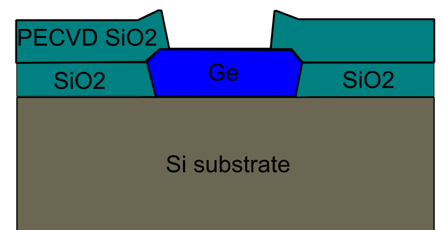

Fig. 4

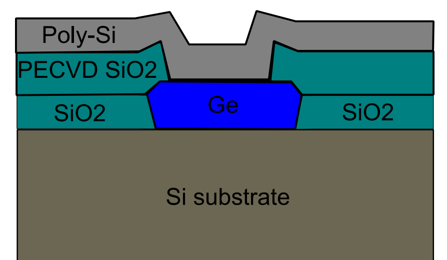

Fig. 5

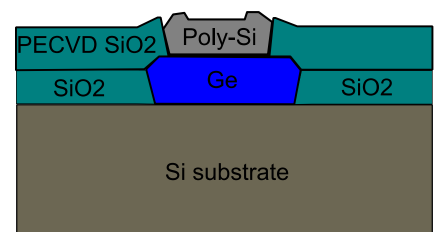

Fig. 6

[4] Surface Engineering Lab in 13-1150
[5] previously approved out-of-MTL process
[6] previously approved recipe

12	TRL	EV1	patterning #2
13	TRL		oxide BOE etching (Fig. 4)
14	TRL	Asher	photo resist strip
15	TRL	RCA	RCA cleaning
16	TRL	Tube B4	amorphous Si deposition (560C) (Fig. 5)
17	Innovion		phosphorus implantation
18	TRL		double Piranha
19	TRL	RCA	RCA cleaning
20	TRL	Tube B3	annealing (700C, 15min)
21	TRL	EV1	patterning #3
22	ICL	AME5000 Ch. B	poly-Si etching (Fig. 6)
23	ICL	Asher	photo resist strip

Appendix V. Ge Selective grown PNN device

Process Step:

Starting with 6” wafers

Step	Lab	Machine	Action
1	ICL	RCA	RCA cleaning
2	ICL	Tube 5C	thermal oxide deposition
3	ICL	Stepper	patterning #1
4	ICL	AME5000 Ch. A	oxide etching, two alternatives: 1) RIE + BOE (for last 10nm oxide) 2) RIE only (Fig. 1)
5	ICL	Asher	photo resist strip
6	ICL		Piranha
7	ICL	RCA	RCA cleaning
8	SEL[7]	UHVCVD	Ge selectively growth[8] with phosphorus in-situ doping. (Fig. 2)
9	ICL	RCA	Ge recipe[9]
10	ICL	DCVD	PECVD oxide deposition (Fig. 3)
12	ICL	Stepper	patterning #2
13	ICL		oxide BOE etching (Fig. 4)
14	ICL	Double Asher	photo resist strip

[7] Surface Engineering Lab in 13-1150
[8] previously approved out-of-MTL process
[9] previously approved recipe

15	TRL	RCA	Ge RCA cleaning
16	TRL	Tube B4	amorphous Si deposition (560C)
17	Innovion		phosphorus implantation
18	TRL		double Piranha
19	ICL	RCA	RCA cleaning
20	ICL	DCVD	Oxide deposition (200nm)
21	ICL	Coater	
22	ICL	LAM	Back Etching of Poly and SiO2
23	ICL	BOE	
24	ICL	Asher	Remove resist
25	ICL	Piranha	
26	ICL	RCA	
27	ICL	RTP	annealing (800C, 3min)
28	ICL	Stepper	patterning #3
29	ICL	AME5000 Ch. B	poly-Si etching (Fig. 6)
30	ICL	Asher	photo resist strip
31	ICL	Endura	Contact Metal
32	ICL	Stepper	Patterning #4
33	ICL	Rainbow	Metal Etching
34	ICL	Asher	Photo resist strip

OR with DCVD Si grown

Process Step:

Starting with 6" wafers n++Si

Step	Lab	Machine	Action
1	ICL	RCA	RCA cleaning
2	ICL	Tube 5D	thermal oxide deposition (500nm)
3	ICL	Photo/i-Stepper	patterning #1
4	ICL	AME5000 Ch. A	oxide etching, two alternatives: 1) RIE + BOE (for last 10nm oxide) 2) RIE only (Fig. 1)
5	ICL	Asher	photo resist strip
6	ICL	Piranha	Piranha
7	ICL	RCA	RCA cleaning
8	SEL[10]	UHVCVD	Ge selectively growth[11] with phosphorus in-situ doping. (Fig. 2)
9	ICL	RCA	Ge recipe[12]
10	ICL	DCVD	PECVD oxide deposition (Fig. 3)
11	ICL	Photo/i-Stepper	patterning #2
12	ICL	BOE station	oxide BOE etching (Fig. 4)
13	ICL	Asher	photo resist strip
14	ICL	RCA	RCA cleaning Ge Recipe
15	ICL	DCVD	amorphous Si deposition (560C)

[10] Surface Engineering Lab in 13-1150
[11] previously approved out-of-MTL process
[12] previously approved recipe

			(Fig. 5)
16	Innovion		phosphorus implantation
17	ICL	Piranha	double Piranha
18	ICL	RCA	RCA cleaning
19	ICL	DCVD	Thin Oxide (25nm)
20	ICL	AME5000	RIE backside etch(SiO_2 etch)
21	ICL	RTP	Activation annealing (700C, 30sec)
22	ICL	Photo/i-Stepper	patterning #3 (Fig.6)
23	ICL	Asher	Photoresist strip
	ICL	Coater	coat photoresist on front side
26	ICL	AME5000	Etch Si Windows
27	ICL	Asher	Strip photoresist on front side (Fig. 7)
28	ICL	Piranha	Piranha
29	ICL	Endura	Ti/Al coating (50nm/500nm)
30	ICL	Photo/i-Stepper	Pattern #4
31	ICL	Rainbow	Metal etcher
32	ICL	Asher	Strip photoresist on front side (Done in around 1 hour from last step to avoid attack of the Chlorine of previous step on the material)

Appendix VI. Contact resistant experiment

Purpose: Determining the best metal contact for lower contact resistance with highly doped silicon. This experiment is important for metal contacts in laser designs.

Starting material: 4 Si substrates p-/SiO2 500nm/ PolySi 200nm thickness silicon implanted with P or B to a level of $1x10^{20}cm^{-3}$. The wafers have been processed in MTL through the following steps, starting with bare Si substrate p-:

1- RCA ICL
2- Tube 5C ICL
3- RCA TRL
4- TubeB4 TRL
5- Innovion Implantation

Used structures for characterization include Kelvin Bridges and TRLTs.

Process Step:

Step	Lab	Machine	Action
1	TRL	Acid-hood	Double Piranha
2	ICL	RCA	RCA cleaning
3	ICL	DCVD	Silicon Oxide Deposition (200nm)
4	ICL	Coater	
5	ICL	LAM	Backside Poly and Oxide removal
6	ICL	BOE	30 sec oxide removal
7	ICL	Asher	Remove photo resist

8	ICL	Piranha	Remove photo resist
9	TRL		Cleaved wafer into 9 pieces
10	TRL	RTA	Ranges between 700 to 800 C for 3-5min
11	TRL	Acid-hood	BOE
12	TRL	E-beam	Metal Deposition (A series of metals will be determined from the ones provided from TRL)
13	TRL	EV1	Patterning for contacts
14	TRL	Acid-hood	Metal strip
15	TRL	Asher	Photo resist strip
16	TRL	Tube B1	Metal Sintering
17	TRL	IV-probe	2-point probe of metal contacts

Appendix VII. a-Si Long annealing for H outdiffusion

The process consisted of a long low temperature annealing providing time and temperature for surface mobility and reduction of total hydrogen concentration in the body.

The process requires a quartz tube with controlled temperature with an error of ± 10℃. The process times and temperatures are listed below:

1) 150℃ - 8hrs
2) 200℃ - 8hrs
3) 250℃ - 8hrs
4) 300℃ - 5hrs
5) 350℃-3hrs
6) 400℃-1hr
7) 420℃-30min

This long process assures loss of the hydrogen and permits further processing with the low quality Si.

Appendix VIII. Threshold energy for CCCH indirect Auger

This derivation was based from Coldren and Corzine [178]. The momentum and energy conservation laws have to be conserved in between different carriers, such that initial stage equals final,

$$\vec{k}_1 + \vec{k}_2 = \vec{k}_3 + \vec{k}_4 \qquad \& \qquad \Delta E_1 + \Delta E_2 = -(E + \Delta E_3) + \Delta E_4$$

where $\vec{k}$ is the momentum vector in k-space and E is the energy reference used in chapter 2. In order to determine the threshold energy E_T for an auger process, we have to find the minimum energy for ΔE_4.

To simplify the problem, we assume that all the bands are parabolic, such that $\Delta E_i \propto \frac{k_i \cdot k_i}{m_{eff}}$, such that m_{eff} is m_L for i=1 ,2; m_Γ for i=4; and $m_{\mathrm{hh\ or\ lh}}$ for i=3. We add the operators $\tau = m_\Gamma / m_L$ and $\mu = m_{\mathrm{hh\ or\ lh}} / m_L$, to further simplify i=3 & 4. Notice that light holes (lh) and heavy holes(hh) are differentiated since their effective mass is different and will change the outcome of the Auger interaction.

The energy at i=4 will be independent of changes in k, ergo, the differential of d(ΔE_4) equals zero. Furthermore, $d(\Delta E_i) \propto k_i \cdot dk_i + dk_i \cdot k_i$.After rearranging and differentiating the conservation laws, we obtained,

$$\tau k_4 \cdot dk_4 = k_1 \cdot dk_1 + k_2 \cdot dk_2 + \mu k_3 \cdot dk_3 = 0 \qquad \& \qquad dk_3 = dk_1 + dk_2 - dk_4$$

Replacing dk_3 on the energy differential, and knowing that k_1=k_2,

$$2(k_1 + \mu k_3) \cdot dk_1 - \mu k_3 \cdot dk_4 = 0$$

As ΔE_4 is minimized, and $k_4 \cdot dk_4 = 0$, then $k_3 \cdot dk_4 = 0$ since $k_4 || k_3$. After substitution of the relevant terms, $k_1 = -\mu k_3$ and $k_4 = -(1 + 2\mu \ \ )k_3$. Consequently, the most possible Auger transition happens when all four transitions are collinear. Since k_3 direction is unknown, we assume two collinear behaviors. Using the equalities and the energy conservation law, it results,

$$k_3{}^2 = \frac{1}{(2\mu + 1)(\tau + 2\mu\tau - \mu)} k_g{}^2$$

The energies of the four states can be derived from this, where

$$\Delta E_1 = \Delta E_2 = \mu \Delta E_3 = \frac{\mu^2}{(2\mu+1)(\tau+2\mu\tau-\mu)} E_g \text{ and } \Delta E_4 = \frac{\tau(2\mu+1)}{(\tau+2\mu\tau-\mu)} E_g$$

This results into two different threshold energies, depending if heavy holes or light holes are used in the transition. The threshold energy for CCCH indirect becomes,

$$E_T = \Delta E_4 = m_{hh\ or\ lh} \frac{(2m_L + m_{hh\ or\ lh})}{(m_{hh\ or\ lh} + 2m_L - m_\Gamma)} E_g$$

References

1. G. E. Moore, "Cramming more components onto integrated circuits," Electronics **38**(1965).
2. I. T. R. f. Semiconductors, "ITRS 2009 Edition" (2009), retrieved http://www.itrs.net/Links/2009ITRS/Home2009.htm.
3. W. Haensch, E. J. Nowak, R. H. Dennard, P. M. Solomon, A. Bryant, O. H. Dokumaci, A. Kumar, X. Wang, J. B. Johnson, and M. V. Fischetti, "Silicon CMOS devices beyond scaling," IBM J. Res. & Dev. **50**, 339-361 (2006).
4. M. Lipson, "Overcoming the limitations of microelectronics using Si nanophotonics: solving the coupling, modulation and switching challenges," Nanotechnology **15**, S622-S627 (2004).
5. R. Kirchain and L. C. Kimerling, "A roadmap for nanophotonics," Nature Photonics **1**, 303-305 (2007).
6. J. Psota, J. Eastep, J. Miller, T. Konstantakopoulos, M. Watts, M. Beals, J. Michel, L. C. Kimerling, and A. Agarwal, "ATAC: On-Chip Optical Networks for Multicore Processors," in *Proceedings of the Fifth Annual Boston Area Architecture Workshop,* (Boston, MA, US, 2007), p. 107.
7. G. Kurian, S. Chen, C. H. O. Chen, J. E. Miller, J. Michel, W. Lan, D. A. Antoniadis, P. Li-Shiuan, L. Kimerling, V. Stojanovic, and A. Agarwal, "Cross-layer Energy and Performance Evaluation of a Nanophotonic Manycore Processor System Using Real Application Workloads," in *Parallel & Distributed Processing Symposium (IPDPS), 2012 IEEE 26th International*, 2012), 1117-1130.
8. C. Kopp, Bernabe, x, S., B. B. Bakir, J. M. Fedeli, R. Orobtchouk, F. Schrank, H. Porte, L. Zimmermann, and T. Tekin, "Silicon Photonic Circuits: On-CMOS Integration, Fiber Optical Coupling, and Packaging," Selected Topics in Quantum Electronics, IEEE Journal of **17**, 498-509 (2011).
9. R. Jones, O. Cohen, M. Paniccia, A. W. Fang, H. Park, and J. Bowers, "A hybrid silicon laser," Photon Spectra **41**, 54-+ (2007).
10. INTEL, "Intel Milestone Confirms Light Beams Can Replace Electronic Signals for Future Computers" (2010), retrieved http://www.intel.com/pressroom/archive/releases/20100727comp_sm.htm.
11. H. Park, A. W. Fang, S. Kodamaa, and J. E. Bowers, "Hybrid silicon evanescent laser fabricated with a silicon waveguide and III-V offset quantum wells," Opt. Express **13**, 9460-9464 (2005).
12. A. W. Fang, H. Park, O. Cohen, R. Jones, M. J. Paniccia, and J. E. Bowers, "Electrically pumped hybrid AlGaInAs-silicon evanescent laser," Opt. Express **14**, 9203-9210 (2006).
13. M. Riordan, L. Hoddeson, and C. Herring, "The invention of the transistor," Reviews of Modern Physics **71**, S336 (1999).
14. J. Bardeen and W. H. Brattain, "Physical Principles Involved in Transistor Action," Physical Review **75**, 1208 (1949).
15. G. K. Teal and E. Buehler, "Single-Crystal Germanium," Proceedings of the IRE **40**, 906-909 (1952).

16. J. Liu, "GeSi Photodetectors and Electro-absorption Modulators for Si Electronic-Photonic integrated Circuit," (Massachusetts Institute of Technology, Cambridge, 2007).
17. J. Liu, D. D. Cannon, K. Wada, Y. Ishikawa, S. Jongthammanurak, D. T. Danielson, J. Michel, and L. C. Kimerling, "Silicidation-induced band gap shrinkage in Ge epitaxial films on Si," Appl. Phys. Lett. **84**, 660-662 (2004).
18. J. Liu, J. Michel, W. Giziewicz, D. Pan, K. Wada, D. D. Cannon, S. Jongthammanurak, D. T. Danielson, L. C. Kimerling, J. Chen, F. O. Ilday, F. X. Kartner, and J. Yasaitis, "High-performance, tensile-strained Ge p-i-n photodetectors on a Si platform," Appl. Phys. Lett **87**, 103501 (2005).
19. D. D. Cannon, "Strain Engineered CMOS compatible Ge photodetectors " (Massachusetts Institute of Technology, Cambridge, 2004).
20. X. Sun, J. Liu, L. C. Kimerling, and J. Michel, "Room Temperature Direct Band Gap Electroluminesence from Ge-on-Si Light Emitting Diodes," Opt Lett **34**, 1198 (2009).
21. J. Liu, X. Sun, R. Camacho-Aguilera, L. C. Kimerling, and J. Michel, "Ge-on-Si laser operating at room temperature," Opt Lett **35**, 679-681 (2010).
22. R. E. Camacho-Aguilera, Y. Cai, N. Patel, J. T. Bessette, M. Romagnoli, L. C. Kimerling, and J. Michel, "An electrically pumped germanium laser," Optics Express **20**, 11316-11320 (2012).
23. S.-L. Cheng, J. Lu, G. Shambat, H.-Y. Yu, K. Saraswat, J. Vuckovic, and Y. Nishi, "Room temperature 1.6 um electroluminescence from Ge light emitting diode on Si substrate," Opt. Express **17**, 10019-10024 (2009).
24. J. Liu, X. Sun, D. Pan, X. Wang, L. C. Kimerling, T. L. Koch, and J. Michel, "Tensile-strained, n-type Ge as a gain medium for monolithic laser integration on Si," Optics Express **15**, 11272-11277 (2007).
25. X. Sun, J. Liu, L. C. Kimerling, and J. Michel, "Optical Bleaching of Thin Film Ge on Si," ECS Trans. **16**, 881-883 (2008).
26. W. Xiaoxin, L. C. Kimerling, J. Michel, and L. Jifeng, "Large transient optical gain from N⁺ Ge-on-Si," in *Group IV Photonics (GFP), 2012 IEEE 9th International Conference on*, 2012), 325-327.
27. X. Sun, "Ge-on-Si light-emitting materials and devices for silicon photonics," Cambrige, 2009).
28. "Semiconductor on NSM", retrieved http://www.ioffe.ru/SVA/NSM/Semicond/Ge/bandstr.html.
29. R. Sun, "Advanced materials, process, and designs for silicon photonic integration," (Massachusetts Institute of Technology Cambridge, 2009).
30. X. Sun, J. Liu, L. C. Kimerling, and J. Michel, "Direct gap photoluminescence of n-type tensile-strained Ge-on-Si," Applied Physics Letters **95**, 011911 (2009).
31. S. L. Chuang, "Physics of Optoelectronic Devices," in (John Wiley & Sons. Inc, 1995), 144.
32. J. Liu, D. D. Cannon, Y. Ishikawa, K. Wada, D. T. Danielson, S. Jongthammanurak, J. Michel, and L. C. Kimerling, "Deformation potential constants of biaxially tensile stressed Ge epitaxial films on Si(100)," Phys. Rev. B **70**, 155309 (2004).
33. C. G. Van de Walle, "Band lineups and deformation potentials in the model-solid theory," Physical Review B **39**, 1871 (1989).

34. W. P. Dumke, "Deformation Potential Theory for n-Type Ge," Physical Review **101**, 531-536 (1956).
35. S. Krishnamurthy and M. Cardona, "Self-consistent calculation of intervalley deformation potentials in GaAs and Ge," Journal of Applied Physics **74**, 2117-2119 (1993).
36. M. V. Fischetti and S. E. Laux, "Band structure, deformation potentials, and carrier mobility in strained Si, Ge, and SiGe alloys," Journal of Applied Physics **80**, 2234-2252 (1996).
37. M. El Kurdi, G. Fishman, S. Sauvage, and P. Boucaud, "Band structure and optical gain of tensile-strained germanium based on a 30 band <equation><bold>k</bold>∙<bold>p</bold></equation> formalism," Journal of Applied Physics **107**, 013710-013710-013717 (2010).
38. J. Liu, D. D. Cannon, K. Wada, Y. Ishikawa, S. Jongthammanurak, D. T. Danielson, J. Michel, and L. C. Kimerling, "Tensile strained Ge p-i-n photodetectors on Si platform for C and L band telecommunications," Appl. Phys. Lett. **87**, 011110 (2005).
39. X. Sun, J. Liu, L. C. Kimerling, J. Michel, and T. L. Koch, "Band-engineered Ge as gain medium for Si-based laser," in *Integrated Photonics and Nanophotonics Research and Applications (IPNRA) Topical Meeting,* (Boston, MA, USA, 2008).
40. I. V. Fistul, *Heavily Doped Semiconductors* (Nauka Press, 1969), p. 418.
41. S. C. Jain and D. J. Roulston, "A simple expression for band gap narrowing (BGN) in heavily doped Si, Ge, GaAs and GexSi1-x strained layers," Solid-State Electronics **34**, 453-465 (1991).
42. S. C. Jain, R. P. Mertens, and R. J. Van Overstraeten, "Bandgap Narrowing and Its Effects on the Properties of Moderately and Heavily Doped Germanium and Silicon," in *Advances in Electronics and Electron Physics*, W. H. Peter, ed. (Academic Press, 1991), pp. 197-275.
43. Y. C. Rodolfo Camacho-Aguilera, Zhaohong Han, Jonathan Bessette Lionel Kimerling, Jurgen Michel, "Band gap narrowing in highly doped Ge," To be review (2012).
44. J. I. Pankove and P. Aigrain, "Optical Absorption of Arsenic-Doped Degenerate Germanium," Physical Review **126**, 956-962 (1962).
45. C. Haas, "Infrared Absorption in Heavily Doped n-Type Germanium," Physical Review **125**, 1965 (1962).
46. R. K. Jain, "Calculation of the Fermi level, minority carrier concentration, effective intrinsic concentration, and einstein relation in n- and p-type germanium and silicon," physica status solidi (a) **42**, 221-226 (1977).
47. H.-C. Luan, "Ge Photodetectors for Si Microphotonics," (Massachusetts Institute of Technology, Cambridge, MA, 2001).
48. M. El Kurdi, T. Kociniewski, T. P. Ngo, J. Boulmer, D. Debarre, P. Boucaud, J. F. Damlencourt, O. Kermarrec, and D. Bensahel, "Enhanced photoluminescence of heavily n-doped germanium," Applied Physics Letters **94**, 191107-191103 (2009).
49. E. Kasper, M. Oehme, T Aguirov, J. Werner, M. Kittler, and J. Schulze, "Room temperature direct band gap emission from Ge p-i-n heterojunction photodiodes," Proceedings of Group IV Photonics 2010 (2010).

50. R. M. Sieg, J. A. Carlin, J. J. Boeckl, S. A. Ringel, M. T. Currie, S. M. Ting, T. A. Langdo, G. Taraschi, E. A. Fitzgerald, and B. M. Keyes, "High minority-carrier lifetimes in GaAs grown on low-defect-density Ge/GeSi/Si substrates," Applied Physics Letters **73**, 3111-3113 (1998).
51. I. V. Karpova, V. I. Perel, and S. M. Syrovegin, "Auger Recombination in heavily doped germanium," Soviet Physics Semiconductors **23**, 826-831 (1989).
52. E. Gaubas and J. Vanhellemont, "Comparative Study of Carrier Lifetime Dependence on Dopant Concentration in Silicon and Germanium," Journal of The Electrochemical Society **154**, H231-H238 (2007).
53. W. Lochmann, "Phonon-assisted auger recombination in indirect gap semiconductors," physica status solidi (a) **45**, 423-432 (1978).
54. R. Olshansky, C. Su, J. Manning, and W. Powazinik, "Measurement of radiative and nonradiative recombination rates in InGaAsP and AlGaAs light sources," Quantum Electronics, IEEE Journal of **20**, 838-854 (1984).
55. C. Y. Tsai, C. Y. Tsai, C. H. Chen, T. L. Sung, T. Y. Wu, and F. P. Shih, "Theoretical model for intravalley and intervalley free-carrier absorption in semiconductor lasers: Beyond the classical Drude model," Ieee J Quantum Elect **34**, 552-559 (1998).
56. Y. Cai, Z. Han, X. Wang, R. Camacho-Aguilera, L. C. Kimerling, J. Michel, and J. Liu, "Analysis of Threshold Current Behavior for Bulk and Quantum Well Germanium Laser Structures," Ieee J Sel Top Quant **In press**, 1 (2013).
57. Xiaoxin Wang, Haofeng Li, Rodolfo Camacho-Aguilera, Yan Cai, Lionel C Kimerling, J. Michel, and J. Liu, "Infrared absorption of n-type tensile-strained Ge-on-Si," Opt Lett **38**, 652 (2013).
58. J. Liu, X. Sun, L. C. Kimerling, and J. Michel, "Direct-gap optical gain of Ge on Si at room temperature," Opt. Lett. **34**, 1738-1740 (2009).
59. L. A. C. a. S. W. Corzine, *Diode Lasers and Photonic Integrated Circuits*, Microwave and Optical Engineering (John Wiley & Sons, Inc. , Santa Barbara, 1995).
60. T. Numai, *Fundamental of Semiconductor Lasers*, Optical Series (Springer, New York, 2004), pp. 83-100.
61. J. Ohtsubo, *Semiconductor Lasers*, Optical Series (Springer, New York, 2008), Vol. 111.
62. B. A. E. Saleh and M. C. Teich, *Fundamental of Photonics* (Wiley, 2007).
63. J. J. B. Alexey V. Kavokin, Guillaume Malpuech, Fabrice P. Laussy, *Microcavities*, Semiconductor Science and Technology (Oxford Science, Oxford, Great Britain, 2007), Vol. 16.
64. Thorlabs.Co., "SOA LD Comparison", retrieved http://www.thorlabs.com/images/TabImages/SOA-LD-Comparison.jpg.
65. V. N. Astratov, S. Yang, S. Lam, B. D. Jones, D. Sanvitto, D. M. Whittaker, A. M. Fox, M. S. Skolnick, A. Tahraoui, P. W. Fry, and M. Hopkinson, "Whispering gallery resonances in semiconductor micropillars," Applied Physics Letters **91**, 071115-071115-071113 (2007).
66. L. Liu, T. Spuesens, G. Roelkens, D. Van Thourhout, P. Regreny, and P. Rojo-Romeo, "A Thermally Tunable III–V Compound Semiconductor Microdisk Laser Integrated on Silicon-on-Insulator Circuits," Photonics Technology Letters, IEEE **22**, 1270-1272 (2010).

67. V. Sherstnev, A. Monakhov, A. Krier, and D. A. Wright, "InAs whispering gallery mode lasers for the mid-infrared spectral range," Optoelectronics, IEE Proceedings - **152**, 1-5 (2005).
68. T. Spuesens, D. Van Thourhout, P. Rojo-Romeo, P. Regreny, and J. M. Fedeli, "CW operation of III–V microdisk lasers on SOI fabricated in a 200 mm CMOS pilot line," in *Group IV Photonics (GFP), 2011 8th IEEE International Conference on*, 2011), 199-201.
69. M. V. Hobden, "Direct optical transitions from the split-off valence band to the conduction band in germanium," Journal of Physics and Chemistry of Solids **23**, 821-822 (1962).
70. J.-H. Park, *Chemical Vapor Deposition*, Surface Enginering Series (ASM International, Ohio, 2001), Vol. 2.
71. A. S. Grove, *Physics and Tehnology of Semiconductor Devices* (John Wiley and Sons, Inc., 1967), Vol. 1.
72. R. P. a. J. C. Bean, "Calculation of critical layer thickness versus lattice mismatch for GexSi1-x/Si strained-layer heteostructures," Applied Physics Letters **47**, 322-324 (1985).
73. H. J. H. E. Kasper, and H. Kibbel, "A one dimensional SiGe Superlattice," Journal of Applied Physics **8**, 1541-1548 (1975).
74. L. C. a. G. A. G. Masini, "Germanium thin films on silicon for detection of near-nfrared light," in *Handbook of Thin Film Materials, Volume 4: Semiconductor and Superconductor Thin Films*, H. S. Nalwa, ed. (2002), pp. 327-367.
75. E. K. a. F. Schäffler., *Semiconductor and Semimetals* (Academic Press, Boston, 1991), Vol. 33.
76. Y. Ishkawa, K. Wada, D. D. Cannon, J. Liu, H.-C. Luan, and L. C. Kimerling, "Strain-induced band gap shrinkage in Ge growth on Si substrate," Appl. Phys. Lett. **82**, 2044-2046 (2003).
77. H.-C. Luan, D. R. Lim, K. K. Lee, K. M. Chen, J. G. Sandland, K. Wada, and L. C. Kimerling, "High-quality Ge epilayers on Si with low threading-dislocation densities," Applied Physics Letters **75**, 2909-2911 (1999).
78. J. C. Bean, T. T. Sheng, L. C. Feldman, A. T. Fiory, and R. T. Lynch, "Pseudomorphic growth of Ge[sub x]Si[sub 1 - x] on silicon by molecular beam epitaxy," Applied Physics Letters **44**, 102-104 (1984).
79. B. S. Meyerson, "Low-temperature Si and SiGe epitaxy by ultrahigh-vacuum chemical deposition: process fundamentals," IBM J. Res. Develop **34**, 806-815 (1990).
80. B. Y. Tsaur, J. C. C. Fan, and R. P. Gale, "Solid-phase heteroepitaxy of Ge on <100>Si," Applied Physics Letters **38**, 176-179 (1981).
81. T. F. Kuech, M. Maenpaa, and S. S. Lau, "Epitaxial growth of Ge on <100> Si by a simple chemical vapor deposition technique," Applied Physics Letters **39**, 245-247 (1981).
82. F. K. LeGoues, B. S. Meyerson, J. F. Morar, and P. D. Kirchner, "Mechanism and conditions for anomalous strain relaxation in graded thin films and superlattices," Journal of Applied Physics **71**, 4230-4243 (1992).
83. G. S. G. Heigle, and E. Kasper, "Elastic Strain energy of graded Si/sub 1-x/Ge/sub x/ buffer layers," Thin Solid Films **222**, 184 (1992).

84. S. B. S. M. T. Currie, T. A. Langdo, C. W. Leitz, and E. A. Fitzgerald, "Controlling threading dislocation densities in Ge on Si using graded SiGe layers and chemical-mechanical polishing," Applied Physics Letters **72**, 1718 (1998).
85. S. B. S. a. E. A. Fitzgerald, "Novel dislocation structure and surface morphology effects in relaxed Ge/Si-Ge(graded)/Si structures," Journal of Applied Physics **81**, 3108 (1997).
86. K. W. H.-C. Luan, L. C. Kimerling, G. Masani, L. Colace, and G. Assanto,, "High efficiency photodetectors based on high quality epitaxial germanium grown on silicon substrates," Optical Materials **17**, 71-73 (2001).
87. C. Claeys and E. Simoen, *Fundamental and Technological Apects of Extended Defects in Germanium*, Springer Series in Materials Science (Springer, Belgium, 2009), Vol. 1.
88. J. Liu, R. Camacho-Aguilera, J. T. Bessette, X. Sun, X. Wang, Y. Cai, L. C. Kimerling, and J. Michel, "Ge-on-Si optoelectronics," Thin Solid Films **520**, 3354-3360 (2012).
89. M. N. Kabler, "Dislocation Mobility in Germanium," Physical Review **131**, 54-58 (1963).
90. H. L. Frisch and J. R. Patel, "Chemical Influence of Holes and Electrons on Dislocation Velocity in Semiconductors," Phys Rev Lett **18**, 784-787 (1967).
91. J. R. Patel, L. R. Testardi, and P. E. Freeland, "Electronic effects on dislocation velocities in heavily doped silicon," Physical Review B **13**, 3548-3557 (1976).
92. J. R. Patel and L. R. Testardi, "Electronic effects on dislocation velocities in heavily doped germanium," Applied Physics Letters **30**, 3-5 (1977).
93. N. A. El-Masry, J. C. Tarn, and N. H. Karam, "Interactions of dislocations in GaAs grown on Si substrates with InGaAs-GaAsP strained layered superlattices," Journal of Applied Physics **64**, 3672-3677 (1988).
94. G. Vanamu, A. K. Datye, and S. H. Zaidi, Journal of Crystal Growth **280**, 66 (2005).
95. T. A. Langdo, C. W. Leitz, M. T. Currie, E. A. Fitzgerald, A. Lochtefeld, and D. A. Antoniadis, "High quality Ge on Si by epitaxial necking," Appl. Phys. Lett. **75**, 3700-3702 (2000).
96. F. M. Ross, J. Tersoff, and R. M. Tromp, "Ostwald Ripening of Self-Assembled Germanium Islands on Silicon(100)," Microscopy and Microanalysis **4**, 254-263 (1998).
97. O. Madelung, *Semiconductors, Landolt Börstein New Series III* (2001).
98. P. Cantu, F. Wu, P. Waltereit, S. Keller, A. E. Romanov, S. P. DenBaars, and J. S. Speck, "Role of inclined threading dislocations in stress relaxation in mismatched layers," Journal of Applied Physics **97**, 103534 (2005).
99. S. H. Jones, L. K. Seidel, K. M. Lau, and M. Harold, "Patterned substrate epitaxy surface shapes," Journal of Crystal Growth **108**, 73-88 (1991).
100. J. Liu, R. Camacho-Aguilera, J. T. Bessette, X. Sun, X. Wang, Y. Cai, L. C. Kimerling, and J. Michel, "Ge-on-Si optoelectronics," Thin Solid Films **520**, 3354-3360 (2011).
101. V. A. Vu, D. E. Ioannou, R. Kamocsai, S. L. Hyland, A. Pomerene, and D. Carothers, "PIN Germanium Photodetector Fabrication Issues and Manufacturability," Semiconductor Manufacturing, IEEE Transactions on **23**, 411-418 (2010).
102. S. B. Samavedam, "Growth and Characterization of High Quality Relaxed Graded Silicon Germanium Layers of Integrated Photodetectors," (Massachusetts Institute of Technolgoy, Cambridge, 1998).
103. K. Wada, J. Liu, S. Jongthammanurak, D. Cannon, D. Danielson, D. Ahn, S. Akiyama, M. Popovic, D. Lim, K. Lee, H. C. Luan, Y. Ishikawa, X. Duan, J. Michel, H. Haus, and

L. Kimerling, "Si Microphotonics for Optical Interconnection," in *Optical Interconnects*, L. Pavesi and G. Guillot, eds. (Springer Berlin / Heidelberg, 2006), pp. 291-310.

104. R. Camacho-Aguilera, J. Bessette, C. Yan, L. C. Kimerling, and J. Michel, "Electroluminescence of highly doped Ge pnn diodes for Si integrated lasers," in *Group IV Photonics (GFP), 2011 8th IEEE International Conference on*, 2011), 190-192.
105. C.-A. R. Bessette J. , Cai Y., Kimerling L. C., Michel J., " Optical characterization of Ge on Si laser gain media," in *Submitted to IEEE Group Four Photonics 2011*, 2011),
106. L. Colace, G. Masini, F. Galluzzi, G. Assanto, G. Capellini, L. D. Gaspare, E. Palange, and F. Evangelisti, "Metal-semiconductor-metal near-infrared light detector based on eptixial Ge/Si," Appl. Phys. Lett. **72**, 3175-3177 (1998).
107. M. de Kersauson, R. Jakomin, M. El Kurdi, G. Beaudoin, N. Zerounian, F. Aniel, S. Sauvage, I. Sagnes, and P. Boucaud, "Direct and indirect band gap room temperature electroluminescence of Ge diodes," Journal of Applied Physics **108**, 023105-023105-023104 (2010).
108. P. Tsouroutas, D. Tsoukalas, I. Zergioti, N. Cherkashin, and A. Claverie, "Diffusion and activation of phosphorus in germanium," Materials Science in Semiconductor Processing **11**, 372-377 (2008).
109. G. Xia, "Silicon-Germanium Interdiffusion and Its Impacts on Enhanced Mobility MOSFETs," (Massachusetts Institute of Technology, Cambridge, 2006).
110. R. Olesinski, N. Kanani, and G. Abbaschian, "The Ge−P (Germanium-Phosphorus) system," Journal of Phase Equilibria **6**, 262-266 (1985).
111. "Germanium (Ge), solubility and segregation data of impurities: groups I-VIIIA," O. Madelung, U. Rössler, and M. Schulz, eds.
112. "Germanium (Ge), distribution coefficient of impurities, general," O. Madelung, U. Rössler, and M. Schulz, eds.
113. E. S. Cor Claeys, *Germanium -Based Technologies* (Elsevier, Oxford, Great Britain, 2007).
114. A. Satta, "Diffusion, activation, and regrowth behavior of high dose P implants in Ge," Appl. Phys. Lett. **88**, 162118 (2006).
115. S. Brotzmann and H. Bracht, "Intrinsic and extrinsic diffusion of phosphorus, arsenic, and antimony in germanium," Journal of Applied Physics **103**, 033508-033508 (2008).
116. J. Wagner, G. Contreras, A. Compaan, M. Cardona, and A. Axmann, "Germanium extremely heavily doped by ion-implantation and laser annealing: a photoluminescence study," Mat. Res. Soc. Symp. Proc. **23**, 147-153 (1984).
117. A. Satta, T. Janssens, T. Clarysse, E. Simoen, M. Meuris, A. Benedetti, I. Hoflijk, B. D. Jaeger, C. Demeurisse, and W. Vandervorst, "P implantation doping of Ge: Diffusion, activation, and recrystallization," in (AVS, 2006), 494-498.
118. T. K. M. El Kurdi, T.-P. Ngo, J. Boulmer, D. Débarre, P. Boucaud, J. F. Damlencourt, O. Kermarrec, and D. Bensahel "Enhanced photoluminescence of heavily n-doped germanium," Applied Physics Letters **94**, 191107 (2009).
119. D. T. P. Tsouroutas, I. Zergioti, N. Cherkashin and A. Claverie, "Diffusion and activation of phosphorus in germanium " Materials Science In Semiconductor Processing **11**, 372-377 (2008).

120. N. R. Zangenberg, J. Lundsgaard Hansen, J. Fage-Pedersen, and A. Nylandsted Larsen, "Ge Self-Diffusion in Epitaxial Si_{1-x}Ge_{x} Layers," Phys Rev Lett **87**, 125901 (2001).
121. Y. Cai, R. E. Camacho-Aguilera, J. T. Bessette, L. C. Kimerling, and J. Michel, "High n-type doped germanium for electrically pumped Ge laser," in OSA Technical Digest (online) (Optical Society of America, 2012), IM3A.5.
122. D. M. D. Plummer J.D., Griffin P.B., *Silicon VLSI Technology: Fundamentas, Practice and Modelling* (Prentice Hall, Upper Saddle River, NJ, 2000).
123. K. G. C.O. Chui, P.B. Griffin, J.D. Plummer and K.C. Saraswat, "Activation and diffusion studies of ion-implanted p and n dopants in germanium," Applied Physics Letters **83**, 2003 (2003).
124. M. S. C. a. R. Koudelka, "Accurate modelling of average phosphorus diffusivities in germanium after long thermal anneals: evidence of implant damage enhanced diffusivities," Semiconductor Science and Technology **22**, 164 (2007).
125. Y. Cai, R. Camacho-Aguilera, J. T. Bessette, L. C. Kimerling, and J. Michel, "High phosphorus doped germanium: dopant diffusion and modeling," Journal of Applied Physics **112**, 034509 (2012).
126. H. Bracht and S. Brotzmann, "Atomic transport in germanium and the mechanism of arsenic diffusion," Materials Science in Semiconductor Processing **9**, 471-476.
127. J. Singh, *Electronic and Optoelectronic Propoerties of Semiconductor Structures* (Cambridge University Press, Cambridge, 2003).
128. M. O. E. Kasper, T.Aguirov, J. werner, M.Kittler, J. Schulze, "Room temperature direct band gap emission from Ge p-i-n heterojunction photodiodes," IEEE 7th International Conference on Group IV Photonics Proceedings (2010).
129. G. D. Dilliway, R. Van Den Boom, B. Van Daele, F. E. Leys, T. Clarysse, B. Parmentier, A. Moussa, C. Defranoux, A. Benedetti, O. Richard, H. Bender, E. Simoen, and M. Meuris, "In-situ phosphorus doping of germanium by APCVD," in *SiGe and Ge: Materials, Processing, and Devices - 210th Electrochemical Society Meeting, October 29, 2006 - November 3, 2006*, ECS Transactions (Electrochemical Society Inc., 2006), 599-609.
130. C. O. C. H. Kim, K. Saraswat, and P. C. McIntyre. , Apply Physics Letters **83**, 2647 (2003).
131. H. O.-S. H. Shang, J. Ott, P. Kozlowski, S. Steen, E. C. Jones, and a. W. H. H. S. Wong, IEEE Electronic Device Letters **24**, 242 (2003).
132. B. Predel, "Ge-P (Germanium-Phosphorus)," O. Madelung, ed.
133. G. J. A. R.W.Olesinski, "The As-Ge System," Bulletin of Alloy Phase Diagrams **6**, 250-254 (1985).
134. G. J. A. R.W. Olesinski "The Ge-Sb System," Bulletin of Alloy Phase Diagrams **7**, 219-222 (1986).
135. C. O. Chui, K. Gopalakrishnan, P. B. Griffin, J. D. Plummer, and K. C. Saraswat, "Activation and diffusion studies of ion-implanted p and n dopants in germanium," Applied Physics Letters **83**, 3275 (2003).
136. S. Koffel, P. Scheiblin, A. Claverie, and V. Mazzocchi, "Doping of germanium by phosphorus implantation: Prediction of diffused profiles with simulation," Materials Science and Engineering: B **154-155**, 60-63 (2008).

137. J. Kim, S. W. Bedell, S. L. Maurer, R. Loesing, and D. K. Sadana, "Activation of Implanted n-Type Dopants in Ge Over the Active Concentration of 1×10[sup 20] cm[sup −3] Using Coimplantation of Sb and P," Electrochemical and Solid-State Letters **13**, H12 (2010).
138. S. Koffel, P. Scheiblin, A. Claverie, and V. Mazzocchi, "Doping of germanium by phosphorus implantation: Prediction of diffused profiles with simulation," Materials Science and Engineering: B **154-155**, 60-63 (2008).
139. P. Tsouroutas, D. Tsoukalas, and H. Bracht, "Experiments and simulation on diffusion and activation of codoped with arsenic and phosphorous germanium," Journal of Applied Physics **108**, 024903-024908 (2010).
140. P. A. Stolk, H. J. Gossmann, D. J. Eaglesham, D. C. Jacobson, C. S. Rafferty, G. H. Gilmer, M. Jaraiz, J. M. Poate, H. S. Luftman, and T. E. Haynes, "Physical mechanisms of transient enhanced dopant diffusion in ion-implanted silicon," Journal of Applied Physics **81**, 6031-6050 (1997).
141. R. E. Camacho-Aguilera, Y. Cai, J. T. Bessette, L. C. Kimerling, and J. Michel, "High active carrier concentration in n-type, thin film Ge using delta-doping," Opt. Mater. Express **2**, 1462-1469 (2012).
142. S. J. Bass, "Silicon and germanium doping of epitaxial gallium arsenide grown by the trimethylgallium-arsine method," Journal of Crystal Growth **47**, 613-618 (1979).
143. C. E. C. Wood, G. Metze, J. Berry, and L. F. Eastman, "Complex free-carrier profile synthesis by "atomic-plane" doping of MBE GaAs," Journal of Applied Physics **51**, 383-387 (1980).
144. H. Gossmann, A. M. Vredenberg, C. S. Rafferty, H. S. Luftman, F. C. Unterwald, D. C. Jacobson, T. Boone, and J. M. Poate, "Diffusion of dopants in B-; and Sb-delta-doped Si films grown by solid-phase epitaxy," Journal of Applied Physics **74**, 3150-3155 (1993).
145. G. Scappucci, G. Capellini, W. C. T. Lee, and M. Y. Simmons, "Ultradense phosphorus in germanium delta-doped layers," Applied Physics Letters **94**, 162106 (2009).
146. G. Scappucci, G. Capellini, W. M. Klesse, and M. Y. Simmons, "Dual-temperature encapsulation of phosphorus in germanium delta layers toward ultra-shallow junctions," Journal of Crystal Growth **316**, 81-84 (2011).
147. S.-M. Jang, K. Liao, and R. Reif, "Chemical vapor deposition of epitaxial silicon-germanium from silane and germane. II. In situ boron, arsenic, and phosphorus doping," Journal of The Electrochemical Society **142**, 3520-3527 (1995).
148. R. Camacho-Aguilera, Z. Han, Y. Cai, J. Bessette, L. Kimerling, and J. Michel, "Band gap narrowing in highly doped Ge," Submited (2012).
149. H. Kalt and M. Rinker, "Band-gap renormalization in semiconductors with multiple inequivalent valleys," Physical Review B **45**, 1139-1154 (1992).
150. P. Lautenschlager, P. B. Allen, and M. Cardona, "Temperature dependence of band gaps in Si and Ge," Physical Review B **31**, 2163-2171 (1985).
151. J. Liu and L. H. Liu, "First-principles study of temperature-dependent optical properties of semiconductors from ultraviolet to infrared regions," Journal of Applied Physics **111**, 083508-083506 (2012).
152. K. P. O'Donnell and X. Chen, "Temperature dependence of semiconductor band gaps," Applied Physics Letters **58**, 2924-2926 (1991).

153. Y. P. Varshni, "Temperature Dependence of Energy Gap in Semiconductors," Physica **34**, 149-& (1967).
154. Y. P. Varshni, "Band-to-Band Radiative Recombination in Groups 4, 6, and 3-V Semiconductors (I)," Phys Status Solidi **19**, 459-& (1967).
155. L. Viña, S. Logothetidis, and M. Cardona, "Temperature dependence of the dielectric function of germanium," Physical Review B **30**, 1979-1991 (1984).
156. R. Camacho-Aguilera, Z. Han, Y. Cai, L. C. Kimerling, and J. Michel, "Direct Band gap narrowing in highly doped Ge," Submited (2013).
157. M. El Kurdi, G. Fishman, S. Sauvage, and P. Boucaud, "Band structure and optical gain of tensile-strained germanium based on a 30 band k center dot p formalism," Journal of Applied Physics **107**, 013710 (2010).
158. H. S. Sommers, Jr., "Degenerate Germanium. II. Band Gap and Carrier Recombination," Physical Review **124**, 1101 (1961).
159. T. Arguirov, M. Kittler, and N. V. Abrosimov, "Room temperature luminescence from Germanium," Journal of Physics: Conference Series **281**, 012021 (2011).
160. H. M. van Driel, A. Elci, J. S. Bessey, and M. O. Scully, "Photoluminescence spectra of germanium at high excitation intensities," Solid State Comm. **20**, 837-840 (1976).
161. E. Kasper, M. Oehme, T. Arguirov, J. Werner, M. Kittler, and J. Schulze, "Room Temperature Direct Band Gap Emission from Ge p-i-n Heterojunction Photodiodes," Advances in OptoElectronics **2012**, 916275 (2012).
162. R. A. Abram, "Chapter 5 Effects of Heavy Doping and High Excitation on the Band Structure of Gallium Arsenide," in *Semiconductors and Semimetals*, K. A. Richard and S. L. Mark, eds. (Elsevier, 1993), pp. 259-316.
163. T. N. Morgan, "Broadening of Impurity Bands in Heavily Doped Semiconductors," Physical Review **139**, A343-A348 (1965).
164. R. E. Camacho-Aguilera, Y. Cai, J. Bessette, L. Kimerling, and J. Michel, "High active carrier concentration in n-type, thin film Ge using delta-doping," Opt Mater Express **2**, 1462-1469 (2012).
165. C. S. LaPorta, J. C. Kimball, J. T. Borenstein, and J. W. Corbett, "Comments on thermal donor states in silicon and germanium," Journal of Physics C: Solid State Physics **19**, L627 (1986).
166. K. F. Berggren and B. E. Sernelius, "Band-gap narrowing in heavily doped many-valley semiconductors," Physical Review B **24**, 1971 (1981).
167. P. Y. Yu and M. Cardona, *Fundamentals of Semiconductors*, Physics and Materials Properties (Springer, 1996).
168. H. Hanson, S. W. Keckler, S. Ghiasi, K. Rajamani, F. Rawson, and J. Rubio, "Thermal response to DVFS: analysis with an Intel Pentium M," in *Proceedings of the 2007 international symposium on Low power electronics and design,* (ACM, Portland, OR, USA, 2007), pp. 219-224.
169. D. C. Herbert, "Electron-phonon interaction and inter-valley scattering in semiconductors," Journal of Physics C: Solid State Physics **6**, 2788 (1973).
170. G. P. Srivastava, *The phyiscs of phonons* (Taylor & Francis, 1990), Vol. 1.
171. M. L. Cohen, "Electron-Phonon Self-Energies in Many-Valley Semiconductors," Physical Review **128**, 131-& (1962).
172. *Handbook Series on Semiconductor Parameters* (World Scientific, 1996).

173. X. Sun, J. Liu, L. C. Kimerling, and J. Michel, "Toward a Germanium Laser for Integrated Silicon Photonics," Selected Topics in Quantum Electronics, IEEE Journal of **16**, 124-131 (2010).
174. S. K. Ghandhi, *Semiconductor Power Devices* (John Wiley & Sons Inc 1977), Vol. 1.
175. W. M. Loh, S. E. Swirhun, T. A. Schreyer, K. Saraswat, and R. M. Swanson, "An accurate method to extract specific contact resistivity using cross-bridge Kelvin resistors," Transaction on Electron Device Letters, IEEE **34**, 441-443 (1987).
176. P. T. Landsberg and D. J. Robbins, "Lifetime broadening of a parabolic band edge of a pure semiconductor at various temperatures," Solid-State Electronics **28**, 137-141 (1985).
177. J. Liu, X. Sun, R. Camacho-Aguilera, L. C. Kimerling, and J. Michel, "Ge-on-Si laser operating at room temperature," Opt. Lett. **35**, 679-681 (2010).
178. L. A. Coldren and S. W. Corzine, *Diode Lasers and Photonic Integrated Circuits* (Wiley-Interscience Publication, Santa Barbara, 1995).
179. R. Leancu, N. Moldovan, L. Csepregi, and W. Lang, "ANISOTROPIC ETCHING OF GERMANIUM," Sensors and Actuators a-Physical **46**, 35-37 (1995).
180. J. Liu, X. Sun, Y. Bai, K. E. Lee, E. A. Fitzgerald, L. C. Kimerling, and J. Michel, "Efficient above-band-gap light emission in germanium," Chin. Opt. Lett. **7**, 271-273 (2009).
181. G. Scappucci, G. Capellini, W. M. Klesse, and M. Y. Simmons, "Phosphorus atomic layer doping of germanium by the stacking of multiple δ layers," Nanotechnology **22**, 375203 (2011).
182. R. E. Camacho-Aguilera, Y. Cai, J. T. Bessette, D. Kita, L. C. Kimerling, and J. Michel, "High active carrier concentration in n-type, thin film Ge using delta-doping," submitted for publication (2012).
183. M. C. T. Bahaa E. A. Saleh, *Fundamentals of Photonics,* 2 ed. (Wiley-Interscience, 2007), p. 1200.
184. H. Park, A. W. Fang, S. Kodama, and J. E. Bowers, "Hybrid silicon evanescent laser fabricated with a silicon waveguide and III-V offset quantum well," Optics Express **13**, 9460-9464 (2005).
185. B. W. Hakki, "Gain spectra in GaAs double-heterostructure injection lasers," Journal of Applied Physics **46**, 1299-1306 (1975).
186. S. Xiaochen, L. Jifeng, L. C. Kimerling, and J. Michel, "Toward a Germanium Laser for Integrated Silicon Photonics," Selected Topics in Quantum Electronics, IEEE Journal of **16**, 124-131 (2010).
187. W. T. Tsang, "Extremely low threshold (AlGa)As graded-index waveguide separate-confinement heterostructure lasers grown by molecular beam epitaxy " Appl. Phys. Lett. **40**, 217-219 (1982).